



IntechOpen

Modeling and Simulation in Engineering Sciences

*Edited by Noreen Sher Akbar
and O. Anwar Beg*



WEB OF SCIENCE™



MODELING AND SIMULATION IN ENGINEERING SCIENCES

Edited by **Noreen Sher Akbar**
and **O. Anwar Bég**

Modeling and Simulation in Engineering Sciences

<http://dx.doi.org/10.5772/62109>

Edited by Noreen Sher Akbar and O. Anwar Beg

Contributors

Mohammad Reza Safaei, Marjan Goodarzi, Akeel Shebeeb Kherbeet, Mahidzal Dahari, Aminhossein Jahanbin, Ali Kianifar, Samira Gharekhani, Guillaume Savriama, Nadjib Semmar, Simon Lopez-Ramirez, Gerardo Mariano Pineda-Torres, Cecilia Durán-Valencia, Fernando Barragán-Aroche, Šarūnas Skuodis, Krzysztof Mogielnicki, Bing Wang, ZhaoXin Ren, Wei Wei, Jorge Oliveira, Tao Huang, Detang Lu, Ion Lancranjan, Dan Savastru, Sorin Miclos, Marina Tautan, Jean-Luc Autran, Daniela Munteanu, Soilihi Moindjie, Tarek Saad Saoud, Victor Malherbe, Gilles Gasiot, Sylvain Clerc, Philippe Roche, Víctor Manuel López-Hirata, Małgorzata Kopytko, Piotr Martyniuk

© The Editor(s) and the Author(s) 2016

The moral rights of the and the author(s) have been asserted.

All rights to the book as a whole are reserved by INTECH. The book as a whole (compilation) cannot be reproduced, distributed or used for commercial or non-commercial purposes without INTECH's written permission.

Enquiries concerning the use of the book should be directed to INTECH rights and permissions department (permissions@intechopen.com).

Violations are liable to prosecution under the governing Copyright Law.



Individual chapters of this publication are distributed under the terms of the Creative Commons Attribution 3.0 Unported License which permits commercial use, distribution and reproduction of the individual chapters, provided the original author(s) and source publication are appropriately acknowledged. If so indicated, certain images may not be included under the Creative Commons license. In such cases users will need to obtain permission from the license holder to reproduce the material. More details and guidelines concerning content reuse and adaptation can be found at <http://www.intechopen.com/copyright-policy.html>.

Notice

Statements and opinions expressed in the chapters are these of the individual contributors and not necessarily those of the editors or publisher. No responsibility is accepted for the accuracy of information contained in the published chapters. The publisher assumes no responsibility for any damage or injury to persons or property arising out of the use of any materials, instructions, methods or ideas contained in the book.

First published in Croatia, 2016 by INTECH d.o.o.

eBook (PDF) Published by IN TECH d.o.o.

Place and year of publication of eBook (PDF): Rijeka, 2019.

IntechOpen is the global imprint of IN TECH d.o.o.

Printed in Croatia

Legal deposit, Croatia: National and University Library in Zagreb

Additional hard and PDF copies can be obtained from orders@intechopen.com

Modeling and Simulation in Engineering Sciences

Edited by Noreen Sher Akbar and O. Anwar Beg

p. cm.

Print ISBN 978-953-51-2608-9

Online ISBN 978-953-51-2609-6

eBook (PDF) ISBN 978-953-51-4188-4

We are IntechOpen, the first native scientific publisher of Open Access books

3,450+

Open access books available

110,000+

International authors and editors

115M+

Downloads

151

Countries delivered to

Our authors are among the
Top 1%

most cited scientists

12.2%

Contributors from top 500 universities



WEB OF SCIENCE™

Selection of our books indexed in the Book Citation Index
in Web of Science™ Core Collection (BKCI)

Interested in publishing with us?
Contact book.department@intechopen.com

Numbers displayed above are based on latest data collected.
For more information visit www.intechopen.com



Meet the editors



Dr. Noreen Sher Akbar joined *National University of Sciences and Technology, Islamabad, Pakistan*, in 2012. She works in fluid mechanics, heat transfer and nanofluids. She obtained her Ph.D. in 2012 in applied mathematics (fluid mechanics). She has published over 230 journal papers and won several awards for teaching and research. She was declared as the best youngest scientist of Pakistan.



Dr. O. Anwar Bég joined Salford University in March 2016. He works in fluid mechanics and heat transfer. He obtained his Ph.D. in 1995 in computational magnetohydrodynamics from Manchester University, UK. He has taught fire, aerospace and mechanical engineering at several universities. He has published over 320 journal papers and 5 books and won several awards for teaching and research.

Contents

Preface XI

Section 1 Mechanical and Aerospace Engineering 1

Chapter 1 **Numerical Simulation in Microforming for Very Small Metal Elements 3**

Krzysztof Mogielnicki

Chapter 2 **Numerical Simulation of Compressible Reactive Flows 29**

Bing Wang, Zhao Xin Ren and Wei Wei

Section 2 Electrical and Electronic Engineering 51

Chapter 3 **Hybrid Time-Frequency Numerical Simulation of Electronic Radio Frequency Systems 53**

Jorge F. Oliveira

Chapter 4 **HgCdTe Mid- and Long-Wave Barrier Infrared Detectors for Higher Operating Temperature Condition 71**

Małgorzata Kopytko and Piotr Martyniuk

Chapter 5 **Numerical Simulation Methods Applied at Fiber Grating Sensors Design 91**

Dan Savastru, Sorin Miclos, Marina Tautan and Ion Lancranjan

Chapter 6 **Charge Collection Physical Modeling for Soft Error Rate Computational Simulation in Digital Circuits 115**

Jean-Luc Autran, Daniela Munteanu, Soilihi Moindjie, Tarek Saad Saoud, Victor Malherbe, Gilles Gasiot, Sylvain Clerc and Philippe Roche

Section 3 Computer Engineering 139

Chapter 7 **Training Images-Based Stochastic Simulation on Many-Core Architectures 141**

Tao Huang and Detang Lu

Section 4 Materials and Metallurgical Engineering 159

Chapter 8 **Numerical Simulation of Laser Processing Materials: An Engineering Approach 161**

Guillaume Savriama and Nadjib Semmar

Chapter 9 **Mathematical Modeling for Nanofluids Simulation: A Review of the Latest Works 189**

Mohammad Reza Safaei, AminHossein Jahanbin, Ali Kianifar, Samira Gharehkhani, Akeel Shebeeb Kherbeet, Marjan Goodarzi and Mahidzal Dahari

Chapter 10 **Application of Phase-Field Method to the Analysis of Phase Decomposition of Alloys 221**

Erika O. Avila-Davila, Victor M. Lopez-Hirata and Maribel L. Saucedo-Muñoz

Section 5 Geotechnical Civil Engineering 243

Chapter 11 **DEM Simulation Based on Experimental Testing 245**

Dr Šarūnas Skuodis

Section 6 Chemical Engineering 265

Chapter 12 **Impact of Fluid Flow on Free Radical Polymerization in a Batch Reactor 267**

Gerardo M. Pineda-Torres, Cecilia Durán-Valencia, Fernando Barragán-Aroche and Simon López-Ramírez

Preface

This book features state-of-the-art contributions in mathematical, experimental and numerical simulations in engineering sciences. The rapid developments in many areas of technology in the twenty-first century have placed increased focus on improving simulation methods and also experimental testing procedures. Both approaches are complimentary to each other and enable optimized delivery of solutions and performance of modern industrial and technological products and systems. The contributions in this book, which comprise twelve chapters, are organized in six sections spanning the major fields of engineering, i.e., mechanical, aerospace, electrical, electronic, computer, materials, metallurgical, geotechnical and chemical engineering. Many complex industrial problems have been addressed by contributors, employing a range of sophisticated modelling and computational simulation techniques. Chapters featured address ABAQUS finite element simulation in micro-forming for extremely small metallic components, weighted essentially non-oscillatory (WENO) numerical analysis of compressible reactive flows (including combustion of fuel droplets), partitioned frequency-time method computational analysis of radio frequency circuits, APSYS-platform based computational modelling for HgCdTe barrier infrared detectors, transfer matrix method numerical computation of optical properties of fiber Bragg and long-period fiber gratings, Monte Carlo simulation of radiation-induced charge carriers in semiconductors, multi-point statistical methods (MPS) simulation of parallel strategies for implementation on many-core architecture computers, Comsol finite element simulation of laser processing of materials, finite difference computation with the “phase field method” for phase decomposition in binary alloys, Lagrangian-Eulerian and Eulerian-Eulerian *mathematical modelling of single and two-phase nanofluid dynamics*, discrete element method (DEM) and experimental testing of geo-materials and finally ANSYS FLUENT computational fluid dynamics simulation of rheo-kinetic mixing processes in a batch reactor with free radical polymerization. Contributors are all very active researchers in their respective fields and are truly international, being based in Poland, China, Portugal, Romania, France, Mexico, Malaysia, Italy, Iran and Lithuania. It is envisaged that the chapters will be well-received by readers and will provide an excellent insight into advanced simulation procedures for multi-physical engineering topics of relevance to many diverse areas of technology in the twenty-first century.

Dr. Noreen Sher Akbar

DBS&H, CEME, National University of Sciences and Technology,
Islamabad, Pakistan

Dr. Anwar Bég

Fluid Mechanics, Spray Research Group,
School of Computing, Science and Engineering,
University of Salford,
Manchester, UK

Mechanical and Aerospace Engineering

Numerical Simulation in Microforming for Very Small Metal Elements

Krzysztof Mogielnicki

Additional information is available at the end of the chapter

<http://dx.doi.org/10.5772/64275>

Abstract

Microforming is a technology of very small metal elements production, which are required as a parts for many industrial products resulting from microtechnology. This chapter gives a review of the state-of-the-art microforming of metals and its numerical simulations. Phenomena occurring in the miniaturization of microbulk-forming technologies are described. The main problems in microforming are size effects, which have physical and structural sources and directly affect the material flow mechanics in microscale. Size effects must be taken into account in all areas of the forming process chain, demanding new solutions, especially in workpiece structure and die surface numerical modeling.

Keywords: microforming, size effects, numerical simulation

1. Introduction

Trend of miniaturization of everyday devices increases industry demand for efficient production of miniature parts. Machining production technologies of small-dimension elements by turning, milling, and polishing are well known for a long time. However, these methods are not efficient enough for the great demand for small and handy devices. This makes engineers to search for new methods of microelements manufacturing or to adapt traditional ones for the requirements of miniaturization.

Microforming is an adopted technology of production of small parts by metal forming. This process is characterized by good productivity, high dimensions accuracy, proper surface smoothness, high material usage, and good mechanical properties of manufactured items,

which makes it a good alternative to machining. Excepting benefits, microforming also brings some limitations, for example, limited forming possibilities of deformed materials or narrow shapes of obtained elements. Approaches of microforming methods are presented in **Figure 1**.

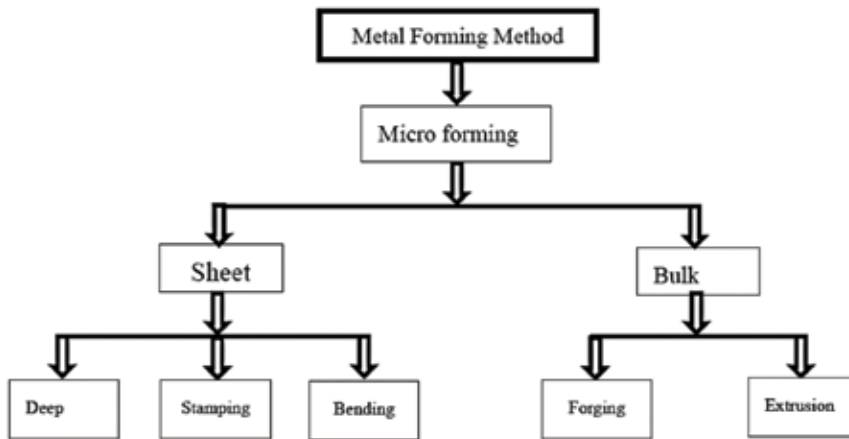


Figure 1. Microforming methods [1].

Comparing microforming to traditional forming process, it is obvious that while going to a microscale some process parameters, such as grain size or surface structure, keep constant [2]. Relationships between the dimensions of treated items and morphometric parameters of their microstructure and surface geometry, in billets as well as in tools, are different in macro- and microscale. This leads to the formation of the size effect phenomenon. In the available technological knowledge relating to conventional macroscale forming methods, presence of size effects does not permit direct application into microforming of metals [3–6]. Microforming is defined as the forming of the part features with at least two dimensions in the submillimeter range [3]. **Figure 2** presents some microparts made by microforming processes.

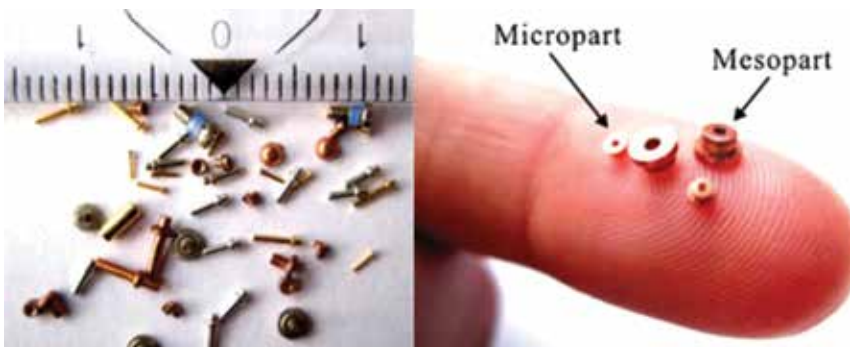


Figure 2. Mechanical microparts formed by microforming [7, 8].

Figure 3 presents all the issues which need to be considered in microforming system. There are four factors influencing the material deformation: tool-workpiece interface condition, grain size, workpiece size, and element feature size [7]. These factors further affect the efficiency of microforming system and the quality of manufactured items influencing on such a process parameters as: deformation load, forming stability (scatter of the process variables), defects of deformation, dimensional accuracy, mechanical properties, and the quality of achieved surface.

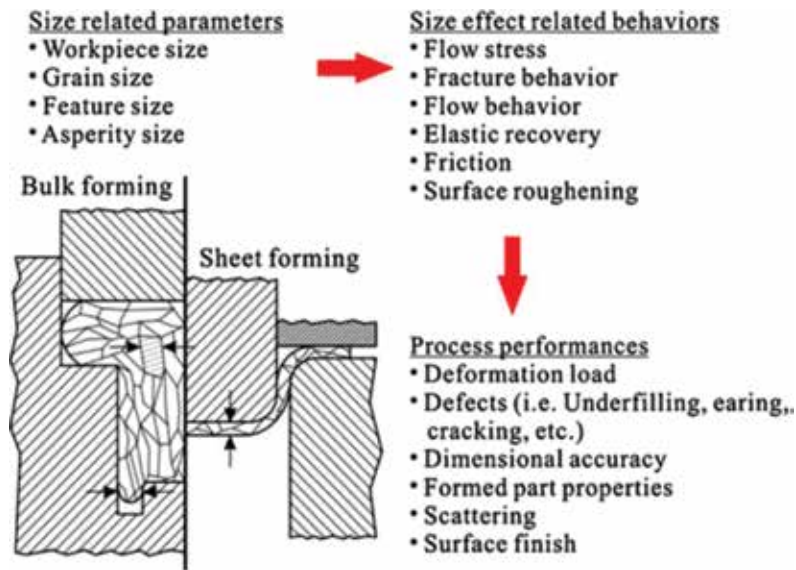


Figure 3. Issues related to size effect in microforming system [7].

The primary problem connected with microforming is the so-called “size effect” ensuing from same miniaturization. The occurrence of unpredictable changes in process parameters, while treating similar scaled workpieces, is called size effect [9]. These effects distinguish described process from conventional methods of metal forming, and significantly influence on the possibilities and limitations of this technology. Sources of size effect formation can be divided into two groups [2, 6]: physical—related to the workpiece size and the forces affecting the process; structural—induced by the microstructure of the material.

Physical sources:

- Surface-to-volume (S/V) ratio size effect—with element size decreasing, the S/V ratio increases, which makes the surface effects more crucial.
- Forces relation size effect: van der Waals forces, surface tension, and gravitation—these forces can be neglected in conventional forming processes. However, they must be taken into account in the case of microforming, because they are relatively considerable regarding the process forces and can directly affect its conditions.

Structural sources:

- Grain size to element thickness size effect—the grain size of metallic materials results from the material properties and determined by the casting condition, the thermal and mechanical treatments. It is impossible to obtain each material with each grain size, thus the grain size cannot be scaled down in parallel to the element dimension. **Figure 4** schematically shows microformability of polycrystalline and amorphous materials.

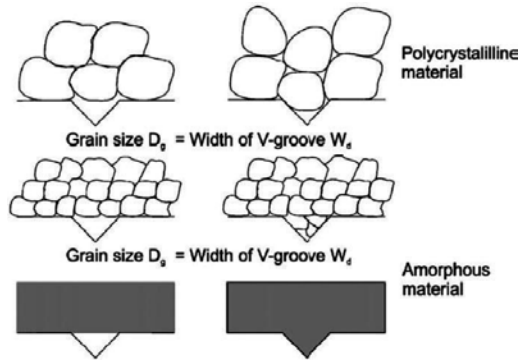


Figure 4. Microformability of polycrystalline and amorphous material [10].

In conventional metal forming operations all treated materials are considered as homogeneous. In microforming processes they are heterogeneous, because of relatively large grains size to the billet volume. As the grain size increases, the grain structure of the billet becomes to be more heterogeneous and the material shows anisotropic behavior in the submillimeter dimensional range. The anisotropic behavior of the workpiece material can directly change local deformation mechanisms as shown in **Figure 5**.

- Surface structure scalability (SSS) size effect—similarly to grain size, it is often not possible to reduce the die and billet surface roughness with the element dimension, due to that the surface structure scalability is the source of size effects. In lubrication as well as in dry conditions, SSS leads to a size-dependent friction behavior.

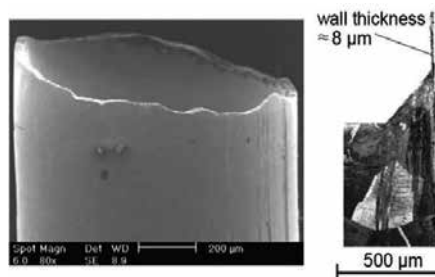


Figure 5. Backward extrusion of a billet composed of heterogeneous grain structure [3].

Microforming is a relatively young technology, developed in the last two decades, but more and more research centers in the world deal with it. Together with reports of experimental work results, attempts of identified numerical simulating phenomena are undertaken and presented.

2. Influence of size effects on deformation behavior in microforming processes

2.1. Flow stress

Flow stress decreases as workpiece size decreases [5, 11, 12]. Surface grains of the deformed material have lesser constraints compared to internal ones. Distribution of dislocations in surface grain boundaries is different from that of internal. The surface grains have a lower flow stress. When the plastically treated detail size is decreased to microscale and the grain size is relatively large, there are small number of grains constituting the workpiece and the volume fraction of surface grains increases significantly—surface layer model (Figure 6). Analogously, increase of grain size in small element reduces their number in its volume. This leads to decrease of grainy material flow stress in microscale (Figure 7).

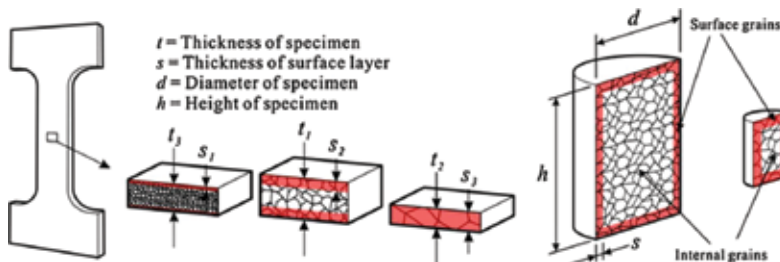


Figure 6. Change of surface grains volume fraction with decreasing of specimen size—surface layer model [13, 14].

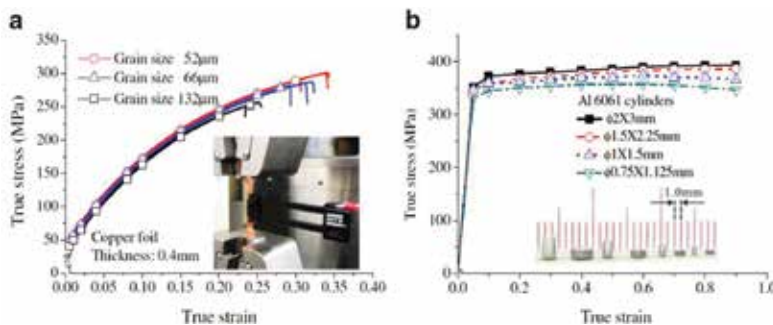


Figure 7. Grain and specimen flow stress size effects in: (a) tensile; (b) compression tests [13, 15].

2.2. Fracture

Similarly to flow stress, fracture strain decreases with the decrease of specimen size [16, 17] and the increase of grain size [12]. This phenomenon was found in tensile tests of wire and thin details. Fracture takes place through the localized shearing in the individual grain (**Figure 8**) [18–20]. The fracture strain increases also with the decrease of workpiece size in compression of bulk metal [21]. The tensile-tested material in microscale can be considered as a chain and each specimen's perpendicular section acts as a chain link (**Figure 9**). Material yields when all the grains in the section yield and the initial yielding occurs at the weakest section consisting of the soft grains [23]. The smaller the number of grains in the section, the higher the probability to find one with a significantly large fraction of soft grains decreasing the fracture strain.

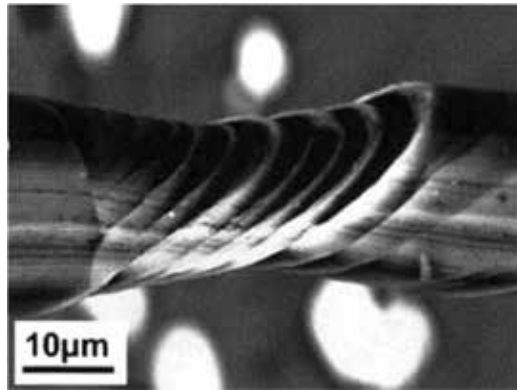


Figure 8. Scanning electron micrograph of a tensile-tested aluminum wire with a diameter of 25 μm [18].

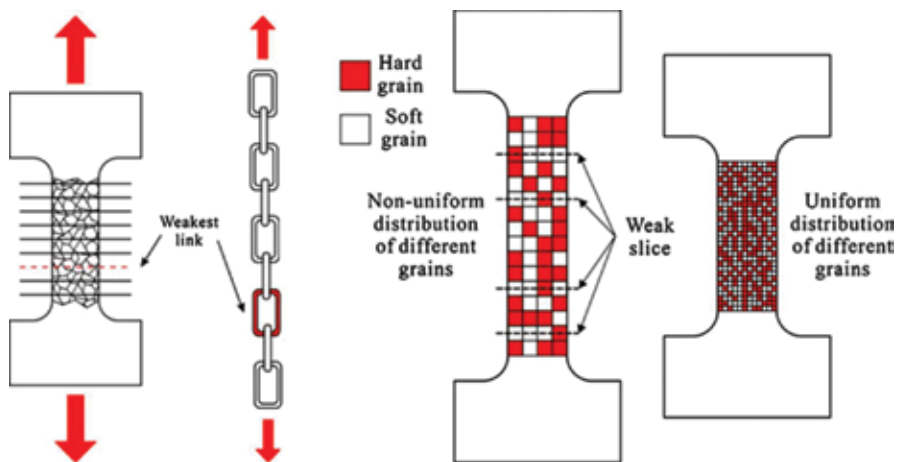


Figure 9. Schematic illustration of yielding at the weakest section of extended material [22].

2.3. Flow behavior

Inhomogeneous and anisotropic material behavior causes the irregular flow of formed workpiece geometry with the decrease of its size and the increase of grain size [24]. Chan et al. [12] experimentally presented decrease of flow stress, scatter of obtained data, and inhomogeneous specimen deformation with decrease of the ratio of element size to its grain size. Flow stress decrease because of grain boundary surface area to billet volume ratio gets small and the grain boundary strengthening effect is reduced. In addition, when the workpiece volume contains only a few grains (**Figure 10**), their size, shape, and orientation affect the deformation process significantly, leading to the scatter of the obtained data, for example stress-strain curves (**Figure 11**), and to the inhomogeneous billet deformation.

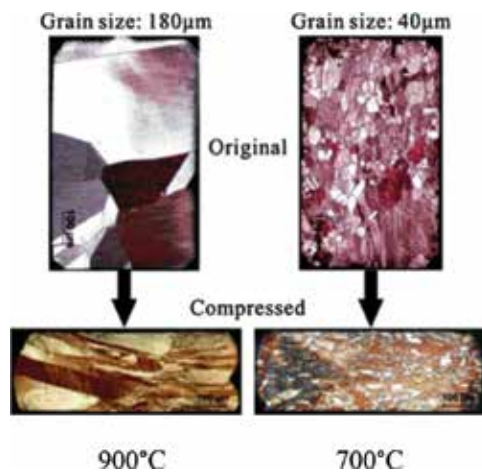


Figure 10. Microstructures of compressed specimens annealed in different temperatures [12].

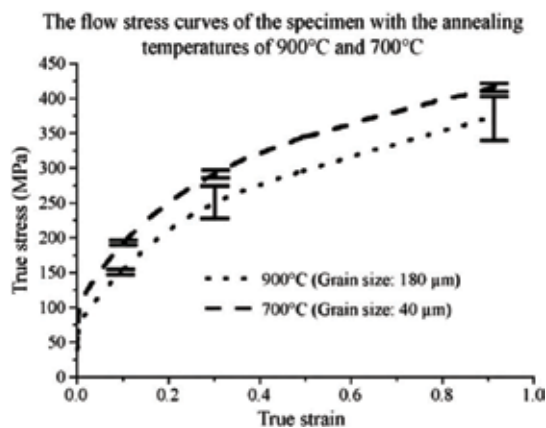


Figure 11. Flow stress curves of the billets with different grain size [12].

Flow stress size effect (**Figure 12**) and inhomogeneous deformation behavior were included in FE simulation of microcompression tests. Grain properties composite model was proposed. Grains were divided into several groups with assigned corresponding stress-strain curves. The flow stress curves of the testing samples and the scatter effect can be then estimated based on Eq. (1):

$$\sigma(\varepsilon) = \sum_{i=1}^n V_i \cdot \sigma_i(\varepsilon) \tag{1}$$

where n is the total number of grains in the billet, V_i is the volume fraction (area fraction in two-dimensional case) of the i th grain, and $\sigma_i(\varepsilon)$ is the flow stress of the i th grain.

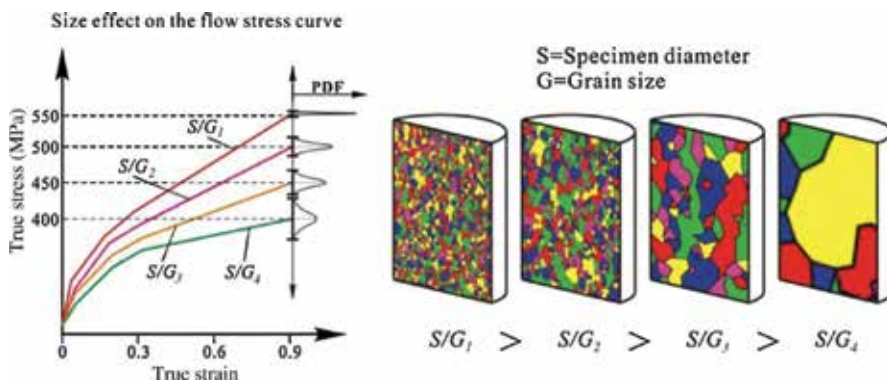


Figure 12. Illustration of flow stress size effect [12].

The volume/area fraction of each grain in the testing sample was estimated based on metallographies. The flow stress curves were then assigned to the grains randomly, as it is shown in Figure 13.

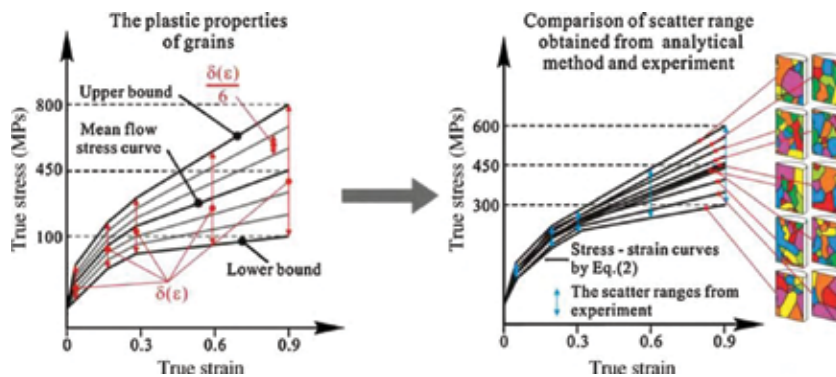


Figure 13. Spread $\sigma(\varepsilon)$ of the grains flow stress-strain curves [12].

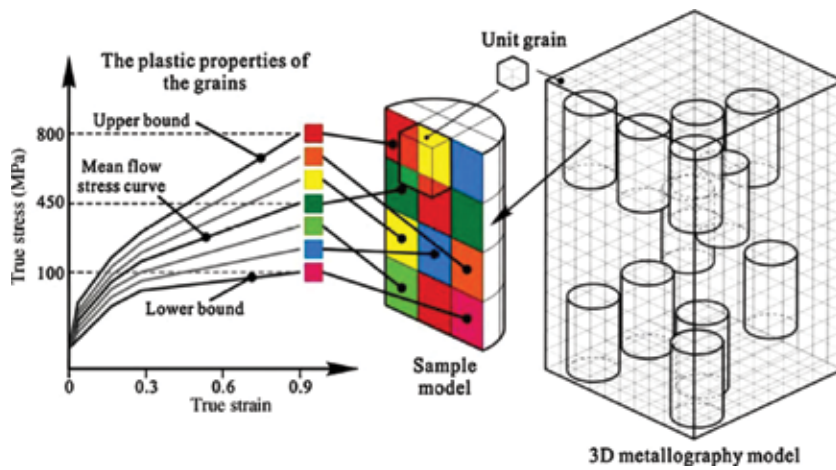


Figure 14. Schematic illustration of the 3D full-scale model with cubic grain.

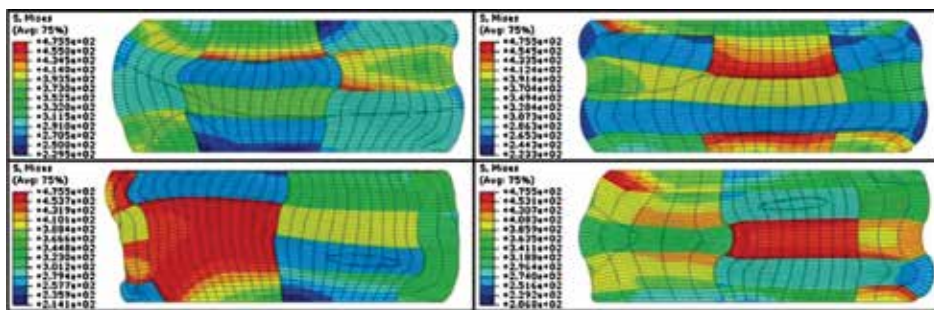


Figure 15. Stress distribution in the 3D full-scale models with surface-to-grain ratio of 2.8 [12].

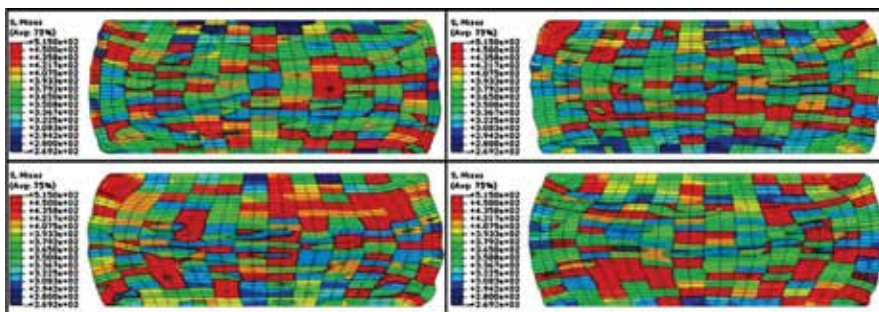


Figure 16. Stress distribution in the 3D full-scale models with surface-to-grain ratio 12.5 [12].

3D full-scale simulations using a commercial CAE system, ABACUS, were conducted with eight-node linear brick element. Grain was represented as a cube for simplification

(Figure 14). The grain properties identified by Eq. (1) were employed into the models. The grain interior and grain boundary were considered as a single body, while the change of grain boundary strengthening effect due to the change of surface-to-grain ratio was taken into account with varying the mean flow stress of grains. FE simulation of compression of billets consisting of individual grains results showed the inhomogeneous workpiece deformation with the decreasing ratio of specimen size to grain size (Figures 15 and 16). In 3D full-scale model, the asymmetry of the material deformation behavior and grain properties was taken into account. The results showed that the scatter effect of the flow stress curve increases with increasing grain size and the achieved scatter range had a good agreement with the experimental result.





| Holding time (h) | 0.1 | 0.5 | 2 | 8 |
|------------------------------|-----------------------------------------------------------------------------------|-----------------------------------------------------------------------------------|-----------------------------------------------------------------------------------|------------------------------------------------------------------------------------|
| Grain size (μm) | 59 | 125 | 240 | 470 |
| λ | 7.5 | 3 | 1.6 | 0.85 |
| Microstructures |  |  |  |  |

Figure 17. Microstructure of specimens and grain size, λ = specimen radius/grain size [25].

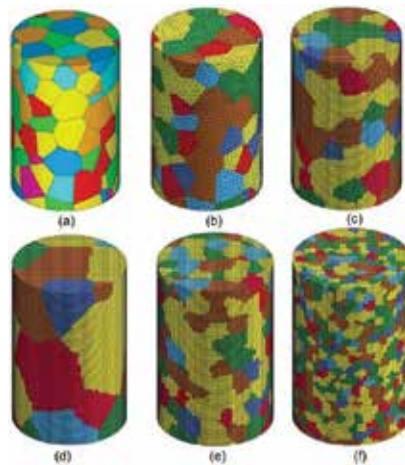


Figure 18. Aggregates of polycrystalline (a) tessellation in 140 Voronoi polyhedra; (b) freely meshed model with 140 subdomains; (c–f) Microstructure mapping on a 1313×60 cubic element mesh and domain with subdomain numbers 140, 26, 385, and 2520, respectively [25].

Voronoi tessellation can be adopted to describe the polycrystalline aggregate [25–27]. Lu et al. [25] proposed a mixed material model based on modified Hall-Petch relationship, surface layer

model, and grained heterogeneity (e.g., grain size, shape, and deformability). Pure copper compression experiment was performed (**Figure 17**). Generated virtual microstructures which can be implemented in the commercial FE code are presented in **Figure 18**.

The deformed part can be represented by a space tessellation into 3D Voronoi diagram which describes grain boundary [25]. Voronoi diagram is defined as n distinct regions, V_i based on an open set Ω , and n different seeds z_i ($i = 0, 1, \dots, n - 1$) such as:

$$V_i = \left\{ w \in \Omega \mid d(w, z_j) > d(w, z_i) \forall j = 0, 1, \dots, j \neq i \right\} \quad (2)$$

where d is the function of distance. Voronoi polyhedra are the influence zones of these grains that are their mass center.

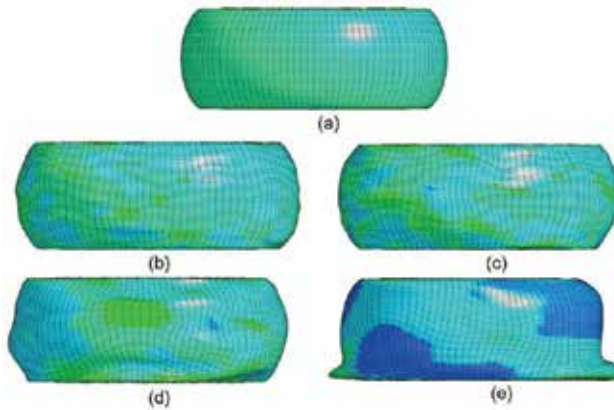


Figure 19. Profile of specimens after compression, (a) homogenous model with $\lambda = 1.6$, (b) $\lambda = 7.5$, (c) $\lambda = 3$, (d) $\lambda = 1.6$, (e) $\lambda = 0.85$ [25].

A 3D domain is decomposed into a certain number of subdomains. Then, the seeds are spread into these subdomains. Assuming the center of a cube is (x, y, z) , the seed will lie $\lambda\delta a/2$ away from the central point. The coordinate of the seed position should be $(x + \lambda\delta a/2, y + \lambda\delta a/2, z + \lambda\delta a/2)$. δ is the maximum distance between the seed and the cubic center, and λ is a random number between -1 and 1 . Both δ and λ are the so-called shape factors which will determine the shapes of the Voronoi cells. A critical distance d between different seeds is defined to prevent each seed from being too close to another. After that, 3D Voronoi polyhedra can be generated by taking these seeds as the generating points [25].

Obtained from nanoindentation hardness of grains was used to identify the deformability of individual grain inside the billet. Applying developed material model, the microcompression test of pure copper was numerically simulated (**Figure 19**) using commercial the FEM software ANSYS/LS-DYNA. Numerical analyses results show that the scatter of deformation behavior becomes significant with decreasing factor λ , where λ is the specimen radius/grain size.

2.4. Elastic recovery

Springback increases with decreasing ratio of workpiece thickness to grain size [15, 28]. Liu et al. [15] used the pure copper sheet foils with the thickness from 0.1 to 0.6 mm as the testing material for tensile test and microbending (**Figure 20**). It was founded that the springback angle increases with the decreasing metal element thickness. This is consistent with the conventional bending knowledge specific for macroscale bending. Increase in the scatter of springback angle with decreasing sheet thickness was also found. It was concluded that the main reason for that is elastic anisotropy of surface grain due to grain orientation difference.

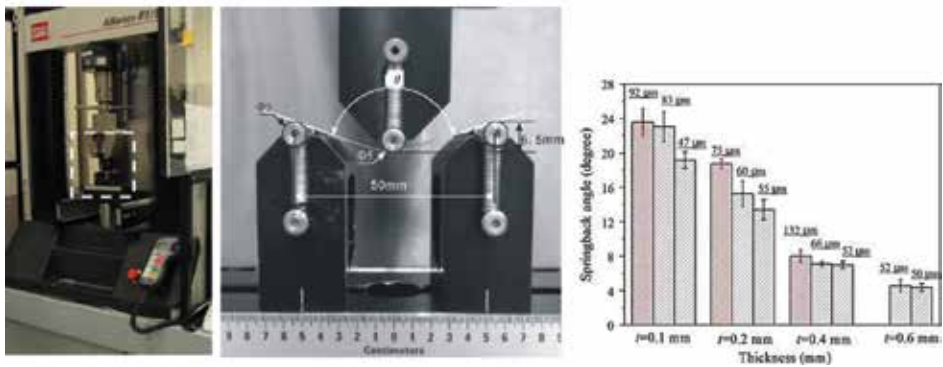


Figure 20. Left: Three-point bending test device and tooling; Right: Influence of grain size on springback angle [15].

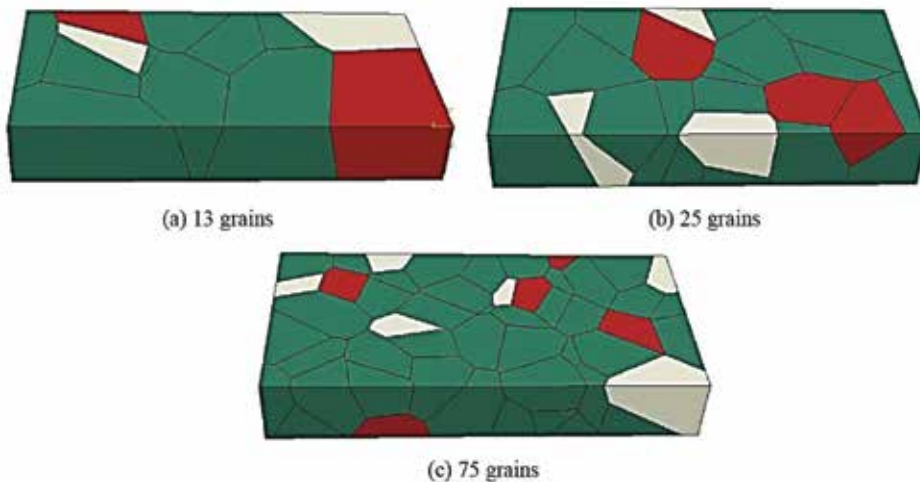


Figure 21. Grained heterogeneity in workpiece with: (a) 13 grains; (b) 25 grains; and (c) 75 grains [29].

Fang et al. [29] conducted numerical simulation to investigate the size effect of the springback, which occurs after the micro-V-bending in terms of Voronoi tessellation. A finite element

model of the micro-V-bending has been designed by using the ABAQUS/Standard commercial software. The workpiece grain sizes of 98, 152, and 201 μm have been adopted in the FE model (**Figure 21**) to recognize the relationship between the size effect and springback angle during the V-bending process. Voronoi tessellation can imitate the microstructure of materials, and represents grained heterogeneity graphically in FE models. Grains were divided into three groups with assigned corresponding stress-strain curves (**Figure 22**). Simulation results display the inhomogeneous deformation behavior during micro-V-bending process and also show that springback effect increases with grain size (**Figure 23**).

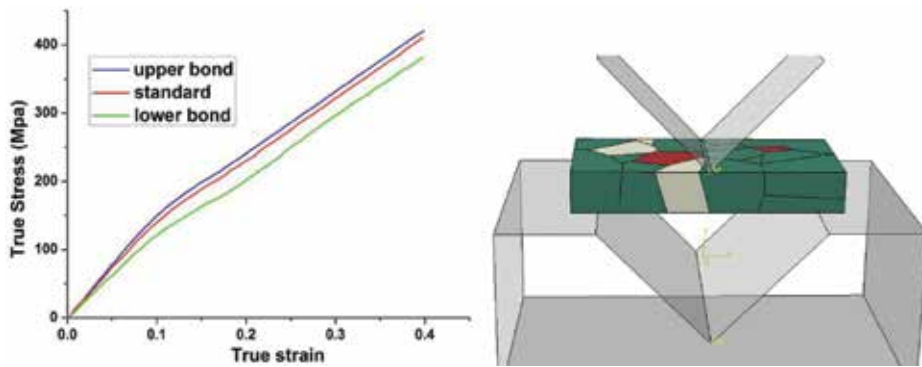


Figure 22. Left: Flow stress curves of the grains in workpiece with grain size 152 μm ; Right: Micro-V-bending FE model with workpiece grain size 152 μm [29].

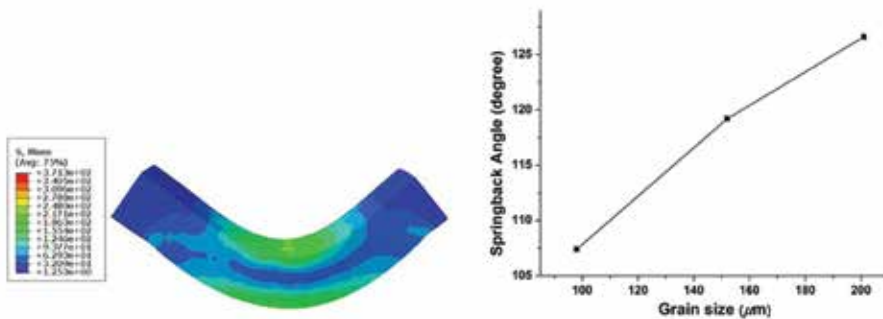


Figure 23. Left: Micro-V-bending result after unloading; Right: Springback angle with different grain size [29].

2.5. Frictional behavior

2.5.1. Open and closed lubricant pockets (CLPs)

Changes of interfacial friction with the decrease of element size in microforming process can be estimated based on the size-scaled ring compression test [5] and double-cup extrusion

(DCE) [30]. The friction is recognized based on the comparison between the geometry of the deformed sample and the finite element simulations results. Change of friction factor with decreasing workpiece size in the DCE process in lubricated conditions is presented in **Figure 24**. It can be seen that the friction increases with the scaled down workpiece size [30].

To recognize the frictional behavior in microforming, the asperity deformation process needs to be taken into account. Surface topography evolution process is shown in **Figure 25**. Before the tool touches the workpiece surface, there is a layer of lubricant on the whole contact surface (**Figure 25a**). When the tool presses the workpiece surface, some lubricant is trapped in the roughness valleys, which results in the formation of the so-called closed lubricant pockets (**Figure 25b**). In the CLPs, a hydrostatic pressure is thus generated and part of the deformation load is shared by the lubricant. Under this condition, material slides along the tooling surface with low friction. At the workpiece edges the lubricant is squeezed out from the roughness valleys and the so-called open lubricant pockets (OLPs) are then created. At the OLPs, the flattened asperities support deformation load and they become to be the real contact areas (RCAs), which increases the interfacial friction (**Figure 25c**). Open and closed pockets model application in FE simulation is presented in **Figure 26** [32]. Presence of CLP and OLP results in the nonuniform deformation of material asperities surface affects the surface properties of the formed microelement.

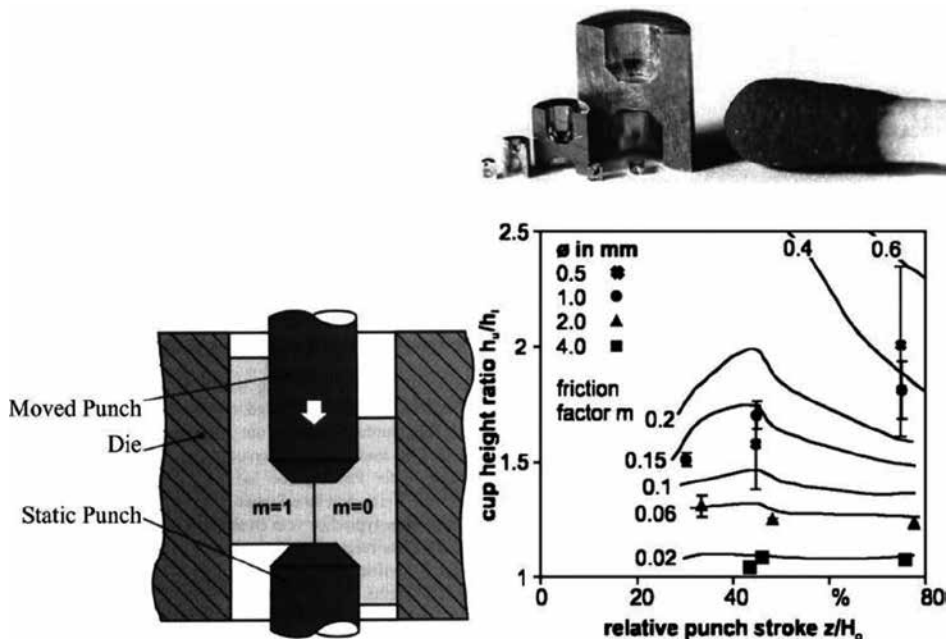


Figure 24. The formed geometries in different size-scaled achieved in double-cup extrusion tests [31].

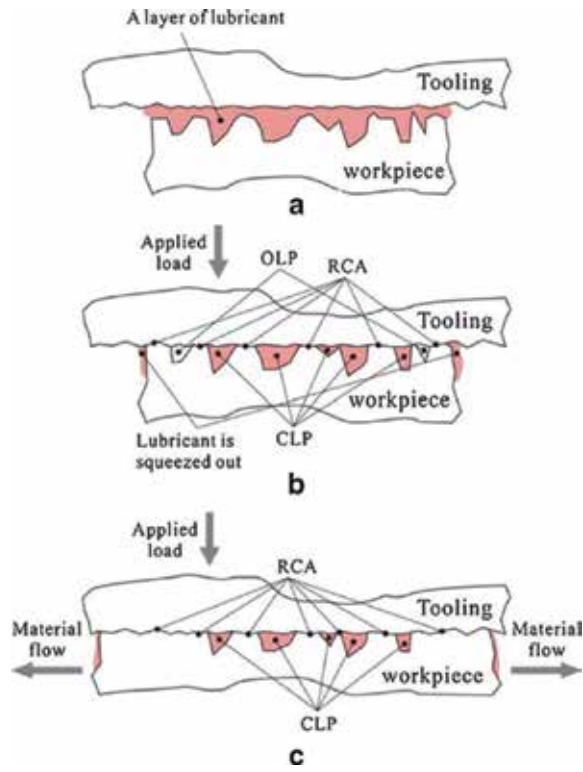


Figure 25. The evolution of workpiece surface asperities in deformation process [32].

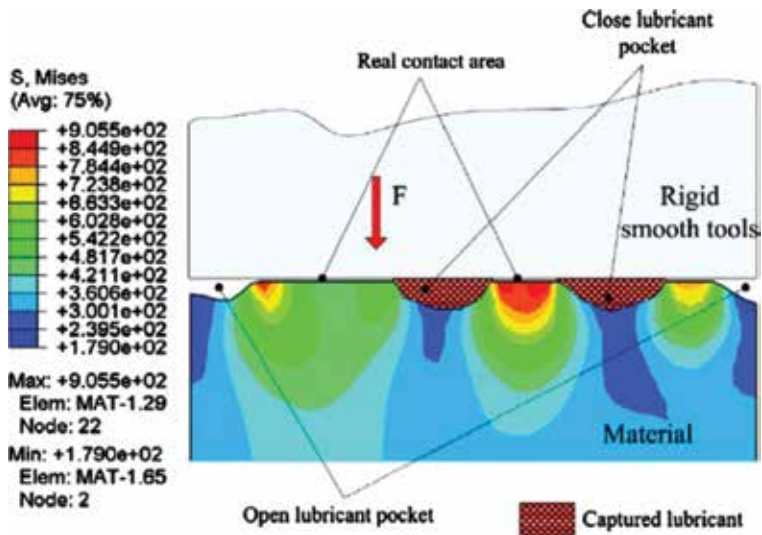


Figure 26. 2D sketch of OLPs, RCAs, and CLPs [32].

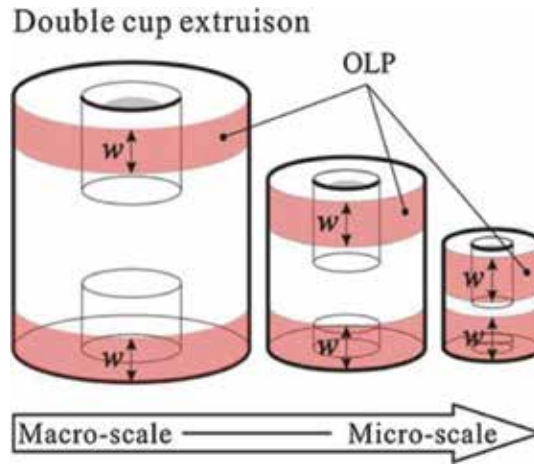


Figure 27. The increase of OLP fraction with the decrease of workpiece size [7].

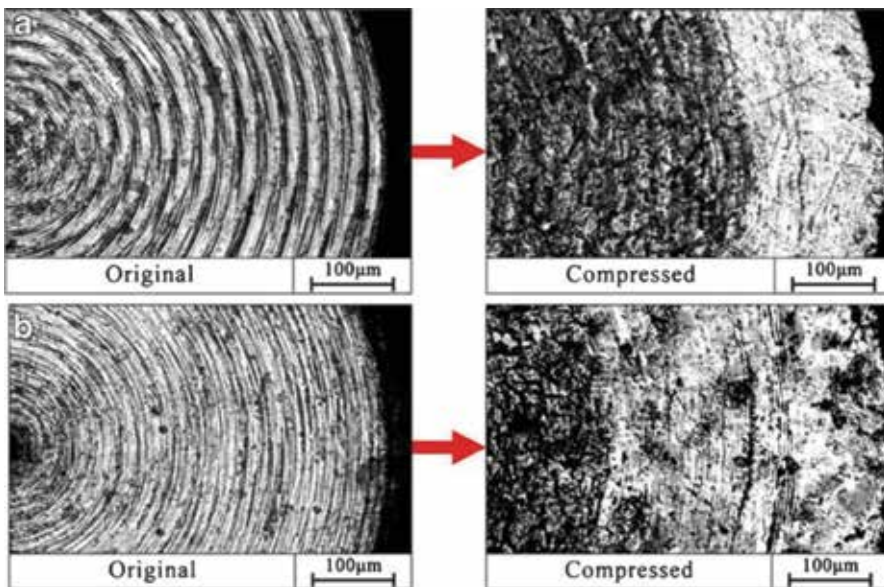


Figure 28. End surface topographies of the specimens ($\text{Ø}1 \times 1.5 \text{ mm}$) with the asperity size of: (a) $25 \mu\text{m}$; and (b) $10 \mu\text{m}$ [32].

Increase of friction with miniaturization is related to the increase of OLP fraction (Figure 27). The influence of different sizes of asperity on the change of the compressed surface topography is shown in Figure 28. The thickness of OLP rim decreases with the increase of asperity size. This reveals that the efficiency of lubricant in load supporting is higher in the surface with large asperities. More lubricant can be then trapped in the roughness valleys, resulting in the increase of the CLP area fraction.

2.5.2. Friction in forward and backward cup extrusion

Material tends to flow backwards (higher cup) with the decrease of the workpiece size when the fine-grained material is used [31]. Coarse grain size (**Figure 29**, case 0.5 mm) is larger than the cup wall thickness, which makes the material flow forward easily (longer shaft). Deformation behavior of fine- and coarse-grained samples in microdouble-cup extrusion is showed in **Figure 30**.

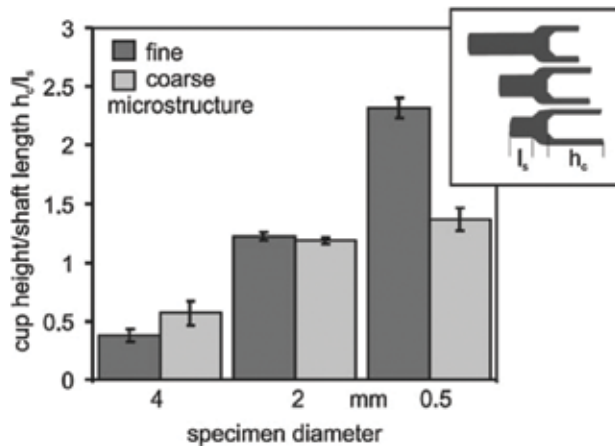


Figure 29. The experimental results of the combined forward rod–backward cup extrusion [31].

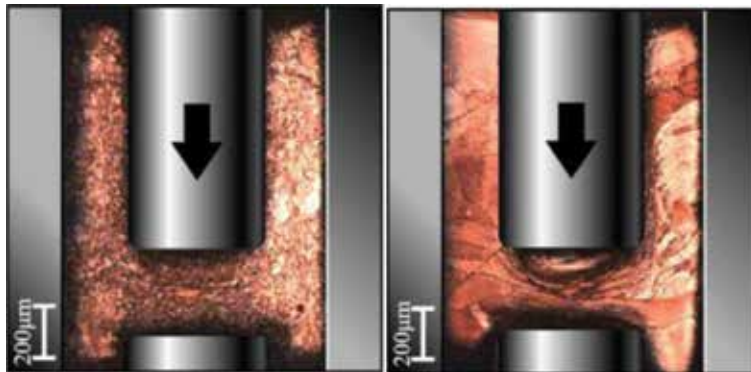


Figure 30. Microstructures of the microformed parts in microdouble-cup extrusion with different grain sizes. (a) 20 and (b) 150 μm [33].

2.5.3. Surface roughening

The ratio of tool asperity size to the formed element size increases with decrease of workpiece size and the increase of grain size [22, 34, 35]. Die workpiece interface effects become significant

in microforming. Geiger et al. [31] has shown that the use of the traditional friction coefficient or friction factor can lead to erroneous results in microscale. Some of the researchers have taken into account the impact of degree of a tool roughness on the material deformation process in numerical analysis. Challen et al. [36] presented the friction model for rough contact of plastic material with a rigid tool. Model is based on a simplified geometry of the tool surface, whose actual profile reflects a triangular wave (**Figure 31**). The surface roughness used in the model is the average of the asperities parameters measured in the experiment.

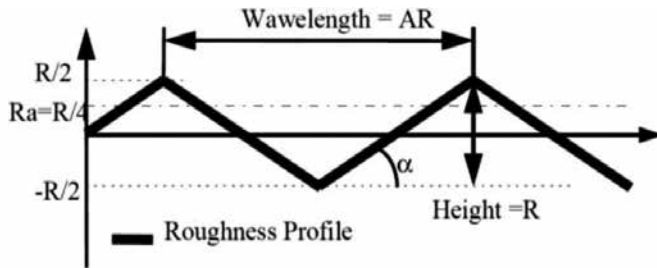


Figure 31. Triangular wave surface roughness model [36].

In that way, using a commercial FE system DEFORM, geometry of the tool surface was modeled in experimentally verified simulations of the forward microextrusion processes [37, 38] (**Figure 32**), where a significant influence of container roughness on the material flow was shown.

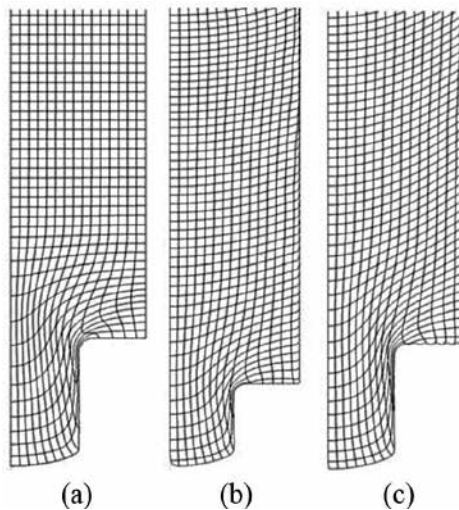


Figure 32. Flow nets of microextruded metal rods with a tool surface characterized by: (a) constant friction factor; (b) and (c) rigid triangular waves [39].

Vidal-Sallé et al. [40, 41] modeled die roughness in the form of a rigid triangular wave and the wave of interconnected arcs—model machined by turning surfaces in FE simulations of cylinder compression (**Figure 33**).

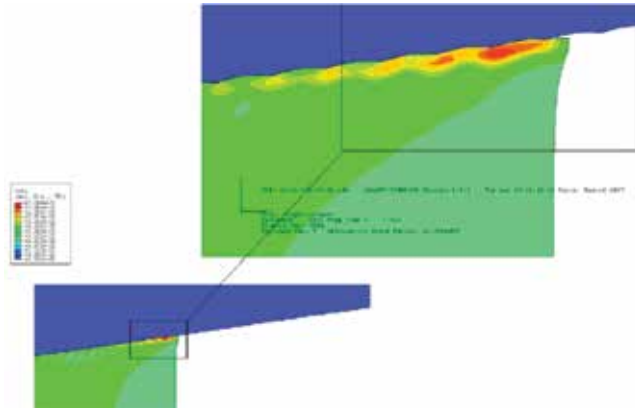


Figure 33. Plastic strain distribution in the compressed billet for perfect slipping [41].

Jeon et al. [42, 43] modeled die surfaces in the form of rigid sinusoidal curve in numerical simulation of the ring compression (**Figure 34**) as opposed to the use of the traditional empirical friction coefficient or factor. This finite-element-based model has been validated experimentally in terms of loads and metal flow using the ring test and actual surface measurements. The curve was referenced to the parameter Ra and the friction factor was determined as $m = f(a, t)$.

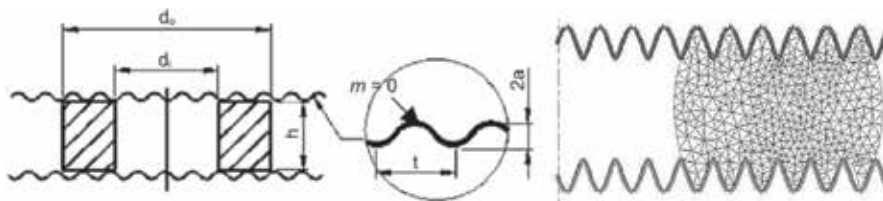


Figure 34. Tool surface geometric model with using an elliptical profile [42].

2.6. Repeatability

The scatter of the measured material properties (**Figure 35**) (e.g., flow stress, material deformation behavior) increases with the increase of grain size and the decrease of the workpiece size. This phenomenon is the result of different properties of individual grains and their less number in the workpiece volume [11, 44]. The deformation behavior of a single grain has an anisotropic nature. When the specimen size decreases and the grain size stays constant, there will be a small number of grains in the specimen volume and so the number of microstructural

features decreases. The uniform distribution of different grains no longer exists. Each grain with each property plays a significant role to the overall material deformation behavior. Different crystallographic orientations, different shapes, and sizes of neighboring grains lead to inhomogeneous deformation, which result in the scatter of achieved material properties.

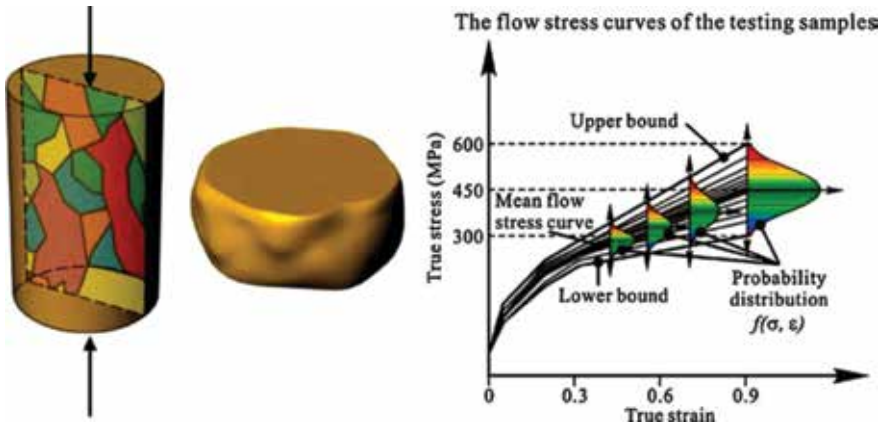


Figure 35. Schematic illustration of the modeling of the scatter effect with a normal distribution function [12].

2.7. Mechanical property of the formed billet

The hardness distribution of the formed billet becomes to be no uniform in microforming (Figure 36) when the grain size is coarse [45, 46]. More even material flow and hardness distribution can be achieved using the ultrafine-grained material. This implies the potential applications of the ultrafine-grained materials in metal microforming processes.

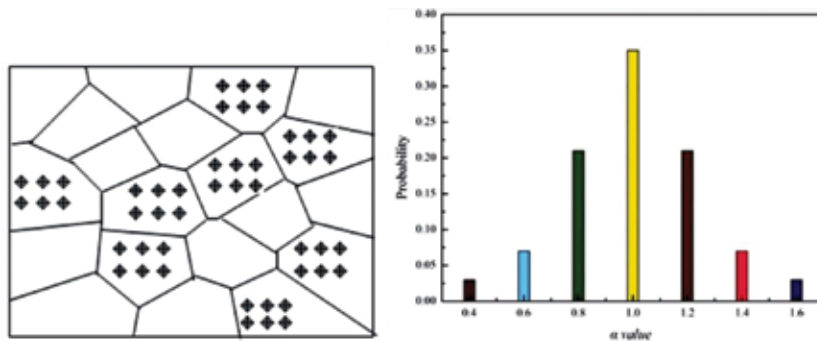


Figure 36. Left: Illustration of nanoindentation; Right: statistical distribution of α -value, α —ratio of the hardness at each class to the average hardness [25].

Billet formability increases with the decrease of workpiece size for a constant grain size [21]. It needs a larger strain to initiate cracking in microforming (Figure 37). Common assumption

is that the damage energy to initiate fracturing is the same in macro- and microscale. The flow stress decreases with the billet size, so the larger deformation is needed to obtain the critical damage energy in microforming.

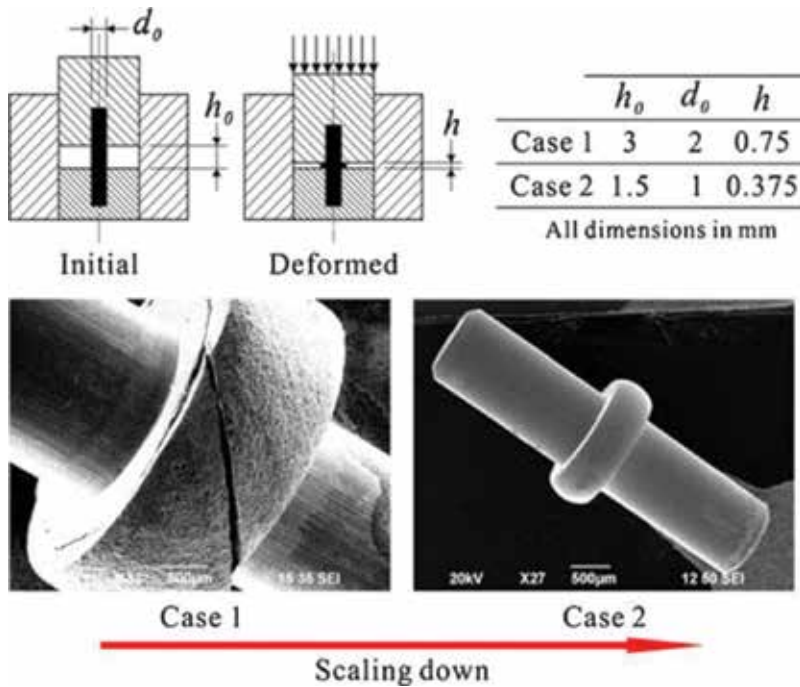


Figure 37. Different size-scaled central headed parts [21].

2.8. Summary

Microforming is considered as an economically competitive process for production of metallic microcomponents. The scaling down of a forming system from macro to micro leads to the occurrence of size effect. This phenomenon differs microforming from forming in macroscale and do not allow applying conventional knowledge. The anisotropic properties of each grain, the random nature of grain distribution, and orientation as well as tool surface roughness become significant. This leads to the inhomogeneous deformation and the scatter of the achieved flow stress. Experimentally recognized size effects, such as flow stress size effect, deformation behavior size effect, or interfacial friction size effect are numerically modeled, giving the ability to more accurately identify their mechanics and to predict the results of the microforming process.

For the microforming process simulations, commercial FE systems such as DEFORM, QFORM, ABACUS, or ANSYS/LS-DYNA are used. Nonlinear code ADINA (developed by KJ Bathe and his team at MIT Mechanical Engineering) may be also recommended to solve some of the complex multiphysical micromechanics phenomena associated with metal forming. Grain

structures are modeled based on metallographies or using Voronoi tessellation and the tool surface roughness using rigid waves. Ortiz atomistic models of material behavior based on atomistic energy laws may be an alternative way to resolve the mechanics of microforming of metals.

Although the polycrystalline material deformation behaviors have been extensively studied and adopted in numerical simulations, the size effects physics is not yet thoroughly understood. The influence of size effect on deformation mechanics in microforming processes is still a challenging issue to be investigated.

Acknowledgements

This chapter has been carried out in the framework of the S/WM/1/2015 statutory work and financed from the Ministry of Science and Higher Education funds.

Author details

Krzysztof Mogielnicki*

Address all correspondence to: k.mogielnicki@pb.edu.pl

Bialystok University of Technology, Bialystok, Poland

References

- [1] Teyfour A, Ahmadi M, Sorooshian S. Mint: A review on micro formings. *Modern Applied Science* 9(9). 2015;230.
- [2] Vollertsen F, Schulze Niehoff H, Hu, Z. Mint: State of the art in micro forming. *International Journal of Machine Tools and Manufacture* 46(11). 2006;1172–1179.
- [3] Engel U, Eckstein R. Mint: Microforming – from basic research to its realization. *Journal of Materials Processing Technology* 125. 2002;35–44.
- [4] Vollertsen F, Biermann D, Hansen HN, Jawahir IS, Kuzman K. Mint: Size effects in manufacturing of metallic components. *CIRP Annals – Manufacturing Technology* 58(2). 2009;566–587.
- [5] Messner A, Engel U, Kals R, Vollertsen F. Mint: Size effect in the FE-simulation of micro-forming processes. *Journal of Materials Processing Technology* 45(1–4). 1994;371–376.

- [6] Vollertsen F, Hu Z, Niehoff HS, Theiler C. Mint: State of the art in micro forming and investigations into micro deep drawing. *Journal of Materials Processing Technology* 151(1–3). 2004;70–79.
- [7] Fu MW, Chan WL. Mint: A review on the state-of-the-art microforming technologies. *The International Journal of Advanced Manufacturing Technology* 67(9–12). 2013; 2411–2437.
- [8] Chan WL, Fu MW. Mint: Meso-scaled progressive forming of bulk cylindrical and flanged parts using sheet metal. *Materials & Design* 43. 2013;249–257.
- [9] Kahnis P. Analyse von Größeneinflüssen bei einer Herabskalierung des Fräsprozesses in den Mikrobereich. [Dissertation] Technische Universität Dortmund, Vulkan Verlag Essen; 2008.
- [10] Saotome Y, Zhang T, Inoue A. Mint: Microforming of MEMS parts with amorphous alloys. In *MRS Proceedings*, Vol. 554. Cambridge University Press; 1998. 385 p.
- [11] Diehl A, Engel U, Geiger M. Mint: Influence of microstructure on the mechanical properties and the forming behaviour of very thin metal foils. *The International Journal of Advanced Manufacturing Technology* 47(1–4). 2010;53–61.
- [12] Chan WL, Fu MW, Lu J, Liu JG. Mint: Modeling of grain size effect on micro deformation behavior in micro-forming of pure copper. *Materials Science and Engineering A: Struct* 527(24–25). 2010;6638–6648.
- [13] Chan WL, Fu MW, Lu J. Mint: The size effect on micro deformation behaviour in micro-scale plastic deformation. *Materials & Design* 32(1). 2011;198–206.
- [14] Chan WL, Fu MW. Mint: Experimental studies and numerical modeling of the specimen and grain size effects on the flow stress of sheet metal in microforming. *Materials Science and Engineering A: Struct* 528(25–26). 2011;7674–7683.
- [15] Liu JG, Fu MW, Lu J, Chan WL. Mint: Influence of size effect on the springback of sheet metal foils in micro-bending. *Computational Materials Science* 50(9). 2011;2604–2614.
- [16] Simons G, Weippert C, Dual J, Villain J. Mint: Size effects in tensile testing of thin cold rolled and annealed Cu foils. *Materials Science and Engineering A: Struct* 416(1–2). 2006;290–299.
- [17] Weiss B, Groger V, Khatibi G, Kotas A, Zimprich P, Stickler R, Zagar B. Mint: Characterization of mechanical and thermal properties of thin Cu foils and wires. *Sensors and Actuators A: Physical* 99(1–2). 2002;172–182.
- [18] Khatibi G, Mingler B, Schafler E, Stickler R, Weiss B. Mint: Microcharacterization of thin copper and aluminium bond wires. *BHM Berg- und Hüttenmännische Monatshefte* 150(5). 2005;176–180.

- [19] Khatibi G, Betzwar-Kotas A, Groger V, Weiss BA. Mint: Study of the mechanical and fatigue properties of metallic microwires. *Fatigue and Fracture of Engineering Materials and Structures* 28(8). 2005;723–733.
- [20] Fu MW, Chan WL. Mint: Geometry and grain size effects on the fracture behavior of sheet metal in micro-scale plastic deformation. *Materials & Design* 32(10). 2011;4738–4746.
- [21] Ran JQ, Fu MW, Chan WL. Mint: The influence of size effect on the ductile fracture in micro-scaled plastic deformation. *International Journal of Plasticity* 41. 2013;65–81.
- [22] Chan WL, Fu MW. Mint: Experimental and simulation based study on micro-scaled sheet metal deformation behavior in microembossing process. *Materials Science and Engineering A: Struct* 556. 2012;60–67.
- [23] Henning M, Vehoff H. Mint: Statistical size effects based on grain size and texture in thin sheets. *Materials Science and Engineering A: Struct* 452. 2007;602–613.
- [24] Eichenhueller B, Egerer E, Engel U. Mint: Microforming at elevated temperature—forming and material behaviour. *International Journal of Advanced Manufacturing Technology* 33(1–2). 2007;119–124.
- [25] Lu HN, Wei DB, Jiang ZY, Liu XH, Manabe K.. Mint: Modelling of size effects in microforming process with consideration of grained heterogeneity. *Computational Materials Science* 77. 2013;44–52.
- [26] Cao J, Zhuang W, Wan S, Ho KC, Zhang N, Lin J, Dean TA. Mint: An integrated crystal plasticity FE system for microforming simulation. *Journal of Multiscale Modelling* 1(01). 2009;107–124.
- [27] Fang Z, Jiang ZY, Wei DB. Mint: Modeling of grained heterogeneity with Voronoi tessellation in microforming process. *Applied Mechanics and Materials* 553. 2014;66–70.
- [28] Gau JT, Principe C, Yu M. Mint: Springback behavior of brass in micro sheet forming. *Journal of Materials Processing Technology* 191(1–3). 2007;7–10.
- [29] Fang Z, Lu H, Wei D, Jiang Z, Zhao X, Zhang X, Wu D. Mint: Numerical study on spring back with size effect in micro V-bending. *Procedia Engineering* 81. 2014;1011–1016.
- [30] Engel U. . Mint: Tribology in microforming. *Wear* 260(3). 2006;265–273.
- [31] Geiger M, Kleiner M, Eckstein R, Tiesler N, Engel U. Mint: Microforming. *CIRP Annals – Manufacturing Technology* 50(2). 2001;445–462.
- [32] Deng JH, Fu MW, Chan WL. Mint: Size effect on material surface deformation behavior in micro-forming process. *Materials Science and Engineering A: Struct* 528(13–14). 2011;4799–4806.

- [33] Chan WL, Fu MW, Yang B. Mint: Study of size effect in microextrusion process of pure copper. *Materials and Design* 32(7). 2011;3772–3782.
- [34] Chan WL, Fu MW, Yang B. Mint: Experimental studies of the size effect affected microscale plastic deformation in micro upsetting process. *Materials Science and Engineering A: Struct* 534. 2012;374–383.
- [35] Chan WL, Fu MW. Mint: Experimental studies of plastic deformation behaviors in microheading process. *Journal of Materials Processing Technology* 212(7). 2012;1501–1512.
- [36] Challen JM, Oxley PLB. Mint: An explanation of the different regimes of friction and wear using asperity deformation models. *Wear* 53. 1979;229–243.
- [37] Piwnik J, Mogielnicki K. Mint: The friction influence on stress in micro extrusion. *Archives of Foundry Engineering* 10. 2010;451–454.
- [38] Piwnik J, Mogielnicki K. Mint: Experimental and FE analysis of aluminium alloy plastic flow in the forward micro-extrusion processes. *Archives of Metallurgy and Materials* 59(2). 2014;521–525.
- [39] Piwnik J, Mogielnicki K. Mint: Deformations in micro extrusion of metals. *Archives of Foundry Engineering* (3). 2010;87–90.
- [40] Vidal-Sallé E, Maisonnète-Masson S, Boyer JC. Mint: About the validity of the plastic wave model for an actual roughness of axisymmetric tooling in bulk forming. *International Journal of Material Forming* 2. 2009;217–220.
- [41] Vidal-Sallé E, Boutabba S, Cui Y, Boyer JC. Mint: An improved «plastic wave» friction model for rough contact in axisymmetric modeling of bulk forming processes. *International Journal of Material Forming* 1(1). 2008;1263–1266.
- [42] Jeon HJ, Bramley AN. Mint: A friction model for microforming. *The International Journal of Advanced Manufacturing Technology* 33. 2007;125–129.
- [43] Becker P, Jeon HJ, Chang CC, Bramley AN. . Mint: A geometric approach to modelling friction in metal forming. *CIRP Annals-Manufacturing Technology* 52(1). 2003;209–212.
- [44] Raulea LV, Goijaerts AM, Govaert LE, Baaijens FPT. Mint: Size effects in the processing of thin metal sheets. *Journal of Materials Processing Technology* 115(1). 2001;44–48.
- [45] Rosochowski A, Presz W, Olejnik L, Richert M. Mint: Microextrusion of ultra-fine grained aluminium. *International Journal of Advanced Manufacturing Technology* 33(1–2). 2007;137–146.
- [46] Egerer E, Engel U. Mint: Process characterization and material flow in microforming at elevated temperatures. *Journal of Manufacturing Processes* 6 (1). 2004;1–6.

Numerical Simulation of Compressible Reactive Flows

Bing Wang, Zhao Xin Ren and Wei Wei

Additional information is available at the end of the chapter

<http://dx.doi.org/10.5772/63906>

Abstract

Numerical simulation has been widely employed to investigate the compressible flows since it is difficult to carry out the experimental measurements, especially in the reactive flows. The shock-wave capturing scheme will be necessary for resolving the compressible flows, and moreover the careful treatments of chemical reaction should be considered for proceeding numerical simulation stable and fast. Recently, the present authors have tried to establish a high-resolution numerical solver for computing the compressible reactive flows. This chapter presents the numerical procedures acquired in this solver for computing the fluxes using weighted essentially non-oscillatory (WENO) scheme, dealing with chemical stiffness problems, and tracing droplets and their interaction with the compressible fluids. As examples, the Taylor-Green vortex (TGV) problem considering the passive scalar mixing, the spatially developing reactive mixing layer flows taken gas-phase hydrogen, and liquid *n*-decane as fuel are simulated, respectively. Many important characteristics of flow, flame, and ignition are analyzed under the supersonic condition.

Keywords: compressible reactive flows, spray combustion, numerical simulation, WENO, Lagrangian trajectory model

1. Introduction

Numerical simulation has become one of important approaches in academia and industry to research-complicated reactive flows in recent years, though it is still a fast developing subject. For combustion in low-speed flows, usually the low-Mach-number assumption is used, which assumes that the change of temperature is unrelated to the hydrodynamic pressure [1,2]. While for transonic or supersonic reactive flows, such as in the scramjet combustor, the compressible effects could not be ignored and the set of fully compressible Navier-Stokes equations should be solved.

There are three numerical simulation methods for compressible reactive flows via solving Navier-Stokes equations, including Reynolds-averaged Navier-Stokes (RANS) equations, large eddy simulation (LES), and direct numerical simulation (DNS). RANS simulates all scales of fluctuations using turbulent models. However, there is still lack of a general model suitable for all flow types, since RANS ignores the details and impacts of turbulent fluctuations. LES divides the flow scales into large and small scales via a low-pass filter. The large-scale flows are solved using the governing equations, and thus LES is able to give the temporal and spatial evolution of large-scale eddies. The small-scale flows are simulated using a sub-grid-scale (SGS) model, but there is also no general SGS model. DNS solves the Navier-Stokes equations for all scales of flows without introducing any models and assumptions, and thus it can accurately predict the full-scale flow characteristics. However, its main limitation in practice is the high cost of calculation.

In the early days, RANS or LES was used to simulate the compressible reactive flows considering the computing cost. Dauplain et al. [3] simulated the supersonic hydrogen flame using the large eddy simulation, and their numerical results agreed well with the experiment measurements. LES was also used to simulate the supersonic flow and combustion in a model scramjet combustor [4], and the velocity and temperature at different cross-sections were compared with the experimental data. Edwards et al. used the hybrid method of LES/RANS to simulate the supersonic reacting wall-jet flow [5]. There are also other examples using RANS or LES [6–9]. Recently, some researchers have used DNS to simulate the compressible reactive flows. For example, O'Brien et al. [10] simulated the time-developing, H_2 /air-reacting mixing layers and investigated the dynamics of backscatter of kinetic energy using DNS; Diegelmann et al. [11] did the direct simulations of reactive shock-bubble interaction with detailed chemistry under varying initial pressure.

One of the main difficulties in the simulation of compressible flows is how to distinguish the discontinuities which may widely exist in supersonic flows. Jiang and Shu [12] proposed the weighted essentially non-oscillatory (WENO) scheme to capture shock waves with almost no oscillations. But the WENO scheme is too dissipative in regions with large shear rates. To overcome this drawback, the hybrid scheme was hence developed, which switches the WENO scheme and the linear (high-order) scheme according to a discontinuity detector. Pirozzoli [13] proposed a hybrid compact-WENO scheme to obtain high resolutions for simulation of shock-turbulence interaction. Furthermore, Ren et al. [14] proposed a Roe type, characteristic-wise compact-WENO scheme. Considering overcoming the complexity and program parallelization of compact schemes, Hu et al. [15] proposed a simple WENO scheme, which switches between the WENO scheme and its optimal linear scheme. A detailed review of numerical methods used for high-speed flows can be seen in [16].

The spray combustion can occur in the scenario of compressible flows [17–24]. Therefore, the methods to treat the dispersed droplets in the flows will be concerned by different approaches, such as Eulerian and Lagrangian methods. The Eulerian one needs complicated modelling of two-phase correlation terms, which is yet to be done. Even though the high computation cost will be taken by the Lagrangian method to track each particle released to the flow fields, it is the physically clear and mathematically simple method in simulations of two-phase reactive

flows. This chapter will also consider the spray combustion in mixing layer flows as a computation example.

This chapter tries to contribute the numerical simulation in the direction of compressible reactive flows. It is organized as follows. In section 2, the governing equations are presented; the methods to calculate the multispecies physical parameters and to deal with the chemical stiffness are also presented. In section 3, the discretization schemes and time integration methods are discussed, including the discretization of inviscid/viscous terms. In section 4, three examples of numerical simulations of compressible flows are presented. In section 5, the conclusions are drawn finally.

2. Governing equations and models of gas properties

2.1. Governing equations

Since this chapter will extend the simulations to the compressible two-phase turbulent flows considering the dispersed droplets' evaporation and gas-phase combustion, the governing equations will describe the Lagrangian transport of droplets through a continuous, compressible and chemically reacting carrier gas flow.

The equations for the gas-phase including mass, momentum, and energy exchange between the gas and the dispersed phase read as

$$\frac{\partial \rho}{\partial t} + \frac{\partial}{\partial x_j}(\rho u_j) = S_m \quad (1)$$

$$\frac{\partial}{\partial t}(\rho u_i) + \frac{\partial}{\partial x_j}(\rho u_i u_j + P \delta_{ij} - \tau_{ij}) = S_F \quad (2)$$

$$\frac{\partial}{\partial t}(\rho e_t) + \frac{\partial}{\partial x_j} \left((\rho e_t + P) u_j - \lambda \frac{\partial T}{\partial x_j} - u_i \tau_{ij} \right) = S_Q \quad (3)$$

$$\frac{\partial}{\partial t}(\rho Y_k) + \frac{\partial}{\partial x_j} \left(\rho Y_k (u_j + V_j^c) - \rho D_k \frac{\partial Y_k}{\partial x_j} \right) = S_{\text{combustion},k} + S_{Y_k} \quad (4)$$

Here, ρ is the gas-phase density, u_i is the velocity, T is the temperature, P is the pressure, Y_k is the mass fraction of the k^{th} species, and δ_{ij} is the Kronecker delta function. The right-hand side terms of the above equations S_m , S_F , and S_Q describe the two-phase couplings of mass, mo-

momentum, and energy, respectively. $S_{\text{combustion},k}$ is the source term due to combustion. τ_{ij} is the Newtonian viscous stress tensor

$$\tau_{ij} = \mu \left(\frac{\partial u_i}{\partial x_j} + \frac{\partial u_j}{\partial x_i} - \frac{2}{3} \frac{\partial u_k}{\partial x_k} \delta_{ij} \right) \quad (5)$$

A correction velocity V_j^c is added to the convection velocity in the species equations to ensure global mass conservation

$$V_j^c = \sum_{k=1}^{N_s} D_k \frac{W_k}{W} \frac{\partial X_k}{\partial x_j} \quad (6)$$

Here, N_s is the total number of species. W_k and X_k are the molecule weight and the mole fraction of the k^{th} species, respectively. e_t is the total energy, that is, kinetic energy plus internal (containing chemical) energy, which is defined as follows:

$$e_t = \sum_{k=1}^{N_s} Y_k \left(\int_{T_{\text{ref}}}^T c_{p,k} dT + h_{f,k}^0 \right) - \frac{P}{\rho} + \frac{u_i u_i}{2} \quad (7)$$

where $c_{p,k}$ and $h_{f,k}^0$ are the specific heat capacity at constant pressure and specific chemical formation enthalpy at the reference temperature, T_{ref} of the k^{th} species, respectively. The values of $c_{p,k}$ are represented by a fifth-order polynomial, and the coefficients can be found in [25]

$$\frac{c_{p,k} W_k}{R} = a_{1,k} + a_{2,k} T + a_{3,k} T^2 + a_{4,k} T^3 + a_{5,k} T^4 \quad (8)$$

The equation of state used for ideal multispecies gas is introduced to close the above equations as

$$P = RT \sum_{k=1}^{N_s} \frac{Y_k}{W_k} \quad (9)$$

where R is the universal gas constant.

2.2. Models of gas properties

The kinetic theory for gases is used to compute the transport and thermodynamic properties of the mixture. The Lennard-Jones potentials are used to calculate the inter-molecular forces.

The thermal conductivity of each species is determined by the modified Eucken model. The dynamic viscosity of each species and the binary diffusivity are computed with the Chapman-Enskog theory, and their formulas can be found in [26]

$$\mu_k = \frac{26.69\sqrt{W_k T}}{\sigma_k^2 \Omega_{v,k}} \quad (10)$$

$$\frac{\lambda_k W_k}{\mu_k C_{v,k}} = 1.32 + \frac{1.77}{(C_{p,k} / R) - 1} \quad (11)$$

$$D_{AB} = \frac{0.00266T^{3/2}}{PW_{AB}^{1/2} \sigma_{AB}^2 \Omega_D} \quad (12)$$

The viscosity and thermal conductivity of the mixture are calculated by the expressions of Wake and Wassiljewa [26], respectively,

$$\mu_m = \frac{\sum_{i=1}^n X_i \mu_i}{\sum_{j=1}^n X_j \phi_{ij}} \quad (13)$$

where $\phi_{ij} = \frac{(1 + (\mu_i / \mu_j)^{1/2} (W_j / W_i)^{1/4})^2}{(8(1 + W_i / W_j))^{1/2}}$.

$$\lambda = \frac{\sum_{i=1}^n X_i \lambda_i}{\sum_{j=1}^n X_j A_{ij}} \quad (14)$$

where $A_{ij} = \frac{(1 + (\lambda_i / \lambda_j)^{1/2} (W_j / W_i)^{1/4})^2}{(8(1 + W_i / W_j))^{1/2}}$.

2.3. Equations of spray droplets

The evaporating fuel droplets are solved individually under the Lagrangian framework. Before describing the Lagrangian model, several usual assumptions should be formulated. The spray of droplets is sparsely dispersed and every droplet is unaware of the existence of the others. The droplet rotations are neglected and an infinite heat conduction coefficient is assumed. Therefore, the inner temperature distribution of each droplet remains uniform.

Because of the high-density ratio between the liquid and gas phases, only the drag force acting on the droplets is significant. The Lagrangian equations for the position (in the i^{th} direction), $x_{d,i}$, velocity, $u_{d,i}$, temperature, T_d , and mass, m_d , of a single droplet are given by

$$\frac{du_{d,i}}{dt} = \frac{F_d}{m_d} = \left(\frac{f_1}{\tau_d} \right) (u_i - u_{d,i}) \quad (15)$$

$$\frac{du_{d,i}}{dt} = \frac{F_d}{m_d} = \left(\frac{f_1}{\tau_d} \right) (u_i - u_{d,i}) \quad (16)$$

$$\frac{dT_d}{dt} = \frac{Q_d + \dot{m}_d L_V}{m_d c_L} = \left(\frac{f_2}{\tau_d} \right) \left(\frac{\text{Nu}}{3\text{Pr}} \right) \left(\frac{c_p}{c_L} \right) (T - T_d) + \left(\frac{\dot{m}_d}{m_d} \right) \frac{L_V}{c_L} \quad (17)$$

$$\frac{dm_d}{dt} = \dot{m}_d = -m_d \left(\frac{1}{\tau_d} \right) \left(\frac{\text{Sh}}{3\text{Sc}} \right) \ln(1 + B_M) \quad (18)$$

where c_p is the specific heat of mixture gas, c_L is the specific heat of the liquid. The momentum response time, τ_d , is defined as

$$\tau_d = \frac{\rho_d d_d^2}{18\mu} \quad (19)$$

where d_d is the droplet diameter. The gas-phase Prandtl and Schmidt numbers in gaseous phase are given by

$$\text{Pr} = \frac{\mu c_p}{\lambda}, \text{Sc} = \frac{\mu}{\rho D} \quad (20)$$

respectively. The Nusselt and Sherwood numbers are

$$\text{Nu} = 2 + 0.552 \text{Re}_d^{1/2} \text{Pr}^{1/3} \quad (21)$$

$$\text{Sh} = 2 + 0.552 \text{Re}_d^{1/2} \text{Sc}^{1/3} \quad (22)$$

respectively. Here, the droplet Reynolds number based on the slip velocity is defined as

$$\text{Re}_d = \frac{\rho |u_i - u_{d,i}| d_d}{\mu} \quad (23)$$

f_1 is an empirical correction to the Stokes drag law and is given as

$$f_1 = 1 + 0.15 \text{Re}_d^{0.687} \quad (24)$$

The corrections of heat transfer for an evaporating droplet are given as

$$f_2 = \frac{\beta}{e^\beta - 1} \quad (25)$$

where the nondimensional evaporation parameter is given by

$$\beta = -1.5 \text{Pr} \tau_d \left(\frac{\dot{m}_d}{m_d} \right) \quad (26)$$

The evaporation rate is controlled by the mass transfer number, B_M , and is given by

$$B_M = \frac{Y_{sf} - Y_V}{1 - Y_{sf}} \quad (27)$$

Here, Y_V is the mass fraction of the vapor on the far-field condition for the droplets and Y_{sf} is the vapor surface mass fraction calculated directly from the surface molar fraction ($\chi_{sf,i}$), which is obtained using the equilibrium assumption

$$Y_{sf} = \frac{\chi_{sf}}{\chi_{sf} + (1 - \chi_{sf}) W / W_V} \quad (28)$$

$$\chi_{sf} = \frac{P_{\text{atm}}}{P} \exp \left(\frac{L_V}{R / W_V} \left(\frac{1}{T_{B,L}} - \frac{1}{T_d} \right) \right) \quad (29)$$

where W is the mean molecular weight of mixture gas, W_V is the molecular weight of the vapor, P_{atm} is the atmospheric pressure, R is the universal gas constant, and $T_{B,L}$ is the liquid boiling temperature at P_{atm} . L_V is the latent heat of fuel vapor at liquid temperature, T_d , and is given as follows:

$$L_v = L_{v,T_{B,L}} \left(\frac{T_{C,L} - T_d}{T_{C,L} - T_{B,L}} \right) \quad (30)$$

where $L_{v,T_{B,L}}$ is the latent heat at $T_{B,L}$ and $T_{C,L}$ is the critical temperature.

2.4. Two-way coupling models

The source terms S , due to interactions between continuous phase and dispersed phase, are expressed by summing total droplets existing in one computation cell, denoting as N_c

$$S_m = -\frac{1}{\Delta V} \sum_{N_c} (\dot{m}_d) \quad (31)$$

$$S_F = -\frac{1}{\Delta V} \sum_{N_c} (F_d + \dot{m}_d u_{d,i}) \quad (32)$$

$$S_Q = -\frac{1}{\Delta V} \sum_{N_c} \left(Q_d + \dot{m}_d \left(\frac{u_{d,i} u_{d,i}}{2} + h_{v,sf} \right) \right) \quad (33)$$

$$S_{Y_k} = \begin{cases} -\frac{1}{\Delta V} \sum_{N_c} (\dot{m}_d) & \text{for fuel} \\ 0 & \text{for other species} \end{cases} \quad (34)$$

where m_d and \dot{m}_d denote the droplet mass and dm_d/dt , respectively, $u_{d,i}$ is the droplet velocity, ΔV is the volume of the computational grid for the gas-phase calculation, and $h_{v,sf}$ is the evaporated vapor enthalpy at the droplet surface. F_d and Q_d are the drag force and the convective heat transfer, respectively, described later. For the combustion reaction model, a one-step global reaction is adopted for the reaction of hydrocarbon-air mixtures. The source term, $S_{\text{combustion},k}$ is expressed using the combustion reaction rate per unit volume, R_F , as follows:

$$S_{\text{combustion},k} = -\frac{n_k}{n_F} \frac{W_k}{W_F} R_F \quad (35)$$

where n_k and n_F are the molar stoichiometric coefficients of the k^{th} species and the fuel for the one-step global reaction (positive for the production side), respectively. W_k and W_F are the molecular weights of the k^{th} species and fuel, respectively.

3. Numerical discretization procedures

A finite difference methodology is used to solve the above governing equations. An explicit Runge-Kutta time-integration methodology is applied, obtaining a third-order time-accurate computation. For example, for a semi-discrete equation of $dU_j = L_j(U)dt$, the iteration from n to iteration $n+1$ is performed as

$$\begin{aligned} U_j^{(1)} &= U_j^n + \Delta t L_j(U^n) \\ U_j^{(2)} &= \frac{3}{4}U_j^n + \frac{1}{4}U_j^{(1)} + \frac{1}{4}\Delta t L_j(U_j^{(1)}) \\ U_j^{n+1} &= \frac{1}{3}U_j^n + \frac{2}{3}U_j^{(2)} + \frac{2}{3}\Delta t L_j(U_j^{(2)}) \end{aligned} \quad (36)$$

where U_j is the conserved variable at the direction j .

The higher-resolution numerical scheme applied for the resolution of supersonic flow is essential to the reliability of simulation. The nonviscous flux $\hat{f}_{j+1/2}$ for the interface at $j+1/2$, is evaluated using a fifth-order hybrid Compact-Weighted Essentially Non-Oscillatory scheme [14] for the resolution of turbulent field and shock-capturing calculation in the supersonic flow. The numerical flux of the hybrid scheme is calculated as

$$\hat{f}_{j+1/2} = \sigma_{j+1/2} \hat{f}_{j+1/2}^{\text{CU}} + (1 + \sigma_{j+1/2}) \hat{f}_{j+1/2}^{\text{WENO}} \quad (37)$$

which is constructed by hybridizing a fifth-order Compact Upwind (CU) scheme, $\hat{f}_{j+1/2}^{\text{CU}}$ and a fifth-order WENO one, $\hat{f}_{j+1/2}^{\text{WENO}}$, through a smoothness indicator r_c . $\sigma_{j+1/2}$ is the weight of the numerical flux,

$$\sigma_{j+1/2} = \min\left(1, \frac{r_{j+1/2}}{r_c}\right) \quad (38)$$

A sixth-order symmetric compact difference scheme is applied for the viscous diffusion terms,

$$\frac{1}{3}\hat{F}_{j-1} + \hat{F}_j + \frac{1}{3}\hat{F}_{j+1} = \frac{28(\hat{f}_{j+1} - \hat{f}_{j-1}) + (\hat{f}_{j+2} - \hat{f}_{j-2})}{36\Delta x} \quad (39)$$

where \hat{F}_j is the difference approximation for $\left(\frac{\partial f}{\partial x}\right)_j$ at the node j .

Because of the stiffness of the equation due to the reactions, the time integration of the equations is performed by means of the point-implicit method [27]. For instance, U is supposed as the unknown variable at time step $n+1$, and the below equation is solved to obtain $U^{n+1}=U^n + \Delta U$

$$\left(I - \left(\frac{\partial S}{\partial U} \right)^n \Delta t \right) \Delta U = (-C^n + V^n + S^n) \Delta t \quad (40)$$

where C is the convection term, V is the viscous term, S is the source term, and I is the unity matrix.

In order to obtain the physical quantities of the fluid at a droplet position, the fluid velocities computed on the Eulerian mesh were interpolated at the droplet locations. A fourth-order Lagrangian interpolation was used for this purpose [28]. When the droplet is located at (x_d, y_d, z_d) in a cell whose coordinates are $(x_0, y_0, z_0) \dots (x_l, y_l, z_l)$, the fluid velocity at the droplet position is obtained via the Lagrangian interpolation, which is expressed as

$$u(x_d, y_d, z_d) = \sum_{i=1-n/2}^{n/2} \sum_{j=1-n/2}^{n/2} \sum_{k=1-n/2}^{n/2} \times \left(\prod_{\substack{l=1-n/2 \\ (l \neq i)}}^{n/2} \frac{x_d - x_l}{x_i - x_l} \prod_{\substack{l=1-n/2 \\ (l \neq j)}}^{n/2} \frac{y_d - y_l}{y_j - y_l} \prod_{\substack{l=1-n/2 \\ (l \neq k)}}^{n/2} \frac{z_d - z_l}{z_i - z_l} \right) u_{i,j,k} \quad (41)$$

where the subscripts i, j, k , and l represents the cell indexes and $n = 4$.

In the Lagrangian droplet-tracking method, the droplet equation of motion was integrated with the third-order Adams-Bashforth scheme in direction, i , for droplet position,

$$x_{d,i}^{n+1} = x_{d,i}^n + \Delta t \left(\frac{23}{12} u_{d,i}^n - \frac{16}{12} u_{d,i}^{n-1} + \frac{5}{12} u_{d,i}^{n-2} \right) \quad (42)$$

The equations of velocity and temperature of the droplet are solved using the same integration method, as Eq. (42).

4. Numerical examples

4.1. Taylor-Green vortex (TGV) case

Taylor-Green vortex problem is an idea test for a numerical scheme whether it has the ability to simulate the transition from laminar to turbulence, since it contains the stages of laminar, transition, and finally turbulence as time develops. The three-dimensional Taylor-Green vortex was first introduced by Taylor and Green, and its initial condition is given as follows:

$$\begin{aligned}
 u &= U_0 \sin x \cos y \sin z \\
 v &= -U_0 \cos x \sin y \sin z \\
 w &= 0 \\
 p &= p_0 + \rho_0 U_0^2 (\cos 2z + 2)(\cos 2x + \cos 2y) / 16
 \end{aligned}
 \tag{43}$$

The computing domain is $[0, 2\pi] \times [0, 2\pi] \times [0, 2\pi]$. The parameters are set as $p_0=100$, $\rho_0=1$, $U_0=1$, then the Mach number is about 0.08 and the flow is nearly incompressible. The boundary conditions in the three dimensions are all periodic. Three numerical schemes are used here, WENO [7], WENO-compact upwind [9] (denoted as WENO-CU), and WENO-linear upwind [10] (denoted as WENO-LU), respectively. Two sets of computation grid are taken as 64^3 and 32^3 for different flow Reynolds numbers.

Figure 1 shows the results of the total kinetic energy integrated in the entire flow field. For $Re = 30,000$, the kinetic energy decays very slowly at the beginning and it has almost no change in the first few seconds. However, when the time is at about 4 s, the sub-grid scales are produced and the kinetic energy begins to decay due to the numerical dissipation, which also can be taken as the implicit sub-grid dissipation. The results of Re number equalling 3000 are similar, since in both cases, the numerical viscosity is larger compared to the physical viscosity. For the results of $Re = 300$, there is only slight difference between the curve of WENO-LU and WENO-CU, since in this case the physical viscosity is dominated.

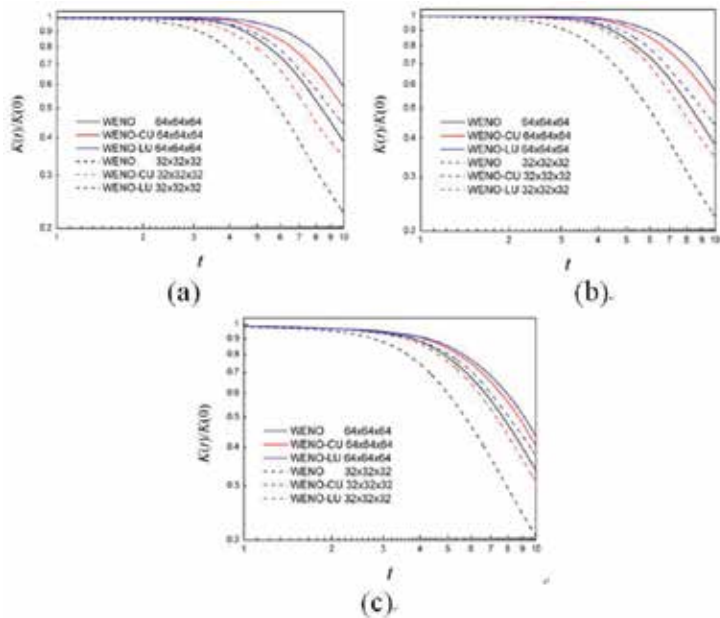


Figure 1. Comparison of the total kinetic energy. (a) $Re = 30,000$; (b) $Re = 3000$; (c) $Re = 300$.

Figure 2 shows the energy spectrum of the TGV with $Re = 30,000$. As the time increases, the slope of energy spectrum also changes. If the time is longer than 4, the turbulence develops and the kinetic energy builds up a Kolmogorov inertial range. The slope is then approximately decayed with the $-5/3$ law. It implies that it can predict the characteristics of turbulence.

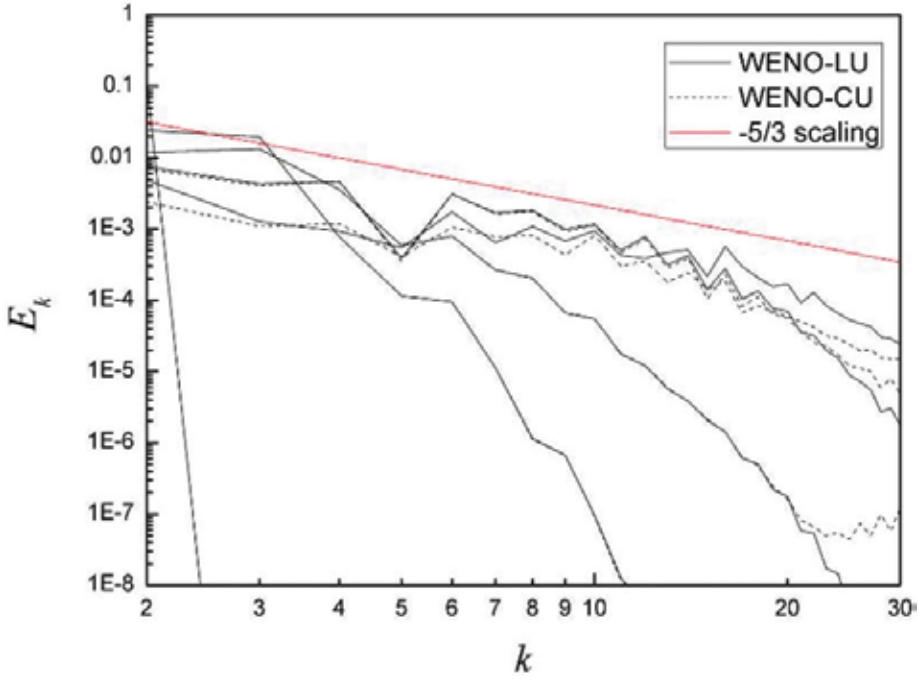


Figure 2. Energy spectrum of TGV with $Re = 30,000$.

Since the passive scalar transportation is very important in many fields, especially in the chemical-reacting process, we also solved the conserved passive scalar transport equation

$$\frac{\partial(\rho f)}{\partial t} + \nabla \cdot (\rho f \vec{U}) = \nabla \cdot (\rho D \nabla f) \tag{44}$$

Here, only the WENO-LU scheme is used since it has less dissipation and costs less computing time. Equation (44) presents the initial condition for f and it is a function of the initial Q distribution, where Q is the value of q -criteria. Different Schmidt numbers are taken in the simulations, 1, 0.1, and 0.01, corresponding to different diffusivity coefficients, respected $D = \mu / (\rho Sc)$

$$f(t=0) = \frac{1 + \text{erf}(C_0 Q)}{2}, C_0 = 100 \tag{45}$$

Here, erf is the error function. **Figure 3** shows the initial distribution of f . As we can see, in most regions, f equals 1 or 0 and there are large gradients of f initially.

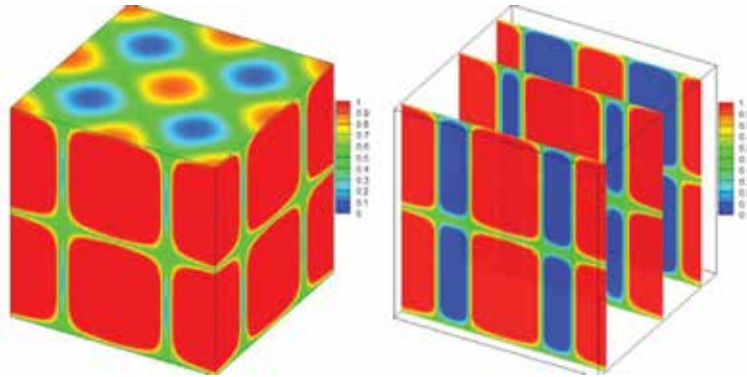


Figure 3. Initial distribution of passive scalar f .

Figure 4 shows the variance of the passive scalar for the $Re = 30,000$ flow in different Schmidt numbers and different grid levels. Similar to the kinetic energy decaying, the scalar variance decays very slowly in the first 4 s, and it can be concluded that the passive scalar mixing goes on with the laminar diffusion. However, the significant decaying can be observed due to the initial large gradients of passive scalar. For the time longer than four, the turbulent mixing occurs and the decaying of passive scalar variance is larger than that in the beginning stage.

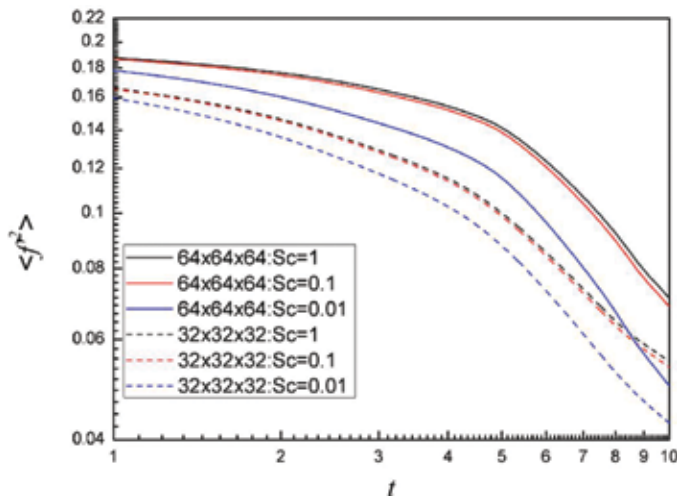


Figure 4. Variance curves of passive scalar.

Figure 5 shows the passive scalar contours for $Re = 30,000$ and $Sc = 1.0$ in the plane of $z = \pi$. During the stage of laminar diffusion, the interface between the high and low f region is clear

while the interface is wrinkled in the stage of turbulent mixing, which enhances the mixing process.

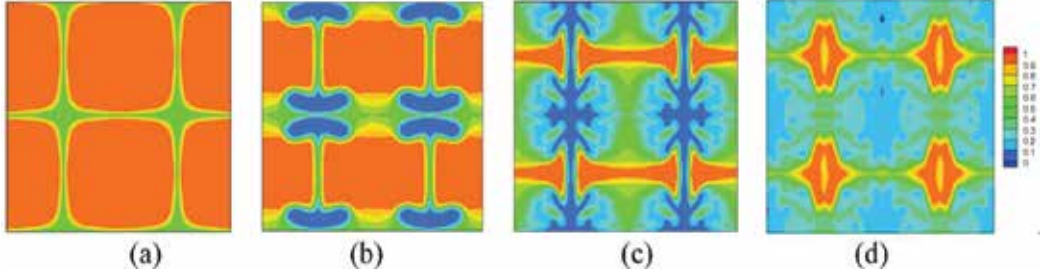


Figure 5. Passive scalar field in the plane of $z = \pi$. (a) $t = 0$ s; (b) $t = 3$ s; (c) $t = 6$ s; (d) $t = 10$ s.

4.2. Reactive H_2 /air spatially developing mixing layer

The schematic of the supersonic mixing layer is shown in **Figure 6**.

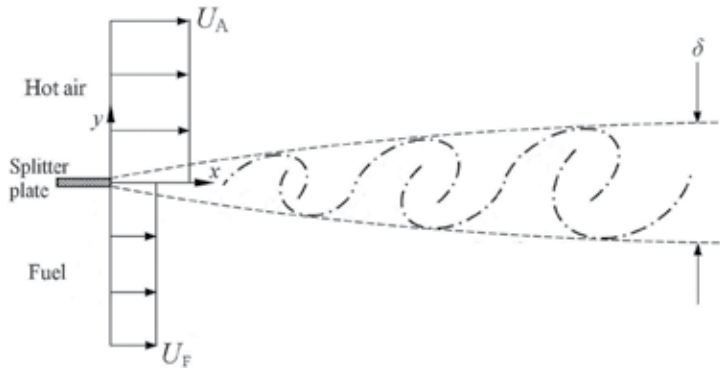


Figure 6. Schematic of computation model of spatially developing mixing layer.

The inlet conditions are set as follows. The average velocity profile in the stream-wise direction is a hyperbolic tangent, and the average velocity in other directions is set to zero

$$\bar{U} = \frac{U_A + U_F}{2} + \frac{U_A - U_F}{2} \tanh\left(\frac{y - 0.5l_y}{2\delta_0}\right) \quad (46)$$

where δ_0 is the inlet layer thickness given as 0.4 mm, and l_y is the length of computational domain in the y direction. U_A is the hot-air inflow velocity, 2000 m/s, U_F is the cold fuel inflow velocity, 1000 m/s. The temperatures of both streams are $T_A = 1600$ K and $T_F = 390$ K. The reactive system pressure is specified as $p_A = 1$ atm.

The stream-wise and transverse domain lengths are l_x and l_y , respectively. By setting $l_x = 4l_y$, the transverse domain size is large enough to have minimal influence on the main flow region of the droplet-laden shear layer. The computation grid in the two-dimensional case is taken as 512×128 equally spaced computational cells in the stream-wise and the transverse directions, respectively, after a series of grid independence tests.

In order to stimulate the flow instability, the inlet velocity perturbation is given as

$$v' = (U_A - U_F)G(y - 0.5l_y) A \sin(2\pi f_o t + \xi) \quad (47)$$

where G is the Gauss function, A is the fluctuation amplitude, f_o is the maximum disturbance frequency, and ξ is the random phase. The nonreflecting conditions are used in the transverse directions. The outflow is treated by an extrapolation of each primitive variable. A 19-step detailed H_2/O_2 reaction mechanism is used, which can be referred in [29].

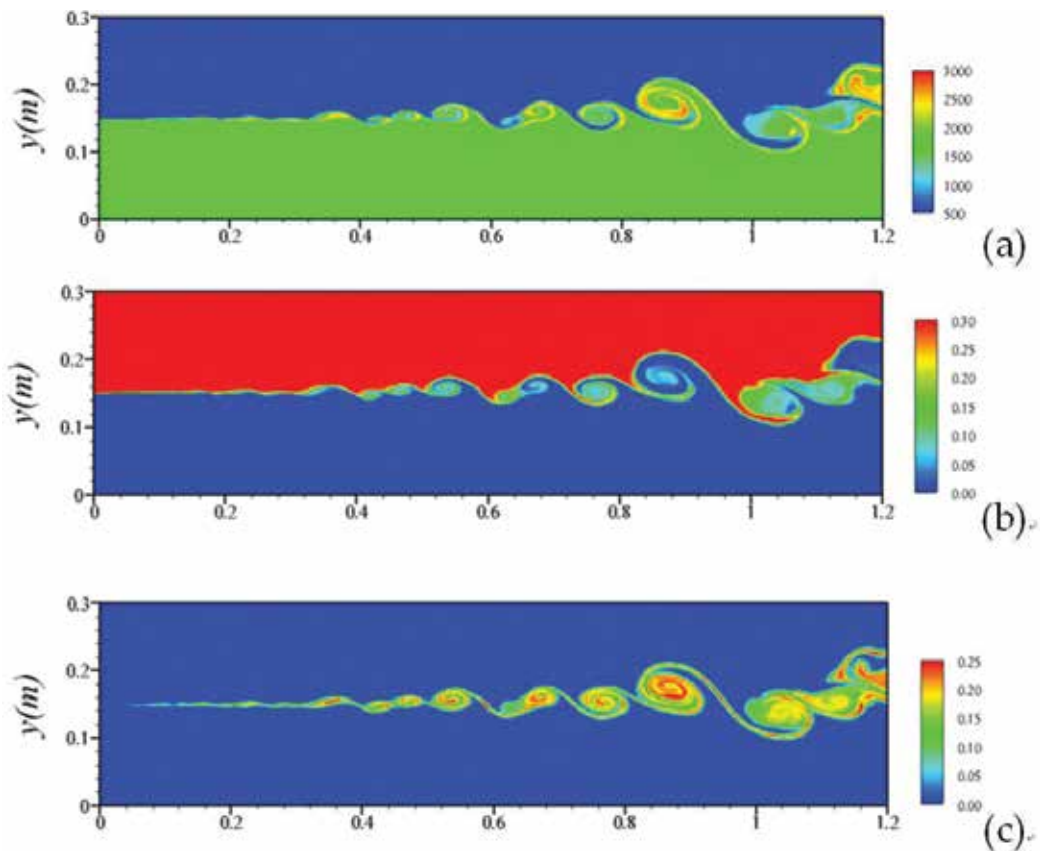


Figure 7. Instantaneous contour distribution of reactive flows. (a) temperature; (b) H_2 ; (c) H_2O .

Instantaneous distributions of temperature and mass fraction of H_2 and H_2O at $t = 2$ ms are shown in **Figure 7**. At about $x = 0.4$ m, the mixing layer loses stability, the large-scale vortices begin to form, and efficient mixing occurs inside the vortices. Due to the relatively high temperature of air, fast reaction occurs and a large amount of water concentrates inside the vortices.

Figure 8 shows the flame structures in the mixing layer flow. The flame structures were obtained by means of plotting all the combustion status in the whole computation domain within the time interval $2 < t < 2.5$ ms, that is, recording and plotting the temperature or species fraction at each calculation node in the observing time interval. Here, the mixture fraction is defined as

$$Z \equiv \frac{W_H}{W_H + W_O} \quad (48)$$

where W_H and W_O are the mass fraction of element H and element O, respectively. For the stoichiometric ratio, $Z_{st} = 0.111$. It can be seen that the peaks of temperature and water are both near Z_{st} . The flame structure is similar with that in the flamelet model, since the non-premixed flame dominates in the current case.

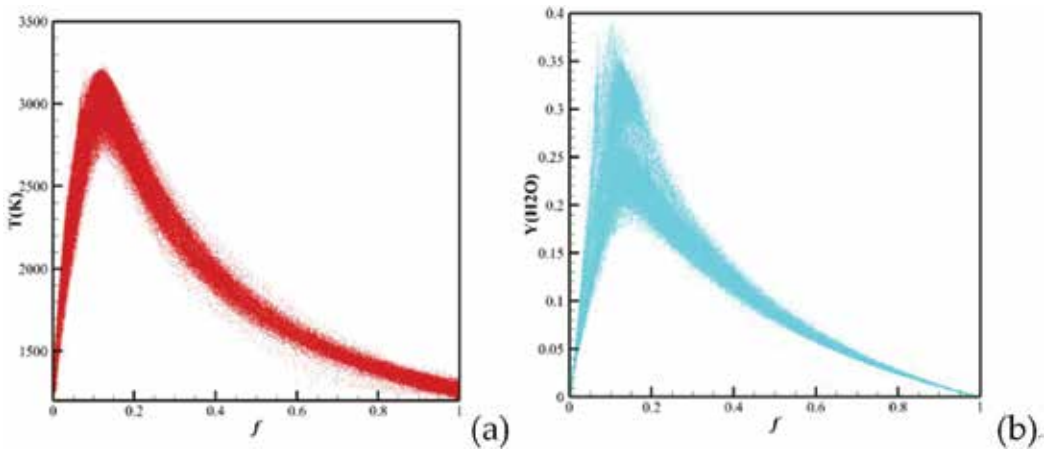


Figure 8. Flame structure. (a) temperature distribution and (b) water distribution.

4.3. Non-premixed combustion of n -decane droplets in turbulent mixing layers

The considered flow configuration is that of a spatially developing shear layer, as depicted in **Figure 9**, which is formed between a stream of hot air moving at velocity U_A and a spray carried

by cold air moving at velocity U_s , x and y refer to the stream-wise and transverse directions, respectively. The inflow parameters of the two streams are listed in **Table 1**.

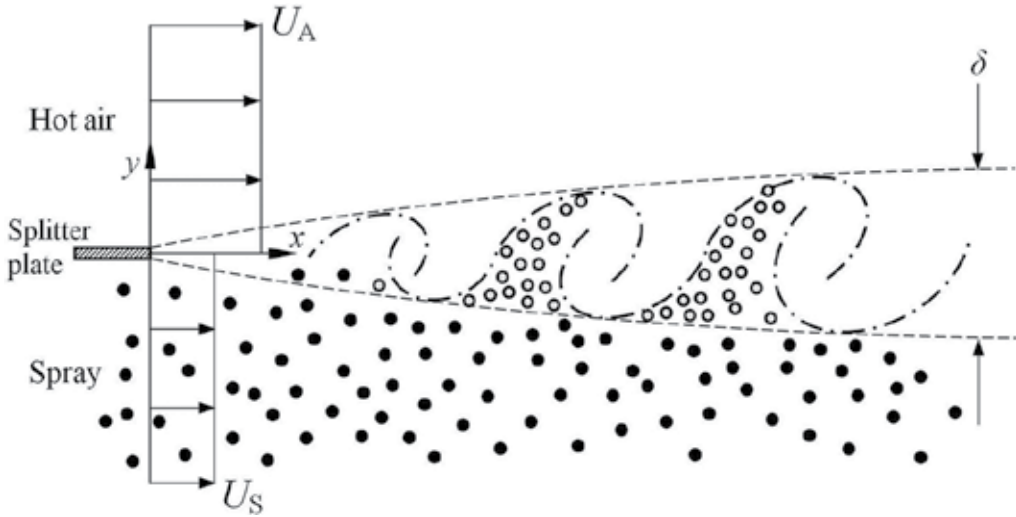
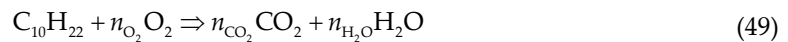


Figure 9. Schematic of a fuel spray in a two-dimensional turbulent shear layer.

| Velocity ratio U_A/U_s | Temperature ratio T_A/T_s | Pressure ratio P_A/P_s | Convective Mach number $M_c = \frac{U_A - U_s}{a_A + a_s}$ |
|-----------------------------|--------------------------------|-------------------------------|-------------------------------------------------------------------------------------------------------------------------------------------------------------------|
| 2 | 4 | 1 | 0.4 |
| U_s (m/s) | T_s (K) | P_s (MPa) | Inflow Reynolds number $Re = \frac{\rho U_A - U_s \delta_0}{\mu}$ |
| 458.3 | 363.3 | 0.1 | 2731.2 |
| u_d (m/s) | T_d (K) | ρ_d (kg/m ³) | Particle Stokes number (St_0) $St_0 = \frac{\tau_d}{\tau_f} = \left(\frac{\rho_d d_{d,0}^2}{18\mu_s} \right) \left(\frac{\delta_0}{ U_A - U_s } \right)$ |
| 458.3 | 298.2 | 642.0 | 10.5 |

Table 1. Inflow parameters.

The initial Mach numbers of the two streams equal 1.2. The cold-air stream is nonuniformly laden with droplets at the cold-air inlet. For the combustion reaction model, a one-step global reaction model of *n*-decane is used [30]. In this model, the chemical reaction is simplified as



where n_i is the molar stoichiometric coefficients of each species. The global reaction constant, k (mol/cm³/s), is given by

$$k = A \cdot T^n \exp\left(-\frac{E}{RT}\right) \left(\frac{\rho \cdot Y_F}{W_F \times 10^6}\right)^a \left(\frac{\rho \cdot Y_{O_2}}{W_{O_2} \times 10^6}\right)^b \quad (50)$$

where A is the coefficient of frequency and E is the activation energy. In the reaction of *n*-decane, these parameters are given as follows: $A = 3.8 \times 10^{11}$, $E = 1.256 \times 10^5$ J/mol, $a = 0.25$, $b = 1.5$, and $n = 0$. Therefore, the combustion reaction rate per unit volume (g/cm³/s) is $R_F = W_V k \times 10^3$.

In all simulation cases, the fuel droplets are initially located in the cold air and cannot vaporize until they traverse into the hot air associated with the rolling-up process of vortices. The hot-air stream provides the heat needed for droplet vaporization. The fuel vapor diffuses into the air stream, and it begins to react with the local oxygen as it reaches the high-temperature regions.

Large eddies rotate and entrain the hot air, providing heat for the evaporation of fuel droplets that preferentially accumulate in the high-strain vortex-braid regions adjoining the hot air. The fuel vapor generated by droplet evaporation diffuses toward the hot air and mixes with the surrounding oxygen, forming reactive pockets. Auto-ignition occurs when the fuel mass fraction is high enough, as depicted in **Figure 10(a)**. Under the instantaneous condition, the time t_{ig} defines the moment that the incipient establishment of ignition kernels occurs. We normalize the gaseous temperature by $T^* = T/T_{in}$ and $T_{in} = (T_A + T_S)/2$. The droplet diameters are normalized by $d^* d = d_d/d_{d0}$ and d_{d0} is the initial droplet diameter.

Large eddies rotate and the reaction kernels between two convection vortices are strained at time $t = t_{ig} + 0.25t_L$, as shown in **Figure 10(b)**. Here, the time t_L is the large eddy turnover time and is defined as

$$t_L = \frac{\delta_L}{|U_A - U_S|} \quad (51)$$

where δ_L is the length of the large eddy. Compared with the reaction rates of the ignition kernels at time t_{ig} , the chemical heat release in the reaction kernels at time $t_{ig} + 0.25t_L$ results in a larger temperature increase and facilitates the self-acceleration of the chemical reaction rate. At time $t = t_{ig} + 0.5t_L$, the reaction kernels are separated into two parts due to the stretch effects, as shown by **Figure 10(c)**. One part of the reaction kernels still exists in the high-strain vortex-braid zone and suffers the shear strain continuously. Evaporating fuel droplets segregate in a thin layer along this reaction kernel and feed fuel vapors for the chemical reaction. The other separated part is entrained in the inner of the large cold eddy. It is difficult for the fuel droplets to penetrate into the high-vorticity core of the large eddy because of the large droplet inertia and fuel droplets surround far from this separated reaction kernel, forming a thick vaporiza-

tion layer. However, the turbulence motion separates the vaporization layer and the flame kernel. Hence, the fuel vapor diffusion is difficult for feeding the chemical reaction in the flame kernel effectively. Here, we call it the weak-fueling mechanism due to the preferential concentration effects of droplets. If we track the separated reaction kernel in the inner of the cold eddy, it is found that the local chemical reaction rate of this flame kernel is decelerated, compared to that of the reaction kernel in the high-strain zone accompanied by the rich reactant supplement. **Figure 10(d)** depicts the extinction phenomena at time $t = t_{ig} + 0.75t_L$. Compari-

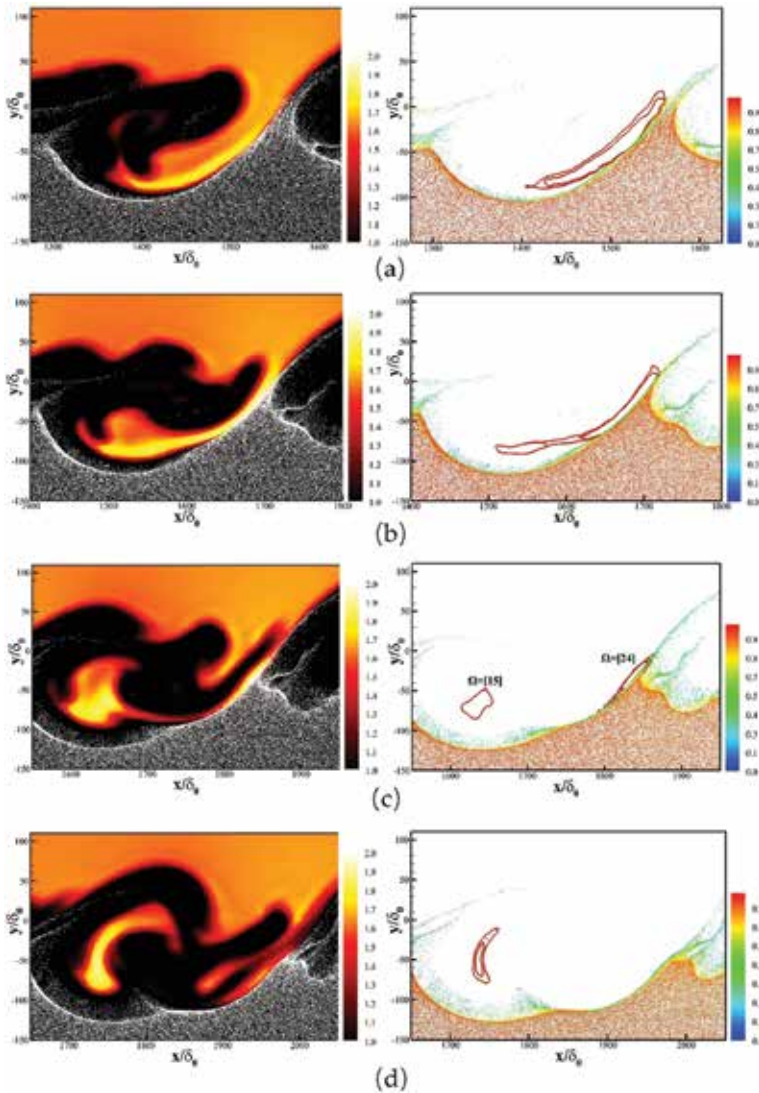


Figure 10. Flame kernels at (a) time $t = t_{ig}$; (b) time $t = t_{ig} + 0.25 t_L$; (c) time $t = t_{ig} + 0.5 t_L$; and (d) time $t = t_{ig} + 0.75 t_L$. Instantaneous distributions of dimensionless gaseous temperature (left) and reaction rate (right), with red isolines given by $\Omega = [11, 15]$ ($\text{kgm}^{-3}\text{s}^{-1}$) in (a) and $\Omega = [15, 24]$ ($\text{kgm}^{-3}\text{s}^{-1}$) in (b)–(d). Here, the dots indicate fuel droplets in the figures, with colors corresponding to dimensionless droplet diameters in the right figures.

son with **Figure 10(c)** shows that the reaction kernels that have high chemical reaction rates in the high-strain region at time $t = t_{ig} + 0.5t_L$ disappear. The other reaction kernel entrained in large eddies is distorted due to the turbulence motions.

5. Conclusions

This chapter introduced the state of art of the numerical simulation on compressible flows. The high-order hybrid WENO scheme, as one of the important issues for simulating the supersonic flows, is required to compute the numerical fluxes, in which the WENO scheme is used near the discontinuities and linear scheme is used in the smooth regions of the flows. In the solver developed by the present authors, the point-implicit method is utilized to treat the chemical stiffness problem.

A TGV problem, defined to investigate the transports of passive scalar, is simulated by the present numerical procedures. The decaying of the kinetic energy and variance of passive scalar due to initial gradients are analyzed based on the numerical results. The spatially developing mixing layer flows are simulated, taking the hydrogen and liquid *n*-decane droplets as fuel and air as oxidizer in the scenario of supersonic inflows. The stable combustion of hydrogen/air and the flame structure are analyzed by the numerical results. The ignition considering the eddy turnover effects is carefully analyzed, since the large-scale structures and droplet dispersion can be captured by the present numerical methods.

This chapter tries to contribute the field of numerically analyzing compressible reactive flows. The new high-order schemes and numerical strategy will be developed in the future, so that the stabilities and robustness will be enhanced by the solver based on the Navier-Stokes equations. Thus, deeply understanding the flow physics of compressible reactive flows will be benefited from results obtained by numerical simulations.

Author details

Bing Wang*, Zhao Xin Ren and Wei Wei

*Address all correspondence to: wbing@tsinghua.edu.cn

School of Aerospace Engineering, Tsinghua University, Beijing, China

References

- [1] Tomboulides, AG, Lee, JCY and Orszag, SA. Numerical simulation of low Mach number reactive flows. *Journal of Scientific Computing*. 1997;12(2):139–167.

- [2] Desjardins O, Blanquart G, Balarac G, et al. High order conservative finite difference scheme for variable density low Mach number turbulent flows. *Journal of Computational Physics*. 2008;227(15):7125–7159.
- [3] Dauplain A, Cuenot B, Poinso T. Large eddy simulation of a supersonic hydrogen-air diffusion flame. *Complex Effects in Large Eddy Simulation*. 2005;71:98.
- [4] Berglund M, Fureby C. LES of supersonic combustion in a scramjet engine model. *Proceedings of the Combustion Institute*. 2007;31(2):2497–2504.
- [5] Edwards J R, Boles J A, Baurle R A. Large-eddy/Reynolds-averaged Navier--Stokes simulation of a supersonic reacting wall jet. *Combustion and Flame*. 2012;159(3):1127–1138.
- [6] Selle L, Lartigue G, Poinso T, et al. Compressible large eddy simulation of turbulent combustion in complex geometry on unstructured meshes. *Combustion and Flame*. 2004;137(4):489–505.
- [7] Lacaze G, Cuenot B, Poinso T, et al. Large eddy simulation of laser ignition and compressible reacting flow in a rocket-like configuration . *Combustion and Flame*. 2009;156(6):1166–1180.
- [8] Boudier G, Gicquel L Y M and Poinso T, et al. Comparison of LES, RANS and experiments in an aeronautical gas turbine combustion chamber. *Proceedings of the Combustion Institute*. 2007;31(2):3075–3082.
- [9] Saghafian A, Terrapon V E, Pitsch H. An efficient flamelet-based combustion model for compressible flows. *Combustion and Flame*. 2015;162(3):652–667.
- [10] O'Brien J, Urzay J, Ihme M, et al. Subgrid-scale backscatter in reacting and inert supersonic hydrogen–air turbulent mixing layers. *Journal of Fluid Mechanics*. 2014;743:554–584.
- [11] Diegelmann F, Tritschler V, Hickel S, et al. On the pressure dependence of ignition and mixing in two-dimensional reactive shock-bubble interaction. . *Combustion and Flame*. 2016;163:414–426.
- [12] Jiang G S, Shu C W. Efficient implementation of weighted ENO schemes. *Journal of Computational Physics*. 1996;126:202–228.
- [13] Pirozzoli S. Conservative hybrid compact-WENO schemes for shock-turbulence interaction. *Journal of Computational Physics*. 2002;178(1):81–117.
- [14] Ren Y X, Zhang H. A characteristic-wise hybrid compact-WENO scheme for solving hyperbolic conservation laws. *Journal of Computational Physics*. 2003;192(2):365--386.
- [15] Hu X Y, Wang B, Adams N A. An efficient low-dissipation hybrid weighted essentially non-oscillatory scheme. *Journal of Computational Physics*. 2015;301:415–424.

- [16] Pirozzoli S. Numerical methods for high-speed flows. *Annual review of fluid mechanics*. 2011;43(163–194)
- [17] Miller R S, Bellan J. Direct numerical simulation of a confined three-dimensional gas mixing layer with one evaporating hydrocarbon-droplet-laden stream. *Journal of Fluid Mechanics*. 1999;384:293–338.
- [18] Miller R S. Effects of nonreacting solid particle and liquid droplet loading on an exothermic reacting mixing layer. *Physics of Fluids*. 2001;13(11):3303–3320.
- [19] Reveillon J, Vervisch L. Analysis of weakly turbulent dilute-spray flames and spray combustion regimes. *Journal of Fluid Mechanics*. 2005;537:317–347. 4
- [20] Wang Y, Rutland C J. Direct numerical simulation of ignition in turbulent n-heptane liquid-fuel spray jets. *Combustion and Flame*. 2007;149(4):353–365.
- [21] Schroll P, Wandel A P, Cant R S, et al. Direct numerical simulations of autoignition in turbulent two-phase flows. *Proceedings of the Combustion Institute*. 2009;32(2):2275–2282.
- [22] Neophytou A, Mastorakos E, Cant R S. The internal structure of igniting turbulent sprays as revealed by complex chemistry DNS. *Combustion and Flame*. 2012;159(2): 641–664.
- [23] Borghesi G, Mastorakos E, Cant R S. Complex chemistry DNS of n-heptane spray autoignition at high pressure and intermediate temperature conditions. *Combustion and Flame*. 2013;160(7):1254–1275.
- [24] Xia J, Zhao H, Megaritis A, et al. Inert-droplet and combustion effects on turbulence in a diluted diffusion flame. *Combustion and Flame*. 2013;160(2):366–383.
- [25] Burcat A, Ruscic B. Third millenium ideal gas and condensed phase thermochemical database for combustion with updates from active thermochemical tables. Argonne National Laboratory Argonne, IL; 2005.
- [26] Reid R C, Prausnitz J M, Poling B E. *The properties of gases and liquids*. McGraw-Hill, New York; 2001.
- [27] Eberhardt S, Imlay S. Diagonal implicit scheme for computing flows with finite rate chemistry. *Journal of Thermophysics and Heat Transfer*. 1992;6(2):208–216.
- [28] Wang Q, Squires K D, Wu X. Lagrangian statistics in turbulent channel flow. *Atmospheric environment*. 1995;29(18):2417–2427.
- [29] Nishioka M, Law C K. A numerical study of ignition in the supersonic hydrogen/air laminar mixing layer. *Combustion and flame*. 1997;108(1):199–219.
- [30] Westbrook C K, Dryer F L. Simplified reaction mechanisms for the oxidation of hydrocarbon fuels in flames. *Combustion science and technology*. 1981;27(1–2):31–43.

Electrical and Electronic Engineering

Hybrid Time-Frequency Numerical Simulation of Electronic Radio Frequency Systems

Jorge F. Oliveira

Additional information is available at the end of the chapter

<http://dx.doi.org/10.5772/64152>

Abstract

This chapter is devoted to the discussion of a hybrid frequency-time CAD tool especially designed for the efficient numerical simulation of nonlinear electronic radio frequency circuits operating in an aperiodic slow time scale and a periodic fast time scale. Circuits driven by envelope-modulated signals, in which the baseband signal (the information) is aperiodic and has a spectral content of much lower frequency than the periodic carrier, are typical examples of practical interest involving such time evolution rates. The discussed method is tailored to take advantage of the circuits and signals heterogeneity and so will benefit from the time-domain latency of some state variables in the circuits. Because the aperiodic slowly varying state variables are treated only in time domain, the proposed method can be seen as a hybrid scheme combining multitime envelope transient harmonic balance based on a multivariate formulation, with a purely time-step integration scheme.

Keywords: partial differential equations, numerical simulation, radio frequency circuits, time-frequency analysis

1. Introduction

In the last two decades, radio frequency (RF) and microwave system design has been found as a significant part of the electronic semiconductor industry's portfolio. Over the years, the necessity of continuously providing new wireless systems' functionalities and higher transmission rates, as also the need to improve transmitters' efficiency, has been gradually reshaping wireless architectures. Heterogeneous circuits combining baseband blocks, digital blocks, and RF blocks, in the same substrate, are commonly found today. Hence, RF and microwave

circuit simulation has been conducted to an increasingly challenging scenario of heterogeneous broadband and strongly nonlinear wireless communication circuits, presenting a wide variety of slowly varying and fast changing state variables (node voltages and branch currents). Thus, RF and microwave design has been an important booster for numerical simulation and device modeling development.

In general, waveforms processed by wireless communication systems can be expressed by a high-frequency RF carrier modulated by some kind of slowly varying baseband aperiodic signal (the information signal). Therefore, the evaluation of any relevant information time window requires the computation of thousands or millions of time instants of the composite modulated signal, turning any conventional numerical time-step integration of the circuits' systems of differential algebraic equations highly inefficient. However, if the waveforms do not require too many harmonic components for a convenient frequency-domain representation, this category of circuits can be efficiently simulated with hybrid time-frequency techniques. Handling the response to the slowly varying baseband information signal in the conventional time step by time step basis, but representing the reaction to the periodic RF carrier as a small set of Fourier components (a harmonic balance algorithm for computing the steady-state response to the carrier), hybrid time-frequency techniques are playing an important role in RF and microwave circuit simulation.

Beyond overcoming the signals' time-scale disparity, the partitioned time-frequency technique discussed in Section 3.2 is also able to efficiently simulate highly heterogeneous RF networks, by splitting the circuits into different subsets (blocks) and computing their state variables with distinct numerical schemes.

2. Theoretical background material

2.1. Mathematical model of an electronic circuit

Dynamic behavior of an electronic circuit can be modeled by a system of differential algebraic equations (DAE) involving electric voltages, currents and charges, and magnetic fluxes. The DAE system can, in general, be formulated as

$$\frac{dq(\mathbf{x}(t))}{dt} + \mathbf{f}(\mathbf{x}(t)) = \mathbf{b}(t), \quad (1)$$

in which $\mathbf{b}(t) \in \mathbb{R}^n$ stands for the excitation vector (independent voltage or current sources) and $\mathbf{x}(t) \in \mathbb{R}^n$ represents the state variable vector (node voltages and branch currents). $\mathbf{f}(\cdot)$ models the memoryless elements of the circuit, as is the case of linear or nonlinear resistors, linear or nonlinear controlled sources, etc. $q(\cdot)$ models the dynamic elements, as capacitors or inductors, represented as voltage-dependent electric charges or current-dependent magnetic fluxes, respectively.

This system of (1) can be constructed from a circuit description using, for example, nodal analysis, which involves applying Kirchhoff currents' law to each node in the circuit, and applying the constitutive or branch equations to each circuit element. Hence, it represents the general mathematical formulation of lumped problems. However, as reviewed in [1], this DAE circuit model formulation can also include linear distributed elements. For that, the distributed devices are substituted by their lumped-element equivalent circuit models, or are replaced, as whole sub-circuits, by reduced order models derived from their frequency-domain characteristics. It must be noted that the substitution of distributed devices by lumped-equivalent models is especially reasonable when the size of the circuit elements is small in comparison to the wavelengths, as is the case of most emerging RF technologies integrating digital high-speed CMOS baseband processing and RFCMOS hardware in the same substrate.

2.2. Transient simulation

Obtaining the solution of (1) over a specified time interval $[t_0, t_{Final}]$ with a specific initial condition $\mathbf{x}(t_0)=\mathbf{x}_0$ is what is usually known as an *initial value problem*, and evaluating such solution is frequently referred to as *transient analysis*. The most natural way to compute $\mathbf{x}(t)$ is to numerically time-step integrate (1) directly in time domain. So, it should be of no surprise that this straightforward technique was used in the first digital computer programs of circuit analysis and is still nowadays widely used. It is present in all SPICE (which means simulation program with integrated circuit emphasis) or SPICE-like computer programs [2]. In order to numerically time-step integrate the DAE system of (1) commercial tools use initial value solvers, such as linear multistep methods (LMM) [3–5], or one-step methods, i.e., Runge-Kutta (RK) methods [3–5]. Either LMM or RK families can offer a great diversity of explicit and implicit (iterative) numerical schemes, suitable to compute the numerical solution of different types of initial value problems with a desired accuracy.

2.3. Steady-state simulation

Although SPICE-like computer programs (which were initially conceived to compute the transient response of electronic circuits) are still widely used nowadays, RF and microwave designers' interest normally resides on the steady-state response. The reason for that is some properties of the circuits are better described, or simply only defined, in steady-state (e.g., harmonic or intermodulation distortion, noise, power, gain, impedance, etc.). Initial value solvers, as linear multistep methods, or Runge-Kutta methods, which were tailored for finding the circuit's transient response, are not adequate for computing the steady-state because they have to pass through the lengthy process of integrating all transients, and expecting them to vanish.

Computing the periodic steady-state response of an electronic circuit can be formulated as finding out a starting condition (left boundary), $\mathbf{x}(t_0)$, for the DAE system modeling the circuit that leads to a solution obeying the final condition (right boundary) $\mathbf{x}(t_0)=\mathbf{x}(t_0+T)$, with T being the period. In mathematics, these problems are usually known as *periodic boundary value*

problems. Taking into account the formulation of (1), these problems will have here the following form,

$$\frac{dq(\mathbf{x}(t))}{dt} + \mathbf{f}(\mathbf{x}(t)) = \mathbf{b}(t), \quad \mathbf{x}(t_0) = \mathbf{x}(t_0 + T), \quad t_0 \leq t \leq t_0 + T, \quad (2)$$

where the condition $\mathbf{x}(t_0)=\mathbf{x}(t_0+T)$ is known as the *periodic boundary condition*.

In order to numerically solve (2), a solution that simultaneously satisfies the differential system and the two-point periodic boundary condition has to be computed. A particular technique has been found especially useful for RF circuit simulation: the *harmonic balance* (HB) [6–8] method.

2.4. Harmonic balance

Harmonic balance (HB) [6–8] handles the circuit, its excitation and its state variables in the frequency-domain. Because of that, it benefits from allowing the direct inclusion of distributed devices (like dispersive transmission lines), or other circuit elements described by frequency-domain measurement data. Frequency-domain methods differ from time-domain steady-state techniques in the way that, instead of representing waveforms as a collection of time samples, they represent those using coefficients of sinusoids in trigonometric series. As a consequence, under moderate nonlinearities, the steady-state solution is typically achieved much more easily in the frequency domain than in the time domain.

In periodic steady-state, any stimulus $b_s(t)$ or state variable $x_v(t)$ can be expressed as a Fourier series

$$b_s(t) = \sum_{k=-K}^{+K} B_k e^{jk\omega_0 t}, \quad x_v(t) = \sum_{k=-K}^{+K} X_k e^{jk\omega_0 t}, \quad (3)$$

where $\omega_0=2\pi/T$ is the fundamental frequency and K is the order adopted for a convenient harmonic truncation. The HB method consists in converting the DAE system of (2) into the frequency domain, to obtain the following $n(2K+1)$ algebraic equations system

$$j\Omega\mathbf{Q}^{[r]} + \mathbf{F}^{[r]} + j\Omega\mathbf{C}^{[r]}[\mathbf{X}^{[r+1]} - \mathbf{X}^{[r]}] + \mathbf{G}^{[r]}[\mathbf{X}^{[r+1]} - \mathbf{X}^{[r]}] = \mathbf{B}, \quad (4)$$

in which the unknowns are the Fourier coefficients of the state variables of the circuit

$$\mathbf{X} = [\mathbf{X}_1^T, \mathbf{X}_2^T, \dots, \mathbf{X}_n^T]^T, \quad (5)$$

where each one of the \mathbf{X}_v , $v=1, \dots, n$, is a $(2K + 1) \times 1$ vector containing the Fourier coefficients of the corresponding state variable $x_v(t)$. \mathbf{F} and \mathbf{Q} are vectors containing the Fourier coefficients of $f(x(t))$ and $q(x(t))$, respectively, and \mathbf{G} and \mathbf{C} denote the $n(2K + 1) \times n(2K + 1)$ conversion matrices (Toeplitz) [7,9] corresponding to $g(x)=df(x)/dx$ and $c(x)=dq(x)/dx$. j is the imaginary unit and Ω is a diagonal matrix defined as

$$\Omega = \text{diag} \left(\underbrace{-K\omega_0, \dots, K\omega_0}_{v=1}, \underbrace{-K\omega_0, \dots, K\omega_0}_{v=2}, \dots, \underbrace{-K\omega_0, \dots, K\omega_0}_{v=n} \right). \quad (6)$$

The system of (4) can be rewritten as

$$\underbrace{j\Omega\mathbf{Q}^{[r]} + \mathbf{F}^{[r]} - \mathbf{B}}_{\mathbf{H}(\mathbf{x}^{[r]})} + \left[\underbrace{j\Omega\mathbf{C}^{[r]} + \mathbf{G}^{[r]}}_{\mathbf{J}(\mathbf{x}^{[r]})} \right] [\mathbf{X}^{[r+1]} - \mathbf{X}^{[r]}] = 0, \quad (7)$$

or, in its simplified form, as

$$\mathbf{H}(\mathbf{X}^{[r]}) + \frac{d\mathbf{H}(\mathbf{X})}{d\mathbf{X}} \Big|_{\mathbf{x}=\mathbf{x}^{[r]}} [\mathbf{X}^{[r+1]} - \mathbf{X}^{[r]}] = 0, \quad (8)$$

in which

$$\mathbf{H}(\mathbf{X}) = j\Omega\mathbf{Q}(\mathbf{X}) + \mathbf{F}(\mathbf{X}) - \mathbf{B} = 0 \quad (9)$$

is known as the *harmonic balance system*, and the $n(2K + 1) \times n(2K + 1)$ composite conversion matrix

$$\mathbf{J}(\mathbf{X}) = \frac{d\mathbf{H}(\mathbf{X})}{d\mathbf{X}} = j\Omega\mathbf{C}(\mathbf{X}) + \mathbf{G}(\mathbf{X}) \quad (10)$$

is known as the *Jacobian matrix* of the error function $\mathbf{H}(\mathbf{X})$. This system of (9) is iteratively solved according to (8), until a sufficiently accurate solution $\mathbf{X}^{[l]}$ is achieved, i.e., until

$$\|\mathbf{H}(\mathbf{X}^{[l]})\| = \|j\Omega\mathbf{Q}(\mathbf{X}^{[l]}) + \mathbf{F}(\mathbf{X}^{[l]}) - \mathbf{B}\| < \delta, \quad (11)$$

where δ is the allowed residual size, and $\| \mathbf{H}(\bullet) \|$ stands for some norm of the error function $\mathbf{H}(\bullet)$.

2.5. Multivariate formulation

The multivariate formulation is a powerful strategy that emerged in the late 1990s, playing an important role in RF circuit simulation today. It was first introduced by Brachtendorf et al. [10] as a sophisticated derivation of quasi-periodic harmonic balance, followed by Roychowdhury [11], who demonstrated that the multivariate formulation can be an efficient strategy to analyze circuits running on distinct time scales. The multivariate formulation uses multiple time variables (artificial time scales) to describe the multirate behavior of the circuits. Thus, it is suitable to describe typical multirate regimes of operation present in RF and microwave systems, as is the case of circuits handling amplitude and/or phase-modulated signals, quasiperiodic signals, or any other kind of multirate signals containing a periodic component.

The main achievements of the multivariate formulation are due to the fact that multirate signals can be represented much more efficiently if they are defined as functions of two or more time variables (artificial time scales), i.e., if they are defined as multivariate functions [11–16]. Therefore, as we see in Section 2.5.2, circuits will be no longer described by ordinary differential algebraic equations in the one-dimensional time t , but, instead, by partial differential algebraic systems.

2.5.1. Multivariate representations

The multivariate (multidimensional) strategy is easily illustrated by applying it to a bidimensional problem (two distinct time scales). So, let us consider, for example, an amplitude-modulated RF carrier of the form

$$b(t) = e(t) \cos(2\pi f_c t), \quad (12)$$

where $e(t)$ is the envelope (a slowly varying signal), while $\cos(2\pi f_c t)$ is the fast-varying RF carrier. Simulating a circuit with this kind of stimulus, using conventional time-step integration schemes (e.g., Runge-Kutta schemes, or linear multistep methods), is computationally very expensive. The main reason is that the solution has to be computed during a long time interval imposed by the slowly varying envelope, whereas the step length is severely constrained by the high-frequency RF carrier.

Consider now the following bidimensional definition for $b(t)$,

$$\hat{b}(t_E, t_C) = e(t_E) \cos(2\pi f_C t_C), \quad (13)$$

where t_E is the slow envelope time scale and t_C is the fast carrier time scale. In this particular case, $\hat{b}(t_E, t_C)$ is a periodic function with respect to t_C but not to t_E , i.e.,

$$\hat{b}(t_E, t_C) = \hat{b}(t_E, t_C + T_C), \quad T_C = 1 / f_C. \quad (14)$$

The univariate form, $b(t)$, with $e(t) = 2e^{-80 \times 10^6 t}$ and $f_C = 2$ GHz, is plotted in **Figure 1** for the [0, 25 ns] time interval. The corresponding bivariate form, $\hat{b}(t_E, t_C)$, is depicted in **Figure 2** for the rectangular region [0, 25 ns] \times [0, 0.5 ns]. There, it can be appreciated that $\hat{b}(t_E, t_C)$ does not have as many undulations as $b(t)$, thus allowing a more compact representation with fewer samples. Furthermore, due to the periodicity of $\hat{b}(t_E, t_C)$ in t_C , we know that its plot repeats over the rest of this time axis. Thus, the bivariate form plotted in **Figure 2** contains all the information necessary to recover the original univariate form depicted in **Figure 1**.

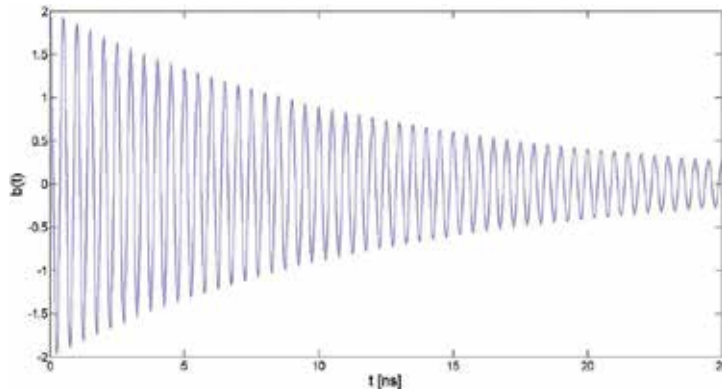


Figure 1. Envelope-modulated signal in the univariate time.

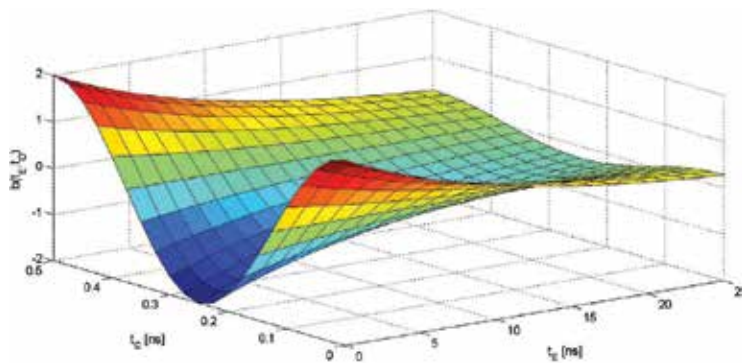


Figure 2. Bivariate representation of the envelope-modulated signal.

2.5.2. Multirate partial differential algebraic equations' systems

Let us consider a general nonlinear RF circuit described by the differential algebraic equations' system of (1), and let us suppose that this circuit is driven by the envelope-modulated signal of (12). Considering the above stated, we are able to reformulate the excitation $\mathbf{b}(t)$ and the state variables $\mathbf{x}(t)$ vectors as bidimensional entities, in which t is replaced by t_E for the slowly varying parts (the envelope time scale) and by t_C for the fast-varying parts (the RF carrier time scale). This bidimensional formulation converts the DAE system of (1) into the following *multirate partial differential algebraic equations'* (MPDAE) system [11]:

$$\frac{\partial \mathbf{q}(\hat{\mathbf{x}}(t_E, t_C))}{\partial t_E} + \frac{\partial \mathbf{q}(\hat{\mathbf{x}}(t_E, t_C))}{\partial t_C} + \mathbf{f}(\hat{\mathbf{x}}(t_E, t_C)) = \hat{\mathbf{b}}(t_E, t_C). \quad (15)$$

The mathematical relation between (1) and (15) establishes that if $\hat{\mathbf{b}}(t_E, t_C)$ and $\hat{\mathbf{x}}(t_E, t_C)$ satisfy (15), then the univariate forms $\mathbf{b}(t) = \hat{\mathbf{b}}(t, t)$ and $\mathbf{x}(t) = \hat{\mathbf{x}}(t, t)$ satisfy (1) [11]. Therefore, univariate solutions of (1) are available on diagonal lines $t_E = t$, $t_C = t$, along the bivariate solutions of (15), i.e., $\mathbf{x}(t)$ may be retrieved from its bivariate form $\hat{\mathbf{x}}(t_E, t_C)$, by simply setting $t_E = t_C = t$. Consequently, if one wants to obtain the univariate solution in the generic $[0, t_{Final}]$ interval, due to the periodicity of the problem in the t_C dimension we will have

$$\mathbf{x}(t) = \hat{\mathbf{x}}(t, t \bmod T_C) \quad (16)$$

on the rectangular domain $[0, t_{Final}] \times [0, T_C]$, where $t \bmod T_C$ represents the remainder of division of t by T_C . The main advantage of this MPDAE approach is that it can result in significant improvements in simulation speed when compared to DAE-based alternatives.

2.5.3. Initial and boundary conditions for envelope-modulated regimes

Dynamical behavior of RF circuits driven by stimuli of the form of (12) can be described by the MPDAE system of (15) together with a set of initial and periodic boundary conditions. In fact, bivariate forms of the circuits' state variables can be achieved by computing the solution of the following initial periodic-boundary value problem

$$\begin{aligned} \frac{\partial \mathbf{q}(\hat{\mathbf{x}}(t_E, t_C))}{\partial t_E} + \frac{\partial \mathbf{q}(\hat{\mathbf{x}}(t_E, t_C))}{\partial t_C} + \mathbf{f}(\hat{\mathbf{x}}(t_E, t_C)) &= \hat{\mathbf{b}}(t_E, t_C), \\ \hat{\mathbf{x}}(0, t_C) &= \mathbf{i}(t_C), \quad \hat{\mathbf{x}}(t_E, 0) = \hat{\mathbf{x}}(t_E, T_C), \end{aligned} \quad (17)$$

on the rectangle $[0, t_{Final}] \times [0, T_C]$. $i(\cdot)$ is a given initial-condition function defined on $[0, T_C]$, satisfying $i(0) = i(T_C) = x(0)$, and $\hat{x}(t_E 0) = \hat{x}(t_E T_C)$ is the periodic boundary condition due to the periodicity of the problem in the t_c fast carrier time scale.

The reason why bivariate envelope-modulated solutions do not need to be evaluated on the entire $[0, t_{Final}] \times [0, t_{Final}]$ domain (which would be computationally very expensive and would turn the multivariate strategy useless), and are restricted to the rectangle $[0, t_{Final}] \times [0, T_C]$, is because the solutions repeat along the t_c time axis. The way how univariate solutions are recovered from their multivariate forms was already defined above by (16).

3. Hybrid time-frequency techniques for computing the solution of MPDAEs

In this section, we will finally discuss the hybrid time-frequency numerical techniques that can be used to evaluate the solution of MPDAEs describing the operation of nonlinear electronic radio frequency circuits running in an aperiodic slow time scale and a periodic fast time scale. Section 3.1 addresses an efficient technique often referred to as *multitime envelope transient harmonic balance* (multitime ETHB). Then, Section 3.2 presents an advanced partitioned time-frequency technique, which is an improved version of multitime ETHB and has demonstrated to be even more efficient than this technique.

3.1. Multitime envelope transient harmonic balance

Let us consider the initial-boundary value problem of (17) and let us define a semi-discretization of the rectangular domain $[0, t_{Final}] \times [0, T_C]$ in the t_E slow time dimension described by the following general non uniform grid

$$0 = t_{E,0} < t_{E,1} < \dots < t_{E,i-1} < t_{E,i} < \dots < t_{E,K_E} = t_{Final}, \quad h_{E,i} = t_{E,i} - t_{E,i-1}, \quad (18)$$

in which K_E represents the total number of steps in t_E and $h_{E,i}$ denotes the grid size at each time step i . If we replace the derivatives of the MPDAE in t_E with a finite-differences approximation (e.g., a backward differentiation formula, the modified trapezoidal rule, etc.), then we obtain for each slow time instant $t_{E,i}$ from $i = 1$ to $i = K_E$, a periodic boundary value problem in t_C . For simplicity, and clarity, let us suppose that the Backward Euler rule is used. In such a case, we obtain

$$\frac{q(\hat{x}_i(t_C)) - q(\hat{x}_{i-1}(t_C))}{h_{E,i}} + \frac{dq(\hat{x}_i(t_C))}{dt_C} + f(\hat{x}_i(t_C)) = \hat{b}(t_{E,i}, t_C), \quad (19)$$

$$\hat{x}_i(0) = \hat{x}_i(T_C),$$

where $\hat{x}_i(t_C)$ is an approximation to the exact solution $\hat{x}(t_{E,i}t_C)$. Thus, once $\hat{x}_{i-1}(t_C)$ is computed, the solution on the next slow time instant, $\hat{x}_i(t_C)$, is evaluated by solving (19). Consequently, it is straightforward to conclude that we have to solve a set of K_E periodic boundary value problems if we want to obtain the solution $\hat{x}(t_{E,i}t_C)$ in the entire $[0, t_{Final}] \times [0, T_C]$ domain. With multitime ETHB, each one of these periodic boundary value problems is solved using the harmonic balance method. For each slow time instant $t_{E,i}$ the resultant HB system is the $n(2K + 1)$ algebraic equation system defined by

$$\frac{\mathbf{Q}(\hat{\mathbf{X}}(t_{E,i})) - \mathbf{Q}(\hat{\mathbf{X}}(t_{E,i-1}))}{h_{E,i}} + j\Omega\mathbf{Q}(\hat{\mathbf{X}}(t_{E,i})) + \mathbf{F}(\hat{\mathbf{X}}(t_{E,i})) = \hat{\mathbf{B}}(t_{E,i}), \quad (20)$$

where $\hat{\mathbf{B}}(t_{E,i})$ and $\hat{\mathbf{X}}(t_{E,i})$ are the vectors containing the Fourier coefficients of the excitation sources and of the solution (the state variables), respectively, at $t_E = t_{E,i}$. $\mathbf{F}(\bullet)$ and $\mathbf{Q}(\bullet)$ are unknown functions that can be computed by evaluating $f(\cdot)$ and $q(\cdot)$ in the time domain and then calculating their Fourier coefficients. Ω is the diagonal matrix (6), and the $\hat{\mathbf{X}}(t_{E,i})$ vector can be described as

$$\hat{\mathbf{X}}(t_{E,i}) = [\hat{\mathbf{X}}_1(t_{E,i})^T, \hat{\mathbf{X}}_2(t_{E,i})^T, \dots, \hat{\mathbf{X}}_n(t_{E,i})^T]^T, \quad (21)$$

where each one of the state variable frequency components, $\hat{\mathbf{X}}_v(t_{E,i})$, $v = 1, \dots, n$, is a $(2K+1) \times 1$ vector defined as

$$\hat{\mathbf{X}}_v(t_{E,i}) = [X_{v,-K}(t_{E,i}), \dots, X_{v,0}(t_{E,i}), \dots, X_{v,K}(t_{E,i})]^T. \quad (22)$$

The HB system of (20) can be rewritten as

$$\mathbf{H}(\hat{\mathbf{X}}(t_{E,i})) = \frac{\mathbf{Q}(\hat{\mathbf{X}}(t_{E,i})) - \mathbf{Q}(\hat{\mathbf{X}}(t_{E,i-1}))}{h_{E,i}} + j\Omega\mathbf{Q}(\hat{\mathbf{X}}(t_{E,i})) + \mathbf{F}(\hat{\mathbf{X}}(t_{E,i})) - \hat{\mathbf{B}}(t_{E,i}) = 0, \quad (23)$$

or simply as

$$\mathbf{H}(\hat{\mathbf{X}}(t_{E,i})) = 0, \quad (24)$$

in which $\mathbf{H}(\hat{\mathbf{X}}(t_{E,i}))$ is the error function at $t_E = t_{E,i}$. In general, the nonlinear algebraic system of (24) is iteratively solved using Newton's method

$$\mathbf{H}(\hat{\mathbf{X}}^{[r]}(t_{E,i})) + \frac{d\mathbf{H}(\hat{\mathbf{X}}(t_{E,i}))}{d\hat{\mathbf{X}}(t_{E,i})} \Big|_{\hat{\mathbf{X}}(t_{E,i})=\hat{\mathbf{X}}^{[r]}(t_{E,i})} [\hat{\mathbf{X}}^{[r+1]}(t_{E,i}) - \hat{\mathbf{X}}^{[r]}(t_{E,i})] = 0, \quad (25)$$

which requires that we have to solve a linear system of $n(2K + 1)$ equations at each iteration r to compute the new estimate $\hat{\mathbf{X}}^{[r+1]}(t_{E,i})$. Consecutive Newton iterations will be computed until a desired accuracy is achieved, i.e., until $\|\mathbf{H}(\hat{\mathbf{X}}(t_{E,i}))\| < \delta$, where δ is the allowed residual size.

The system of (25) requires the computation of the Jacobian matrix $\mathbf{J}(\hat{\mathbf{X}}(t_{E,i}))$, i.e., the derivative of the vector $\mathbf{H}(\hat{\mathbf{X}}(t_{E,i}))$, with respect to the vector $\hat{\mathbf{X}}(t_{E,i})$,

$$\mathbf{J}(\hat{\mathbf{X}}(t_{E,i})) = \frac{d\mathbf{H}(\hat{\mathbf{X}}(t_{E,i}))}{d\hat{\mathbf{X}}(t_{E,i})} = \begin{bmatrix} \frac{\partial \mathbf{H}_1(\hat{\mathbf{X}}(t_{E,i}))}{\partial \hat{\mathbf{X}}_1(t_{E,i})} & \frac{\partial \mathbf{H}_1(\hat{\mathbf{X}}(t_{E,i}))}{\partial \hat{\mathbf{X}}_2(t_{E,i})} & \dots & \frac{\partial \mathbf{H}_1(\hat{\mathbf{X}}(t_{E,i}))}{\partial \hat{\mathbf{X}}_n(t_{E,i})} \\ \frac{\partial \mathbf{H}_2(\hat{\mathbf{X}}(t_{E,i}))}{\partial \hat{\mathbf{X}}_1(t_{E,i})} & \frac{\partial \mathbf{H}_2(\hat{\mathbf{X}}(t_{E,i}))}{\partial \hat{\mathbf{X}}_2(t_{E,i})} & \dots & \frac{\partial \mathbf{H}_2(\hat{\mathbf{X}}(t_{E,i}))}{\partial \hat{\mathbf{X}}_n(t_{E,i})} \\ \dots & \dots & \dots & \dots \\ \frac{\partial \mathbf{H}_n(\hat{\mathbf{X}}(t_{E,i}))}{\partial \hat{\mathbf{X}}_1(t_{E,i})} & \frac{\partial \mathbf{H}_n(\hat{\mathbf{X}}(t_{E,i}))}{\partial \hat{\mathbf{X}}_2(t_{E,i})} & \dots & \frac{\partial \mathbf{H}_n(\hat{\mathbf{X}}(t_{E,i}))}{\partial \hat{\mathbf{X}}_n(t_{E,i})} \end{bmatrix} \quad (26)$$

This matrix has a block structure, consisting of $n \times n$ square submatrices (blocks), each one with dimension $(2K + 1)$. The general block of row m and column l can be expressed as

$$\frac{d\mathbf{H}_m(\hat{\mathbf{X}}(t_{E,i}))}{d\hat{\mathbf{X}}_l(t_{E,i})} = \frac{1}{h_{E,i}} \frac{d\mathbf{Q}_m(\hat{\mathbf{X}}(t_{E,i}))}{d\hat{\mathbf{X}}_l(t_{E,i})} + j\Omega \frac{d\mathbf{Q}_m(\hat{\mathbf{X}}(t_{E,i}))}{d\hat{\mathbf{X}}_l(t_{E,i})} + \frac{d\mathbf{F}_m(\hat{\mathbf{X}}(t_{E,i}))}{d\hat{\mathbf{X}}_l(t_{E,i})}. \quad (27)$$

3.2. Partitioned time-frequency technique

Although multitime ETHB can take advantage of the signals' time rate disparity, it does not take into account the circuit's heterogeneities, i.e., it uses the same numerical algorithm to compute all the circuit's state variables. Thus, if the circuit evidences some heterogeneity (e.g., modern wireless architectures combining RF, baseband analog circuitry, and digital components in the same circuit), this tool cannot benefit from such a feature. This lack of ability to perform some distinction between nodes or blocks within the circuit had already been identified by Rizzoli et al. [17] and is the main limitation of multitime ETHB. To cope with this deficiency, the partitioned time-frequency technique separates the circuit's state variables (node voltages and branch currents) into fast (*active*) and slowly varying (*latent*) subsets. That

implies the MPDAE system of (15) to be first considered as coupled active-latent MPDAE subsystems

$$\begin{aligned} \frac{\partial q_A(\hat{x}_A(t_E, t_C), \hat{x}_L(t_E, t_C))}{\partial t_E} + \frac{\partial q_A(\hat{x}_A(t_E, t_C), \hat{x}_L(t_E, t_C))}{\partial t_C} + f_A(\hat{x}_A(t_E, t_C), \hat{x}_L(t_E, t_C)) &= \hat{b}(t_E, t_C) \\ \frac{\partial q_L(\hat{x}_A(t_E, t_C), \hat{x}_L(t_E, t_C))}{\partial t_E} + \frac{\partial q_L(\hat{x}_A(t_E, t_C), \hat{x}_L(t_E, t_C))}{\partial t_C} + f_L(\hat{x}_A(t_E, t_C), \hat{x}_L(t_E, t_C)) &= \hat{b}(t_E, t_C) \end{aligned} \quad (28)$$

with

$$x(t) = \hat{x}(t, t) = \begin{bmatrix} x_A(t) = \hat{x}_A(t, t) \\ x_L(t) = \hat{x}_L(t, t) \end{bmatrix}, \quad x_A(t) \in \mathbb{R}^{n_A}, \quad x_L(t) \in \mathbb{R}^{n_L}, \quad n_A + n_L = n, \quad (29)$$

where $x_A(t)$ and $x_L(t)$ are the vectors containing, respectively, the fast-varying and the slowly varying state variables. As we will see, with this partition stratagem, fast-varying state variables can be computed with multitime ETHB, while slowly varying ones are being evaluated with a unidimensional time-step integration scheme. This tactic also allows the moderate nonlinearities to be treated in the frequency domain, while severe nonlinearities are appropriately evaluated in the time domain [16].

With the purpose of providing an elucidatory explanation of the partitioned time-frequency technique, let us consider a typical wireless system, composed of RF and baseband blocks. In such a case, the state variables in the RF block can be described as fast carrier envelope modulated waveforms defined as

$$x_A(t) = x_{A,v}(t) = \sum_{k=-K}^K X_{k,v}(t) e^{jk2\pi f_c t}, \quad v = 1, \dots, n_A \quad (30)$$

while state variables in the baseband block can be seen as slowly varying aperiodic functions of the form

$$x_L(t) = x_{L,v}(t) = \psi_v(t), \quad v = 1, \dots, n_L. \quad (31)$$

In (30), $X_{k,v}(t)$ represents the Fourier coefficients of $x_{A,v}(t)$, which are slowly varying in the baseband time scale, and f_c is the high-frequency carrier. As stated above, signals of the form $x_{A,v}(t)$ will be denoted as active, whereas signals of the form $x_{L,v}(t)$ will be designated as latent. The latency (slowness) of $x_{L,v}(t)$ indicates that these variables belong to a circuit block where there are no fluctuations dictated by the fast carrier. Thus, it is straightforward to conclude that all of the $x_{L,v}(t)$ can be efficiently represented with much less sample points than any of

the $x_{A,v}(t)$. Moreover, since the $x_{L,v}(t)$ state variables do not evidence any periodicity, they cannot be evaluated in the frequency domain. In contrast, if the number of harmonics K is not too large, the fast carrier oscillation components of $x_{A,v}(t)$ can be efficiently computed with harmonic balance. Taking the above into account we can easily conclude that distinct numerical strategies will be required if we want to simulate, in an efficient way, circuits having such signal format disparities.

In the following we provide a brief theoretical description of the partitioned time-frequency technique fundamentals. For that, let us now consider the bivariate forms of $x_{A,v}(t)$ and $x_{L,v}(t)$, denoted by $\hat{x}_{A,v}(t_E, t_C)$ and $\hat{x}_{L,v}(t_E, t_C)$, and defined as

$$\hat{x}_{A,v}(t_E, t_C) = \sum_{k=-K}^K X_{k,v}(t_E) e^{jk2\pi f_C t_C} \quad (32)$$

and

$$\hat{x}_{L,v}(t_E, t_C) = \psi_v(t_E), \quad (33)$$

where t_E and t_C are, respectively, the slow envelope time dimension and the fast carrier time dimension. As can be seen, since the $\hat{x}_{L,v}(t_E, t_C)$ state variables have no dependence on t_C they have no fluctuations in the fast time axis. The reason is that they belong to a circuit block where there are no carrier frequency oscillations. As a result, for each slow time instant $t_{E,i}$ defined on the grid of (18), each of the $\hat{x}_{L,v}(t_{E,i}, t_C)$ is merely a constant signal that can be simply represented by the $k=0$ component. Therefore, there is no necessity to perform the conversion between time and frequency domains for $\hat{x}_{L,v}(t_{E,i}, t_C)$, which means that these state variables can be processed in a purely time-domain scheme. In contrast, for each slow time instant $t_{E,i}$ each of the $\hat{x}_{A,v}(t_{E,i}, t_C)$ is a waveform that has to be represented as a Fourier series adopting a convenient harmonic truncation at some order $k = -K, \dots, K$, i.e., each of the $\hat{x}_{A,v}(t_{E,i}, t_C)$ is a waveform that requires a total of $2K + 1$ harmonic components for a convenient frequency domain representation. In summary, while active state variables have to be represented by a set of $2K + 1$ Fourier coefficients arranged in $(2K + 1) \times 1$ vectors of the form

$$\hat{\mathbf{X}}_{A,v}(t_{E,i}) = [X_{A,v,-K}(t_{E,i}), \dots, X_{A,v,0}(t_{E,i}), \dots, X_{A,v,K}(t_{E,i})]^T, \quad v = 1, \dots, n_A, \quad (34)$$

latent state variables can be represented as 1×1 scalar quantities, i.e., they can be simply represented as

$$\hat{\mathbf{X}}_{L,v}(t_{E,i}) = X_{L,v,0}(t_{E,i}), \quad v = 1, \dots, n_L. \quad (35)$$

By considering this, we can easily deduce that the size of the $\hat{\mathbf{X}}(t_{E,i})$ vector defined by (21) will be significantly decreased, as well as the total number of equations in the HB system of (23). Furthermore, another crucial aspect is that we are no longer forced to carry out the conversion between time and frequency domains for the latent state variables expressed in the form of (35), as well as for the components of $\mathbf{H}(\hat{\mathbf{X}}(t_{E,i}))$ corresponding to latent blocks of the circuit. Given that the $k=0$ order Fourier coefficient $X_{v,0}(t_{E,i})$ is exactly the same as the constant t_c time value $\hat{x}_v(t_{E,i})$, components of the HB system of (23) that have no dependence on active state variables will not be required for any direct or inverse Fourier transformation operations.

Considerable Jacobian $\mathbf{J}(\hat{\mathbf{X}}(t_{E,i}))$ matrix size reductions will also be achieved with this technique. Indeed, by considering the latency of state variables in some parts of the circuit, some blocks of the Jacobian matrix (26) are simply reduced to 1×1 scalar elements. These scalar elements contain the dc sensitivity of $\mathbf{H}(\hat{\mathbf{X}}(t_{E,i}))$ to the latent components of $\hat{\mathbf{X}}(t_{E,i})$.

With the state variable $\hat{\mathbf{X}}(t_{E,i})$ and the error function $\mathbf{H}(\hat{\mathbf{X}}(t_{E,i}))$ vector size reductions, as also the resulting Jacobian $\mathbf{J}(\hat{\mathbf{X}}(t_{E,i}))$ matrix size reduction, it is possible to avoid dealing with large linear systems in the iterations of (25). Thus, a less computationally expensive Newton-Raphson iterative solver is required to solve (23). In conclusion, partitioning the circuit into active and latent sub-circuits (blocks) can lead us to significant computation and memory savings when computing the solution.

4. Efficiency of the partitioned time-frequency technique

The effectiveness of the multitime ETHB technique is nowadays widely recognized by the RF and microwave community. The efficiency of the partitioned time-frequency simulation technique described in the previous section was also already established, as a consequence of the considerable reductions in the computational effort required to obtain the numerical solution of several RF circuits with distinct topologies and levels of complexity [16]. Even so, a brief comparison between this method, the previous state-of-the-art multitime ETHB and a conventional univariate time-step integration scheme (SPICE-like simulation), is included in this section. This will help the reader to get a perception of the potential of the partitioned hybrid technique. For that, we considered the RF mixer (frequency translation device) depicted in **Figure 3** as the illustrative application example. The circuit was simulated in MATLAB with three different techniques: (i) the partitioned time-frequency simulation technique, (ii) the multitime ETHB, and (iii) the Gear-2 multistep method [5] (a time-step integrator commonly used by SPICE-like commercial simulators).

Numerical computation times for simulations in the $[0, 1.0 \mu\text{s}]$ and $[0, 10.0 \mu\text{s}]$ intervals are presented in **Table 1**. For simplicity, in the hybrid time-frequency techniques we assumed a uniform grid in the t_E slow time scale (we have chosen $h_E = 10 \text{ ns}$ as the step size in that dimension) and we considered $K = 11$ as the maximum harmonic order for the HB evaluations in the t_c fast carrier time scale.

By comparing the CPU times obtained with the methods, we can attest the superiority of the partitioned time-frequency method. Indeed, speedups of more than two times were obtained with this method in comparison to multitime ETHB. We can also attest the inefficiency of univariate time-step integration when dealing with RF problems. Finally, it must be noted that the efficiency gain of the partitioned time-frequency technique was achieved without compromising accuracy. Indeed, the maximum discrepancy between solutions computed with this technique and multitime ETHB was in the order of 10^{-7} for all the state variables of the circuit.

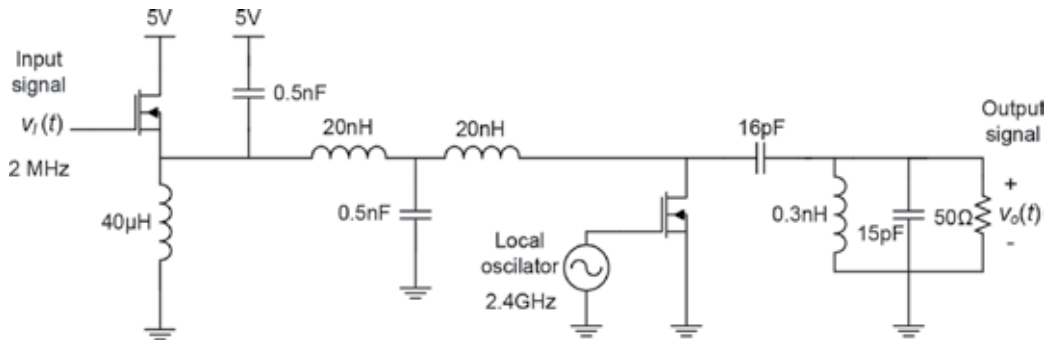


Figure 3. Simplified schematic diagram of a mixer (frequency translation device).

| Simulation time interval | Partitioned time-frequency technique | Multitime ETHB | Univariate time-step integration (Gear-2 method) |
|--------------------------|--------------------------------------|----------------|--------------------------------------------------|
| [0, 1.0 μs] | 00:00:04.9 | 00:00:11.3 | 00:19:21 |
| [0, 10.0 μs] | 00:00:39.6 | 00:01:35.1 | 02:47:33 |

Table 1. CPU time (h:min:sec)—simulation of the circuit depicted in Figure 3.

5. Conclusions

In this chapter, we have presented a partitioned time-frequency numerical technique especially designed for the efficient simulation of RF circuits operating in a periodic fast time scale and an aperiodic slow time scale. This technique can be viewed as a wise combination of multitime ETHB based on a multivariate formulation, with a conventional univariate time-step integration scheme. With this technique fast changing (active) state variables are computed in a bivariate mixed time-frequency domain, whereas slowly varying (latent) state variables are evaluated in the natural one-dimensional time domain. By partitioning the circuits into active and latent parts and exploiting the fact there is no obligation to perform conversion between time and frequency for latent blocks, considerable reductions in the computational effort can be achieved without compromising the accuracy of the results.

Although the speedups obtained with the simulation of the illustrative application example presented in Section 4 are already notable, it must be noted that higher efficiency gains should be expected when simulating RF networks containing a number of latent blocks larger than the active ones.

Acknowledgements

This work is funded by National Funds through FCT - Fundação para a Ciência e a Tecnologia, under the project UID/EEA/50008/2013.

Author details

Jorge F. Oliveira

Address all correspondence to: jorge.oliveira@ipleiria.pt

School of Technology and Management, Polytechnic Institute of Leiria, Leiria, Portugal, and Institute of Telecommunications, University of Aveiro, Aveiro, Portugal

References

- [1] Achar R, Nakhla M. Simulation of high-speed interconnects. *Proceedings of the IEEE*. 2001;89:693–728. DOI: 10.1109/5.929650
- [2] Nagel L. *A Computer Program to Simulate Semiconductor Circuits*. Berkeley: Electronics Research Laboratory, University of California. 1975;Memo ERL-M520
- [3] Hairer E, Nørsett S, Wanner G. *Solving Ordinary Differential Equations I: Nonstiff Problems*. 1st ed. Berlin: Springer-Verlag; 1987. DOI: 10.1007/978-3-662-12607-3
- [4] Hairer E, Wanner G. *Solving Ordinary Differential Equations II: Stiff and Differential Algebraic Problems*. 2nd ed. Berlin: Springer-Verlag; 1996. DOI: 10.1007/978-3-642-05221-7
- [5] Lambert J. *Numerical Methods for Ordinary Differential Systems: The Initial Value Problem*. 1st ed. West Sussex: Wiley; 1991.
- [6] Rodrigues P. *Computer-Aided Analysis of Nonlinear Microwave Circuits*. Norwood, MA: Artech House; 1998.
- [7] Maas S. *Nonlinear Microwave and RF Circuits*. 2nd ed. Norwood, MA: Artech House; 2003.

- [8] Kundert K, White J, Sangiovanni-Vincentelli A. *Steady-State Methods for Simulating Analog and Microwave Circuits*. Norwell, MA: Springer; 1990.
- [9] Pedro J, Carvalho N. *Intermodulation Distortion in Microwave and Wireless Circuits*. 1st ed. Norwood, MA: Artech House; 2003.
- [10] Brachtendorf H, Welsch G, Laur R, Bunse-Gerstner A. Numerical steady-state analysis of electronic circuits driven by multi-tone signals. *Electrical Engineering (Springer-Verlag)*. 1996;79(2):103–112. DOI: 10.1007/BF01232919
- [11] Roychowdhury J. Analyzing circuits with widely separated time scales using numerical PDE methods. *IEEE Transactions on Circuits and Systems*. 2001;5(48):578–594. DOI: 10.1109/81.922460
- [12] Mei T, Roychowdhury J, Coffey T, Hutchinson S, Day D. Robust stable time-domain methods for solving MPDEs of fast/slow systems. *IEEE Transactions on Computer-Aided Design of Integrated Circuits and Systems*. 2005;24(2):226–239. DOI: 10.1109/TCAD.2004.841073
- [13] Zhu L, Christoffersen C. Adaptive harmonic balance analysis of oscillators using multiple time scales. In: *3rd International IEEE Northeast Workshop on Circuits and Systems*; 2005; Québec City. 2005. pp. 187–190. DOI: 10.1109/NEWCAS.2005.1496738
- [14] Oliveira J, Pedro J. An efficient time-domain simulation method for multirate RF nonlinear circuits. *IEEE Transactions on Microwave Theory and Techniques*. 2007;55(11):2384–2392. DOI: 10.1109/TMTT.2007.908679
- [15] Oliveira J, Pedro J. A multiple-line double multirate shooting technique for the simulation of heterogeneous RF circuits. *IEEE Transactions on Microwave Theory and Techniques*. 2009;57(2):421–429. DOI: 10.1109/TMTT.2008.2011228
- [16] Oliveira J, Pedro J. Efficient RF circuit simulation using an innovative mixed time-frequency method. *IEEE Transactions on Microwave Theory and Techniques*. 2011;59(4):827–836. DOI: 10.1109/TMTT.2010.2095035
- [17] Rizzoli et al. Domain-decomposition harmonic balance with block-wise constant spectrum. In: *Proceedings of the IEEE MTT-S International Microwave Symposium Digest*; June 2006; San Francisco, CA. 2006. pp. 860–863. DOI: 10.1109/MWSYM.2006.249827

HgCdTe Mid- and Long-Wave Barrier Infrared Detectors for Higher Operating Temperature Condition

Małgorzata Kopytko and Piotr Martyniuk

Additional information is available at the end of the chapter

<http://dx.doi.org/10.5772/63943>

Abstract

In the last decade, a new architecture design such as nBn device or unipolar barrier photodiode has been proposed to achieve high operating temperature condition. This idea has also been implemented into HgCdTe ternary material system. In this chapter, we present the status of HgCdTe barrier detectors grown by metalorganic chemical vapor deposition with emphasis on numerical simulations of their properties. The device concept of a specific barrier bandgap architecture integrated with Auger suppression is a proper solution for high operating temperature infrared detectors. The device performance is comparable with state-of-the-art HgCdTe photodiodes.

Theoretical modeling of the HgCdTe barrier detectors has been performed using our original numerical program developed at the Institute of Applied Physics, Military University of Technology (MUT) and the commercially available APSYS platform (Crosslight Inc.). The detector's performance was assessed taking into account a wide spectrum of generation-recombination mechanism: Auger, Shockley-Read-Hall, and tunneling processes.

Keywords: HgCdTe, infrared detectors, barrier infrared detectors, high operating temperature, MOCVD growth

1. Introduction

The importance of infrared (IR) radiation technology results from the prevalence of infrared radiation. Infrared is invisible to the human eye radiant energy emitted by any object at temperature above absolute zero. Of particular importance is the spectrum of objects at temperature close to the average temperature of the Earth. It provides the comprehensive

information about their position in space, temperature, surface properties, as well as information about the chemical composition of the atmosphere through which the radiation is transmitted.

All information carried by the infrared radiation can be read and processed by suitable sensors (detectors) that transform infrared energy into other forms, directly and easy to measure. The sensors used to detect infrared radiation are usually equipped with two types of detectors: thermal detectors and photon detectors.

At present, the technology of the mid- (MWIR, 3–8 μm) and long-wave (LWIR, 8–14 μm) infrared radiation is mainly connected with photon detectors, designed on the basis of complex semiconductor materials, such as mercury cadmium telluride (HgCdTe) or indium gallium arsenide (InGaAs). The incident radiation is absorbed within the material by interaction with electrons, and the detector signal is caused by changes of the electric energy distribution. They exhibit both perfect signal-to-noise performance and a very fast response. But to achieve this, the present photon detectors require cryogenic cooling. Cryogenic cooling creates the cost and inconvenient limitations, especially in civil applications.

Thus, higher operation temperature (HOT) condition is one of the most important research areas in infrared technology. The development of a new detector's architecture has been driven by applications requiring multispectral detection, high-frequency response, high detectivity, small size, low weight and power consumption (SWaP), and finally HOT condition. Significant improvements in the reduction of the dark current leading to HOT condition have been achieved by the suppression of Auger thermal generation [1]. In practice, most of the HgCdTe Auger suppressed photodiodes are based on complex graded gap and doping multilayer structures, complicated to grow in terms of technology. The $\text{P}^+\pi\text{N}^+$ or $\text{N}^+\nu\text{P}^+$ device structures with a combination of exclusion (P^+/π or N^+/ν) and extraction (N^+/π or P^+/ν) junctions have demonstrated the suppression of Auger mechanisms by reducing the absorber carrier density below thermal equilibrium in reverse bias condition. A recent strategy to achieve HOT detectors includes simple nBn (B: barrier layer) barrier structures [2].

This chapter exhibits the fundamental properties of HgCdTe semiconductors and relates those material parameters that have successful applications as an IR barrier detector alloy. It presents different barrier HgCdTe structures in terms of dark current. The intent of this chapter is to concentrate on a barrier device approach having the greatest impact on IR industry development today.

2. Fundamental HgCdTe properties

The mercury cadmium telluride ($\text{Hg}_{1-x}\text{Cd}_x\text{Te}$) (MCT) is a practically perfect IR detector material system. Its distinctive position depends on three key features:

- cadmium (Cd) composition-dependent energy bandgap (sensing wavelength can be tuned by varying its alloy composition x over the 1–30 μm range),
- large optical coefficients that enable high quantum efficiency, and

- favorable inherent recombination mechanisms that lead to long carrier lifetime and high operating temperature.

Additionally, extremely small change of lattice constant versus composition makes it possible to grow high-quality layers and heterostructures.

2.1. Energy bandgap

The electrical and optical properties of $\text{Hg}_{1-x}\text{Cd}_x\text{Te}$ are determined by energy gap E_g . Energy gap of this compound ranges from -0.30 eV for semimetallic HgTe goes through 0 eV for approximately Cd composition $x = 0.15$ and finally up to 1.608 eV for CdTe. A number of expressions approximating E_g dependence on composition and temperature are available at present. The most widely used formula is given by Hansen et al. [3]:

$$E_g(x, T) = -0.302 + 1.93x - 0.81x^2 + 0.832x^3 + 5.35 \times 10^{-4}T(1 - 2x) \quad (1)$$

where E_g is the energy gap in eV, T is the temperature in K, and x is the Cd molar composition.

Figure 1 shows the empirical fit of the $\text{Hg}_{1-x}\text{Cd}_x\text{Te}$ bandgap according to Hansen et al. [3] versus the Cd molar composition, x at temperature 77 and 300 K. The cutoff wavelength λ_c , defined as that wavelength at which the response drops to 50% of its peak value, is also plotted.

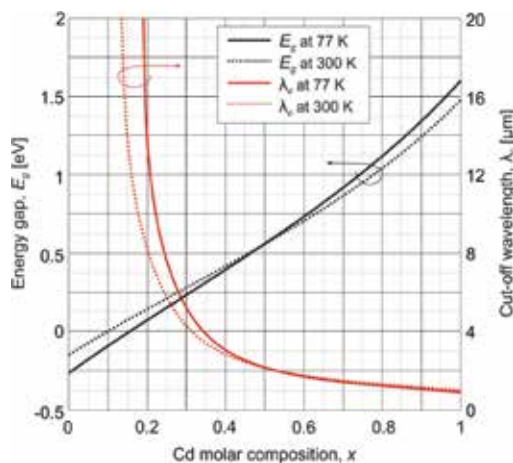


Figure 1. The bandgap structure of $\text{Hg}_{1-x}\text{Cd}_x\text{Te}$ according to Hansen et al. [3] as a function of Cd molar composition, x at temperature of 77 K (solid line) and 300 K (dashed line).

2.2. Electron affinity

For a semiconductor-vacuum interface, electron affinity is defined as the energy obtained by moving an electron from the vacuum just outside the semiconductor to the bottom of the

conduction band just inside the semiconductor. For HgCdTe, electron affinity X can be calculated from [4]:

$$X = 4.23 - 0.813(E_g - 0.083) \quad (2)$$

2.3. Intrinsic concentration

The most widely used expression for intrinsic carrier concentration n_i is that of Hansen and Schmit [5]:

$$n_i = (5.585 - 3.82x + 1.753 \times 10^{-3}T + 1.364 \times 10^{-3}) \times 10^{14} E_g^{3/4} T^{3/2} \exp\left(-\frac{E_g}{2k_B T}\right) \quad (3)$$

where k_B is the Boltzmann constant in eV/K.

The effective mass of electron, m_e , in the narrow gap HgCdTe can be expressed by Weiler's formula that can be approximated by $m_e/m_0 \approx 0.071E_g$, while the effective mass of heavy hole, m_h , is often assumed in modeling of IR detectors according to $m_h = 0.55m_0$.

2.4. Mobility

Due to small effective masses the electron mobility in HgCdTe is high. Mobility Cd molar composition dependence results primarily from the x -dependence of the bandgap and the temperature dependence of the scattering mechanisms. The electron mobility in $\text{Hg}_{1-x}\text{Cd}_x\text{Te}$ in composition range $0.2 < x < 0.6$ and temperature $T > 50$ K can be approximated as [6, 7]

$$\mu_e = \frac{9 \times 10^8 s}{T^{2r}} \quad (4)$$

where μ_e is the electron mobility in $\text{m}^2/\text{V s}$, $s = (0.2/x)^{7.5}$, and $r = (0.2/x)^{0.6}$.

For modeling IR HgCdTe photodetectors, the hole mobility is usually calculated assuming that the electron-to-hole mobility ratio, μ_e/μ_h is constant and equal to 100.

2.5. Absorption coefficient

High-quality HgCdTe samples exhibit absorption coefficient α in the short-wavelength region to be in proper agreement with the Kane model. The problems appear to be complicated in the LWIR region by the appearance of an absorption tail extending at energies lower than the energy gap attributed to the composition inhomogeneity. In simulations, a modified Urbach's rule is implemented [8]:

$$\alpha = \alpha_0 \exp\left[\frac{\sigma(E - E_0)}{T + T_0}\right] \quad (5)$$

where α is the absorption coefficient in cm^{-1} , $\alpha_0 = \exp(53.61x - 18.88)$, E is energy in eV, T is the temperature in K, $T_0 = 81.9$ in K, $E_0 = -0.3424 + 1.838x + 0.148x^2$, and $\sigma = 3.267 \times 10^4(1 + x)$.

An empirical formula was thereby employed in the Kane region [9]:

$$\alpha = \alpha_g \exp[\beta(E - E_g)]^{1/2} \quad (6)$$

where the β parameter after Chu et al. [9] is $\beta = -1 + 0.083T + (21 - 0.13T)x$.

2.6. Dielectric constant

The dielectric constants ϵ are not a linear function of x and temperature dependence was not observed within the experimental resolution. These dependences can be described by the following relations [10]:

$$\epsilon_\infty = 15.2 - 5.6x + 8.2x^2 \quad (7)$$

$$\epsilon_s = 20.5 - 15.6x + 5.7x^2 \quad (8)$$

where ϵ_∞ is the high-frequency dielectric constant and ϵ_s is the static dielectric constant.

3. Numerical procedure and generation-recombination mechanisms

Theoretical modeling of the HgCdTe barrier detectors has been performed using our original numerical program developed at the Institute of Applied Physics, Military University of Technology (MUT), and the commercially available APSYS platform (Crosslight Inc.). Both programs are based on numerical solution of the Poisson's and the electron/hole current continuity Eqs. (9)–(11) [11, 12]. In addition, both programs include the energy balance Eq. (12):

$$\frac{\partial n}{\partial t} = \frac{1}{q} \nabla \cdot \vec{j}_n + G - R \quad (9)$$

$$\frac{\partial p}{\partial t} = -\frac{1}{q} \nabla \cdot \vec{j}_p + G - R \quad (10)$$

$$\nabla^2 \psi = -\frac{q}{\epsilon \epsilon_0} \rho - \frac{1}{\epsilon} \nabla \psi \nabla \epsilon \quad (11)$$

$$C_V \frac{\partial T}{\partial t} - H = -\nabla(\chi \cdot \nabla T) \quad (12)$$

where q is the elementary charge, j is the current density, G is the generation rate, and R is the recombination rate. Indices n and p denote electron and hole, respectively. In Poisson's Eq. (11) Ψ is the electrostatic potential and ρ is the electrical charge. In the last term, C_V is the specific heat, χ is the thermal conductivity coefficient, and H is the heat generation term. A Joule heat is introduced as the heat generation in order to include the thermoelectric effect and heat balance.

Current density is usually expressed as functions of quasi-Fermi levels:

$$\vec{j}_n = q\mu_e n \nabla \Phi_n \quad (13)$$

$$\vec{j}_p = q\mu_h p \nabla \Phi_p \quad (14)$$

where Φ_n and Φ_p denote the quasi-Fermi levels.

The difference $G - R$ (Eqs. (9) and (10)) is the net generation of electron-hole pairs and depends on all generation recombination (GR) effects including influence of thermal mechanisms as well as tunneling mechanisms.

Depending on this approach, either two or three important carrier thermal GR processes, Shockley-Read-Hall (SRH), Auger, and radiative mechanisms were included in simulations. A radiative GR process could be ignored because photon recycling restricts the influence of that process on the performance of HgCdTe photodiodes [13, 14]. Tunneling mechanisms were considered due to band-to-band tunneling (BTB) and trap-assisted tunneling (TAT).

Thermal generation could be given as a sum of radiative, Auger 1, Auger 7, and SRH mechanisms. BTB and TAT effects can also be included as a GR process:

$$(G - R) = (G - R)_{RAD} + (G - R)_{AUG} + (G - R)_{SRH} + (G - R)_{BTB} + (G - R)_{TAT} \quad (15)$$

The set of transport Eqs. (9)–(11) is commonly known; however, their solution consists of serious mathematical and numerical problems. The equations are nonlinear, and are complex functions of electrical potential, quasi-Fermi levels, and temperature. The details concerning the solutions of Poisson's equation are presented in Appendix A.

3.1. Radiative process/photon recycling

For a long time, internal radiative GR processes have been considered to be the main fundamental limit to detector performance and the performance of practical devices have been compared to that limit. The following relation can be used to estimate radiative $(G - R)_{RAD}$ contribution [15]:

$$(G - R)_{RAD} = B(np - n_i^2) \tag{16}$$

$$B = 5.9052 \times 10^{18} n_i^{-2} \varepsilon T^{3/2} \sqrt{\frac{1+x}{(81.9+T)}} \exp\left(-\frac{E_g}{k_B T}\right) (E_g^2 + 3k_B T E_g + 3.75k_B^2 T^2) \tag{17}$$

Due to photon recycling effect, the radiative lifetime is highly extended. According to Humphreys [13], most of the photons emitted in photodetectors as a result of radiative decay are immediately reabsorbed and the observed radiative lifetime is only a measure of how well photons can escape from the volume of the detector. In many cases, especially in the case of semiconductors with high reflective index, radiative mechanism can be omitted in numerical modeling.

3.2. Auger processes

There are several types of Auger processes, and among them Auger 1 and Auger 7 are the most dominant due to the smallest threshold energies. The Auger 1 generation is the impact ionization by an electron, generating an electron-hole pair and is dominant in n-type material while Auger 7 is the impact generation of electron-hole pair by a light hole and dominates in p-type material.

The Auger generation and recombination rates strongly depend on temperature via the dependence of carrier concentration and intrinsic time on temperature. Therefore, cooling is a natural and a very effective way to suppress Auger processes according to the following relation [16]:

$$(G - A)_{AUG} = (C_n n + C_p p)(np - n_i^2) \tag{18}$$

$$C_n = 5 \times 10^{-22} |F_1 F_2| \left[\left(\frac{E_g}{k_B T} \right)^3 \exp\left(1 + 2 \frac{m_e^*}{m_h^*}\right) \left(\frac{E_g}{k_B T (m_e^* / m_h^*)} \right) \right]^{-1/2} \tag{19}$$

$$\times n_i^{-2} [3.8 \times 10^{-18} \varepsilon^2 \left(\frac{1}{m_e^*} \right) \cdot \left(1 + 2 \frac{m_e^*}{m_h^*} \right) \sqrt{1 + \frac{m_e^*}{m_h^*}}]^{-1}$$

$$C_p = \gamma \cdot C_n \quad (20)$$

where $|F_1 F_2|$ is the overlap integrals for Bloch functions. The ratio γ has been calculated as a function of composition and temperature and is assumed to be ranging from 3 to 60 depending on temperature [17, 18].

3.3. Shockley-Read-Hall processes

The Shockley-Read-Hall (SRH) mechanism is not an intrinsic process because it occurs via levels in the forbidden energy gap. Metal site vacancies (mercury vacancies) are considered as an SRH centers in HgCdTe. The reported position of SRH centers for both n- and p-type material is assumed as $1/3 E_g$ or $3/4 E_g$ from the conduction band. The $(G - R)_{SRH}$ rate could be calculated according to the following formula [19–21]:

$$(G - R)_{SRH} = \frac{np - n_i^2}{\tau_{p0}(n_0 + n_1) + \tau_{n0}(p_0 + p_1)} \quad (21)$$

where

$$n_1 = n_i \exp\left(\frac{E_T - E_{Fi}}{k_B T}\right) \quad (22)$$

$$p_1 = n_i \exp\left(\frac{E_{Fi} - E_T}{k_B T}\right) \quad (23)$$

n_1 and p_1 mean concentrations in the case in which the trap level E_T coincides with the Fermi level E_{Fi} . The terms $\tau_{n0} = (c_n N_T)^{-1}$ and $\tau_{p0} = (c_p N_T)^{-1}$ are the shortest possible time constants for the electron and hole capture coefficients (c_n and c_p), respectively. N_T denotes the mercury vacancy concentration.

3.4. Tunneling processes

BTB tunneling is calculated as a function of the applied electric field F [22–24]:

$$(G - R)_{BTB} = \frac{q F m^*}{2\pi^2 \hbar^3} P_0 \bar{E} \quad (24)$$

where \hbar is the reduced Planck constant and m^* is the electron effective mass related to the tunneling mechanism defined as

$$m^* = \frac{m_c m_v}{m_c + m_v} \quad (25)$$

where m_c and m_v are the effective masses in conduction and valence bands, respectively.

Tunneling probability P_0 with a zero perpendicular (to the x -direction) momentum can be estimated using the following relations:

$$P_0 = \exp\left(\frac{\pi(m^*)^{1/2} E_g^{3/2}}{2\sqrt{2}qF\hbar}\right) \quad (26)$$

$$\bar{E} = \frac{\sqrt{2}qF\hbar}{2\pi(m^*)^{1/2} E_g^{1/2}} \quad (27)$$

where \bar{E} is a measure of significance of perpendicular momentum range. In other words, tunneling probability decreases with increasing value of \bar{E} . If is \bar{E} small, the only electrons with perpendicular momentum near zero can tunnel through the energy barrier. Typically \bar{E} is in a range of 5–100 meV.

TAT contribution was estimated according to formula similar to the SRH process described by Eq. (21) [25]. However, the trapping rate strongly depends on the ionization energy E_T ; the electric field can essentially influence τ_{n0} and τ_{p0} values that are inversely proportional to trapping rates. This means that the electric field enhances a GR process around the mercury vacancy by decreasing the energy required both for the emission of an electron with energy level E_T to the conduction band as well as for the emission of a hole with the empty level E_T to the valence band. Taking into account this mechanism, the c_n and c_p parameters are modified. For this purpose, Eq. (21) is modified with δ_n and δ_p parameters that determine the relative changes in the size of the emission factors of electrons and holes caused by the effects associated with the electric field. The TAT effect expressed by GR process is

$$(G - R)_{TAT} = \frac{np - n_i^2}{\frac{\tau_{p0}}{\delta_p}(n_0 + n_1) + \frac{\tau_{n0}}{\delta_n}(p_0 + p_1)} \quad (28)$$

4. HgCdTe barrier detectors—principle of operation for higher operating temperatures

The introduction of unipolar barrier in various photovoltaic configurations causes a drastic change in architecture and the principle of operation of IR detectors. The idea of unipolar

barrier infrared detector (BIRD) implies that barriers can block one carrier type (electron or hole) but allow the unimpeded flow of the other. Assuming that Simple BIRD nB_n detector can be concluded as a hybrid of a photoconductor and a photodiode. The nB_n detector looks like a photodiode in a part except that the junction (space charge region) is replaced by a unipolar barrier (B_n : n-type doped barrier layer) blocking the electrons, whereas p-contact is replaced by the n-contact. The nB_n detector is nearly lacking the depletion region in an active layer, which leads to the reduction of SRH contribution to the net dark current. In low temperatures (below the crossover temperature), the nB_n detector should exhibit a higher signal-to-noise ratio in comparison with a conventional $p-n$ photodiode operating at the same temperature and should operate at a higher temperature with the same dark current.

The idea of the nB_n detector was proposed for bulk III-V materials; however, its introduction to the second type of superlattices has allowed the implementation of the concept of nB_n with a greater control of arrangement of optimal band structure. Contrary to III-V materials, uniformly n-type-doped HgCdTe does not exhibit valence band offset (VBO) ≈ 0 eV between the absorber and the barrier (e.g., MWIR HgCdTe – VBO < 200 meV depending on both the absorber/barrier composition and doping, $T = 200$ K), which is a key limiting detector performance [26]. Depending on the wavelength of operation, a relatively high bias (so-called “turn on” voltage) is required to be applied to the device to collect the photogenerated carriers. This leads to strong BTB and TAT effects due to a high electric field at the barrier-absorber heterojunction.

Proper p-type doping at the cap barrier and barrier absorber heterojunctions should lower VBO in HgCdTe. However, p-type doping is the technological challenge posed by dopant activation after molecular beam epitaxy (MBE) growth. Metalorganic chemical vapor deposition (MOCVD) technology is considered more favorable, which allows both *in situ* donor and acceptor doping. It seems to be more attractive in terms of the growth of pB_p and pB_p (B_p : p-type barrier) HgCdTe barrier structures. Barrier structures with p-type-doped constituent layers grown by MOCVD were presented by Kopytko et al. [27, 28].

5. Numerical simulations of barrier detectors

Theoretical modeling of the HgCdTe barrier detectors has been performed using our original numerical program developed at the Institute of Applied Physics, Military University of Technology (MUT) and the commercially available APSYS platform (Crosslight Inc.). Both programs are based on numerical solution of the Poisson’s and the electron/hole current continuity Eqs. (9)–(11). In addition, both programs include the energy balance Eq. (12).

In simulations, we chose HgCdTe barrier detectors with different 50% cutoff wavelengths up to 3.6 μm (MWIR) and 9 μm (LWIR) at 230 K. MWIR devices were investigated by using our original numerical program, while LWIR device was investigated by the APSYS platform. **Table 1** presents selected parameters applied in the numerical modeling of MWIR HgCdTe barrier detectors.

| | MWIR (own program) | LWIR (APSYS) |
|------------------------------------------------------------------------------|--------------------------------------|----------------------------------------|
| Trap concentration, N_T (cm^{-3}) | 1.5×10^{-7} | 10^{14} |
| Trap ionization energy, E_T | $3/4E_g$ | $1/3E_g$ |
| Trap capture coefficient, c_n, c_p ($\text{cm}^3 \text{s}^{-1}$) | | $1.5 \times 10^{-7}, 3 \times 10^{-9}$ |
| Dislocations density, G_{DIS} (cm^{-2}) | 10^6 | – |
| Dislocations ionization energy, E_{DIS} | $0.32E_g$ | – |
| Dislocations capture coefficient, c_n, c_p ($\text{cm}^3 \text{s}^{-1}$) | $3 \times 10^{-7}, 6 \times 10^{-8}$ | – |
| Overlap matrix F_1F_2 | | 0.3 |

Table 1. Parameters taken in modeling of MWIR and LWIR HgCdTe barrier detectors.

5.1. Design and fabrications of HgCdTe barrier detectors

The epitaxial structures were grown by MOCVD. Generally, the analyzed MWIR $p^+B_p nN^+$ and $p^+B_p pN^+$ (a capital letter denotes wider band; the symbol “+” denotes strong doping) structures consists of four HgCdTe layers: p^+B_p cap-barrier structural unit (highly doped with arsenic p-type cap contact layer and p-type wide bandgap barrier), intentionally undoped (due to donor background concentration with n-type conductivity) or low p-type-doped absorption layer and wide bandgap highly doped N^+ bottom contact layer. In the LWIR $n^+p^+B_p pN^+$ device, the cap contact is a combination of highly doped n- and p-type layers. Such design should create a tunneling junction to allow collection of photogenerated holes. Moreover, the cap n^+ layer provides low-resistance ohmic contact. **Figure 2** shows the considered MWIR and LWIR HgCdTe heterostructure with parameters assumed for the growth and modeling.

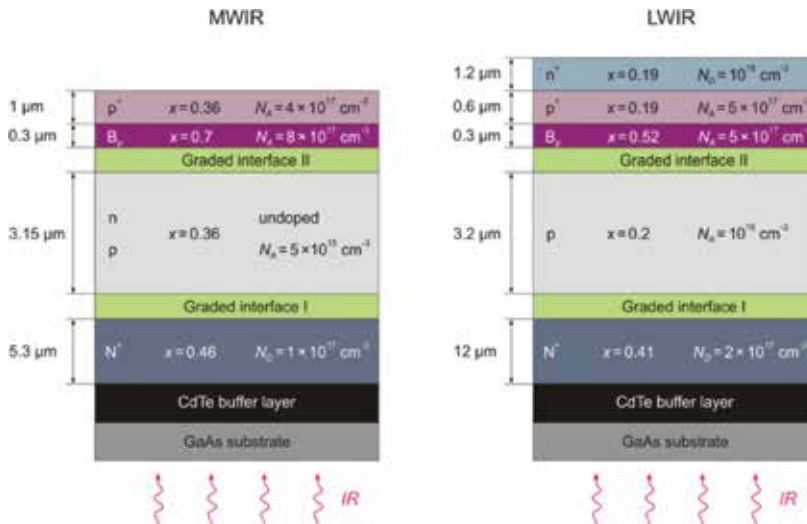


Figure 2. MWIR and LWIR HgCdTe heterostructure with parameters assumed for the growth and modeling. x is the alloy composition, N_A is the acceptor concentration, and N_B is the donor concentration.

5.2. MWIR HgCdTe barrier detectors

Our original numerical program incorporates HgCdTe electrical properties to estimate MWIR device performance taking into account Auger, SRH, as well as BTB and TAT tunneling mechanisms. Two types of SRH centers were included in the model: metal site vacancies and dislocation related centers [29, 30]. The two types of centers are characterized by different ionization energies and capture coefficients (**Table 1**).

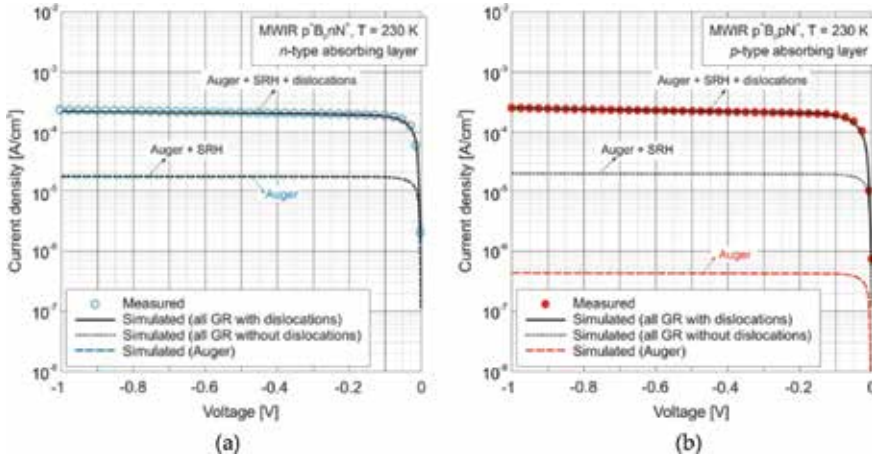


Figure 3. Measured current-voltage characteristics for MWIR HgCdTe (a) p^+B_i,nN^+ and (b) p^+B_i,pN^+ barrier detectors operated at 230 K. The experimental data are compared to the theoretical prediction considering overall GR effect and Auger processes.

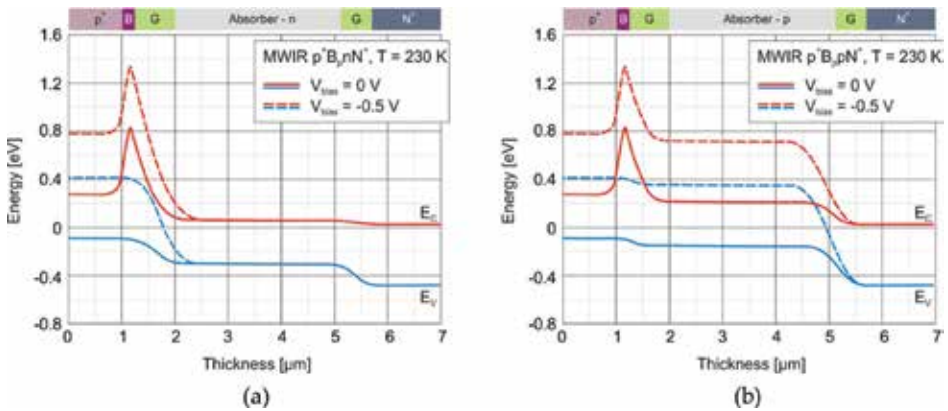


Figure 4. Simulated band diagram for MWIR HgCdTe (a) p^+B_i,nN^+ and (b) p^+B_i,pN^+ photodetectors operated at 230 K, unbiased, and under 0.5 V reverse bias.

Figure 3 presents an example of simulated fitting characteristics of MWIR HgCdTe barrier detectors at a temperature of 230 K. The calculations were made taking into account all

considered mechanisms of thermal generation, tunneling, and impact ionization. As we can see, in a wide region of bias voltages, an excellent agreement has been obtained between the experimental and calculated results. What is more, the Auger and the SRH parts of the dark current are clearly visible. The SRH GR process was calculated both for dislocation-free structures and structures containing misfit dislocations. In both types of detectors, the SRH mechanism associated with misfit dislocations has an impact on the dark currents.

Figure 4 presents the calculated bandgap diagrams of the simulated structures for unbiased and under 0.5 V reverse bias. As expected, the p-type doping of the barrier, with controlled interdiffusion process, and *x*-graded region at the barrier and absorber interfaces introduce a zero offset in the valence band. Bandgap diagrams under reverse bias clearly indicates that in the $p^+B_p nN^+$ device a decisive heterojunction is at the barrier and absorber interface while in the $p^+B_p pN^+$ photodiode at the absorber and highly doped bottom contact layer.

Dislocation-free structures should provide one order of magnitude lower dark currents. For the device with an n-type absorbing layer, saturated dark current is limited by Auger mechanisms. In the case of good-quality p-type HgCdTe, with a reduced number of a structural defect, the influence of exclusion and extraction effects might be more effective than in the n-type material due to a larger diffusion length of electrons than holes. It is apparent that Auger 1 mechanism prevails over Auger 7 mechanism and determines the minority carrier lifetime in intrinsic, n-type, and low-doped p-type materials.

5.3. LWIR HgCdTe barrier detectors

The commercially available APSYS platform (Crosslight Inc.) was implemented for LWIR device simulation procedures. The applied model incorporates HgCdTe electrical properties to estimate device performance taking into account Auger, SRH, as well as BTB and TAT tunneling mechanisms.

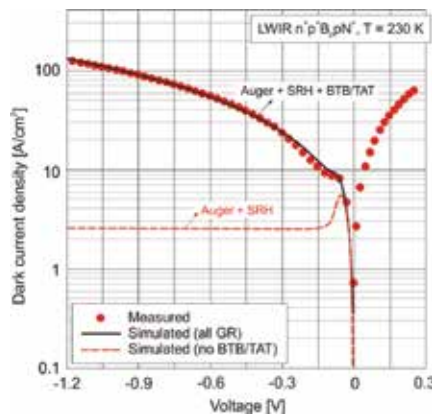


Figure 5. Measured current-voltage characteristics for the LWIR HgCdTe $n^+p^+B_p pN^+$ barrier photodiode operated at 230 K. The experimental data are compared to the theoretical prediction considering Auger, SRH, and BTB/TAT mechanisms.

The measured and calculated dark current characteristics of the LWIR HgCdTe $n^+p^+B_p pN^+$ photodiode are presented in **Figure 5**. It is shown that the most effective current transport mechanism in the LWIR HgCdTe barrier photodiode are tunneling effects at the decisive heterojunctions (especially TAT). **Figure 6** presents the calculated bandgap diagrams of the simulated structures for unbiased and under -0.5 V bias. Bandgap diagrams under reverse bias clearly indicates that the tunneling mechanism occurs at the absorber and highly doped bottom contact heterojunction.

Tunneling between trap centers and valence and conduction bands are main reasons of increasing SRH processes with the increasing reverse bias voltage. In contrast to our numerical program, the APSYS platform does not distinguish trap centers between metal site vacancies and dislocation-related centers. The best fit of experimental data with theoretical predictions has been obtained for the trap density (N_T) assumed at the level of 10^{14} cm^{-3} with ionization energy (E_T) counted from the conduction at $1/3E_g$. In TAT simulation, the Hurkx et al. model was implemented [24].

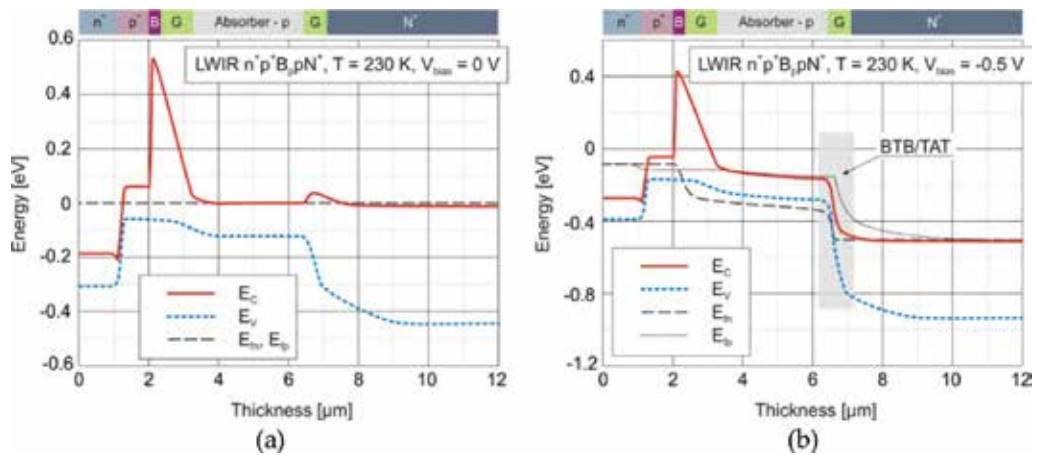


Figure 6. Simulated band diagram for the LWIR HgCdTe $n^+p^+B_p pN^+$ photodiode operated at 230 K: (a) unbiased and (b) under 0.5 V reverse bias.

Dominant SRH process override Auger suppression due to the exclusion and extraction effect. For a low reverse biases, up to the threshold voltage (-60 mV), an increase in the dark current is observed. In this voltage region, the differential resistance increases and at the final stage becomes infinite. Above the threshold voltage, the dark current decreases (the current-voltage characteristics exhibits a negative differential resistance) reaching the minimum value.

Under reverse bias, the electrons are extracted from the absorber region by positive electrode connected to a bottom N^+ -layer. The electrons are also excluded from the absorber near the barrier layer. The energy barrier between the cap layer and absorber regions blocks the electron flow from the cap layer. As a consequence, the hole concentration also decreases. The exclusion effect is limited by the level of acceptor concentration (electrical carrier neutrality), as well as by thermal generation that restores the thermal equilibrium state.

6. Summary

The current-voltage characteristics of MWIR and LWIR HgCdTe barrier detectors operating with Peltier cooling were investigated by computer simulations confronted with experimental data. Two numerical programs—our original program developed at the Institute of Applied Physics, Military University of Technology (MUT) and the commercially available APSYS platform (Crosslight Inc.)—have been used for modeling. Both programs are based on numerical solution of commonly known Poisson's and electron/hole current continuity equations. The applied model incorporates HgCdTe electrical properties to estimate device performance taking into account Auger, SRH, as well as BTB and TAT tunneling mechanisms. Due to reabsorption of photons generated by carrier recombination, also called the photon recycling, the radiative recombination is not assumed to limit the performance of HgCdTe photodetectors and was omitted in the simulations.

Typically, reverse biased infrared detectors are characterized by diffusion and tunnel-like dark current. At low reverse biases, the diffusion dark current is mainly limited by the Auger and SRH processes. At higher voltages, field-enhanced TAT via traps located at dislocation cores as well as mercury vacancies seems to be the most important mechanism of dark current generation, especially in the LWIR device. This mechanism is significant at the p-N⁺ interface, characterized by a large electric field.

The architecture of the LWIR n⁺p⁺B_ppN⁺ photodiode needs to be optimized to reduce the tunneling mechanisms at the p-N⁺ heterojunction. Numerical analysis is a proper tool to indicate the fields of improving device performances. For example, one possibility to reduce TAT is tuning of composition at interfaces aimed to locate highly dislocated region at a wider gap part of the p-N⁺ transition region where they have little effect on the dark current.

Numerical calculations have been performed for the structures of HgCdTe; however, the models may also be generalized for other semiconductor materials.

Acknowledgements

The work has been carried out under the financial support of the Polish National Science Centre as research Projects Nos. DEC-2013/08/M/ST7/00913 and DEC-2013/08/A/ST5/00773.

Appendices

Appendix A

Numerical solution of transport equations for semiconductor devices

The numerical method applied in this study employs Newton's algorithm to obtain a steady-state solution to the set of transport Eqs. (9)–(11) using an initial distribution of the electrostatic

potential in thermodynamic equilibrium that is obtained from conditions of electrical neutrality. Poisson's equation under equilibrium conditions gives the first solution function in the iterative procedure that leads to the solution of the set of transport equations under nonequilibrium conditions.

First, we have to solve the Poisson's equation in steady-state conditions. If the charge density in the semiconductor structure does not depend on the gradient of the potential, the Poisson's Eq. (11) can be represented in the following form:

$$\varepsilon\varepsilon_0\nabla^2\psi + \varepsilon_0\nabla\psi\nabla\varepsilon + q\rho = 0 \quad (\text{A1})$$

where

$$\rho = p - n + N_D^+ - N_A^- \quad (\text{A2})$$

is the difference between the density of positive and negative charge carriers (the hole concentrations p plus the concentration of ionized donors N_D^+ minus the electron concentrations n and the concentration of ionized acceptors N_A^-).

To find the numerical solution of the nonlinear Poisson Eq. (A1) by using a diffusion-equation differential scheme, we replaced it by an equivalent diffusion equation as it was postulated in reference [31]:

$$\frac{\partial\psi}{\partial t} = \varepsilon\varepsilon_0\nabla^2\psi + \varepsilon_0\nabla\psi\nabla\varepsilon + q\rho \quad (\text{A3})$$

where t is the pseudotime.

The initial values of the electrostatic potential ψ^0 at every point of the semiconductor structure can be numerically calculated assuming the electrical neutrality conditions. It is expressed by an equation of electrical neutrality:

$$p(\psi) - n(\psi) + N_D^+(\psi) - N_A^-(\psi) = 0 \quad (\text{A4})$$

The concentration of ionized acceptors and donors are expressed as

$$N_A^- = \frac{N_A}{1 + a \exp[(E_A - E_{Fi}) / k_B T]} \quad (\text{A5})$$

$$N_D^+ = \frac{N_D}{1 + b \exp[(E_{Fi} - E_D) / k_B T]} \quad (A6)$$

where E_A and E_D are the ionization energies of acceptors and donors, respectively.

Then, an iterative approach should be used to solve the set of transport Eqs. (9)–(11). Let us bring an iterative algorithm to solve Poisson’s equation which was presented in reference [31]. Eq. (A1) may be expressed in the following form:

$$L(\psi) = 0 \quad (A7)$$

The iterative form of Eq. (A7) can be expressed as follows:

$$L(\psi^{n+1}) = L(\psi^n) + \frac{\partial L(\psi^n)}{\partial \psi^n} \delta \psi^{n+1} \quad (A8)$$

where Ψ^{n+1} is a vector of $n + 1$ iterative correction of vector Ψ . Similarly, Eq. (A3) can be expressed as

$$\frac{\partial \psi}{\partial t} = L(\psi) \quad (A9)$$

and the iterative form of Eq. (A9) can be expressed as

$$\delta \psi^{n+1} = \Delta t L(\psi^n) + \frac{1}{2} \Delta t \frac{\partial L(\psi^n)}{\partial \psi^n} \delta \psi^{n+1} \quad (A10)$$

where Δt is the pseudotime step.

An iteration method allows the calculation of corrections to electrical potential, quasi-Fermi levels, and temperature [32]:

$$\psi = \psi^0 + \delta \psi, \quad \Phi_n = \Phi_n^0 + \delta \Phi_n, \quad \Phi_p = \Phi_p^0 + \delta \Phi_p, \quad T = T^0 + \delta T \quad (A11)$$

and consequently to other physical parameters:

$$n = n^0 + \frac{\partial n}{\partial \psi} \delta \psi + \frac{\partial n}{\partial \Phi_n} \delta \Phi_n + \frac{\partial n}{\partial T} \delta T \quad (A12)$$

$$p = p^0 + \frac{\partial p}{\partial \psi} \delta \psi + \frac{\partial p}{\partial \Phi_p} \delta \Phi_p + \frac{\partial p}{\partial T} \delta T \quad (\text{A13})$$

$$G - R = G^0 - R^0 + \delta(G - R) \quad (\text{A14})$$

where

$$\begin{aligned} \delta(G - R) = & \frac{\partial(G - R)}{\partial n} \left(\frac{\partial n}{\partial \psi} \delta \psi + \frac{\partial n}{\partial \Phi_n} \delta \Phi_n + \frac{\partial n}{\partial T} \delta T \right) \\ & + \frac{\partial(G - R)}{\partial p} \left(\frac{\partial p}{\partial \psi} \delta \psi + \frac{\partial p}{\partial \Phi_p} \delta \Phi_p + \frac{\partial p}{\partial T} \delta T \right) \end{aligned} \quad (\text{A15})$$

Finally, knowing the electric potential Ψ , the electron affinity X , and the bandgap energy E_g , we can determine the energy values for the edge of the conduction and valence bands:

$$E_c = -X - q\psi \quad (\text{A16})$$

$$E_v = -X - q\psi - E_g \quad (\text{A17})$$

Author details

Małgorzata Kopytko* and Piotr Martyniuk

*Address all correspondence to: malgorzata.kopytko@wat.edu.pl

Institute of Applied Physics, Military University of Technology, Warsaw, Poland

References

- [1] T. Ashley and C. T. Elliott, "Nonequilibrium devices for infra-red detection," *Electron. Lett.* 21, 451–452 (1985).
- [2] S. Maimon and G. Wicks, "nBn detector, an infrared detector with reduced dark current and higher operating temperature," *Appl. Phys. Lett.* 89, 151109 (2006).
- [3] G. L. Hansen, J. L. Schmidt and T. N. Casselman, "Energy gap versus alloy composition and temperature in $\text{Hg}_{1-x}\text{Cd}_x\text{Te}$," *J. Appl. Phys.* 53, 7099 (1982).

- [4] J. Wenus, J. Rutkowski and A. Rogalski, "Two-dimensional analysis of double-layer heterojunction HgCdTe photodiodes," *IEEE Trans. Electron Dev.* 48, 1326–1332 (2001).
- [5] G. L. Hansen and J. L. Schmit, "Calculation of intrinsic carrier concentration in $\text{Hg}_{1-x}\text{Cd}_x\text{Te}$," *J. Appl. Phys.* 54, 1639–1640 (1983).
- [6] J. P. Rosbeck, R. E. Star, S. L. Price and K. J. Riley, "Background and temperature dependent current–voltage characteristics of $\text{Hg}_{1-x}\text{Cd}_x\text{Te}$ photodiodes," *J. Appl. Phys.* 53, 6430–6440 (1982).
- [7] W. Scott, "Electron mobility in $\text{Hg}_{1-x}\text{Cd}_x\text{Te}$," *J. Appl. Phys.* 43, 1055–1062 (1972).
- [8] E. Finkman and S. E. Schacham, "The exponential optical absorption band tail of $\text{Hg}_{1-x}\text{Cd}_x\text{Te}$," *J. Appl. Phys.* 56, 2896–2900 (1984).
- [9] J. Chu, B. Li, K. Liu and D. Tang, "Empirical rule of intrinsic absorption spectroscopy in $\text{Hg}_{1-x}\text{Cd}_x\text{Te}$," *J. Appl. Phys.* 75, 1234–1235 (1994).
- [10] R. Dornhaus, G. Nimtz and B. Schlicht, "Narrow-gap semiconductors," Springer, Berlin (1983).
- [11] W. van Roosbroeck, "Theory of the electrons and holes in germanium and other semiconductors," *Bell Syst. Tech. J.* 29, 560–607 (1950).
- [12] M. Kurata, "Numerical analysis of semiconductor devices," Lexington Books, DC Heath (1982).
- [13] R. G. Humphreys, "Radiative lifetime in semiconductors for infrared detectors," *Infrared Phys. Technol.* 26, 337–342 (1986).
- [14] K. Józwiowski, M. Kopytko and A. Rogalski, "Numerical estimation of carrier generation-recombination processes and photon recycling effect in 3- μm n-on-p HgCdTe photodiodes," *Opt. Eng.* 50, 061000-1–061000-8 (2011).
- [15] W. van Roosbroeck and W. Shockley, "Photon-radiative recombination of electrons and holes in germanium," *Phys. Rev.* 94, 1558–1560 (1954).
- [16] A. R. Beattie and P. T. Landsberg, "Auger effect in semiconductors," *Proc. R. Soc. Lond. A* 249, 16–28 (1959).
- [17] M. A. Kinch, F. Agariden, D. Chandra, P.-K. Liao, H. F. Schaake and H. D. Shih, "Minority carrier lifetime in p-HgCdTe," *J. Electron. Mater.* 34, 880 (2005).
- [18] S. Krishnamurthy and T. N. Casselman, "A detailed calculation of the Auger lifetime in *p*-type HgCdTe," *J. Electron. Mater.* 29, 828–831 (2000).
- [19] W. Shockley and W. T. Read, "Statistics of recombinations of holes and electrons," *Phys. Rev.* 87, 835–842 (1952).
- [20] R. N. Hall, "Electron-hole recombination in germanium," *Phys. Rev.* 87, 387 (1952).

- [21] R. Kiran, "Optimization of the $\text{Hg}_{1-x}\text{Cd}_x\text{Te}$ surface and its characterization by electrical and optical techniques," Ph.D. dissertation, University of Illinois at Chicago, Chicago, IL (2008).
- [22] E. O. Kane, "Zener tunneling in semiconductors," *Phys. Chem. Solids* 2, 181–188 (1960).
- [23] C. B. Duke, "Tunneling in Solids," volume 10 of *Solid state physics: advances in research and applications*, Academic Press, New York (1969).
- [24] J. L. Moll, "Physics of semiconductors," chapter 12, McGraw-Hill, New York (1964).
- [25] G. A. Hurkx, D.B.M. Klaassen and M. P. G. Knuyvers, "A new recombination model for device simulation including tunneling," *IEEE Trans. Electron Dev.* 39(2), 331 (1992).
- [26] A. M. Itsuno, J. D. Phillips and S. Velicu, "Mid-wave infrared HgCdTe nBn photodetector," *Appl. Phys. Lett.* 100, 161102 (2012).
- [27] M. Kopytko, "Design and modeling of high-operating temperature MWIR HgCdTe nBn detector with *n*- and *p*-type barriers," *Infrared Phys. Technol.* 64, 47–55 (2014).
- [28] M. Kopytko, K. Jóźwikowski and A. Rogalski, "Fundamental limits of MWIR HgCdTe barrier detectors operating under non-equilibrium mode," *Solid-State Electron.* 100, 20–26 (2014).
- [29] K. Jóźwikowski, M. Kopytko, J. Piotrowski, A. Jóźwikowska, Z. Orman and A. Rogalski, "Near-room temperature MWIR HgCdTe photodiodes limited by vacancies and dislocations related to Shockley–Read–Hall centres," *Solid-State Electron.* 66(1), 8–13 (2011).
- [30] K. Jóźwikowski, A. Jóźwikowska, A. Rogalski and L. R. Jaroszewicz, "Simplified model of dislocations as a SRH recombination channel in the HgCdTe heterostructures," *Infrared Phys. Technol.* 55(1), 98–107 (2012).
- [31] A. Jóźwikowska, "Numerical solution of the nonlinear Poisson equation for semiconductor devices by application of a diffusion-equation finite difference scheme," *J. Appl. Phys.* 104, 063715 (2008).
- [32] A. Jóźwikowska, K. Jóźwikowski, J. Rutkowski and A. Rogalski, "Generation-recombination effects in high temperature HgCdTe heterostructure photodiodes," *Opto-Electron. Rev.* 12(4), 417–428 (2004).

Numerical Simulation Methods Applied at Fiber Grating Sensors Design

Dan Savastru, Sorin Miclos, Marina Tautan and
Ion Lancranjan

Additional information is available at the end of the chapter

<http://dx.doi.org/10.5772/63890>

Abstract

The paper presents the results obtained in simulation of fiber Bragg grating (FBG) and long-period grating (LPG) sensors and their applications. The optical properties of FBG and LPG are firstly analyzed and, consequently, the basics of simulation models are provided. Coupled-mode theory and the transfer matrix methods are the two techniques used for the simulation of FBG and LPG. The numerical simulations are performed for an improved design of these types of fiber sensors, designs dedicated to specified applications. The different FBG types, i.e. the normal, chirped, apodized, according to different laws and tilted cases, are analyzed. Also, various LPG configurations are numerically simulated. The two main categories of sensing applications, for temperature and for mechanical stress/strain evaluation, are simulated for each type of fiber grating sensor. The chapter is intended to be a synthesis of already obtained results to which some results of research in development are added.

Keywords: Distributed feedback devices, Optical fibers, Fiber gratings, Fiber Bragg grating, Long-period grating fiber, Optical fiber communication, Optical fiber devices, Optical fiber filters

1. Introduction

Into an increasing number of scientific, medical, industrial and military sensing and telecommunication applications, optic fibers are used, which have a spatial periodic variation of the refractive index inscribed in the core, δn , periodic variation defined as grating, the fiber optic being denoted under the general name "fiber grating" [1–5]. There are two main types of such

optic fibers: the fiber Bragg grating (FBG) ones and the long-period grating (LPG) kind [5–7]. In literature, FBGs are considered as short-period grating (300–700 nm), while LPGs as long ones (10–1000 μm). For both FBGs and LPGs, the amplitude of the core refractive index is extremely small, in the range 0.0001–0.0005 or even smaller [5–12]. It is important to mention that only step index optic fibers for which the weakly guiding approximation relying on a very small difference between the values of the core and cladding refractive index, $n_{co}-n_{cl}$, is applicable are analyzed [5–7, 11–15]. Related to this, it has to be underlined the fact that the amplitude of the spatial periodic variation of the refractive index inscribed in the core is smaller than $n_{co}-n_{cl}$ [11–15]. The basic functions as sensors and/or wavelength filter of both FBG and LPG are accomplished by controlled, observed and measured variations of optical fiber refractive indexes of the core (n_{co}) and cladding (n_{cl}) to which the refractive index of the ambient (n_{amb}) is added, where the optical fiber is mounted. Consequently, the spectral characteristics that can be observed in fiber reflection (FBG) and transmission (LPG) gratings will be described [13–19]. For an improved design of experimental setups dedicated to the above-mentioned applications, it is obvious that, for both FBG and LPG, the principles for understanding and tools for designing fiber gratings are emphasized [11–20]. The emphasized understanding principles and designing tools are applicable for the wide variety of optical properties that are possible in fiber gratings [19–28]. There are given examples related to the large number of fiber grating subtypes of both FBG and LPG, considering uniform, apodized, chirped, discrete phase-shifted and superstructure gratings; symmetric and tilted gratings; and cladding-mode and radiation-mode coupling gratings [20–33].

Both FBGs and LPGs are manufactured in single-mode silicate optic fiber by modifying in a periodic manner its core refractive index using UV-irradiation delivered by Ar or other UV laser [20]. Most commonly, the LPG is created by altering the core in a periodic manner, but another class of manufacturing methods physically deforms the fiber to create the required optical modulation [34–40]. These include the following: irradiation from a carbon dioxide laser, radiation with femtosecond pulses and writing by electric discharge, ion implantation, periodic ablation and/or annealing, corrugation of the cladding, micro-structuring of tapered fibers and dopant diffusion into the fiber core.

2. Theory

This section presents the optical properties of FBG and LPG. Consequently, the basics of simulation models are provided. Coupled-mode theory and the transfer matrix methods are the two techniques used for the simulation of FBG and LPG [13, 14, 17, 20, 22–28]. Thus, the physical mechanism of the grating electric field interaction is given and aims to provide the reader with insight into the operation principles of FBG and LPG. The gratings are inscribed into the core of a step index optic fiber; consequently, the step index optic fiber case is analyzed.

Optical fiber mainly consists of a core, cladding and a protective layer called the primary plastic buffer coating. The optical fiber acts as a waveguide for optical frequencies and is normally cylindrical in shape. The core is a dielectric cylinder surrounded by the cladding to form a

larger dielectric cylinder [13, 14]. The optical fiber has a uniform refractive index up to the core-cladding conjunction, where it undergoes a sharp change in refractive index. The refractive index of the core and the cladding is given as n_{co} and n_{cl} , respectively, the relation $n_{co} > n_{cl}$ being valid [13, 36, 37]. This is the necessary condition for total internal reflection to occur. The structure and material of the fiber confines the electromagnetic waves to a direction parallel to the axis and also affects the transmission properties of the optic fiber [13, 20]. The light transmitted through the fiber is confined due to total internal reflection within the material. There are practically no electromagnetic fields outside the cladding because of exponential decay within this region [13]. The difference between n_{co} and n_{cl} is very small, of 10^{-4} order. This is the necessary condition for the weakly guiding approximation to be applicable. This approximation results into a mathematical apparatus, which allows description of fiber grating processes as a byproduct. **Figure 1** shows the schematics of a typical optical fiber layout. For a single-mode step index fiber commonly used for grating to be inscribed into the core, the core radius is in the range 1.5–5 μm , the cladding radius being typically of 62.5 μm .

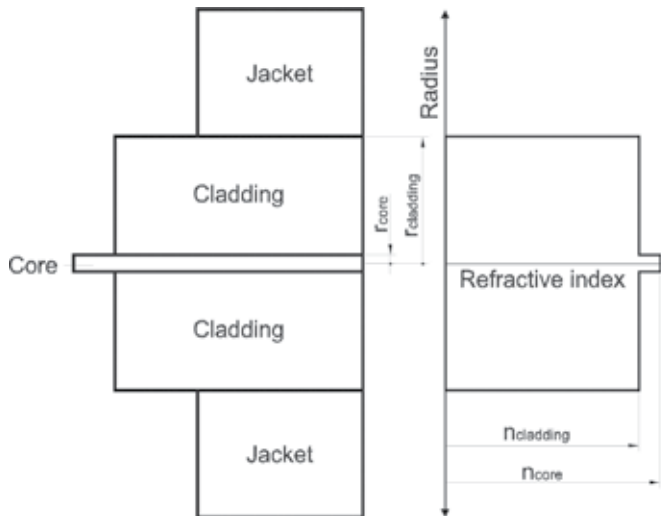


Figure 1. The schematics of a typical optical fiber layout.

It is assumed that a perturbation to the effective refractive index of the guided mode(s) can be defined as follows [13]:

$$\delta n_{eff}(z) = \delta n_{effmean}(z) \left\{ 1 + v \cdot \cos \left[\frac{2\pi}{\Lambda} z + \varphi(z) \right] \right\} \quad (1)$$

where $\delta n_{effmean}$ is the amplitude of the perturbation, evaluated as the index change spatially averaged on a grating period, v is the fringe visibility of the index change, Λ is the nominal period and $\varphi(z)$ is the grating chirp, which represents a variation of nominal period. In the case

of a step index fiber without a grating, the core power confinement factor, Γ , is defined. For uniformity across the core-induced grating, with an induced index change δn_{co} created in core, for the propagation mode, the following relation is defined [13, 21–28, 36]:

$$\delta n_{eff} \cong \Gamma \cdot \delta n_{co} \quad (2)$$

Since FBG or LPG is manufactured starting from single-mode light is propagating along the core as LP_{01} modes for which an effective index parameter b is introduced. It is useful to introduce the normalized frequency, V , a parameter synthetically characterizing the geometrical and optical materials fiber properties [13, 36, 37]. V is defined as follows:

$$V = \left(\frac{2\pi}{\lambda} \right) \cdot a_{co} \cdot \sqrt{n_{co}^2 - n_{cl}^2} \quad (3)$$

where a_{co} is the core radius. The effective index parameter is a solution to the dispersion relation [20]:

$$V\sqrt{1-b} \cdot \frac{J_{l-1}(V\sqrt{1-b})}{J_l(V\sqrt{1-b})} = -V\sqrt{b} \cdot \frac{K_{l-1}(V\sqrt{b})}{K_l(V\sqrt{b})} \quad (4)$$

where l is the Azimuthal order of the mode LP_{01} . In Eq. (4), J_l are the Bessel functions of the first kind and K_l are the modified Bessel functions of the second kind. The effective index n_{eff} is related to through the relation [13, 20–28]:

$$b = \frac{n_{eff}^2 - n_{cl}^2}{n_{co}^2 - n_{cl}^2} \quad (5)$$

Once b and V are known, Γ can be determined from

$$\Gamma = \frac{b^2}{V^2} \left[1 - \frac{J_l^2(V\sqrt{1-b})}{J_{l+1}(V\sqrt{1-b})J_{l-1}(V\sqrt{1-b})} \right] \quad (6)$$

A fiber grating, FBG or LPG, is the periodic variation of refractive index within the core of a step index single-mode optical fiber. In **Figures 2** and **3**, the schematics of the two considered types of an optical fiber with a grating written in the core of the fiber are shown. The core inscribed refractive index changes can be described as cylinders. The refractive index changes

of a fiber grating usually have a near sinusoidal variation. Firstly, the simple case of a uniform grating fiber grating is considered.

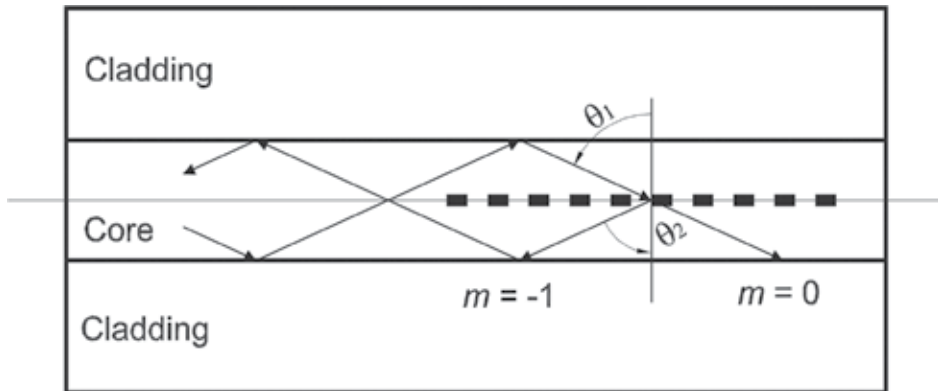


Figure 2. Propagation in a FBG.

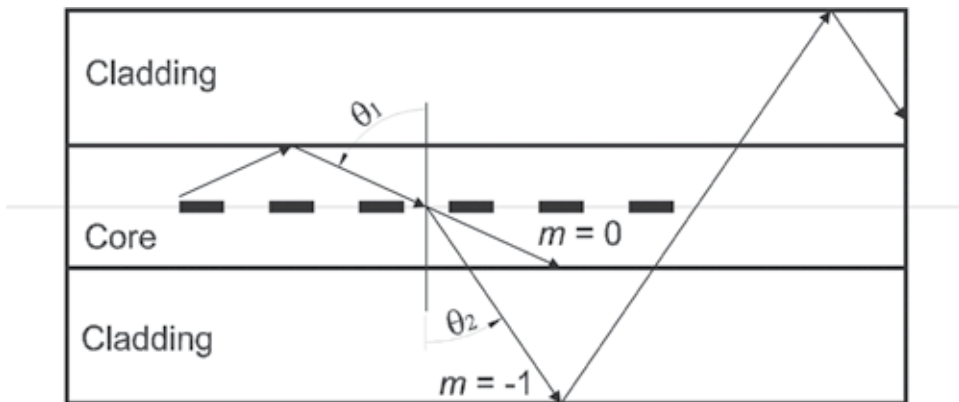


Figure 3. Propagation in a LPG.

A fiber grating produces coupling between two fiber modes [13, 14, 20, 21]. The quantitative analysis of this phenomenon is achieved using coupled-mode theory. It is helpful to consider a qualitative analysis of the basic interactions of interest. A fiber grating is simply an optical diffraction grating, at each refractive index change junction, refraction and reflection occur, and thus its effect upon a light wave incident on it can be described by the familiar grating equation. The diffraction of the light incident on the diffraction grating at an angle θ_1 can be described by the equation from Snell's law [13, 14]:

$$n \cdot \sin \theta_2 = n \cdot \sin \theta_1 + m \cdot \frac{\lambda}{\Lambda} \quad (7)$$

where m determines the diffraction order and θ_2 is the angle of the diffracted wave λ and Λ are the wavelength of the incident light and the period of the diffraction grating, respectively. Eq. (6) can predict only the directions θ_2 into which constructive interference occurs, but it is not useful for determining the wavelength at which a fiber grating most efficiently couples light between two modes.

A fiber grating's main function is based on coupling between the modes propagating through the fiber, modes which can travel in opposite directions or in the same direction—this being the basic criterion for classification of fiber gratings into two main types: (a) modes traveling in the opposite directions, denoted as the short-period gratings, the fiber Bragg gratings (FBG), working as the reflection gratings; (b) modes traveling in the same direction, denoted as Long-Period Gratings (LPG), working as transmission gratings.

In **Figure 2**, the mode reflection by a Bragg grating is schematically presented. The incident mode has a bounce angle of θ_2 and becomes the same mode traveling in the opposite direction with a bounce angle of $\theta_2 = -\theta_1$. It is worth to underline that the entire process is taking place only inside the core. For the incident and diffracted rays, the propagation constants are calculated as follows [13, 14]:

$$\begin{aligned}\beta_1 &= \frac{2\pi}{\lambda} n_{\text{eff}1}, n_{\text{eff}1} = n_{\text{co}} \sin \theta_1 \Rightarrow \beta_1 = \left(\frac{2\pi}{\lambda} \right) n_{\text{co}} \sin \theta_1 \\ \beta_2 &= \frac{2\pi}{\lambda} n_{\text{eff}2}, n_{\text{eff}2} = n_{\text{co}} \sin \theta_2 \Rightarrow \beta_2 = \left(\frac{2\pi}{\lambda} \right) n_{\text{co}} \sin \theta_2\end{aligned}\quad (8)$$

Eq. (7) can be rewritten in terms of the propagation constant of the incident beam and the reflected/diffracted light as follows [13, 14, 20–28]:

$$\beta_2 = \beta_1 + m \frac{2\pi}{\Lambda} \quad (9)$$

where the subscripts 1 and 2 describe the incident and reflected/diffracted propagation constant. For first-order diffraction, which usually dominates in a fiber grating, $m = -1$. Eq. (9) is modified to [13, 14, 20]

$$\beta_2 = \beta_1 - \frac{\lambda}{\Lambda} \quad (10)$$

For the bound core modes, the following relation is fulfilled:

$$n_{\text{cl}} < n_{\text{eff}} < n_{\text{co}} \quad (11)$$

In order to be rigorous, for the cladding modes, a relation similar to Eq. (11) is obtained by considering the value of optic fiber ambient medium, usually air, refractive index:

$$1 < n_{eff} < n_{cl} \tag{12}$$

Fiber modes that propagate in the negative (-z) direction are described by negative β values. Using Eq. (9) and observing that $\beta_2 < 0$, the resonant wavelength is obtained for reflection of a mode of index n_{eff1} into reflection of a mode of index n_{eff2} as defined by the relation:

$$\lambda = (n_{eff1} + n_{eff2}) \cdot \Lambda \tag{13}$$

Normally, the two counter propagating fiber modes have propagation constants with the same absolute value and the following relation is defined:

$$n_{eff} = n_{eff1} = n_{eff2} \tag{14}$$

From (14), the familiar result for Bragg reflection peak wavelength is obtained:

$$\lambda_B = 2 \cdot n_{eff} \cdot \Lambda \tag{15}$$

In **Figure 3**, the diffraction is schematically presented by a transmission of a fiber core mode with a bounce angle θ_1 on the grating into a cladding co-propagating fiber mode with an angle θ_2 [13, 14, 20–28]. Since, in the case illustrated in **Figure 1**, both incident core and transmitted cladding fiber modes propagate in positive +z direction, it follows that $\beta \neq 0$. As a consequence, Eq. (9) predicts the resonant wavelength of an absorption peak for a transmission grating as follows:

$$\lambda = (n_{eff1} - n_{eff2}) \cdot \Lambda \tag{16}$$

The Bragg condition required for a (fundamental) mode to couple to another mode (backward propagating or forward propagating) results from two requirements [20, 21]:

1. Energy conservation. It means that the frequency of the incident and reflected radiation is constant—no wavelength shift is observed because of reflection.
2. Momentum conservation. It means that the wave vector of the scattered radiation \vec{k}_f is equal to the sum of the incident wave vector \vec{k}_i and the grating wave vector \vec{K}

$$\vec{K} + \vec{k}_i = \vec{k}_f \quad (17)$$

$$K = |\vec{K}| = \frac{2\pi}{\Lambda} \quad (18)$$

Coupled-mode theory is used for quantitative information about the diffraction efficiency and spectral characteristics of fiber gratings by assuming the approximation of a weakly guiding fiber [13, 14, 36, 37]. Implicitly, it is assumed that the propagating fiber modes have slowly varying along the z direction amplitudes. Also it is assumed that a fiber mode has a transverse component of the electric field defined as a superposition of the modes labeled “ j ” traveling in the $+z$ and $-z$ directions such that [13, 20, 36]

$$\vec{E}_i(x, y, z, t) = \sum_j \left[A_j(z) \exp(i\beta_j z) + B_j(z) \exp(-i\beta_j z) \right] \cdot \vec{e}_{ji}(x, y) \exp(-i\omega t) \quad (19)$$

where $A_j(z)$ and $B_j(z)$ are slowly varying amplitudes of the j^{th} mode, respectively. Eq. (19) describes the transverse mode electric fields of the bound core or radiation LP_{il} modes, as given in [8], or of the cladding modes. Into an ideal uniform optical fiber, the modes are orthogonal and hence do not exchange energy; the presence of a dielectric perturbation such as a grating causes the modes to be coupled such that the amplitudes $A_j(z)$ and $B_j(z)$ of the j^{th} mode evolution along the z axis are defined according to

$$\frac{dA_j}{dz} = i \sum_k A_k (K_{kj}^t + K_{kj}^z) \exp[i(\beta_k - \beta_j)z] + i \sum_k B_k (K_{kj}^t - K_{kj}^z) \exp[-i(\beta_k + \beta_j)z] \quad (20)$$

$$\frac{dB_j}{dz} = -i \sum_k A_k (K_{kj}^t - K_{kj}^z) \exp[i(\beta_k + \beta_j)z] - i \sum_k B_k (K_{kj}^t + K_{kj}^z) \exp[-i(\beta_k - \beta_j)z] \quad (21)$$

In (20) and (21), two coupling coefficients are introduced: transverse and longitudinal. The transverse coupling coefficient between modes k and j is given by

$$K_{kj}^t(z) = \frac{\omega}{4} \iint_{\infty} dx dy \Delta \varepsilon(x, y, z) \cdot \vec{e}_{kt}(x, y) \cdot \vec{e}_{jt}^*(x, y) \quad (22)$$

where $\Delta \varepsilon$ is the perturbation to the electric permittivity, which has a very small value in the weakly guiding approximation. When $\delta n \ll n$, the $\Delta \varepsilon$ perturbation can be approximated as $\Delta \varepsilon \cong 2n\delta n$. The longitudinal coupling coefficient $K_{kj}^z(z)$ is analogous to $K_{kj}^t(z)$, but for slow

longitudinally varying fiber modes approximation, the condition $K_{kj}^z(z) < K_{kj}^t(z)$ is fulfilled and thus this coefficient is usually neglected.

In most fiber gratings, the induced index change $\delta n(x, y, z)$ is approximately considered as uniform across the core and nonexistent outside the core. Thus, it becomes possible to define index by an expression similar to Eq. (1), but with $\delta n_{effmean}(z)$ replaced by $\delta n_{co}(z)$. As a consequence, it becomes convenient to define two new coefficients [13, 14, 20]

$$\sigma_{kj}(z) = \frac{\omega n_{co}}{2} \cdot \delta n_{co}(z) \iint_{core} dx dy \cdot \bar{e}_{kt}(x, y) \cdot \bar{e}_{jt}^*(x, y) \quad (23)$$

$$\kappa_{kj}(z) = \frac{v}{2} \sigma_{kj}(z) \quad (24)$$

where σ is a “DC” (period-averaged) coupling coefficient and κ is an “AC” coupling coefficient, then the general coupling coefficient can be written as follows:

$$K_{kj}^t(z) = \sigma_{kj}(z) + 2\kappa_{kj}(z) \cdot \cos\left[\frac{2\pi}{\Lambda}z + \varphi(z)\right] \quad (25)$$

Eqs. (20)–(23) are the coupled-mode equations forming a set used to describe fiber grating spectra below.

2.1. FBG reflection spectra

In the FBG case, the dominant interaction in the fiber grating is the reflection of a mode $A(z)$ into an identical counter-propagating mode; at the Bragg resonance wavelength, Eqs. (20) and (21) are simplified by retaining only terms that involve the particular modes [13], neglecting terms on the right-hand sides of Eqs. (20) and (21) that contain rapidly oscillating z dependence, since these have low contributions to the variations of the mode amplitude. The resulting equations can be written as follows:

$$\frac{dR(z)}{dz} = i\hat{\sigma}R(z) + i\kappa S(z) \quad (26)$$

$$\frac{dS(z)}{dz} = -i\hat{\sigma}S(z) - i\kappa^*R(z) \quad (27)$$

In (26) and (27), as a starting hypothesis, it is assumed that $R(z)$ and $S(z)$ are defined as follows:

$$R(z) \equiv A(z) \cdot \exp\left(i\delta z - \frac{\varphi}{2}\right) \quad (28)$$

$$S(z) \equiv B(z) \cdot \exp\left(-i\delta z + \frac{\varphi}{2}\right) \quad (29)$$

In these equations, the “AC” coupling coefficient from (23) and the general “DC” self-coupling coefficient appear. The “AC” coupling coefficient is defined as follows:

$$\hat{\sigma} \equiv \delta + \sigma - \frac{1}{2} \frac{d\varphi}{dz} \quad (30)$$

The detuning δ , considered independent of z for all gratings, is defined as follows:

$$\delta \equiv \beta - \frac{\pi}{\Lambda} = \beta - \beta_D = 2\pi n_{\text{eff}} \left(\frac{1}{\lambda} - \frac{1}{\lambda_D} \right) \quad (31)$$

where λ_D is the “design wavelength” for Bragg scattering by an infinitesimally weak grating with a period $\delta n_{\text{eff}} \rightarrow$. The “design wavelength” λ_D is defined as follows:

$$\lambda_D = 2n_{\text{eff}}\Lambda \quad (32)$$

When $\delta = 0$, λ_D fulfill the Bragg condition, i.e. the following relation is accomplished

$$\lambda_D = \lambda_B \quad (33)$$

The “DC” coupling coefficient σ is defined in Eq. (23). Absorption loss in the grating is described by a complex coefficient $\hat{\sigma}$. The power loss coefficient α is the proportional to imaginary part of the complex coefficient $\hat{\sigma}$, being defined as follows:

$$\alpha = 2\text{Im}(\sigma) \quad (34)$$

Light not reflected by the grating experiences a transmission loss TL expressed in dB/cm as follows:

$$TL = 10 \cdot \log_{10}(e)\alpha \tag{35}$$

The derivative describes possible chirp of the grating period, where $\varphi(z)$ is defined using different variation laws. For a single-mode Bragg reflection grating, the following simple relations are useful:

$$\sigma = \frac{2\pi}{\lambda} \delta n_{\text{effmean}} \tag{36}$$

$$\kappa = \kappa^* \tag{37}$$

$$\hat{\sigma} = \frac{\pi}{\lambda} v \delta n_{\text{effmean}} \tag{38}$$

If the grating is uniform along z , then $\delta n_{\text{effmean}}$ is a constant, meaning no chirping of the grating, consequently $\frac{d\varphi}{dz}=0$, and thus κ , σ and $\hat{\sigma}$ are constants. Thus, Eqs. (26) and (27) form a system of coupled first-order ordinary differential equations with constant coefficients and appropriate boundary conditions for which closed-form solutions can be found. As the boundary conditions, for a grating of length L , it is assumed that a forward-going wave incident from $z \rightarrow -\infty$, the grating reflectivity, is unitary, $R(z=-L/2)=1$, and that no backward-going wave exists for z larger or equal to $L/2$, $S(z=L/2)=0$. The amplitude and power reflection coefficients q and r , respectively, can then be shown to be defined as

$$\rho = \frac{-\kappa \sinh\left(L\sqrt{\kappa^2 - \hat{\sigma}^2}\right)}{\hat{\sigma} \sinh\left(L\sqrt{\kappa^2 - \hat{\sigma}^2}\right) + i\sqrt{\kappa^2 - \hat{\sigma}^2} \cosh\left(L\sqrt{\kappa^2 - \hat{\sigma}^2}\right)} \tag{39}$$

$$r = \frac{\sinh^2\left(L\sqrt{\kappa^2 - \hat{\sigma}^2}\right)}{\cosh^2\left(L\sqrt{\kappa^2 - \hat{\sigma}^2}\right) - \frac{\hat{\sigma}^2}{\kappa^2}} \tag{40}$$

From (40), it is found that the maximum reflectivity for a Bragg grating, r_{max} is defined as

$$r_{\max} = \tanh^2(\kappa L) \quad (41)$$

This value occurs when $\hat{\sigma}=0$, or at the wavelength λ_{\max} which is defined as

$$\lambda_{\max} = \left(1 + \frac{\delta n_{\text{effmean}}}{n_{\text{eff}}} \right) \lambda_D \quad (42)$$

2.2. LPG transmission spectra

In the LPG case, the coupled-mode equations are rearranged in the sense that near the peak resonance wavelength at which mode “1” of amplitude $A_1(z)$ is strongly coupled to a co-propagating mode “2” with amplitude $A_2(z)$, Eqs. (20) and (21) may be simplified by keeping only terms that involve the amplitudes of these two modes and then making use of the synchronous approximation of modes. The resulting equations can be written as follows:

$$\frac{dR(z)}{dz} = i\hat{\sigma}R(z) + i\kappa S(z) \quad (43)$$

$$\frac{dS(z)}{dz} = -i\hat{\sigma}S(z) + i\kappa^*R(z) \quad (44)$$

where the new amplitudes $R(z)$ and $S(z)$ are defined as

$$R(z) \equiv A_1 \exp\left[-i\frac{(\sigma_{11} + \sigma_{22})z}{2}\right] \exp\left(i\delta z - \frac{\varphi}{2}\right) \quad (45)$$

$$S(z) \equiv A_2 \exp\left[-i\frac{(\sigma_{11} + \sigma_{22})z}{2}\right] \exp\left(-i\delta z + \frac{\varphi}{2}\right) \quad (46)$$

and where σ_{11} and σ_{22} are “DC” coupling coefficients [13, 14]. From Eqs. (36), (37) and (38), the “AC” cross-coupling coefficient, κ , and, $\hat{\sigma}$, a general “DC” self-coupling coefficient are defined as

$$\kappa = \kappa_{21} = \kappa_{12}^* \quad (47)$$

and

$$\hat{\sigma} = \delta + \frac{\sigma_{11} - \sigma_{22}}{2} - \frac{1}{2} \frac{d\varphi}{dz} \quad (48)$$

Here the detuning, δ , which is assumed to be constant along z , is defined as

$$\delta \equiv \frac{1}{2}(\beta_1 - \beta_2) - \frac{\pi}{\Lambda} \quad (49)$$

or

$$\delta \equiv \pi \Delta n_{eff} \left(\frac{1}{\lambda} - \frac{1}{\lambda_D} \right) \quad (50)$$

In Eqs.(49) and (50), λ_D is the design wavelength for an infinitesimally weak grating; as for Bragg gratings, λ_D is defined as follows:

$$\lambda_D \equiv \Delta n_{eff} \Lambda \quad (51)$$

As for the Bragg grating case, $\delta = 0$ corresponds to the grating resonance condition predicted by the qualitative picture of grating diffraction, schematically presented in **Figures 2** and **3**.

In the usual case of a uniform grating, $\hat{\sigma}$ and κ are constants. In the LPG case, unlike for a Bragg grating reflection of a single mode, here the coupling coefficient generally cannot be simply defined as in (38). For coupling between two different modes in the LPG case of transmission gratings, the overlap integrals (23) and (24) must be evaluated numerically. Like the analogous Bragg grating, Eqs. (43) and (44) are coupled first-order ordinary differential equations with constant coefficients. Thus, closed-form solutions can be found when appropriate initial conditions are specified for a grating of length L . The transmission can be found by assuming only one mode is incident from $z \rightarrow -\infty$, and assuming that $R(0) = 1$ and $S(0) = 0$. The power bar and cross-transmission, $t_{\bar{}}$ and t_{\times} , respectively, can be defined as follows:

$$t_{\bar{}} = \frac{|R(z)|^2}{|R(0)|^2} = \cos\left(z\sqrt{\kappa^2 + \hat{\sigma}^2}\right) + \frac{\hat{\sigma}^2}{\hat{\sigma}^2 + \kappa^2} \sin\left(z\sqrt{\kappa^2 + \hat{\sigma}^2}\right) \quad (52)$$

$$t_x = \frac{|S(z)|^2}{|R(0)|^2} = \frac{\kappa^2}{\hat{\sigma}^2 + \kappa^2} \sin\left(z\sqrt{\kappa^2 + \hat{\sigma}^2}\right) \quad (53)$$

The maximum cross-transmission (which occurs when $\hat{\sigma}=0$) is defined as

$$t_{x,\max} = \sin^2(\kappa L) \quad (54)$$

and it occurs at the wavelength

$$\lambda_{\max} = \frac{1}{1 - (\sigma_{11} - \sigma_{22}) \frac{\Lambda}{2\pi}} \lambda_D \quad (55)$$

For coupling between a core mode "1" and a cladding mode "2" with an induced index change in the core only, $\sigma_{11} = \sigma$ from Eqs. (36), $\sigma_{22} \ll \sigma_{11}$ and for low cladding confinement factor, λ_{\max} can be approximated as

$$\lambda_{\max} \cong \left(1 + \frac{\delta n_{\text{effmean}}}{\Delta n_{\text{eff}}}\right) \lambda_D \quad (56)$$

In Eq. (56), it is assumed that $\delta n_{\text{effmean}}$ the induced change in the core-mode effective index, is much smaller than Δn_{eff} which is the common case. Analyzing Eqs. (56) and (42), a major difference is observed between the FBG and LPG cases, difference which consists in the fact that the wavelength of maximum coupling in a long-period cladding-mode coupler grating shifts toward longer wavelengths as the grating is being written many times more rapidly, meaning a longer grating period, than the shift occurring in the Bragg grating case.

3. Simulation results

Because of their various and important sensing and communication applications, the FBGs and LPGs are intensively studied in the last 20 years. Since the first reported results concerning their characteristics, fabrication and engineering their applications, in time, it became more and more clear that FBG and LPG simulation models are urgently needed for a proper design of their applications, especially the sensing ones. The design of FBG's and LPG's sensing applications involves a large number of input parameters or parameters having large variation

domains. In time, more or less accurate FBG and LPG simulation models were reported in literature [13, 14, 17, 20-28, 36-40]. These FBG and LPG simulation models are crucial for design of their applications.

However, in spite of the complicated mathematical apparatus defined in Section 2 used for describing the FBG or LPG mode of operation, there are several ideas which a researcher, using or designing FBG and LPG application, has to keep in mind:

1. The FBG and LPG applications are based on the fiber interaction with the environment. The FBG and LPG applications are developed starting by processing single mode fibers for grating formation.
2. In the FBG case, the whole process is taking place in the core of the optic fiber, without any direct interaction of the fiber grating with the environment. This means that only modes counter-propagating in pairs through the core are involved being coupled by the grating, i.e. exchanging energy. As a consequence, into the more or less broad emission spectrum of a light source connected at one end of the fiber, there will appear a reflection band which can be measured at the same fiber end or an absorption band as observed at the other fiber end. Usually, for the sake of spectroscopic measurements accuracy, the reflection band is mostly used. The peak wavelength and bandwidth of this band are the parameters of interest to be observed in applications. The main task of FBG simulations consists in defining the peak of the reflection band. The spectral shift of this peak wavelength of reflection band is correlated with grating period which can be modified by simple or simultaneous mechanical or thermal loads applied indirectly on the fiber grating.
3. In the LPG case, the process is different in the sense that co-propagating fiber modes are coupled by the grating. The LPG operation process is taking place in the entire fiber cross section. The LPG operation is based on the coupling of a core mode with the possible cladding propagating modes. Inherently, two possible single-mode fiber simulation models are to be considered: (a) two layers (core and cladding or cladding and environment) and (b) three layers (core, cladding and environment). As a consequence, into the more or less broad emission spectrum of a light source connected at one end of the fiber, there will appear several absorption bands with the strength and bandwidth depending on how much the transverse intensity distributions of core mode and cladding modes are overlapping, the values of "DC" and "AC" coupling coefficients depending on this mode superposition. The resulting absorption bands are usually observed at the other fiber end. The main task of LPG simulation consists in defining the peaks and bandwidths of these absorption bands appearing in the test light source transmission spectrum. The spectral shifts of absorption peaks and bandwidth broadenings can be correlated with grating period changes imposed by simple or simultaneous mechanical or thermal loads applied on the fiber grating. It becomes possible to correlate any modification of environment refraction index modification induced chemically or thermally by external factors. The spectral peak shifts and bandwidth broadenings of this absorption bands are to be evaluated.

Nevertheless, there are several steps to be accomplished in development of an accurate FBG or LPG simulation model, based on which a practical simulation algorithm can be defined. The first steps are identical for FBG and LPG simulation cycles. The first two identical steps of FBG and LPG simulations consist of:

- STEP 1—the usual gathering of input data, meaning core and cladding diameters, core and cladding refractive index values, to which the environment refractive index has to be added in LPG case and is only informal for FBG model. Any data concerning the geometry of the fiber grating has to be considered in this stage. For example, if fiber grating is supposed to be bent, or elongated, or longitudinally compressed or not.
- STEP 2—evaluation of fiber core effective value of the refractive index. This task is achieved by graphically or numerically solving the dispersion Eq. (4) for b and using Eq. (5). For more strictness, the confinement factor can be calculated using (6). The results of Step 2 consist of variation curves with wavelength of core effective refractive index, normalized frequency V and, eventually, of confinement factor Γ .

In this stage, the FBG and LPG simulation cycles separate into different ways of evolution. In the FBG case:

- STEP 3 FBG—evaluation of fiber short-period grating reflectivity spectrum in the domain including the Bragg wavelength by solving the system of differential equations defined from coupled-mode theory applied for core counter-propagating modes, i.e. using Eqs. (39)–(42). The obtained reflectivity spectrum will depend on the grating length, period and if it is uniform or has a variable period according to a predefined law on z along the grating (sine, sinc, positive tanh or Blackman) but keeping a constant amplitude of δn_{eff} , this being the chirping technique, or it is apodized, meaning that the period is constant and the amplitude of δn_{eff} is defined by a variation law on z as the argument (also sine, sinc, positive tanh or Blackman functions are applicable). Once the Bragg grating reflectivity spectrum is obtained, it is possible to correlate its spectral shift with mechanical or thermal load applied on the FBG device, meaning to use it as a sensor. FBG chirping or apodization is used for smoothing the reflectivity spectrum wings.

In this moment, two ideas have to be underlined:

- The matrix transfer theory, which is based on dividing the fiber grating into a number of segments of short length (in comparison to the propagating light wavelength), the light propagating through these segments, the output signal (power) of one being the input for the next one and so on, the input of the first segment being the initial conditions for coupled-mode differential equations. Finally, in the matrix transfer theory, an iteration equation is defined, and solving it leads to the reflectivity spectrum. For FBG, coupled-mode and matrix transfer theories conduct to similar results.
- Tilted FBG consisting of a Bragg grating with pitches having an angle with z fiber axis represents an attempt to couple the core specific processes to the environment via cladding. The analysis of tilted FBG is beyond the purposes of this Chapter.

The LPG case:

- STEP 3 LPG—evaluation of refractive index values for the possible cladding propagation modes and of resonance peak wavelength of absorption bands created into the grating transmission band. This task can be accomplished by using a two layers or three layers model of the optic fiber for solving the dispersion Eq. (4) in order to define the effective values of cladding possible propagation modes. The Two Layers model means to consider the fiber itself as a core placed into an infinite cladding and to solve Eq. (4). It is a modified procedure applied at STEP 2. The two layers model is an approximation. The more accurate three layers model means to solve a modified version of dispersion equation obtained by a complicated algebra calculation taking into account the refractive index values of core, cladding and environment. This procedure is continued by evaluation of the peak wavelengths of the absorption bands created in the LPG transmission spectrum using the resonance relation Eq. (16). The differences observed between simulation results obtained using the Two or Three Layers models are of 5-10%, depending on the computational hardware and software capacity. These differences are observed for cladding modes propagating near the core.
- STEP 4 LPG—evaluation of coupling coefficients and the bandwidths of the corresponding absorption bands created in the LPG spectrum and consequently the entire transmission spectrum simulation. STEPS 3 and 4 LPG can be used for simulation of absorption bands peaks shifting and bandwidth broadening corresponding to applying mechanical or thermal loads on the LPG device or environment refractive index variation, i.e. the use of LPG as a sensor device.

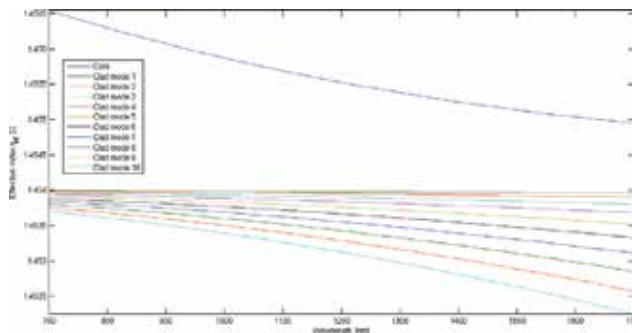


Figure 4. The variations of core and clad refractive indices versus propagating radiation wavelength.

In the following, several examples of FBG and LPG optical characteristic simulations developed in the above-described steps are presented. In the FBG case, the presented examples are obtained for uniform, chirped or apodized, the grating reflectivity being the main target. For LPG, its transmission characteristics are to be simulated. In the presented examples, simulation was performed considering the geometry and refractive index core and cladding values characteristic for Fibercore SM750 optical fiber (core radius $2.8 \mu\text{m}$, $n_{co} = 1.4575$, cladding radius $62.5 \mu\text{m}$, $n_{cl} = 1.4545$). Fibercore SM750 optical fiber is commonly used as host for FBG or LPG.

For both FBG and LPG sensors design, the first step consists in simulation of core and cladding effective refractive indices of propagation modes. **Figure 4** displays the results obtained in simulation of core and cladding refractive indices variations versus the wavelength of light propagating through the fiber. There are analyzed possible values of refractive index for which the radiation modes can propagate through the optic fiber.

Results obtained in the analyzed FBG cases are presented in **Figures 5-10**. The primary task accomplished by simulation consists in defining the variation of the FBG reflectivity with wavelength around the Bragg resonance wavelength. In simulation of chirped and/or apodized Bragg grating, for its period variation law, sine, sinc, positive tanh and Blackman profiles were considered.

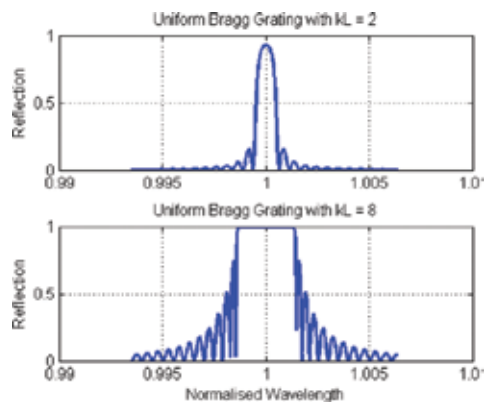


Figure 5. Variation of FBG reflectivity versus wavelength for a uniform Bragg grating displaying different grating strength kL . Length of the grating $L = 1$ mm, grating visibility $v = 1$, number of grating pitches $N = 10,000$, grating amplitude $\Delta n_{eff} = 1e-4$, design wavelength $\lambda_D = 1550$ nm.

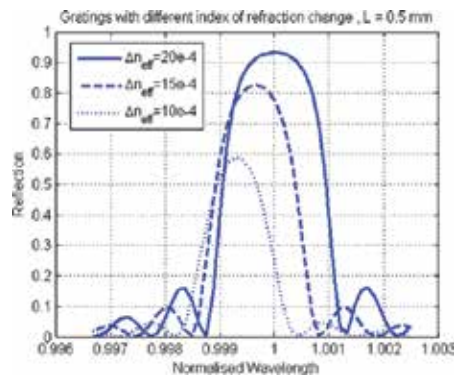


Figure 6. Effect of change in refractive indices on reflection spectra of uniform Bragg gratings. Length of the grating $L = 1$ mm, grating visibility $v = 1$, number of grating pitches $N = 10,000$, grating amplitudes $2206 = 20e-4$, $15e-4$ and $10e-4$, design wavelength $\lambda_D = 1550$ nm.

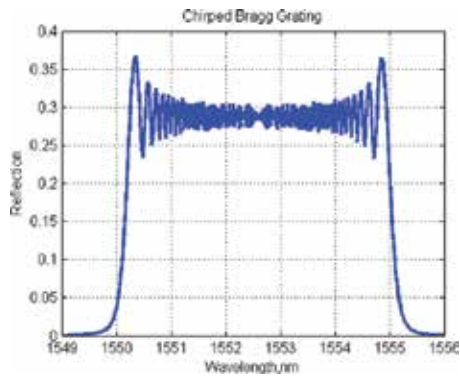


Figure 7. Reflection of a Gaussian profile chirped Bragg grating. Length of the grating $L = 50$ mm, grating visibility $v = 1$, number of grating pitches $N = 10,000$, grating amplitude $= 20e-4$, design wavelength $\lambda_D = 1550$ nm.

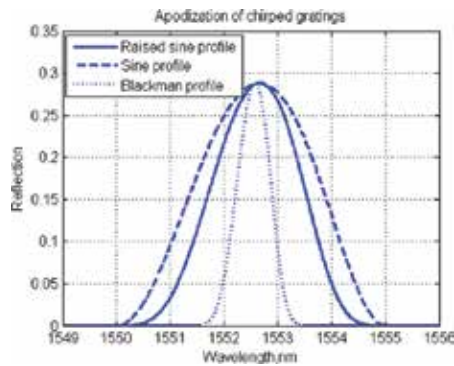


Figure 8. Apodization of a chirped grating using different profiles. Length of the grating $L = 50$ mm, grating visibility $v = 1$, number of grating pitches $N = 10,000$, grating amplitude $\Delta n_{eff} = 20e-4$, design wavelength $\lambda_D = 1550$ nm.

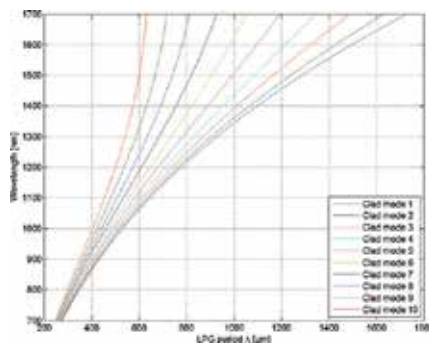


Figure 9. Variations of the resonance wavelength versus LPG period, calculated for the first 10 possible clad propagation modes. LPG length $L = 75$ mm, grating amplitude $\Delta n_{eff} = 25e-4$.

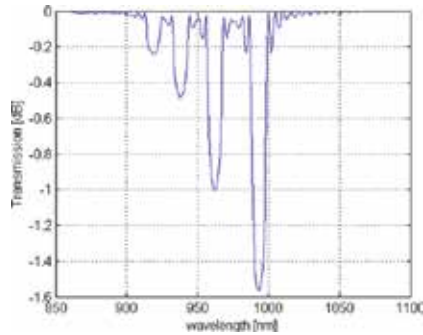


Figure 10. LPG transmission spectra simulated for an optic fiber in normal state. LPG period = 400 μm , LPG length $L = 75$ mm, grating amplitude $\Delta n_{\text{eff}} = 25\text{e-}4$.

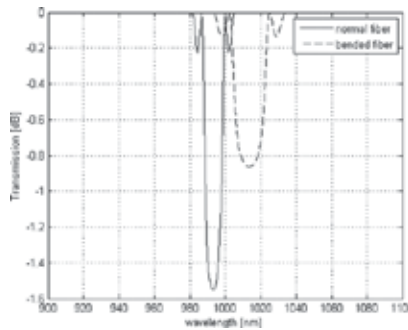


Figure 11. LPG transmission spectra simulated for a bent optic fiber in normal state. LPG period = 400 μm , LPG length $L = 75$ mm, grating amplitude $\Delta n_{\text{eff}} = 25\text{e-}4$.

Results obtained in the analyzed LPG cases are presented in **Figures 9–11**. In **Figure 9** are presented simulation results obtained regarding the variations of the resonance wavelengths of the absorption peaks in the LPG transmission spectra, peaks defined using (16)-the “second key task to be accomplished” in the design of LPG fiber sensors. In **Figures 10** and **11** are presented the LPG transmission spectra simulated for an unperturbed fiber and for a bent fiber.

4. Conclusions

The chapter refers to a broad research domain concerning the optic fiber and fiber grating physics. One of the two main purposes of the chapter consists in presenting the theoretical tools and simulation procedures used for analysis of optical properties of short-period FBG and fiber LPG. The second purpose of the chapter consists in providing the basics of simulation models. Examples of simulation results obtained using coupled-mode theory, verified using

the transfer matrix theory in the FBG case, are presented. The presented simulation results are in fairly good agreement with experimental and simulation results presented in literature.

Acknowledgments

This work was funded by Core Program, under the support of ANCS, project PN 16.40.01.02

Author details

Dan Savastru*, Sorin Miclos, Marina Tautan and Ion Lancranjan

*Address all correspondence to: j_j_f_l@yahoo.com

National Institute of Research and Development for Optoelectronics, Magurele, Ilfov, Romania

References

- [1] A. Othonos, K. Kalli. *Fiber Bragg gratings, fundamentals and applications in telecommunications and sensing*. Boston: Artech House; 1999. 433 p. ISBN 0-89006-344-3
- [2] A. Hongo, S. Kojima, S. Komatsuzaki. Application of fiber Bragg grating sensors and high speed interrogation techniques. *Structural Control & Health Monitoring*. 2005;12(3-4):269-282. doi:10.1002/stc.70
- [3] L. Dong et al. Single-pulse Bragg gratings written during fiber drawing. *Electronics Letters*. 1993;29(17):1577-1578. doi:10.1049/el:19931051
- [4] B.H. Lee, J. Nishii. Self-interference of long-period fibre grating and its application as temperature sensor. *Electronics Letters*. 1998;34(21):2059-2060. doi:10.1049/el:19981420
- [5] S.W. James, R.P. Tatam. Optical fibre log-period grating sensors: characteristics and applications. *Measurement Science and Technology*. 2003;14(5):R49-R61. doi:10.1088/0957-0233/14/5/201
- [6] J-L. Archambault, L. Reekie, P. J. Russel. 100-percent reflectivity Bragg grating reflectors produced in optical fibers by single excimer laser pulses. *Electronic Letters*. 1993;29(5):453-455. doi:10.1049/el:19930303
- [7] Y-J Rao. In-fiber Bragg grating sensors. *Measurement Science and Technology*. 1997;8(4):355-375. PII: S0957-0233(97)72999-0
- [8] S. A. Slattery, D. N. Nikogosyan. High intensity UV laser inscription of fiber Bragg gratings and comparison with other fabrication techniques. In: B. W. Bowe, et al.,

- editors. Opto-Ireland 2005: Photonic Engineering; 5–6 Apr 2005; Dublin, Ireland. Bellingham, WA, USA: SPIE-Int Soc Optical Eng; 2005. p. 200–210. doi: 10.1117/12.601158
- [9] C. G. Askins et al. Stepped wavelength optical-fiber Bragg grating array fabricated in line on a draw tower. *Optics Letters*. 1994;19(2):147–149. doi:10.1364/OL.19.000147
- [10] K. Schroeder, W. Ecke, R. Mueller, R. Willsch, A. Andreev. A fibre Bragg grating refractometer. *Measurement Science and Technology*. 2001;12(7):757–764. doi: 10.1088/0957-0233/12/7/301
- [11] G. Laffont, P. Ferdinand. Fiber Bragg grating-induced coupling to cladding modes for refractive index measurements. In: A.G. Mignani, H.C. Lefevre, editors. 14th International Conference on Optical Fiber Sensors; 11–13 Oct 2000; Venice, Italy. Bellingham, WA, USA: SPIE-Int Soc Optical Eng; 2000. p. 326–329. WOS:000167396300080
- [12] G. Laffont, P. Ferdinand. Tilted short-period fibre-Bragg-grating-induced coupling to cladding modes for accurate refractometry. *Measurement Science and Technology*. 2001;12(7):765–770. doi:10.1088/0957-0233/12/7/302
- [13] T. Erdogan. Fiber grating spectra. *Journal of Lightwave Technology*. 1997;15(8):1277–1294. doi:10.1109/50.618322
- [14] R. Kashyap. *Fiber Bragg gratings*, 1st ed. London: Academic Press; 1999. 458 p. ISBN: 0124005608
- [15] B.H. Lee, Y. Chung, W-T. Han, U-C. Paek. Temperature sensor based on self-interference of a single long-period fiber grating. *IEICE Transactions on Electronics*. 2000;E83C(3):287–292. WOS:000086147100004
- [16] G. Keiser. *Optical fiber communications*, 3rd ed. Singapore: McGraw Hill; 1999. 688 p. ISBN: 0-07-232101-6
- [17] A.W. Snyder, J.D. Love. *Optical waveguide theory*, 1st ed. New York, USA: Chapman & Hall; 1983. 738 p. ISBN: 0412099500
- [18] K. O. Hill, Y. Fujii, D. C. Johnson, B. S. Kawasaki. Photosensitivity in optical fiber waveguides: application to reflection filter fabrication. *Applied Physics Letters*. 1978;32(10):647–649. doi:10.1063/1.89881
- [19] G. Meltz, W. W. Morey, W.H. Glenn. Formation of Bragg gratings in optical fibers by a transverse holographic method. *Optics Letters*. 1989;14(15):823–5. doi:10.1364/OL.14.000823
- [20] D. Marcuse. *Theory of dielectric optical waveguides*. 1st ed. New York: Academic Press; 1974. 257 p. doi: ISBN: 0124709508
- [21] H. Tai. Simple numerical simulation of strain measurement. In: R.M. Wasserman, S.L. DeVore, editors. *Conference on Electro-Optical System Design, Simulation, Testing*,

- and Training; 09–10 July, 2002; Seattle, USA. Bellingham, WA, USA: SPIE-Int Soc Optical Engineering; 2002. p. 13–24. doi:10.1117/12.451768
- [22] R. Savastru, I. Lancranjan, D. Savastru, S. Miclos. Numerical simulation of distributed feed-back fiber laser sensors. In: V.I. Vlad, editor. 10th Conference on Optics—Micro-to Nanophotonics III (ROMOPTO); 03–06 Sep 2012; Bucharest, Romania. Bellingham, WA, USA: SPIE-Int Soc Optical Engineering; 2013. p. UNSP 88820Y. doi: 10.1117/12.2032724
- [23] I. Lancranjan, S. Miclos, D. Savastru, R. Savastru, C. Opran. Numerical simulation of a laser - acoustic landmine detection system. In: T. Graf, JI. Mackenzie, H. Jelinkova, J. Powell, editors. Conference on Laser Sources and Applications; 16–19 Apr 2012; Brussels, Belgium. Bellingham, WA, USA: SPIE-Int Soc Optical Engineering; 2012. p. 843315. doi:10.1117/12.922158
- [24] I. Lancranjan, S. Miclos, D. Savastru, A. Popescu. Numerical simulation of a DFB-fiber laser sensor (II)—theoretical analysis of an acoustic sensor. *Journal of Optoelectronics and Advanced Materials*. 2010;12(12):2456–2461. WOS: 000286043000019
- [25] I. Lancranjan, S. Miclos, D. Savastru. Numerical simulation of a DFB-fiber laser sensor (I). *Journal of Optoelectronics and Advanced Materials*. 2010;12(8):1636–1645. WOS: 000281695300002
- [26] S. Miclos, D. Savastru, I. Lancranjan. Numerical simulation of a fiber laser bending sensitivity. *Romanian Reports in Physics*. 2010;62(3):519–527. WOS: 000287272300008
- [27] S. Miclos, D. Savastru, R. Savastru, I. Lancranjan. Design of a smart superstructure FBG torsion sensor. In: J.L. Sanchez Rojas, R. Brama, editors. Conference on Smart Sensors, Actuators, and MEMS VII 1st SPIE Conference on Cyber-Physical Systems; 04–06 May 2015; Barcelona, Spain. Bellingham, WA, USA: SPIE-Int Soc Optical Engineering; 2015. p. 95172B. doi:10.1117/12.2188231
- [28] D. Savastru, S. Miclos, R. Savastru, I. Lancranjan. Numerical analysis of a smart composite material mechanical component using an embedded long period grating fiber sensor. In: J.L. Sanchez Rojas, R. Brama, editors. Conference on Smart Sensors, Actuators, and MEMS VII 1st SPIE Conference on Cyber-Physical Systems; 04–06 May 2015; Barcelona, Spain. Bellingham, WA, USA: SPIE-Int Soc Optical Engineering; 2015. p. 95172B. doi:10.1117/12.2188231
- [29] K. O. Hill, B. Malo, F. Bilodeau, D. C. Johnson. Photosensitivity in optical fibers. *Annual Review of Materials Science*. 1993;23:125–157. WOS: A1993LQ76400005
- [30] R. J. Campbell, R. Kashyap. The properties and applications of photosensitive germanosilicate fiber. *International Journal of Optoelectronics*. 1994;9(1):33–57. WOS: A1994PL77900004
- [31] P. St. J. Russell, J.-L. Archambault, L. Reekie. Fiber gratings. *Physics World*. 1993;6(10): 41–46. WOS: A1993MB88600025

- [32] I. Bennion, J. A. R. Williams, L. Zhang, K. Sugden, N. J. Doran. UV-written in-fiber Bragg gratings. *Optical and Quantum Electronics*. 1996;28(2):93–135. doi: WOS: A1996TV07200001
- [33] V. Mizrahi, J. E. Sipe. Optical properties of photosensitive fiber phase gratings. *Journal of Lightwave Technology*. 1993;11(10):1513–1517. doi:10.1109/50.249888
- [34] M. Born, E. Wolf. *Principles of optics*. 7th ed. Cambridge, UK: Cambridge University Press; 1999. 952 p. ISBN: 0521642221
- [35] A. Yariv. Coupled-mode theory for guided-wave optics. *IEEE Journal of Quantum Electronics*. 1973;QE-9(9):919–933.
- [36] J. E. Sipe, L. Poladian, C. M. de Sterke. Propagation through nonuniform grating structures. *Journal of the Optical Society of America A-Optics Image Science and Vision*. 1994;11(4):1307–1320. doi:10.1364/JOSAA.11.001307
- [37] H. Kogelnik. Filter response of nonuniform almost-periodic structures. *Bell System Technical Journal*. 1976;55(1):109–126. doi:10.1002/j.1538-7305.1976.tb02062.x
- [38] K.O. Hill. Aperiodic distributed-parameter waveguides for integrated optics. *Applied Optics*. 1974;13(8):1853–6. doi:10.1364/AO.13.001853
- [39] B. Malo, S. Theriault, D. C. Johnson, et al. Apodised in-fiber Bragg grating reflectors photoimprinted using a phase mask. *Electronics Letters*. 1995;31(3):223–225. doi: 10.1049/el:19950150
- [40] F. Ouellette. Dispersion cancellation using linearly chirped Bragg grating filters in optical waveguides. *Optics Letters*. 1987;12(10):847–9. doi:10.1364/OL.12.000847

Charge Collection Physical Modeling for Soft Error Rate Computational Simulation in Digital Circuits

Jean-Luc Autran, Daniela Munteanu,
Soilihi Moindjie, Tarek Saad Saoud, Victor Malherbe,
Gilles Gasiot, Sylvain Clerc and Philippe Roche

Additional information is available at the end of the chapter

<http://dx.doi.org/10.5772/64277>

Abstract

This chapter describes a new computational approach for accurately modeling radiation-induced single-event transient current and charge collection at circuit level. This approach, called random-walk drift-diffusion (RWDD), is a fast Monte Carlo particle method based on a random-walk process that takes into account both diffusion and drift of carriers in a non-constant electric field both in space and time. After introducing the physical insights of the RWDD model, the chapter details the practical implementation of the method using an object-oriented programming language and its parallelization on graphical processing units. Besides, the capability of the approach to treat multiple node charge collection is presented. The chapter also details the coupling of the model either with an internal routine or with SPICE for circuit solving. Finally, the proposed approach is illustrated at device and circuit level, considering four different test vehicles in 65 nm technologies: a stand-alone transistor, a CMOS inverter, a SRAM cell and a flip-flop circuit. RWDD results are compared with data obtained from a full three-dimensional (3D) numerical approach (TCAD simulations) at transistor level. The importance of the circuit feedback on the charge-collection process is also demonstrated for devices connected to other circuit nodes.

Keywords: single event effects, radiation transport modeling, random walk, drift-diffusion, radiation-induced charge generation and transport, Monte Carlo computational approach, numerical simulation, soft error, soft error rate, CMOS inverter, SRAM, flip-flop

1. Introduction

Natural radiation at ground level, including both terrestrial cosmic rays and telluric radioactivity (alpha decay from radioactive ultra-traces in materials), is considered today as a major reliability issue for integrated circuits (IC), since they are increasingly sensitive to this radiation as long as CMOS technologies scale down [1]. The basic mechanism taking place when an ionizing particle crosses a circuit is the generation in the semiconductor region of a high-density charge track; the generated charge can be collected at circuit level through biased contacts and especially reverse-biased drain junctions and create parasitic transient currents at the circuit nodes. In the case of a memory cell, the collected charge may be sufficient to induce the cell upset; this phenomenon is called single event upset (SEU). When combinational logic is concerned, the charge induced by the particle may lead to a single event transient (SET) [2].

Researchers have always used modeling and simulation approaches to better understand the physical processes and to predict the consequences on the circuit operation of such single events. The study of these phenomena, and more precisely, the computation of the electrical response of devices and circuits submitted to ionizing radiation imply the accurate modeling of various physical mechanisms at different scales, as charge generation, transport and collection of charges within the circuit. The solutions developed to solve this kind of problem include full numerical methods (such as TCAD) and approximate analytical models used in circuit simulators [3]. Full numerical methods, such as TCAD, exactly solve this coupled problem (radiation + electrostatics + transport) and offer a very accurate solution. But the huge computation time and computer resources needed to solve this high complexity problem restrict its application to small simulation domains, limited to, at most, several devices (very small circuits). In order to overstep these limitations, several approximated solutions have been developed in the literature: these approaches generally calculate the current transients induced by single events (SETs) in devices and circuits by decoupling the radiation-induced charge transport from the electrostatic problem. The so-called diffusion-collection model is one of the most interesting and physically accurate approaches developed for this purpose [4–6]. This model makes the assumption that the main carrier driving mechanisms is a pure spherical ambipolar diffusion in the semiconductor region. Moreover, the model can be easily implemented since an ionizing particle track can be divided into a series of discrete punctual charges to compute (or to analytically derive) single or multiple node charge collection. Although interesting improvements have been made [6, 7] and in spite of its capability to be parallelized [8], the diffusion collection model does not correctly take into account the electric field effects in the vicinity of the collecting contact, which is a serious intrinsic limitation. To overcome this drawback, the diffusion coefficient D (i.e. the mobility μ) and the carrier collection velocity v are generally fine-tuned on results obtained from numerical simulation (TCAD) in order to fit the transients for a series of typical radiation events. But, with this procedure the value of D (or μ) does not quantify the real diffusion process (the diffusion will be overestimated or underestimated), since, it artificially reproduces the combination of both the diffusion process and the collection by a reverse-biased junction. Another limitation of this approach is its inability to take into account a non-constant electric field or the nodes bias changes during the collection process.

This chapter presents a new computational method for accurately modeling single-event transient current and charge collection at circuit level. This approach is called random-walk drift-diffusion (RWDD) [9, 10] and consists in a fast Monte Carlo particle method based on a random-walk process [11] that includes both the diffusion and the drift of carriers in an electric field that is nonconstant in both space and time. This method has been successfully used in previous works, as shown in Refs. [12, 13]. In the present work, we considerably improve this approach by a series of developments that make it capable of fast and intensive simulation of full circuits with an accuracy degree similar to that of the TCAD simulation. The considered improvements are briefly described below, but they will be extensively detailed in the following sections. Firstly, the method models the charge carrier transport and collection process using exclusively physical parameters (for example for the carrier mobility or the minority carrier lifetime) and physical constants. In particular, transport and collection processes are modeled by the same mathematical equations, without any fitting parameter. Secondly, the new method implements a model fully derived in C++ environment, which authorizes the use of powerful capabilities such as advanced structures (classes and containers) to model the different problems to solve (geometry, particle track, charge transport, collection, recombination and extraction). Finally, the third important improvement concerns the intrinsic ability of the model to be parallelized on graphic unit processors (GPUs) for charge carrier transport and dynamically coupled with SPICE to take into account the impact of charge collection on biased nodes not considered as stand-alone contacts but embedded in a circuit and connected to other nodes.

This chapter describes in-depth the RWDD approach and illustrates all of these points in the three following sections. Section 2 details the physical insights of the model. The practical implementation of the method using an object-oriented programming language and its parallelization on GPUs is presented in Section 3. Besides, the capability of the approach to treat multiple-node charge collection is presented. Section 4 details the coupling of the model either with an internal routine or with SPICE program for circuit solving. Finally, Section 5 illustrates this proposed approach at device and circuit-level, considering four different test vehicles in 65 nm technologies: a stand-alone transistor, a CMOS inverter, a SRAM cell and a flip-flop circuit. RWDD results are compared with data obtained from a full three-dimensional (3D) numerical approach (TCAD simulations) at transistor level. The importance of the circuit feedback on the charge-collection process is also demonstrated for devices connected to others.

2. Random-walk drift-diffusion (RWDD) model

This section introduces the basis of the RWDD model and the modeling methodology used to describe the main simulation steps, i.e. the charge deposition induced by the passage of an ionizing particle at silicon level, the radiation-induced charge transport within the structure and the computation of the collection current on the collecting node(s).

2.1. Charge deposition

In the RWDD approach, an ionizing particle track crossing a circuit at silicon-level is modeled as a series of charge packets (**Figure 1**) spread along a straight segment whose length equals the ionizing particle range (R) in target material. The linear density of the charge packet along the particle track takes into account the non-constant linear energy transfer (LET) of the particle. SRIM tables are used to compute both LET and range using appropriate numerical functions [14]. The accuracy of this charge discretization is ensured by the degree of “granularity” [11] that can be fine-tuned by selecting the packets size, in practice from 1 to 100 elementary charges.

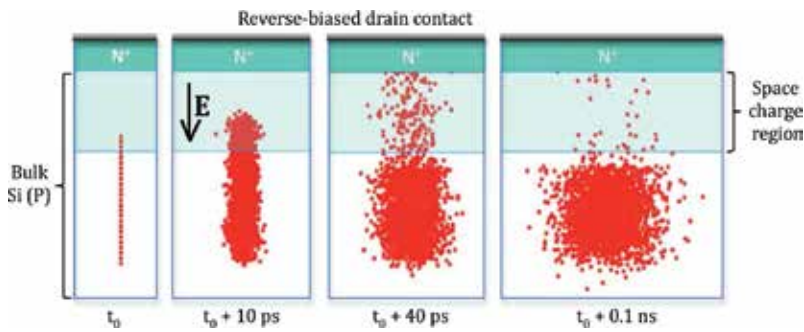


Figure 1. Cartoon illustrating the charge transport and collection processes after a 5 MeV alpha-particle strike in a reverse-biased junction (its geometrical and electrical parameters correspond to the 65 nm node). The biased contact collects charges that diffuse in silicon and are accelerated by the electric field developed in the space charge region. (Reprinted with permission from Glorieux et al. [12], © 2014, IEEE).

2.2. Charge transport modeling

The transport of each charge packet starts immediately after the particle crosses the device (**Figure 1**). For modeling the charge transport, the RWDD approach implements the popular drift-diffusion model [15], where the electron (J_n) and hole (J_p) current densities are computed as the sum of two components: the drift current component (first term) that is driven by the electric field and the diffusion component (second term) that models the current induced by the gradient of carrier concentration. J_n and J_p are given by:

$$J_n = qn\mu_n E + qD_n \text{grad}(n) \quad (1)$$

$$J_p = qn\mu_p E - qD_p \text{grad}(p) \quad (2)$$

In these equations, n and p are, respectively, the electron and hole densities; μ_n and μ_p are, respectively, the electron and hole mobilities; E is the electric field; and D_n and D_p are,

respectively, the diffusion coefficients that may be calculated from the carrier mobility using the Einstein's equation:

$$D_{n,p} = \frac{k_B T}{q} \mu_{n,p} \quad (3)$$

In Eq. (3), k_B is the Boltzmann constant and T is the carrier temperature; as the carrier gas in the drift-diffusion approximation is assumed to be in thermal equilibrium, T is equal to the lattice temperature.

The next calculation step in conventional full numerical methods (TCAD) is to inject the current densities given by Eqs. (1) and (2) into the conservation laws for electrons and holes also called continuity equations; they are next self-consistently solved with Poisson's equation. For this purpose, the simulation domain is meshed, and all previous equations are discretized on this mesh grid and then solved. Contrary to this procedure, in the RWDD model, no meshing is need since charge packets have continuous coordinates. Also in RWDD, a random-walk algorithm [11] is used to model the diffusion process, and the drift-induced current is directly calculated using the electrical field present in the considered region. For a charge packet situated at the position (x, y, z) at time t , its new position at time $t+\delta t$ is given by $(x+\delta x, y+\delta y$ and $z+\delta z)$, where δx , δy and δz are calculated as follows:

$$\begin{cases} \delta x = N_1 \times \sqrt{D \delta t} + E_x \times \mu \delta t \\ \delta y = N_2 \times \sqrt{D \delta t} + E_y \times \mu \delta t \\ \delta z = N_3 \times \sqrt{D \delta t} + E_z \times \mu \delta t \end{cases} \quad (4)$$

In Eq. (4), N_1 , N_2 and N_3 are three independent normal random numbers, D is the diffusion coefficient, μ is the carrier mobility and $E(E_x, E_y, E_z)$ is the electric field vector at the corresponding position and time.

2.3. Collection current computation

At each time step of the simulation, the radiation-induced collection current is computed from the transport dynamic of minority charge carriers described in the previous Section 2.2. For the estimation of this current, two main procedures may be employed: the first technique is to use the semi-conductor transport equations and the second one is to employ the Schockely-Ramo's theorem. Simulation tools used in microelectronics generally consider the first option; the transport equations are implemented in TCAD simulator that numerically solve them self-consistently with Poisson's equation. This approach considers the free-charge carrier distributions as continuous functions in time and space coordinates. The second option is generally used in instrumentation or high-energy physics for the calculation of detector responses to radiation events. In this second approach, the Ramo's theorem is used to treat each carrier

considered individually and all the interesting effects due to particular carriers are summed [16]. In our work, we implemented the first formalism (transport equations) by applying the continuity equation at the collecting (drain) contact. The transient current at the collecting node is directly computed from the number of carriers Δn that reach this contact during the time step Δt , i.e.

$$I = q \times \frac{\Delta n}{\Delta t} \quad (5)$$

In this expression, the displacement current is neglected; that is a reasonable approximation in this case [17]. This collection current is then injected in the electrical simulation to model the circuit response.

2.4. Model limitations

Although the model embeds a microscopic physical description of charge generation, transport and collection, the present approach suffers from two evident limitations that should be amended in a future enhanced code version: (1) the calculation is not self-consistent with the electrostatic potential (i.e. the electric field) and (2) it does not implement electrostatic interactions taking place between charge packets. For this reason, the RWDD model should especially fail in high carrier injection conditions, i.e. at high LETs. These drawbacks will be carefully estimated and quantified in a future work. Another interesting point should be to compare the two methods for computing the collection current to also evaluate the impact of the displacement current on transient characteristics.

3. Model implementation

3.1. C++ implementation

To implement the RWDD model described previously, we choose a C++ programming environment, an object-oriented programming language that offers considerable advantages in terms of advanced structures, such as classes, objects and containers. The C++ code implementing the RWDD approach was named RWDDCPP.

In this code, the particle track is defined as a C++ container including all the charge packets described as independent objects. The members of the charge packet class include the geometrical coordinates of the packet and the electrical charge amount per packet. The container content may change during the simulation due to two different mechanisms: (1) minority carrier recombination or (2) carrier extraction that correspond to particles that escape the simulation domain. For modeling the carrier recombination mechanisms, we use a simple exponential law that adjust the number of charges as a function of time: $N(t) = N_0 \exp(-t/\tau)$. In this exponential law, N_0 is the initial number of charges deposited by the particle at $t = 0$ s and the time constant τ is equal to the carrier lifetime.

In RWDDCPP code, the circuit geometry is implemented as a series of 3D rectangular boxes that represent respectively the substrate, the source and drain contacts at the silicon level and the different wells; all these elements constitute the Front-End-Of-Line (FEOL) structure. A simplified Back-End-Of-Line (BEOL) structure may be also modeled, as a stack of insulating material and metal layers. The fine modeling of the reversely biased drain contacts collecting the minority carriers created along the particle track is the most important improvement of the RWDD model at the circuit level. A special “drain class” has been developed, embedding in the same C++ object both the drain contact geometry and the 3D distribution of the electric field induced by the drain bias. At this level, different doping profiles can be taken into account for the p-n junctions: abrupt, gradual or user-defined profiles.

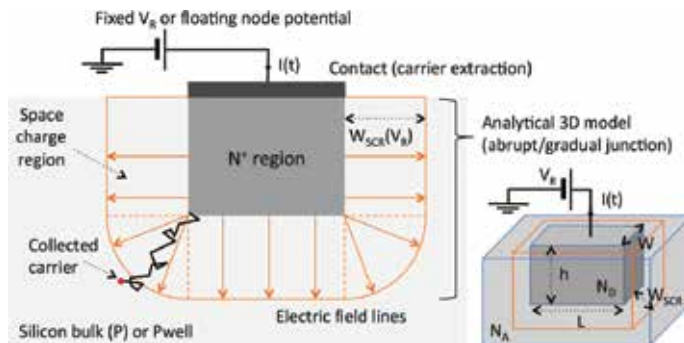


Figure 2. Schematic illustrations of a reversely biased drain junction taken into account in the RWDD approach. The p-n junction is defined by its geometry and the bias V_R applied to collect and extract carriers from the bulk. A 3D analytical model is used to model the space charge region (SCR) in the case of a gradual or an abrupt doping profile. Both the electric field developed in the SCR (E) and the SCR width (W) are controlled by the bias V_R . V_R (and consequently E and W) may vary in time due to external circuit feedback. (Reprinted with permission from Autran et al. [10], © 2014, Elsevier).

An object of the class “drain” is shown in **Figure 2**; this class is defined by its doping profile (an abrupt junction in this case), its geometrical dimensions (W , L , h), the doping levels of the p and n+ regions (N_A and N_D , respectively) and the bias (V_R) applied to the collecting contact. A 3D analytical model is used to compute the space charge region, since an abrupt p-n junction is considered in this example. The electric field (E) developed in this space charge region and its width (W_{SCR}) are functions of the drain bias potential and can be calculated using the following relations:

$$W_{SCR} = \sqrt{\frac{2\epsilon_{Si}(V_{bi} + V_R)}{qN_A}} \quad (6)$$

$$E = \frac{2(V_{bi} + V_R)}{W_{SCR}} \quad (7)$$

where V_{bi} is the internal potential of the junction and ϵ_{si} is the permittivity of silicon.

It must be noted that both W_{SCR} and E can dynamically vary during the transient simulation as a function of the effect of carrier collection on the circuit node potential V_R , as illustrated in the following.

3.2. GPU parallelization

As explained in the previous section, in the RWDD approach, the behavior of each packet of charge is computed independently of the other charges. These processes being independent, the calculation task of the charge transport can be easily parallelized on a graphic processing unit (GPU) whose internal architecture is perfectly adapted to such a massive parallelism. Moreover, RWDD model needs to implement a random number generation procedure that is usually very time-consuming; if the random numbers are independent, this task can also be easily parallelized on GPU. These two characteristics of the RWDD model are expected to offer a considerable computation speed, since the number of parallelizable tasks in RWDD is relatively high. In this work, we used the CUDA programming framework proposed by NVIDIA (CUDA version 5.5 64 b) [18]. Random numbers are generated using the CUDA cuRAND random number generation library (Mersenne Twister) within the parallel kernels running on the GPU. **Figure 3** illustrates this parallel implementation of the RWDDCPP code. For the purpose of this work, we separately tested the RWDD algorithm implemented in series on a CPU and in parallel on a GPU. Tests have been performed on a machine equipped with a 3.2 GHz Intel Core i5 and with a NVIDIA GeForce GTX 675 MX (960 threads at 600 MHz). Our results show that for the simulation of 100,000 charge packets with 1000 time steps the speedup on GPU was 140× with respect to the classical CPU implementation.

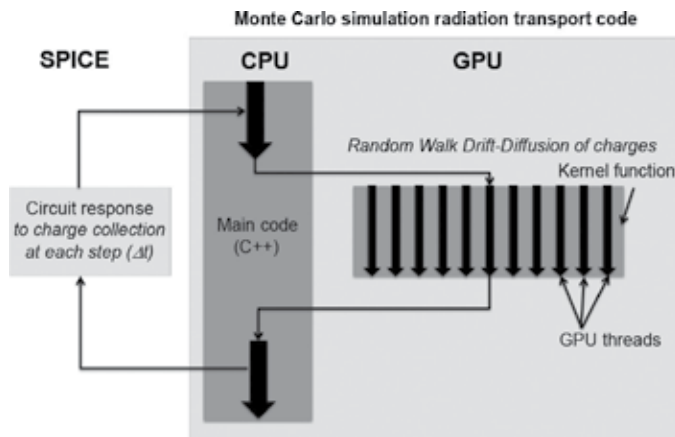


Figure 3. Program flow for the parallel version of the RWDDCPP code. The main part is executed on the CPU (host), and the RWDD computational part is executed on the GPU (device). The code is also dynamically coupled with SPICE for circuit simulation within the transient event time domain. (Reprinted with permission from Glorieux et al. [12], © 2014, IEEE).

3.3. Multiple node charge collection

Since the RWDD model has been implemented in an object-oriented language (C++) using dynamic containers, as previously explained in 3.1, complex circuits with an arbitrary number of sensitive areas and collecting nodes can be simulated, intrinsically considering, in this case, multiple node charge collection in the simulation process. The simulation begins with the initialization of the structure and the definition of the circuit nodes corresponding to the different simulated drains. In a second step, the electrical potential of each node is extracted from a steady-state circuit simulation. The values of these potentials are used to initialize the electrical field in the complete structure. Starting the time-domain analysis, at each time step of the transient simulation, the magnitudes of the current sources corresponding to the different collection processes (simultaneously occurring at different circuit nodes) are updated as a function of the number of collected charge packets. **Figure 4** illustrates this multiple node charge collection process in the simple case of two adjacent drain junctions. The time evolution

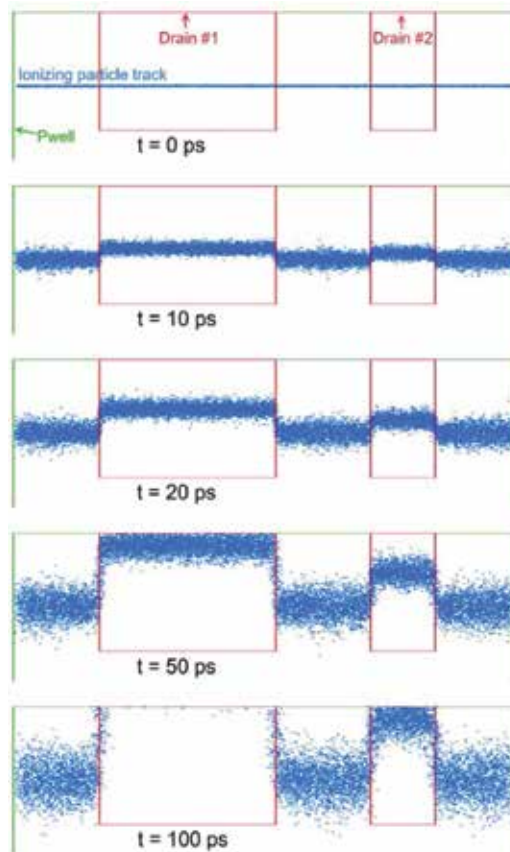


Figure 4. Cartoon (at five different times after the ionizing particle impact) illustrating the time evolution of the charge packets induced by a horizontal ionizing particle impacting two adjacent drains. The collection efficiency is different for these two drains since their biasing state is different (Reprinted with permission from Glorieux et al. [12], © 2014, IEEE.).

of the charge packets induced by a horizontal ionizing particle in this two-node structure is shown at five different times after the ionizing particle impact. As evidenced in **Figure 4**, the collection efficiency of the two drains differs because they correspond to two different nodes in the circuit and their electrical potential (i.e., internal electric field) is not the same in this example.

4. Circuit solving

Once the current transients have been evaluated using the RWDD model on the different collection nodes of interest in a given device or circuit, one must evaluate the transient electrical response of the circuit. This latter can be directly computed using an internal routine (solving the Kirchoff's circuit laws) or with an external circuit simulator program. We examine here these two solutions, both implemented in our code RWDDCPP.

4.1. Internal routine

For circuit architectures composed of only a few connected devices, such as CMOS inverters or SRAM cells, the steady-state circuit electrical solution can be simply solved considering Kirchoff's circuit laws and compact models for transistors. In the following, the method is illustrated for the solving of an inverter and a SRAM cell. **Figure 5** (left) defines the different terminal voltages and the source-to-drain current for the NMOS and PMOS transistors; **Figure 5** (right) shows the circuit schematic of a SRAM cell consisting of two cross-coupled CMOS inverters. Considering that the particle strikes the OFF-state NMOS transistor termed NMOS₁ (initial conditions $V_1 = 0$, $V_2 = V_{DD}$) the time variations of potential V_2 for the sole and isolated inverter #1 can be written as:

$$\frac{dV_2}{dt} = \frac{-I(t) + I_{DP1}(V_1 - V_{DD}, V_2 - V_{DD}) - I_{DN1}(V_1, V_2)}{C_N} \quad (8)$$

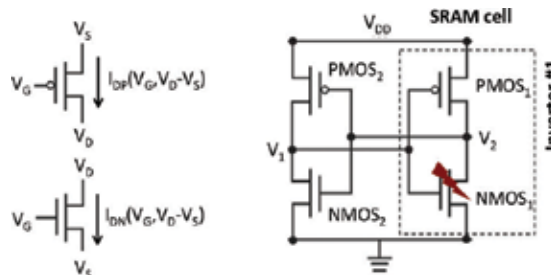


Figure 5. Definition of the terminal voltages and the source-to-drain current in n-channel (NMOS) and p-channel (PMOS) transistors (left). Circuit schematic of a SRAM cell formed by two cross-coupled CMOS inverters (right). (Reprinted with permission from Autran et al. [10], © 2014, Elsevier).

where $I(t)$ is the current pulse given by Eq. (5) due to the particle strike and collected on the node 2, I_{DN1} and I_{DP1} are the currents of the NMOS₁ and PMOS₁ transistors, respectively, and C_N is the node capacitance.

Considering this time, the full SRAM cell composed of the two cross-coupled inverters, we obtain the following system of two coupled differential equations:

$$\begin{cases} \frac{dV_1}{dt} = \frac{I_{DP2}(V_2 - V_{DD}, V_1 - V_{DD}) - I_{DN2}(V_2, V_1)}{C_N} = F(t, V_1, V_2) \\ \frac{dV_2}{dt} = \frac{-I(t) + I_{DP1}(V_1 - V_{DD}, V_2 - V_{DD}) - I_{DN1}(V_1, V_2)}{C_N} = G(t, V_1, V_2) \end{cases} \quad (9)$$

Eq. (8) for the sole and isolated inverter #1 or Eqs. (8) and (9) for the full SRAM cell can be easily solved in the time domain, using a fourth-order Runge-Kutta method [19] with a time step Δt identical to the one used in the RWDD algorithm for charge transport and collection. Using notations introduced in Eq. (8), the incremental results for $t_{n+1} = t_n + \Delta t$ are:

$$V_1^{n+1} = V_1^n + \frac{K_1 + 2K_2 + 2K_3 + K_4}{6} \quad (10)$$

$$V_2^{n+1} = V_2^n + \frac{L_1 + 2L_2 + 2L_3 + L_4}{6} \quad (11)$$

with:

$$K_1 = F(t^n, V_1^n, V_2^n) \Delta t \quad (12)$$

$$L_1 = G(t^n, V_1^n, V_2^n) \Delta t \quad (13)$$

$$K_2 = F(t^n + \Delta t/2, V_1^n + K_1/2, V_2^n + L_1/2) \Delta t \quad (14)$$

$$L_2 = G(t^n + \Delta t/2, V_1^n + K_1/2, V_2^n + L_1/2) \Delta t \quad (15)$$

$$K_3 = F(t^n + \Delta t/2, V_1^n + K_2/2, V_2^n + L_2/2) \Delta t \quad (16)$$

$$L_3 = G(t^n + \Delta t/2, V_1^n + K_2/2, V_2^n + L_2/2) \Delta t \quad (17)$$

$$K_4 = F(t^n + \Delta t, V_1^n + K_3, V_2^n + L_3) \Delta t \quad (18)$$

$$L_4 = G(t^n + \Delta t, V_1^n + K_3, V_2^n + L_3)\Delta t \quad (19)$$

Eqs. (10)–(19) constitute the core model implemented in the code RWDDCPP for CMOS inverter and SRAM cell solving. In Eq. (9), NMOS and PMOS source-to-drain currents are analytically modeled using the EPFL-EKV model 2.6 [20, 21], here implemented in C++ as numerical functions (I_{DN} and I_{DP}) having two arguments (see **Figure 5**). The EKV 2.6 MOSFET model is a predictive (scalable) compact model for the simulation of submicron CMOS technologies. It was built taking into account fundamental physical characteristics of the MOS structure. The model offers a continuous modeling of the different regimes of the transistor operation (weak, moderate and strong inversion), which is mandatory for circuit modeling. The version 2.6 takes into account numerous essential issues for the transistor modeling such as the effects of the doping profile, substrate effects, process-related aspects (oxide thickness, effective channel length and width and junction depth), mobility effects due to vertical and lateral electric fields, the velocity saturation, short-channel effects, etc. Section 5 details several examples of simulations using this code RWDDCPP.

4.2. SPICE simulator

For more complex circuit architectures than a single inverter or a SRAM cell, an external SPICE circuit simulator can be otherwise used in the place of the internal subroutine for circuit solving. In this case, the circuit simulator is instantiated in interactive mode by the executable code with a circuit netlist corresponding to the simulated structure. Current source(s) emulating the transient collected current(s) at the different circuit nodes is (are) automatically added to the netlist by the RWDDCPP program. At each time step of the simulation, the magnitude of each current source is updated as a function of the number of charge packets collected by the corresponding biased junction, following Eq. (5). Then, the SPICE simulator computes the new voltages on the circuit nodes and finally, from Eqs. (6) and (7), the width of the space charge region(s) and the distribution of the electrical field can be updated, time step by time step. The whole circuit counteraction to the radiation transient can then be taken into account. This approach has been successfully implemented in this work using both NGSPICE [22] and ELDO [23] simulators.

5. Simulation results on various circuits

Four typical simulation cases are presented in this section to validate the proposed model and its computational implementation. All examples have been derived from the same generic 65 nm CMOS technology. In the first example, the RWDD transient response of an isolated transistor subjected to an alpha particle has been compared to TCAD simulation. In the second example, a CMOS inverter has been considered to the effect of the feedback of the node voltage on the modulation of the space charge region related to the impacted junction. The two last examples concern a SRAM cell and a master-slave D flip-flop, with an isolated output,

illustrating the internal/external solutions for circuit solving and charge-sharing effects at the level of circuit sensitive nodes.

5.1. Model validation—isolated NMOS

This simplest case corresponds to an isolated transistor subjected to single event irradiation. The radiation-induced collected current and charge have been separately computed using the RWDDCPP code and the commercial Synopsys TCAD simulation platform [24]. **Figure 6** (top) shows the 3D structure of a single NMOS transistor implanted in a Pwell region (delimited in depth by a deep N-well) built in Synopsys Sentaurus using geometrical and technological parameters corresponding to the considered 65 nm CMOS technology.

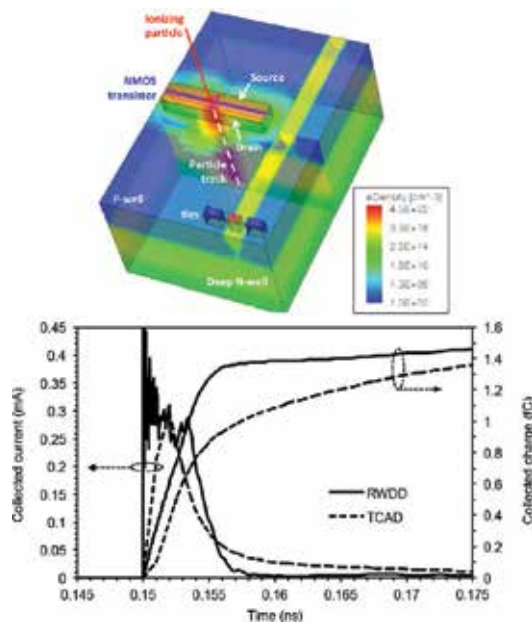


Figure 6. Top: 3D electron density distribution obtained by TCAD simulation at 2 ps after an alpha particle strikes the drain of an OFF-state isolated NMOS transistor (designed in 65 nm CMOS technology). To facilitate the picture analysis, spacers, gate material and isolation oxide are not shown here. The long arrow indicates the location and direction of the ionizing particle strike. Bottom: Current and charge collected by an isolated OFF-state NMOS transistor after the alpha particle strike computed by TCAD and by the RWDD model. (Reprinted with permission from Autran et al. [10], © 2014, Elsevier).

Figure 6 also shows the electron density 2 ps after the passage of an alpha particle (incident energy of 5 MeV) at the level of the drain of the transistor maintained in the OFF-state. A similar structure has been built and simulated with the RWDDCPP program; the main simulation parameters and options in both approaches have been forced to the same values: drift-diffusion model, constant carrier mobility for electrons (400 cm²/V/s) and holes (200 cm²/V/s), identical minority carrier lifetime (10⁻⁸ s), etc. **Figure 6** (bottom) shows the transient current and the corresponding charge collected by the drain of the NMOS transistor subjected to a 5 MeV alpha

particle striking the center of the drain perpendicularly to the device. A good agreement between results obtained with RWDD and TCAD are shown in this graph. One can observe a few differences between the two curves, especially in the early stages of the transient, mainly due to: (i) the arrival of discrete charge packets at the level of the collecting drain contact in the RWDD approach which induces inherent granularities; and (ii) the characteristic time (2 ps) of the Gaussian time distribution used in the TCAD simulation. Values of the collected charges obtained from TCAD and RWDD are very close at the end of the transient event, with a difference limited to a maximum of 15%, indicating that both modeling approaches have very similar charge collection efficiencies. We confirmed this point by comparing the results given by RWDD and TCAD concerning the space charge region width and the electric field: a very good agreement between the two series of results was obtained and then reiterated for different bias conditions. This shows that both transport and charge collection processes of the RWDD model provide results very similar to those of TCAD simulations without employing any fitting or unphysical parameter. This is a significant advantage of the RWDD approach over other previously developed methods (see [25] for example).

5.2. Transient simulation of a CMOS inverter

We explored next the case of the same NMOS transistor but embedded in a CMOS inverter, as shown in **Figure 7**. In the present case, the voltage node V_2 is not fixed, as was the case for the study of a NMOS transistor standalone; the operation of the second transistor of the CMOS inverter (see **Figure 7**) leads to the variation of the voltage V_2 during the transient process. These node bias changes may modify the charge collection efficiency at the drain of the NMOS transistor, through the variation of both E and W_{SCR} by a feedback process. In the following,

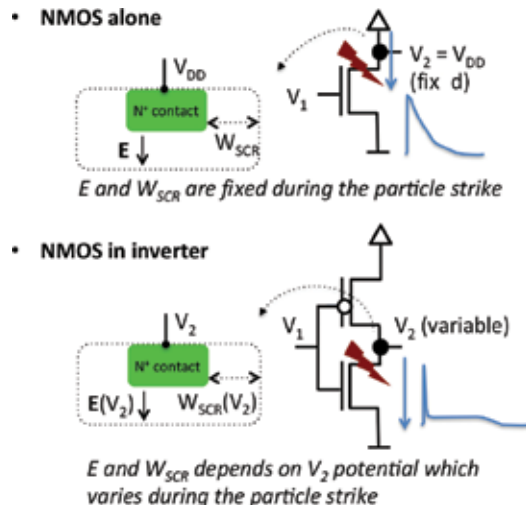


Figure 7. Schematics illustrating the differences in the charge collection process between an isolated NMOS and the same structure embedded in a CMOS inverter (OFF-state). The drain junction is biased at fixed V_{DD} in the transistor alone, whereas it is subjected to the node potential V_2 in the inverter. This voltage is susceptible to vary during the transient event due to circuit retroaction. (Reprinted with permission from Autran et al. [10], © 2014, Elsevier).

this case is called “with SCR feedback.” By opposition, we name “without SCR feedback” the case when the same (fixed) SCR parameters are maintained during the entire transient simulation. With respect to the charge collection process, this last case is equivalent to that of considering a standalone NMOS transistor. Simulated transients of the CMOS inverter (under the initial conditions $V_1 = 0$ and $V_2 = V_{DD}$) obtained with the RWDD model when a 5 MeV alpha particle passes across the NMOS drain are shown in **Figure 8**. These results reveal the influence of the circuit feedback on the SCR characteristics, through the time changes of V_2 . Without the circuit feedback on the SCR, the radiation effect is to turn V_2 to negative values for a period of time equal to about 30 ps. This obviously evidences a hazardous condition for a cross-coupled inverter in the case of an SRAM cell (somewhat reduced by the gate capacitance in the case where the second inverter is coupled). **Figure 8** illustrates an important issue concerning the inverter operation: the hazardous condition described above persists 2× as long when SCR feedback is activated.

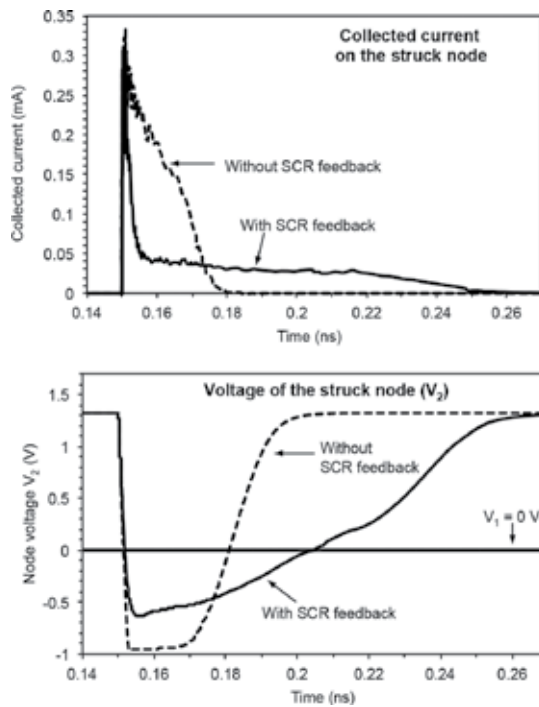


Figure 8. RWDD simulation of the impact of an ionizing particle on an off-state NMOS transistor embedded in a CMOS inverter with and without the feedback effect of the space charge region (width and electric field dependence on V_2) on the collected current (top) and on the voltage on the struck node (bottom). (Reprinted from Autran et al. [10], © 2014, Elsevier).

Figure 8 also shows that the shape of the transient current is essentially modified when the “SCR feedback” is taken into account. The results show a plateau on the collected current curve, in good accordance with TCAD simulations published in [2]. In the case “without feedback,” the transient current shows a classical shape (being composed from a fast drift component and

a slower decay) because the SCR of the struck NMOS is maintained constant without feedback. When the “SCR feedback” is considered, the SCR of the struck NMOS can vary when V_2 changes. As explained by Ferlet-Cavrois et al. [2], when the NMOS is disturbed by a single event, it momentarily biases the on-state load PMOS transistor in a condition for drain current to flow. After a short-duration current peak corresponding to the output capacitance support of the drain voltage at its pre-strike value, the drain voltage collapses, which causes a reduction of both the electric field and the extension of the space charge region; as a consequence, the NMOS single event current becomes governed by the depressed drain voltage (that impacts the collection efficiency of the junction) and the compensating PMOS transistor drive current. The result of this dynamic interaction of the node voltage and the PMOS transient current is a characteristic current equilibrium or “plateau,” as shown in **Figure 8**. The amplitude of this current plateau is linked to the PMOS drive, and the duration of the plateau is synchronous with the depressed drain voltage. As soon as most of the deposited charge flows out of the struck transistor, the current flow cannot be maintained, the equilibrium conditions relax, the drain voltage recovers and the current pulse again decreases toward zero [2, 26]. This second example illustrates the importance of device coupling effects at circuit-level and its consequences on the charge collection dynamics in the impacted device. The soft-error rate consequence of such effects has to be investigated in future works, notably in SRAM cells composed of two cross-coupled inverters for which a very similar behavior as highlighted in **Figure 8** is expected at the level of the impacted OFF-state transistor.

5.3. Alpha-particle SEU in SRAM

In this third example, the single-event upset alpha particle cross-section of a 65 nm SRAM cell has been simulated using the RWDD approach and compared with experiments. The alpha cross-section experimental measurement was performed using an Americium 241 source (3.7 MBq), at room temperature and under nominal voltage 1.2 V), following all the recommendations of the JESD98A test standard [27]. Since the alpha source has a high activity, several thousand errors are measured and cross-section uncertainties are very low.

For the RWDD simulation, several additional assumptions have been introduced to estimate the electrical response of the 65 nm bit cell: (i) all of the electron-hole pairs generated inside or below the deep N-well (see the structure of the transistor in **Figure 6** top) are not taken into account; (ii) minorities charge carriers that reach well limits are considered as recombined and are eliminated from the simulation. **Figure 9** (top) shows the 65 nm bit cell composed of a centered Nwell and two Pwells. The four drains of the transistors constituting the two inverters have been placed in structure and connected to the corresponding nodes in the circuit netlist. The total simulation area is larger than the bit cell area to take into account an alpha particle with a high tilt angle, which strikes around the bit cell. The maximum tilt angle has been calculated using the range of the alpha particle and the thickness of the back-end layer. We computed a simulated cross-section by performing simulations for several thousand impacts of alpha particles, considering random impact locations and particles with random directions; the number of upsets was divided by the simulated fluency.

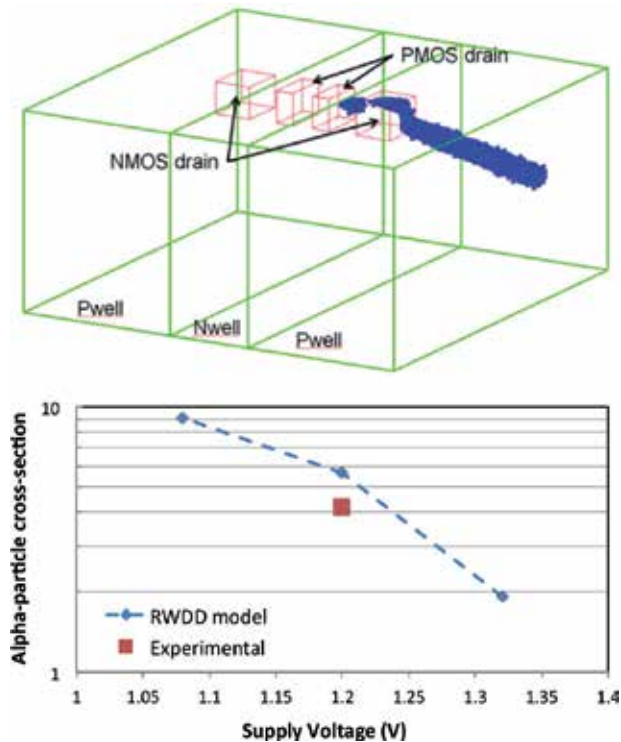


Figure 9. *Top:* Schematic representation of the 65 nm bit cell with the charge deposited by an alpha particle and computed by the RWDD model. The figure shows that in the impacted drain area, the electric field has extracted most of the deposited charge. *Bottom:* Corresponding bit cell alpha-simulated cross section compared with the experimental value (Reprinted With permission from Glorieux et al. [12], © 2014, IEEE).

The measured alpha particle cross-section of the 65 nm bit cell is compared with their simulated counterparts in **Figure 9** (bottom). Three different voltages from 1.08 to 1.32 V have been considered in simulation. This figure illustrates the nice agreement between the results obtained with the RWDD model and experimental measurements. **Figure 9** also demonstrates that this model is able to take into account the supply voltage dependence for the evaluation of the bit cell cross-section. Unfortunately, the comparison between experiment and simulation was not possible for this bit cell at both 1.1 and 1.3 V because experimental data were not available.

5.4. Flip-flop circuit

The final step was to confirm the ability of the RWDD model to simulate more complex circuit architectures and considering a large LET range. For this purpose, we simulated the heavy ion cross-section of a 65 nm flip-flop and we compared the simulation results with experimental measurements. To model the geometrical structure of the flip-flop, we took into account simulation hypothesis identical to those considered for the SRAM. Heavy ion measurements have been performed on a 65 nm test-chip, at nominal supply voltage and room temperature.

The measurements have been performed at the RADEF facility, Jyväskylä University (Finland), with a fluency of 10^6 heavy ions per square centimeter for five different ion LETs.

The functional schematic of the considered flip-flop (classical, unhardened master slave D-flip-flops) is shown in **Figure 10** (top). Data are transmitted between the master and slave latch using a pass gate. In this study, we include in the modeled structure all drains of all the transistors present in the flip-flop, unlike to our previous simulation works that only considered the bistable transistors [6, 28]. In this way, all of the possible upset mechanisms can be taken into account. This is specifically the case when an ionizing particle strikes a clock network transistor that can involve the latching of new data, these mechanisms being particularly important for high LET ions.

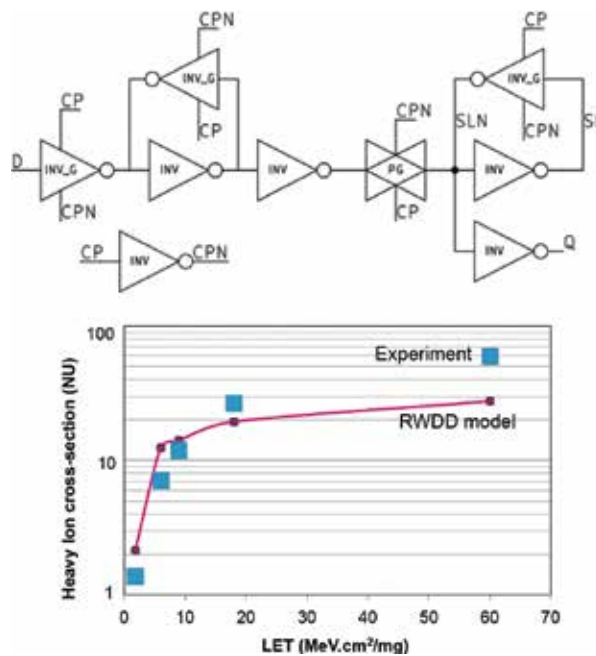


Figure 10. Top: Schematic of the modeled 65 nm flip-flop that corresponds to master-slave D flip-flop, with an isolated output. Bottom: Comparison of simulated and measured heavy-ion cross-sections of the 65 nm flip-flop. (Adapted with permission from Glorieux et al. [12]).

Figure 10 (bottom) shows the measured and simulated heavy ion cross-section of the flip-flop. This graph shows the excellent correlation of the simulated cross-section with the measurements for low LET ions. For higher LET impacts, the non-modeled multi-cell upsets induces a difference between measured and simulated data. Several reasons can explain these differences:

- The main reason for the lack of accuracy is the contribution of non-modeled multi-cell upset (MCU) in the measured data: indeed, flip-flop cross-sections have been measured in a shift register structure where flip-flops are next to each other. Thus, a single ionizing

particle can upset several flip-flops. Experimentally, this phenomenon has been verified (some MCUs have been recorded) but it was not possible to precisely quantify it since the number of stages in the shifter structure is not constant between the physical neighbor's cells, and the test has been performed dynamically.

- A second reason that can explain the differences in the cross-section at high LET energies concerns modeling of the charge carrier reaching the good limits and more specifically the approximation used to calculate this charge. Charge packets that reach the good interface are considered in the charge transport model as recombined and are then removed from the simulation. Another limitation concerns the impact location of the ionizing particle: the current implementation of our model is not totally adequate for an impact close to the good interface. Owing to the punctual character of the track profile, all charge packets are generated on the impacted well since, if taking into account the particle track radius, a non-negligible part of these packets should be considered in the adjacent well(s).

The SEU sensitive areas for each simulated LET can be identified on the flip-flop layout using the RWDD model, as in the case for other Monte Carlo simulation methods [29, 30]. The map of the simulated impacts inducing an upset for each ion LET is illustrated in **Figure 11**. This map has been generated on the slave latch of the flip-flop, with a high logic state stored in the latch. This figure indicates that, as the LET of the ionizing particles increases, the sensitive transistors are more abundant. The explanation is that upsets are uniquely produced on bistable transistors for ions with low LET, while for higher ion LET, other transistors (clock and pass gate transistors) become sensitive to SEU, in addition to those impacted at low LET.

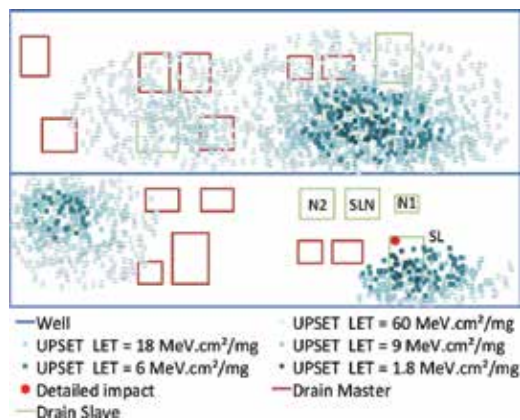


Figure 11. Mapping of the upsets in the slave latch, for different ion LET. The number of SEU-sensitive transistors increases with the LET of the incident heavy ions. The location labeled “detailed impact” has been considered for charge-sharing analysis discussed in the text. (Adapted with permission from Glorieux et al. [12]).

Finally, in order to evaluate the capability of the RWDD model to simulate charge-sharing mechanisms, a dedicated study has been performed. The SEU impact map of **Figure 11** shows that the top part of the bottom right drain of the flip-flop (labeled node “SL”) is not sensitive

to SEU. A detailed study of the collected currents in this area has then been conducted. For this purpose, a specific ion impact location (shown in **Figure 11**, labeled “detailed impact” in the top left corner of node SL) has been fixed and the collected current waveform following the ion impact at this location has been systematically analyzed, as well as the voltage waveform of the two bistable nodes. As expected, this node SL collects most of the charge as it corresponds to the stricken drain. However, the fine analysis (not shown) of the different transient currents indicates that the nodes SLN, N1 and N2 collect later, by a diffusion mechanism, a small quantity of charge, which is high enough to keep the voltage of the SLN node at the low logic state and to prevent a latch upset. In order to validate this affirmation, we removed from the circuit netlist in a separate simulation batch the drains corresponding to nodes SLN, N1 and N2. In this case, since no charge is collected on the NMOS of the SLN node to counter-balance the feedback loop of the latch, the electrical potential of the SLN node increases and an upset occurs.

To conclude, this particular charge-sharing mechanism in the area of the top left corner of collecting node SL has been observed whatever the value of the LET in the range 1.8–60 MeV cm²/mg, demonstrating the capability of the RWDD approach to treat such complex circuit response to single events.

6. Conclusion

A new computational method for the simulation of single event effects in integrated circuits has been presented. This approach is a Monte Carlo method based on a random-walk drift-diffusion algorithm that transports the radiation-induced charge, segmented into discrete charge packets, in the semiconductor regions of a given circuit architecture. Carrier diffusion is very well reproduced with the random-walk algorithm while the carrier “drift” component of the model perfectly captures the effects of the electric field developed in the space-charge region of the reversely biased collecting contact(s). The model has been fully derived in C++ using advanced structures to model device/circuit geometry, particle track and charge transport, collection, recombination and extraction. This approach has been dynamically coupled with an internal subroutine or an external circuit simulator to take into account spatial and temporal variations of the electric field in the vicinity of the collecting structure(s). Thus, complex architectures, such as flip-flops, can be easily modeled and charge-sharing mechanisms are accurately simulated.

This chapter mainly focused on the model implementation and the way to solve the circuit response in the time domain, taking into account the circuit feedback on the charge collection process. Four simulation test cases have been explored and compared to radiation experiments or TCAD simulations in order to validate the proposed model. These test cases show good quantitative agreement between measurements and simulated data over a large range of LETs up to 60 MeV.cm²/mg and structure complexity. This first implementation remains therefore not self-consistent with the electrostatic potential (in other words, Poisson’s equation is not solved during the transient computation) and does not take into account the possible interac-

tions between charge packets. The model ability to accurately reproduce a regime of high carrier injection is therefore uncertain. The limitations of the method will be more quantitatively explored in a forthcoming dedicated study, as well as possible improvements in terms of self-consistency with the electrostatic problem.

Acknowledgements

This work is conjointly supported by France's General Directorates DGA and DGE, under convention #132906128 "EVEREST" (Evaluation of the soft error rate of FD-SOI technologies for strategic applications).

Author details

Jean-Luc Autran^{1,3*}, Daniela Munteanu^{1,3}, Soilihi Moindjie^{1,3}, Tarek Saad Saoud^{1,3}, Victor Malherbe^{2,3}, Gilles Gasiot^{2,3}, Sylvain Clerc^{2,3} and Philippe Roche^{2,3}

*Address all correspondence to: jean-luc.autran@univ-amu.fr

1 Aix Marseille University, University of Toulon, CNRS, IM2NP, Marseille, France

2 STMicroelectronics, Crolles, France

3 Radiation Effects and Electrical Reliability (REER) Joint Laboratory, Aix Marseille University, University of Toulon, CNRS and STMicroelectronics, Marseille, France

References

- [1] P. Roche, J.L. Autran, G. Gasiot, D. Munteanu, "Technology Downscaling Worsening Radiation Effects in Bulk: SOI to the Rescue," International Electron Device Meeting (IEDM'2013), Washington, D.C., USA, December 9–11, 2013, pp. 31.1.1–31.1.4.
- [2] V. Ferlet-Cavrois, L.W. Massengill, P. Gouker, "Single event transients in digital CMOS – a review," IEEE Trans. Nucl. Sci., vol. 60, no. 3, pp. 1767–1790, 2013.
- [3] D. Munteanu, J.L. Autran, "Modeling of digital devices and ICs submitted to transient irradiations," IEEE Trans. Nucl. Sci., Vol. 55, no. 4, pp. 1854–1878, 2008.
- [4] J.M. Palau, G. Hubert, K. Coulie, B. Sagnes, M.C. Calvet, S. Fourtine, "Device simulation study of the SEU sensitivity of SRAMs to internal ion tracks generated by nuclear reactions," IEEE Trans. Nucl. Sci., Vol. 48, no. 2, pp. 225–231, 2001.

- [5] V. Correas, F. Saigne, B. Sagnes, J. Boch, G. Gasiot, D. Giot, P. Roche, "Innovative simulations of heavy ion cross sections in 130 nm CMOS SRAM," *IEEE Trans. Nucl. Sci.*, Vol. 54, pp. 2413–2418, 2007.
- [6] S. Uznanski, G. Gasiot, P. Roche, C. Tavernier, J-L. Autran, "Single event upset and multiple cell upset modeling in commercial bulk 65 nm CMOS SRAMs and flip-flops," *IEEE Trans. Nucl. Sci.*, vol. 57, no. 4, pp. 1876–1883, 2010.
- [7] L. Artola, G. Hubert, S. Duzellier, and F. Bezerra, "Collected charge analysis for a new transient model by TCAD simulation in 90 nm technology," *IEEE Trans. Nucl. Sci.*, vol. 57, no. 4, pp. 1869–1875, 2010.
- [8] J.L. Autran, S. Uznanski, S. Martinie, P. Roche, G. Gasiot, D. Munteanu, "A GPU/CUDA implementation of the collection-diffusion model to compute SER of large area and complex circuits," *IEEE International Conference on IC Design and Technology (ICICTD'10)*, June 2–4, 2010, Grenoble, France, pp. 67–70.
- [9] G. Sai-Halasz, M. Wordeman, "Monte Carlo modeling of the transport of ionizing radiation created carriers in integrated circuits," *IEEE Electron Device Lett.*, vol. 1, no. 10, pp. 211–213, Oct. 1980.
- [10] J.L. Autran, M. Glorieux, D. Munteanu, S. Clerc, G. Gasiot, P. Roche, "Particle Monte Carlo modeling of single-event transient current and charge collection in integrated circuits," *Microelectronics Reliability*, vol. 54, no9–10, pp. 2278–2283, 2014.
- [11] I. Plante, F.A. Cucinotta, "Monte-Carlo Simulation of Particle Diffusion in Various Geometries and Application to Chemistry and Biology," in *Theory and Applications of Monte Carlo Simulations*, Edited by V.W.K. Chan, Intech, Rijeka, Croatia, 2013, doi: 10.5772/53203.
- [12] M. Glorieux, J.L. Autran, D. Munteanu, S. Clerc, G. Gasiot, P. Roche, "Random-walk drift-diffusion charge-collection model for reverse-biased junctions embedded in circuits," *IEEE Trans. Nucl. Sci.*, vol.61, no.6, pp. 3527–3534, 2014.
- [13] G.R. Srinivasan, H.K. Tang, P. Murley, "Parameter-free, predictive modeling of single event upsets due to protons, neutrons, and pions in terrestrial cosmic rays," *IEEE Trans. Nucl. Sci.*, vol. 41, no. 6, pp. 2063–2070, 1994.
- [14] S. Martinie, T. Saad-Saoud, S. Moindjie, D. Munteanu, J.L. Autran, "Behavioral modeling of SRIM tables for numerical simulation," *Nucl. Instr. Meth. Phys. Res. B*, vol. 322, pp. 2–6, 2014.
- [15] S. Selberherr, "Simulation of Semiconductor Devices and Processes," Springer-Verlag, Wien, New York, 1984.
- [16] W. Dabrowski, "Transport equations and Ramo's theorem: applications to the impulse response of a semiconductor detector and to the generation-recombination noise in a semiconductor junction," *Progr. Quantum Electron.*, vol. 13, no. 3, pp. 233–266, 1989.

- [17] J.S. Laird, T. Hirao, S. Onoda, and H. Itoh, "High-injection carrier dynamics generated by MeV heavy ions impacting high-speed photodetectors," *J. Appl. Phys.* Vol. 98, p. 013530, 2005.
- [18] CUDA. NVIDIA, 2014. [Online]. Available: http://www.nvidia.com/object/cuda_home_new.html
- [19] J.C. Butcher, *Numerical Methods for Ordinary Differential Equations*, Wiley-Blackwell, Hoboken, New Jersey, États-Unis, 2nd edition, 2008.
- [20] C.C. Enz, F. Krummenacher, E.A. Vittoz, "An analytical MOS transistor model valid in all regions of operation and dedicated to low-voltage and low-current applications," *Analog Integr. Circuits Signal Process.*, vol.8, no.1, 1995.
- [21] M. Bucher, C. Lallement, C. Enz, F. Théodoloz, F. Krummenacher, "The EPFL-EKV MOSFET model equations for simulation," Technical Report EPFL-DE-LEG, 1998. Available online: http://ekv.epfl.ch/files/content/sites/ekv/files/pdf/ekv_v262.pdf
- [22] Ngspice, a mixed-level/mixed-signal circuit simulator. Online: <http://ngspice.sourceforge.net/>
- [23] Mentor Graphics ELDO simulator. Online: <http://www.mentor.com/>
- [24] Synopsys TCAD. Online: <http://www.synopsys.com/tools/tcad/>
- [25] J.L. Autran, S. Semikh, D. Munteanu, S. Serre, G. Gasiot, P. Roche, "Soft-error rate of advanced SRAM memories: modeling and Monte Carlo simulation," in *Numerical Simulation - From Theory to Industry*, Edited by M. Andriychuk, Intech, Vienna, Chapter 15, 2012.
- [26] J. Kauppila, A. Sternberg, M. Alles, A. Francis, J. Holmes, O. Amusan, L. Massengill, "A bias-dependent single-event compact model implemented into BSIM4 and a 90 nm CMOS process design kit," *IEEE Trans. Nucl. Sci.*, vol. 56, no. 6, pp. 3152–3157, 2009.
- [27] Measurement and Reporting of Alpha Particle and Terrestrial Cosmic Ray-Induced Soft Errors in Semiconductor Devices, JESD89A, JEDEC Solid State Technology Association Standard.
- [28] S. Uznanski, G. Gasiot, P. Roche, S. Semikh, J.L. Autran, "Combining GEANT4 and TIARA for neutron soft error-rate prediction of 65 nm flip-flops," *IEEE Trans. Nucl. Sci.*, vol. 58, no. 6, pp. 2599–2606, 2011.
- [29] S. Uznanski, G. Gasiot, P. Roche, J.L. Autran, V. Ferlet-Cavrois, "Monte Carlo based charge sharing investigations on a bulk 65 nm RHBD flip-flop," *IEEE Trans. Nucl. Sci.*, vol. 57, no. 6, pp. 3267–3272, 2010.
- [30] K. Lilja, M. Bounasser, S.-J. Wen, R. Wong, J. Holst, N. Gaspard, S. Jagannathan, D. Loveless, and B. Bhuvva, "Single-event performance and layout optimization of flip-flops in a 28-nm bulk technology," *IEEE Trans. Nucl. Sci.*, vol. 60, no. 4, pp. 2782–2788, 2013.

Computer Engineering

Training Images-Based Stochastic Simulation on Many-Core Architectures

Tao Huang and Detang Lu

Additional information is available at the end of the chapter

<http://dx.doi.org/10.5772/64276>

Abstract

In the past decades, multiple-point geostatistical methods (MPS) are increasing in popularity in various fields. Compared with the traditional techniques, MPS techniques have the ability to characterize geological reality that commonly has complex structures such as curvilinear and long-range channels by using high-order statistics for pattern reconstruction. As a result, the computational burden is heavy, and sometimes, the current algorithms are unable to be applied to large-scale simulations. With the continuous development of hardware architectures, the parallelism implementation of MPS methods is an alternative to improve the performance. In this chapter, we overview the basic elements for MPS methods and provide several parallel strategies on many-core architectures. The GPU-based parallel implementation of two efficient MPS methods known as SNESIM and Direct Sampling is detailed as examples.

Keywords: geostatistics, multiple point, stochastic simulation, training image, many-core architecture

1. Introduction

Geostatistical stochastic simulation is important for the research of geological phenomenon. In the past several decades, a large number of geostatistical methods have been developed based on the spatial covariance properties of the geological data. The traditional tool to quantify the spatial covariance is known as variogram, which measures the covariance among any two points separated by a certain distance [1]. Although variogram-based methods are successfully applied to multi-Gaussian system, they have limitations for the characterization of complex systems such as the curvilinear or long-range continuous facies [2–4]. An alternative known as multiple-

point geostatistical (MPS) simulation was proposed to produce geologically realistic structure by using high-order spatial statistics based on conceptual training images [5, 6]. The concept of training image is introduced from explicit to represent geological structures with a numeral image generated from outcrops, expert sketching, or conditional simulations of variogram-based methods. Since the training images can incorporate additional information such as the expert guesses, prior database, and physical models, besides the spatial features, the simulation using TIs is straightforward and smart [7].

Due to the ability of reconstructing geological realistic, MPS methods are gaining popularity, and various algorithms have been proposed including pixel-based algorithms [5, 8, 9], pattern-based algorithms [10–13], and optimal algorithms [14–16]. These algorithms have been applied to broad fields such as oil and gas industry [17–19], fluid prediction [20, 21], climate modeling [22]. However, some application suffers from the computational burden routinely. Since MPS methods need to scan the training image, abstract patterns, and reconstruct the patterns in the simulation grid, physical memory and running time are challenging or even unusable for large-scale or pattern-rich simulation models.

Many efforts have been made to decrease the central processing units (CPU) and RAM expense. Approaches such as multiple grid technique [23], optimization of data storage with a list structure [24], hierarchical decomposing [25], Fourier space transform [26] have been introduced, while the computational burden remains heavy for very large grids and complex spatial models.

With the development of hardware, utilization of multiple-core central processing units (CPU), or graphic processing units (GPU), for parallel applications are increasing in popularity in various fields including geostatistical simulation. In 2010, Mariethoz investigated the possibility to parallelize the MPS simulation process on realization level, path-level, or node-level and proposed a general conflict management strategy [27]. This strategy has been implemented on a patch-based SIMPAT method [28]. Parallel implementations for other geostatistical algorithms, such as the parallel two-point geostatistical simulation [29], parallel pixel-based algorithms [30], and parallel optimal algorithms [31] have been proposed constantly.

In this article, we will present the parallel several schemes of MPS simulation on many-core and GPU architectures. The Compute Unified Device Architecture (CUDA) that provides access between CPUs and GPUs is used to illustrate the parallel strategies [32, 33]. Examples of the two general MPS algorithms known as SENSIM and DS are implemented and compared [34, 35] with the original algorithms to present the ability of pattern reproduction and the improvement of computational performance.

2. Methodology

Currently, geostatistical simulations are processed with a large number of MPS algorithms using various techniques. Besides the difference in process definition and algorithmic implementation, these algorithms share similarities of the fundamental elements [36].

2.1. General framework

Generally, the overall framework of these algorithms is constructed as follows:

1. Migrate conditioning points to the corresponding grid nodes.
2. Define data template to abstract or clustering patterns from the training image.
3. Define a simulation path for the nodes to be simulated.
4. Using the conditioning data and previous simulated nodes as priori data to sample from the training image.
5. Place the sample to the simulation grid.
6. Repeat three–five until meeting the stopping criterion.

For each algorithm, one or some of the basic steps may have some identity. In this section, we will focus on the two algorithms following different theory, single normal equation simulation (SNESIM) and DS, to illustrate the application of parallel strategies on MPS simulations.

2.2. SNESIM review

The methodology of single normal equation simulation (SNESIM) is a sequential paradigm developed from the random concepts theory with the property of generating conditional distribution with local conditioning instead of global conditioning. The local conditional distribution is aggregated with the local data event. Considering a category property S with K possible states $\{s(k), k = 1, \dots, K\}$, a data template τ_n is comprised of a geometry of n vectors $\{h_\alpha, \alpha = 1, \dots, n\}$. The data event d_n centered at u is defined with the template and the corresponding n values $\{s(u + h_\alpha), \alpha = 1, \dots, n\}$. Consequently, the conditional probability of the occurrence of state s_k denoted as $\text{Prob}\{S(u) = s_k | S(u_\alpha), \alpha = 1 \dots n\}$ or $\text{Prob}\{S(u) = s_k | d_n\}$ is defined following Bayes' theorem:

$$\text{Prob}\{S(u)=s_k|d_n\} = \frac{\text{Prob}\{S(u)=s_k \text{ and } d_n\}}{\text{Prob}\{d_n\}} \quad (1)$$

Where $\text{Prob}\{d_n\}$ and $\text{Prob}\{S(u) = s_k \text{ and } d_n\}$ are the probability of the occurrence of d_n and the associated to a central value $S(u) = s_k$ respectively. In practice, this probability can be obtained by counting the number of replicates of the training image, which is calculated by:

$$\text{Prob}\{S(u)=s_k|d_n\} = \frac{c_k(d_n)}{c(d_n)} \quad (2)$$

$c\{d_n\}$ is the number of replicates of the conditioning data d_n , and $c_k\{d_n\}$ is the number of replicates inferred from $c_k(d_n)$ of which the central node $S\{u\}$ has a value of $s(k)$.

To reduce the computational burden of scanning the training image, SNESIM analyzes the training image and constructs a search tree to store all the patterns before sequential simulation. Then the same data template is used to aggregate the local distribution of the simulation grid for sampling values from the data base to the simulation grid.

The implementation of SNESIM algorithm is shown in **Figure 1**.

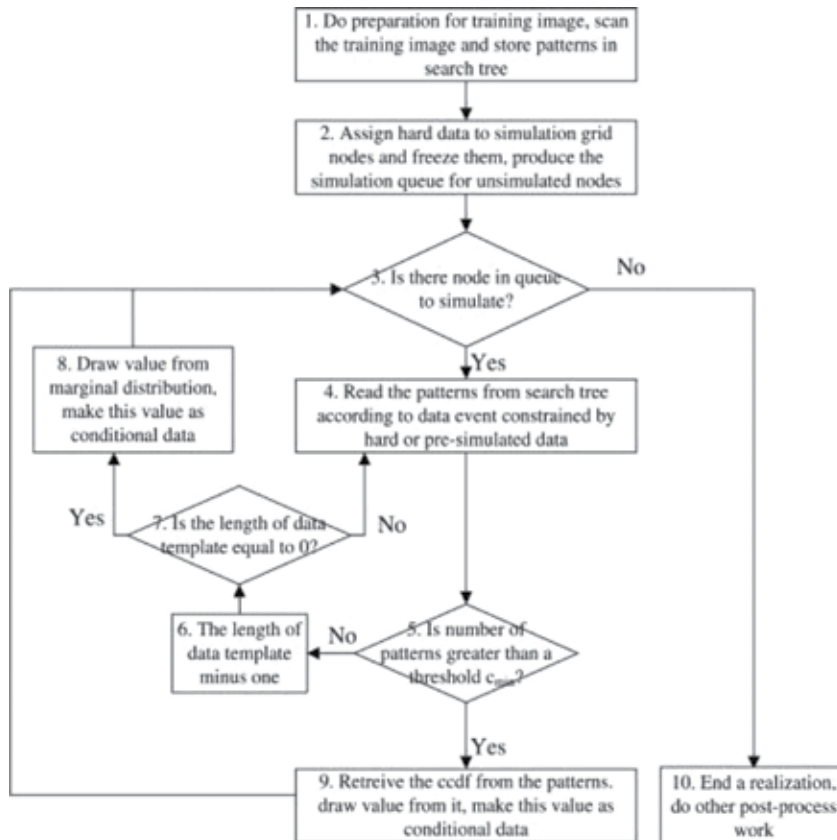


Figure 1. Flowchart for SNESIM process.

As described, the memory consumption is largely related to the size of data template and the pattern richness of the training image. At the same time, the pattern retrieving time also increases for the complex cases. To address this problem, a GPU-based parallel method is proposed in the following section.

2.3. Direct Sampling review

Direct Sampling is a novel MPS technique that borrows ideas from a sampling method introduced by Shannon totally abandoning the conditional probability approach. Instead of the conditional distribution, a measurement distance is used to calculate the similarity between

the local conditioning and the data event got from the training image along a random path. The distance method enables the application to both categorical and continuous variables. During the sequential simulation, for each node to be simulated in the simulation grid, the training image is scanned along a circular unilateral path [37] and the distance is calculated. As long as the distance is smaller than the defined threshold, the current data event in the training image is sampled, and the central value is assigned to the node to be simulated in the simulation grid directly. The flowchart of Direct Sampling is shown in **Figure 2**.

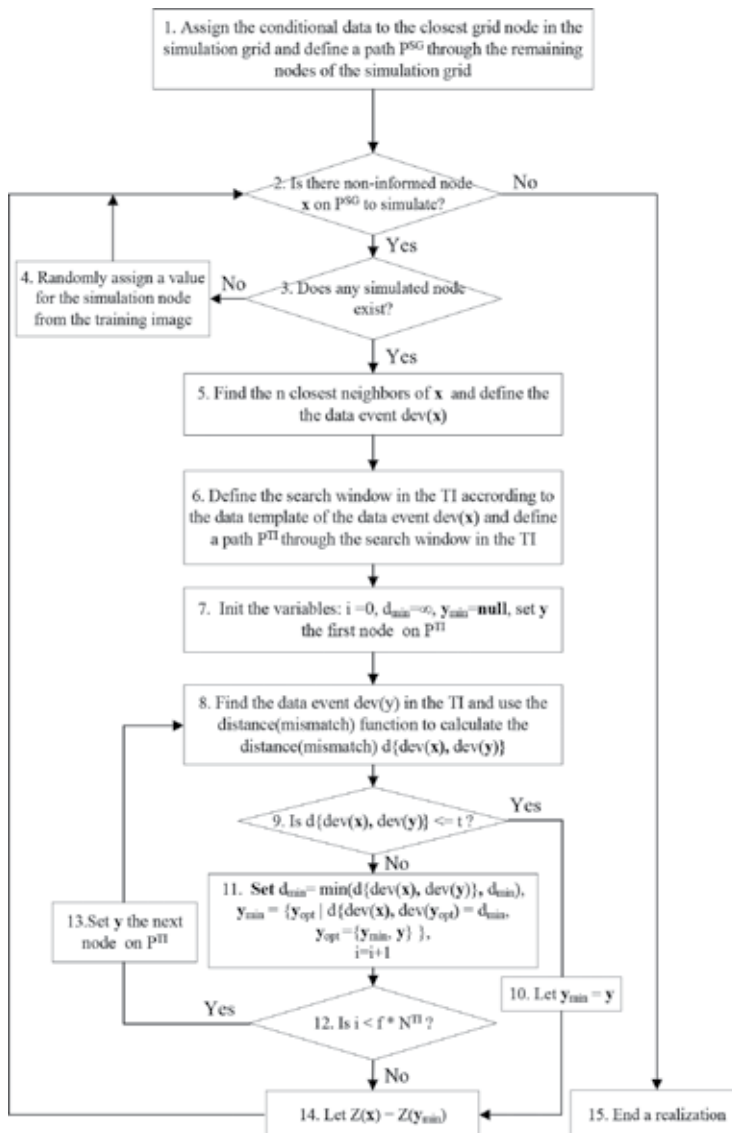


Figure 2. Flowchart for Direct Sampling process.

Since this method does not need to store patterns, it releases the memory intensity; on the other hand, parameter is the key factor for Direct Sampling.

There are three main input parameters:

1. Maximum number of closest neighbors n , namely, the size of data template of SNESIM.
2. The distance threshold t . A value of $t = 0$ means a trend of verbatim copy of the training and the increasing value introduce more variabilities between realizations in pattern reproduction.
3. The fraction of scanned TI f . The fraction is defined to stop the process of scanning the training image while no distances are under the threshold. If the percentage of nodes in the training image reach f , the scanning stops and the pattern with lowest distance is sampled.

Sensitivity analysis of parameters [38] shows trade-offs between the quality of realizations and the CPU times.

3. Many-core architectures

3.1. Overview

A computing component that featured with two or more processing units to execute program instructions independently is known as a multicore processor. With the ability of running multiple instructions at the same time, multicore processors increase overall speed for many general-purpose computing. Currently, adding support for more execution threads is the norm avenue to improve the performance of high-end processors. The many-core architectures are formed by manufacturing massive multicores on a single component. For general-purpose parallel computing, many-core architectures on both the central processing unit (CPU) and the graphics processing unit (GPU) are available for different tasks.

Compared with a many-core CPU architecture known as a supercomputer, the general GPU has many more cores, which are constructively cheap and suitable for intensive computing.

3.2. GPU and CUDA

Originally, a GPU is a graphic card attached with a cluster of streaming processors aimed at graphic-oriented details that needs the ability of extremely fast processing of large-volume data sets. To apply the special-purpose GPU to general-purpose application, NVIDIA provides a user-friendly development environment that is Compute Unified Device Architecture (CUDA). The CUDA platform enables the generation of parallel codes on GPUs by driving the process from the CPU to GPU. A CUDA program is a unified code that consists of executions on both the host (CPU) and the device (GPU) by CUDA kernel functions that are called out from the host to the device for asynchronously execution. The massive parallelism is carried out in each kernel on CUDA threads that are the basic executing units on the GPU. The CUDA

provides an interface named Peripheral Component Interconnect Express (PCI-e) for the intercommunication between host and device and shared memory for synchronization among the parallel threads. The general architecture of CUDA and CUDA memory is illustrated in **Figures 3 and 4**. More details could be referred from the Guides of NVIDIA.

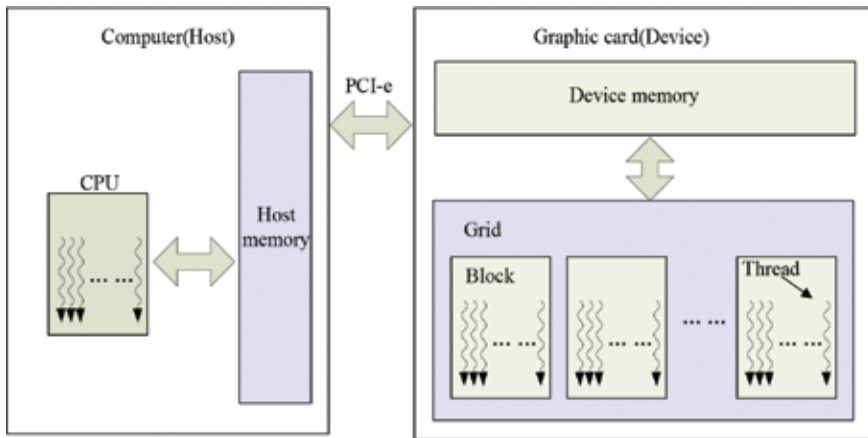


Figure 3. The general architecture of CUDA.

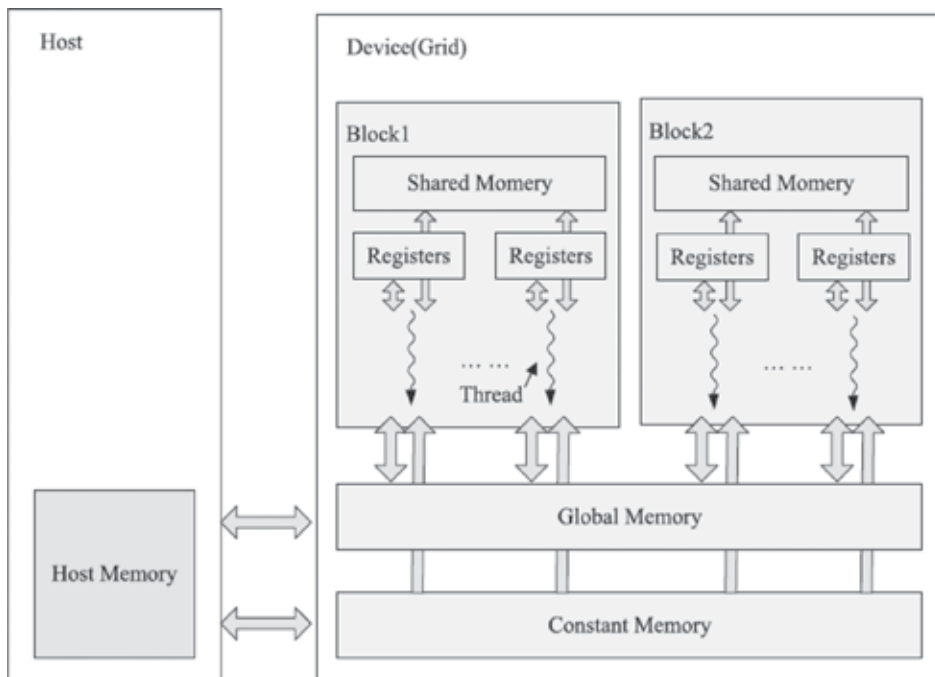


Figure 4. CUDA device memory organization.

4. Parallel strategies

Generally, there are three strategies to implement the parallelism of MPS algorithms, that is, realization-level, path-level, and the node-level parallelization. The bottleneck for large-scale application focuses on the millions' of nodes in the training image and simulation grids. So we present two parallel implementations on node-level for SNESIM and on both node-level and path-level for Direct Sampling in this section.

4.1. GPU-based SNESIM implementation

In 2013, a node-level parallelization was applied to SNESIM algorithm and achieved significant performance improvement [34]. The overall parallel scheme is illustrated in **Figure 5**.

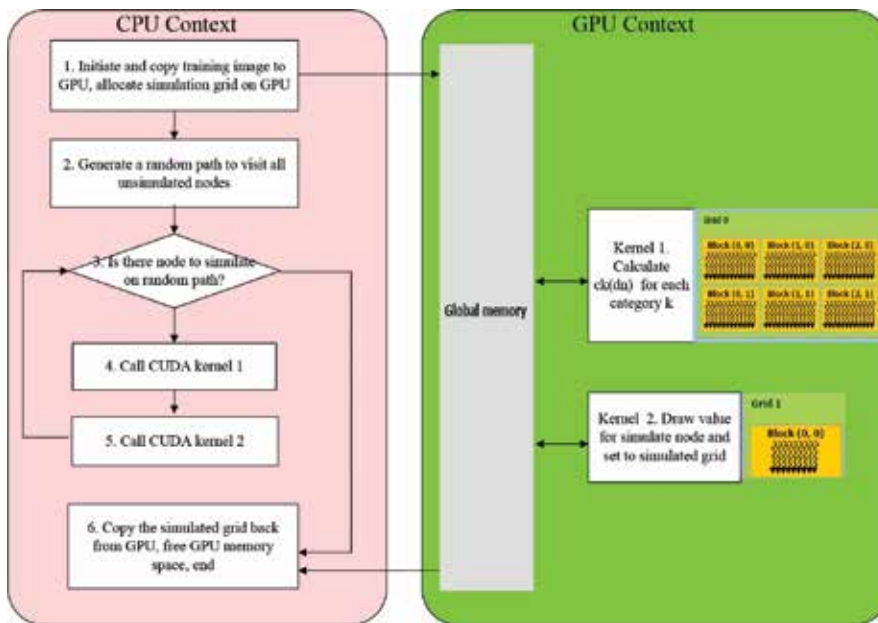


Figure 5. Procedure of GPU-based SNESIM implementation.

By transferring the training image and simulation grid from the CPU to GPU, each node is assigned to a CUDA thread. For each unsimulated node along the random simulation path, Kernel 1 compares each value of the given data template d_n with every central nodes in the training image simultaneously and returns the number of replicates $c_k(d_n)$ for each stage k . With these outputs, Kernel 2 calculates the conditional cumulative distribution function (CCDF) and uses Monte Carlo sampling to draw a value to this node. Repeat the kernels along a random path until all the nodes in the simulation grid are simulated. Transfer the results from GPU to CPU.

Since the most time-consuming part, that is getting data event for each node, is parallelized in Kernel 1, this GPU-based implementation gains significant speedup. Moreover, in contrast with the increasing physical memory demanding along the template sizes of original implementation, the proposed GPU implementation fixes the amount of memory.

4.2. GPU-based Direct Sampling implementation

Similar parallelization could also be applied to the Direct Sampling algorithm. Besides the parallelism of the data template, the searching fraction could also be parallelized. The two-stage parallel scheme was implemented in 2013 [35]. The procedure of the GPU-based implementation is illustrated in Figure 6.

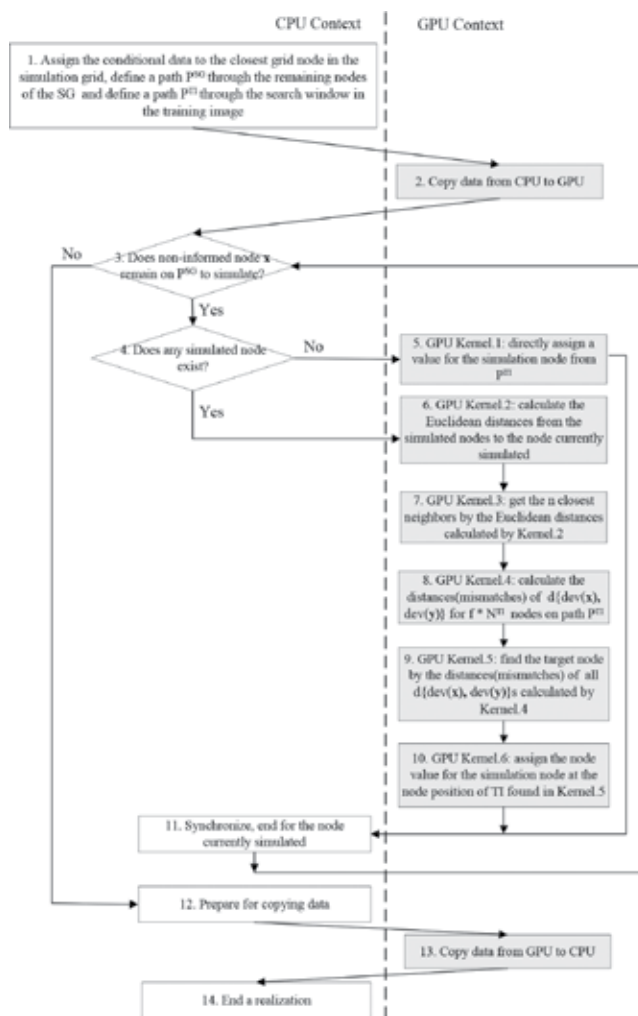


Figure 6. Procedure of GPU-based Direct Sampling implementation.

As described, there are three important parameters controlling the simulation of Direct Sampling, that is t , n , and f . This scheme implements the parallelism on two of the three parameters that is n and f .

4.2.1. Parallelism of n

The number of neighbor is the n closest previously simulated nodes to define a data template. Different from the data template used in SNESIM that is controlled by the predefined geometry, the data templates consisted of the n closest simulation nodes and have the flexibility of adaption shape and searching range. Due to these flexibilities, this approach can directly catch large-scale structures and easily condition to hard data. On the other hand, the searching for the n neighbors is also the most time-consuming part in the serial implementation.

The parallelism of n is achieved in Kernel 2 and Kernel 3. In Kernel 2, each previously simulated node is allocated to a CUDA thread and calculates the Euclidean distance to the node to be simulated simultaneously. These distances are transferred to Kernel 3 and sorted using a parallel sorting algorithm.

4.2.2. Parallelism of f

In the serial program if the similarity-distance between data events of the simulation grid and the one sampled from the current training image node is higher than the threshold, a new central node will be sampled from the training image along a random path. Most nodes of the training image that may be visited is defined as $f \times N^{TI}$, as a result, large amount of data event will be sampled in large-scale 3-days simulations.

The parallelization of f is implemented in Kernel 4 that allocates $f \times N^{TI}$ threads to $f \times N^{TI}$ central nodes in the training image using a unique random path denoting each node. Thus these similarity distances are calculated simultaneously. There are two possibilities for the similarity distance and the data sampling strategy is shown as follows:

1. There are values lower than the threshold t , choose the one that has the smallest path index from the data events with a lower distance.
2. There are no values lower than the threshold t , choose the one that has the smallest path index from the data events with the lowest distance.

Finally, the central value of the chosen data event is assigned to the simulation grid by Kernel 6. Repeat all these kernels until all the nodes in the simulation grid are simulated.

5. Experiments

In this section, the performance of the GPU-based implementations is compared with that obtained using SGeMS software [39]. A computer with 4 GB main memory, Intel Core i3540 3.07 GHz CPU, and NVIDIA GeForce GTX 680 GPU that contains eight streaming multiprocessors with 192 CUDA Cores/MP and 2 GB device memory is used for the simulation. The

programming platform is the NVIDIA driver version 301.42 with CUDA version 4.2 implemented on VS2010 using C++.

To test the performance of the GPU-based SNESIM algorithm, a 2D porous slice image obtained by CT scanning is used as the training image. The 200×200 pixels training image and the corresponding histogram for background and the pore are shown in **Figure 7**.

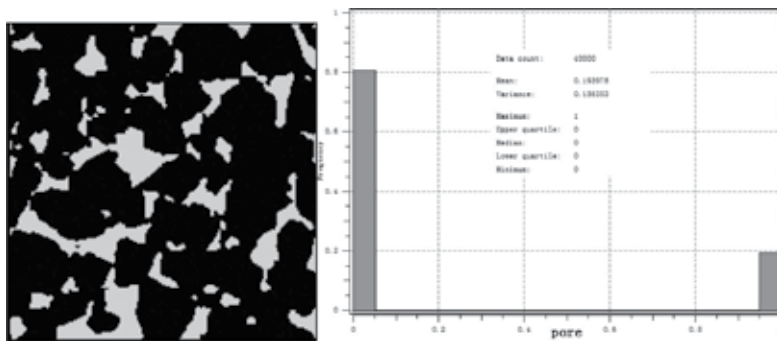


Figure 7. Training image of porous slice and the Histogram.

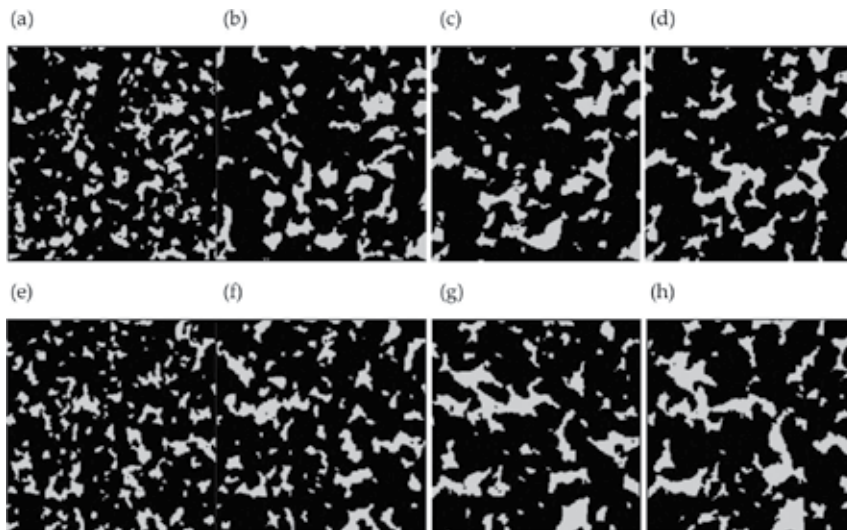


Figure 8. SNESIM realization using CUP and GPU. (a)–(d) CPU-based realizations with the number template equals 50, 120, 200 and 350, respectively; (e)–(h) GPU-based realizations with the number template equals 50, 120, 200 and 350, respectively.

Realizations of the same size as the training image using data template of 50, 120, 200, and 350 nodes are generated for each simulation. The realizations generated with CPU and GPU are shown in **Figure 8**. The average variograms for each simulation are shown in **Figure 9a**, and

the performance is shown in **Figure 9b**. The results show that the proposed GPU-based algorithm can generate similar realizations as the original algorithm, whereas significantly increases the performance. The speedup ranges from six to 24 times depending on the template size than a larger template size resulting in a larger speedup.

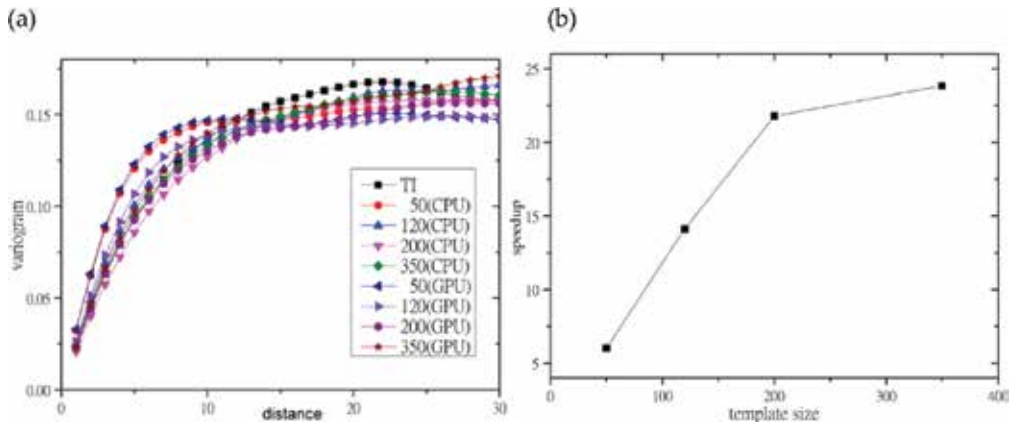


Figure 9. Results and performance comparison between the CPU and GPU implementation. (a) Variogram of the training image and the average variogram of the realizations of **Figure 8** and (b) speedup obtained by using the GPU-based parallel scheme.

The performance of the GPU-based Direct Sampling algorithm is also compared with the original algorithm on a 100×130 by 20 fluvial reservoir training image as shown in **Figure 10**.



Figure 10. A 100×130 by 20 fluvial reservoir training image.

Parameter sensitivities are analyzed on $n = 30, 50, 100, 200, f = 0.005, 0.01, 0.02, 0.05$, and $t = 0.01, 0.02, 0.05, 0.1$, respectively, with which reasonable realizations are generated. The performance times are shown in **Figure 11**.

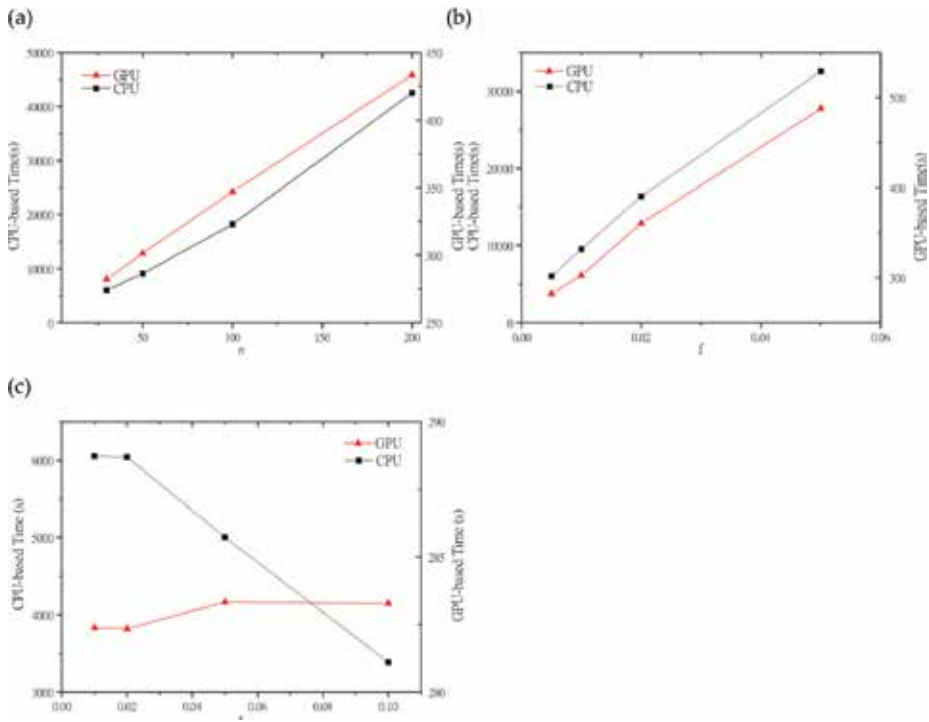


Figure 11. Performance comparison. (a) Performance with fixed $t = 0.2$, $f = 0.005$ and varying $n = 30, 50, 100$, and 200 ; (b) performance with fixed $n = 30$, $t = 0.02$ and varying $f = 0.005, 0.01, 0.02$, and 0.05 ; (c) performance with fixed $n = 30$, $f = 0.005$ and varying $t = 0.01, 0.02, 0.05$, and 0.1 .

The results show that GPU-based implementation significantly improves the performance for all the tests. Moreover, the sensitivity of parameters to performance is alleviated with the parallel scheme. The time difference is around 200 s for n and f and almost none for t for the GPU-based implementation, whereas it can be as large as several magnitudes for the CPU-based implementation.

In summary, both the presented GPU-based parallel schemes for SNESIM and Direct Sampling achieve significant speedups, especially for large-scale simulations with their node-level parallelism strategy. Moreover, the parallel implementations are insensitive to parameters that are the key points not only for performance but also for simulation results implying for better results in application. These strategies could be further improved with other parallel optimization methods as well. In fact, besides the node-level parallel schemes for SNESIM and Direct Sampling, various parallelisms have been proposed and new optimizations are keeping introduced aimed at further improvements. Up to now, almost all kinds of MPS algorithms could be implemented on a parallel scheme. Many-core architectures are the current main-streams to improve the performance of extremely massive computing tasks. The developing of computer hardware and parallel interface techniques promise the wider and wider utilization of high-performance parallelization. These parallel schemes of training images-based stochastic simulations approve the application to high-resolution and large-scale simulations.

Acknowledgements

This work was financially supported by the CAS Strategic Priority Research Program under Grant XDB10030402 and the CNPC-CAS Strategic cooperation Research Program (2015A-4812) and the Fundamental Research Funds for the Central Universities (WK2090050038).

Author details

Tao Huang and Detang Lu

*Address all correspondence to: thwang@ustc.edu.cn

University of Science and Technology of China, Hefei, Anhui, China

References

- [1] Goovaerts, P. Geostatistical tools for characterizing the spatial variability of microbiological and physico-chemical soil properties. *Biology and Fertility of Soils*. 1998; 27(4): 315–334.
- [2] Journel, A.G., *Geostatistics: Roadblocks and Challenges*, in *Geostatistics Tróia '92: Volume 1*, A. Soares, Editor. 1993, Springer Netherlands: Dordrecht. p. 213–224.
- [3] Krishnan, S., Journel, A.G. Spatial connectivity: from variograms to multiple-point measures. *Mathematical Geology*. 2003;35(8):915–925.
- [4] Journel, A.G., *Beyond Covariance: The Advent of Multiple-Point Geostatistics*, in *Geostatistics Banff 2004*, O. Leuangthong and C.V. Deutsch, Editors. 2005, Springer Netherlands: Dordrecht. p. 225–233.
- [5] Strebelle, S., Journel, A.G. Sequential simulation drawing structures from training images. *Geostatistics Capetown 2000*. pp. 381–392.
- [6] Strebelle, S., Conditional simulation of complex geological structures using multiple-point statistics. *Mathematical Geology*. 2002;34(1):1–21.
- [7] Hu, L., Chugunova, T. Multiple-point geostatistics for modeling subsurface heterogeneity: a comprehensive review. *Water Resources Research*. 2008;44(11):W11413.
- [8] Mariethoz, G., Renard, P., Straubhaar, J., The Direct Sampling method to perform multiple-point geostatistical simulations. *Water Resources Research*. 2010;46(11):1–14.

- [9] Mustapha, H., Dimitrakopoulos, R., HOSIM: a high-order stochastic simulation algorithm for generating three-dimensional complex geological patterns. *Computers & Geosciences*. 2011;37(9):1242–1253.
- [10] Arpat, G.B. *Sequential Simulation with Patterns*. Ph.D. Dissertation. Stanford [dissertation]. Stanford, CA; 2005. 166 p.
- [11] Zhang, T., Switzer, P., Journel, A. Filter-based classification of training image patterns for spatial simulation. *Mathematical Geology*. 2006;38(1):63–80.
- [12] Tahmasebi, P., Hezarkhani, A., Sahimi, M. Multiple-point geostatistical modeling based on the cross-correlation functions. *Computational Geosciences*. 2012;16(3):779–797.
- [13] Mahmud, K., Mariethoz, G., Caers, J., Tahmasebi, P., Baker, A. Simulation of Earth textures by conditional image quilting. *Water Resources Research*. 2014;50(4):3088–3107.
- [14] Deutsch, C., Wen, X. Integrating large-scale soft data by simulated annealing. *Mathematical Geology*. 2000;32(1):49–67.
- [15] Caers, J.K., Srinivasan, S., Journel, A.G. Geostatistical quantification of geological information for a fluvial-type North Sea reservoir. *SPE Reservoir Evaluation & Engineering*. 2000;3(5):457–467.
- [16] Srivastava, M. An overview of stochastic methods of reservoir characterization. *AAPG Computer Applications in Geology*. 1995; Tulsa:3–16.
- [17] Okabe, H., Blunt, M.J. Pore space reconstruction using multiple-point statistics. *Journal of Petroleum Science and Engineering*. 2005;46(1):121–137.
- [18] Zhang, T., Bombarde, S., Strebelle, S., Oatney, E. 3D porosity modeling of a carbonate reservoir using continuous multiple-point statistics simulation. *SPE Journal*. 2006;11(3): 375–379.
- [19] Falivene, O., Arbus, P., Gardiner, A., Pickup, G., Muoz, J.A., Cabrera, L. Best practice stochastic facies modeling from a channel-fill turbidite sandstone analog (the Quarry outcrop, Eocene Ainsa basin, northeast Spain). *AAPG Bulletin*. 2006;90(7):1003–1029.
- [20] Hiroshi O, Blunt M J. Pore space reconstruction of vuggy carbonates using microtomography and multiple-point statistics[J]. *Water Resources Research*, 2007, 43(12): 179–183.
- [21] Tahmasebi P., Sahimi M. Cross-correlation function for accurate reconstruction of heterogeneous media. *Physical Review Letters*. 2013;110(7):078002
- [22] Jha, S.K., Mariethoz, G., Evans, J.P., McCabe, M.F. Demonstration of a geostatistical approach to physically consistent downscaling of climate modeling simulations. *Water Resources Research*. 2013;49(1):245–259.

- [23] Strebelle, S. New multiple-point statistics simulation implementation to reduce memory and cpu-time demand. In: Conference of the international association for mathematical geology. September; Portsmouth, UK. 2003.
- [24] Straubhaar, J., Renard, P., Mariethoz, G., Froidevaux, R., Besson, O. An improved parallel multiple-point algorithm using a list approach. *Mathematical Geosciences*. 2011;43(3):305–328.
- [25] Maharaja, A., Journel, A.G. Hierarchical Simulation of Multiple-Facies Reservoirs Using Multiple-Point Geostatistics. SPE Annual Technical Conference and Exhibition. Society of Petroleum Engineers, Dallas, Texas. 2005
- [26] Tahmasebi, P., Sahimi, M., Caers, J. MS-CCSIM: accelerating pattern-based geostatistical simulation of categorical variables using a multi-scale search in Fourier space. *Computers & Geosciences*. 2014;67:75–88.
- [27] Mariethoz, G. A general parallelization strategy for random path based geostatistical simulation methods. *Computers and Geosciences*. 2010;36(7):953–958.
- [28] Tahmasebi, P., Sahimi, M., Mariethoz, G., Hezarkhani, A. Accelerating geostatistical simulations using graphics processing units (GPU). *Computers & Geosciences*. 2012;46:51–59.
- [29] Nunes, R., Almeida, J.A. Parallelization of sequential Gaussian, indicator and direct simulation algorithms. *Computers and Geosciences*. 2010;36(8):1042–1052.
- [30] Straubhaar, J., Renard, P., Mariethoz, G., Froidevaux, R., Besson, O. An improved parallel multiple-point algorithm using a list approach. *Mathematical Geoscience*. 2011;43(3):305–328.
- [31] Peredo, O., Ortiz, J.M., Parallel implementation of simulated annealing to reproduce multiple-point statistics. *Computers and Geosciences*. 2011;37(8):1110–1121.
- [32] Nvidia, C. C Programming Guide v 4.0. Santa Clara, CA, USA: NVIDIA Corporation; 2011.
- [33] Nvidia, CUDA C Best Practices Guide Version 4.0. Technical report. Santa Clara, CA, USA: NVIDIA Corporation; 2009.
- [34] Huang, T., Lu, D.T., Li, X., Wang, L. GPU-based SNESIM implementation for multiple-point statistical simulation. *Computers & Geosciences*. 2013;54:75–87.
- [35] Huang, T., Li, X., Zhang, T., Lu, D.T. GPU-accelerated Direct Sampling method for multiple-point statistical simulation. *Computers & Geosciences*. 2013;57:13–23.
- [36] Mariethoz, G., Caers, J. Multiple-point geostatistics: stochastic modeling with training images. John Wiley & Sons, Ltd, Chichester, UK; 2014.

- [37] Daly, C. Higher order models using entropy, Markov random fields and sequential simulation. In: Leuangthong, O., Deutsch, C. (Eds). In: *Geostatistics Banff 2004*; Springer Netherlands; 2005. p. 215–224.
- [38] Pirot, G., Meerschman, E., Mariethoz, G., Straubhaar, J., Van Meirvenne, M, Renard, P. Optimizing Direct Sampling algorithm's parameters to performing multiple-points geostatistical simulations. *AGU Fall Meeting Abstracts*. 2011;1:1475.
- [39] Remy, N., Boucher, A., Wu, J., editors. *Applied Geostatistics with SGeMS: A User's Guide*. Cambridge University Press, Cambridge, UK; 2008.

Materials and Metallurgical Engineering

Numerical Simulation of Laser Processing Materials: An Engineering Approach

Guillaume Savriama and Nadjib Semmar

Additional information is available at the end of the chapter

<http://dx.doi.org/10.5772/63945>

Abstract

The following chapter aims at giving an overview of the use of numerical simulation in the field of laser processing. Indeed, the past two decades saw an increasing demand for lasers in various areas such as healthcare, microelectronics, cartography, optoelectronics, aeronautics, etc. Thus, the comprehension of the laser-material interaction and the removal mechanism became primordial to predict and improve the efficiency of a process. After a nonexhaustive literature review, two simulation approaches (Finite Element and Design Of Experiment, DOE) will be presented to demonstrate the importance of numerical simulation in laser applications.

Keywords: laser machining, multiphysics simulation, design of experiment

1. Introduction

As diverse as laser applications are, they have one thing in common: the complexity of the interaction of photons with matter and the multiphysics nature of the phenomena (thermal, fluidic, optical, mechanics, etc.) involved during laser processing whether it is drilling [1], grooving [2], cutting [3], welding [4], estimating ablation threshold limits [5] or simply predicting the thermal effects on the material [6]. Several mechanisms can be involved before, during and after the material ejection and they strongly depend on the laser characteristics (wavelength, pulse duration, beam shape, polarization, etc.) and the process parameters (scanning speed, repetition rate, pulse energy, etc.). The development in computer sciences (calculation capability and software) gave the opportunity to better understand the preponderance or the concomitance of mechanisms depending on the application and the objective of the researcher. Moreover, given the dynamic and short time-scale nature of the laser

process, numerical simulation can give an insight of what is happening inside the workpiece, which is delicate by experimental means.

Multiphysics packages such as ANSYS, ABAQUS, ADINA, or COMSOL are effective for the aforementioned issue and for fundamental investigation. In the industry, another semiempirical modeling method is useful when direct answers are expected regarding parameters optimization, predicting the system behavior or analyzing the effect of a modification. The Design Of Experiment (DOE) methodology shows its efficiency especially when the experimental investigation suffers from constraints such as the availability of the device, the experimenter, the material, the risks, the costs, or the environment.

Although nonexhaustive, a list of laser applications and how they were modeled will be presented in the following parts. Multiphysics models will be presented first, followed by the DOE approach. A laser application will be discussed for both types of numerical simulations.

2. Multiphysics simulation of laser processing

2.1. Introduction

In general, for a solid, the laser ablation process strongly depends on the absorption of photons by the material. Hence, it relies on the laser wavelength, its pulse duration, its fluence (energy density per surface area), and also on the material properties. The photon energy is absorbed and converted into kinetic energy by vibration of the electron cloud. This energy is then transmitted to the volume by phonon-electron coupling [7, 8]. Above picosecond pulse duration, a laser beam can be treated as a heat source. Hence, whether it is drilling, cutting, welding..., a laser process can be seen as a thermodynamic problem and the classical heat transfer equation (Eq. (4)) can be used to determine the spatial and temporal distribution of the temperature in the workpiece. Then for advanced studies, the Navier-Stokes equations can be implemented when phase transition is involved (Eq. (2)). The final thermo-mechanical state of the substrate or the plasma generation during laser ablation and its effect on the efficiency of the laser process can be investigated as well.

To be precise, there should be one equation describing the temperature evolution for the electron network and another one for the ions lattice (Section 2.3.1). Indeed, the characteristic time of energy transfer between electrons and ions is between 0.1 a few ps. For pulse duration longer than 500 fs, electrons and ions are both heated during the laser pulse. Hence, one equation is sufficient. Below 500 fs, the lattice is poorly affected because it is decoupled with the electrons and two equations are required [9]. However, as seen in the literature, one temperature model could be used to describe glass welding [10] or the formation of waveguides with femtosecond laser when high frequency is used (hundreds of kHz to MHz range) [11]. After a short review of the use of multiphysics simulation, the heat transfer model will be detailed and will lead to the investigation of picosecond laser induced periodic surface structuring (LIPSS) on copper film.

2.2. Laser applications and their simulation in the literature

2.2.1. Laser welding

One of the main processes to be modeled is probably laser welding since it is widely used in various industries. Laser is contactless, repeatable, automated, generates low distortion due to heat, and generates high throughput. The main concern for the manufacturer is the quality of the weld, which is characterized by the geometry of the bead (the bead width and the depth of penetration of the weld) and also the tensile strength of the joint. The bead geometry is directly linked to the laser parameters which will determine how and what quantity of material is melted. Moreover, the heating and cooling cycle can be analyzed and this is relevant for the study of residual stresses and more importantly for the mechanical strength of the joint.

This kind of analysis is performed by Balasubramanian et al. [12], for instance, during the study of laser welding of AISI304 stainless steel sheet with the finite element method (FEM) package SYSWELD. A 3D conical Gaussian beam was modeled, thermal dependency of material properties was taken into account, and the laser was a solid-state Nd:YAG operating in CW (continuous wave) mode. The important part was about the Gaussian beam, which had to be modeled according a specific way to take into account the high depth/width aspect-ratio of a welding process. Former models would use a simple coefficient $0 < A < 1$ for the surface absorptivity and it would underestimate the penetration depth of the weld because it is a volume process and not a surface process. Also, the thermal property dependency with temperature is important for the thermal diffusion and therefore the final analysis of the HAZ and the weld depth. Satisfactory results were obtained since the standard deviation between the experimental weld pool geometry and the simulation one was 4.54%. The laser parameters were a laser power of 1250 W, a scanning speed of 750 mm/min, and a beam angle of 90° (Figure 1).

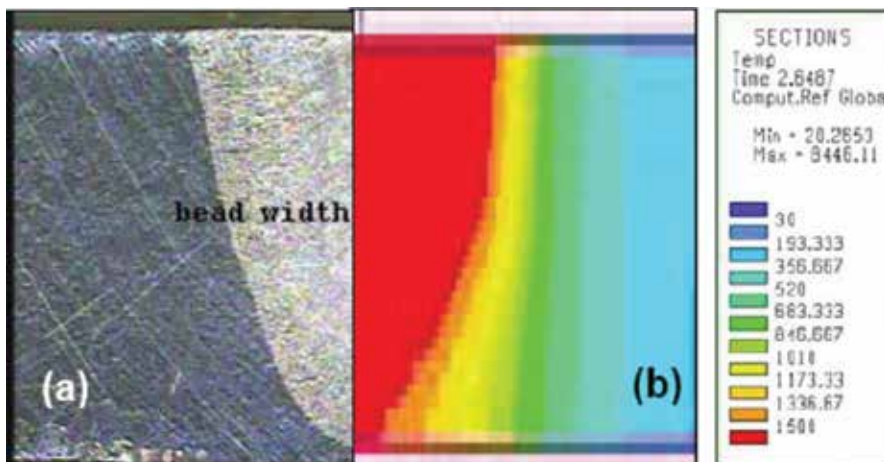


Figure 1. Comparison of fusion zone. (a) Microstructure image, (b) FEM analysis [12].

2.2.2. Laser ablating process

Andreas Otto et al. went a step further with the integration of fluid dynamics [1]. They wanted to discuss the dynamics of the process such as welding or evaporative cutting (keyhole/melt pool oscillations and vapor flows) with the help of simulation. They combined the use of OpenFOAM (Open Field Operation and Manipulation) and COMSOL simulation to do so. OpenFOAM was used to solve the fluid dynamics part by the means of Volume Of Fluid (VOF) approach. Automatic remeshing is also implemented to cope up with material deformation during melting and evaporation. The VOF method is used to track the deforming surfaces and open boundaries. A fraction function is defined and is set at zero when the computational cell is only solid and increases (up to 1) as the cell is filled with liquid. In this chapter, the VOF method was adjusted so that vapor flow could be evaluated as well. Indeed, a compression algorithm for cells marked as vapor is activated by default in the software and causes discontinuities in the fraction function and thus in the resulting tracing of the interfaces. The position of the boundary relative to the mesh can be tracked by the Level Set method. This method also uses a tracking variable, but on the entire domain this time. However, VOF is preferred as the mass of the traced cell is conserved. The electromagnetic wave propagation (laser beam propagating inside the material and potential vapor formed during laser ablation) and thermo-mechanical part were simulated with COMSOL (finite element method, FEM). It is also used to couple the equations.

The fluid dynamics is modeled according to the Navier-Stokes equation (Eq. (2)). The fluid is assumed to be incompressible as its speed does not exceed half of the sound velocity. However, vapor is compressible and a mixed model is planned for future investigation. Mass conservation is assumed (Eq. (1)).

$$\frac{\partial \rho}{\partial t} + \nabla \rho \bar{u} = 0 \text{ (mass conservation equation)} \quad (1)$$

$$\rho \frac{\partial \bar{u}}{\partial t} + \rho \bar{u} \nabla \bar{u} = -\rho \nabla P + \eta \Delta \bar{u} \text{ (Navier-Stokes)} \quad (2)$$

$$P_0 + P_v + P_L = 2K\sigma \quad (3)$$

where ρ is the material density, t is the time variable, u is the velocity field, P_0 is the atmospheric pressure, P_v is the vapor pressure, P_L is the pressure in the liquid that interacts with the surface tension σ caused by the curvature K of the metal surface. The surface tension depends on the fluid temperature and is also important for tracking the interface deformation.

The temperature appears in the vapor pressure equation and thus in the Navier-Stokes equation (Eq. (2)). It needs to be coupled with the heat transfer equation (Eq. (4)) that will describe the temperature variation during laser irradiation. The temperature variation will

have an effect on the fluid flow as understood from Navier-heat transfer equation coupling. As mentioned before, in this case, the laser beam can be modeled as a heat source Q :

$$\frac{\partial \rho H}{\partial t} - \nabla k \nabla T + \nabla \rho \bar{u} H = Q \quad (4)$$

$$H = L + C_p \times T \quad (5)$$

where T is the temperature, C_p is the heat capacity, k is the heat conductivity, H is the total enthalpy, and L is the latent heat of phase change. L is adjusted step by step by comparing the new result with the previous one until the difference is lower than a defined threshold (it takes approximately 5–10 iteration steps with L being neglected at first). Eq. (5) is thus used to evaluate the mass flow which is implemented as an input in the Navier-Stokes equation to simulate the fluid flow.

Important observations were made. For a deep welding process for instance, it is known that the melt pool will oscillate and cause keyhole width variation and porosity might appear depending on laser parameters and render the joint more fragile. The simulation reveals that waves of molten material run down the front of the keyhole. They cause a periodical modification of the keyhole diameter (keyhole oscillations). The liquid is accelerated around the keyhole. At about two thirds of the length of the melt pool, the liquid hits the backflow from the back of the melt pool and turbulences are observed in the lower rear part. On the other hand, the flow pattern is more laminar in the upper part of the melt pool. It causes the melt flow to change direction and reclose the keyhole. At higher scanning speeds, the simulation reveals the formation of pores.

For ablative processes (**Figure 2**) such as cutting, drilling, or structuring, it was found that droplets would be expelled from the groove in a periodical way while using laser intensities above 10^8 W/cm².

The same authors studied the effect of the laser wavelength on the dynamics of a welding process [13]. Indeed, the temperature variation of the material depends on the absorption of the laser beam. The propagation of the beam also depends on the topology changes during melting and evaporation. Changes of propagation and absorption will impact the attenuation or amplification of the keyhole instabilities discussed previously. The pore formation (and thus the weld quality) depends on these oscillations and on the recoil pressure exerted on the weld pool when the material is evaporated. In order to study the beam absorption effect on the welding quality, they used a CO₂ laser operating at a wavelength of 10.6 μm and a Nd:YAG laser operating at 1.064 μm. The feed rate was fixed at 0.1 mm/s, the laser power at 4.2 kW, and the beam radius at 200 μm. Compared to the previous model, the heat source term was modified so that Fresnel equations were taken into account. They took into account the absorption dependency on wavelength, angle of incidence, and polarization of the beam. It was found that oscillations are strongly influenced by fluctuations at the keyhole front for a wavelength of 1.064 μm. At 10.6 μm, most of the laser energy is absorbed at the keyhole front,

provided that the surface of the molten steel is parallel to the incident laser beam. The absorption is reduced when parts of the keyhole front are nearly normal to the incident laser beam.

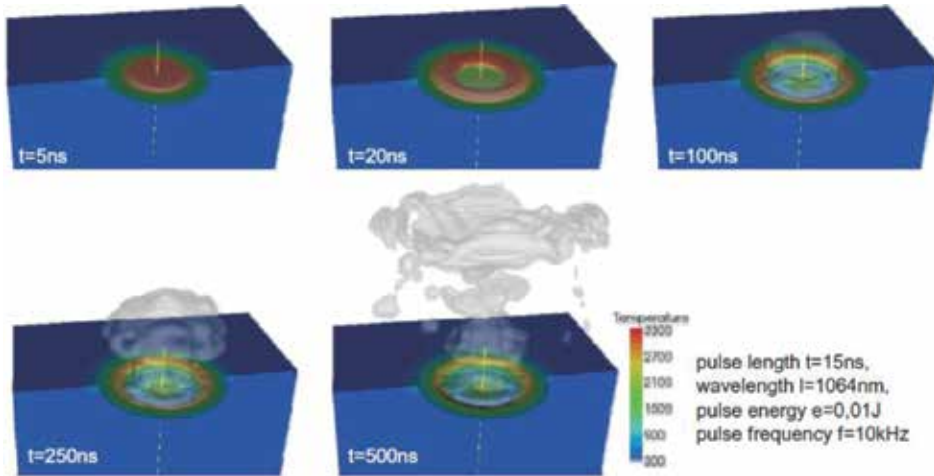


Figure 2. Simulation of laser beam drilling with short pulsed lasers [1].

The same kind of model coupling the heat transfer and the Navier-Stokes equations is used by other authors [14, 15]. In Ref. [14], the convection induced by the surface state and volume force is represented using the Boussinesq approximation (which states that the fluid is partially incompressible). The Marangoni effect (surface tension gradient depends on temperature gradient) was also taken into account. In Ref. [15], the Marangoni effect is neglected and the melt pool is considered as an incompressible fluid. The Level Set method is chosen as it is said to be efficient in treating the complex changes at the interfaces. Thus, it can model more easily the pores formation in the weld bead. Another approach was used to predict the ablated crater geometry in a PMMA substrate. Radice et al. [16] used a phase change tracking equation $h(T)$ (inspired from the VOF method) in COMSOL Multiphysics to monitor the material modification over the phase change temperature range (Eq. (6)).

$$h(T) = flc2hs(T - T1, T2 - T1) \quad (6)$$

where $T1$ is the temperature where the phase change begins, $T2$ is the temperature where it ends, and $flc2hs$ is a smoothed Heaviside function used in COMSOL. $T1$, $T2$, and the latent heat of phase change were determined by a differential scanning calorimeter (DSC). $h(T)$ is null when the material is in its solid state and it equals 1 when the material vaporizes. Coupled with the conventional heat transfer equation (latent heat of phase change is taken into account) (Eq. (4)), the authors were able to determine the hole geometry which revealed to be in good agreement with experimental results.

2.2.3. Example of nonablative process

Other applications where thermo-mechanical studies are important were also investigated. Glass cutting, for example, is still a hot topic today. Due to its brittleness, cracks and chipping on the edges are generated during cutting (mechanical or laser). Better quality is sought for precision engineering in the microelectronics, display, and watch jewelry industries among others. The mechanical behavior of the material depends on its temperature variation. During heating, thermal expansion occurs and creates tensile stresses in the material. During cooling, the material shrinks and compressive stresses are generated in the material. These two types of thermal stresses coupled with the change of material properties result in residual stresses, which is important to analyze and predict the mechanical strength of the material and “in fine”, the product lifetime.

A process combining laser heating and water cooling was even used to cut glass substrate [17]. While scanning, the laser beam is followed by a water jet. A crack is generated at the concordance point between the tensile stresses (laser heating) and compressive stresses (water cooling) acting in opposite directions (**Figure 3**). Laser-material interaction and the crack propagation are analyzed according to thermal stresses generation through numerical simulation in this article [17]. This process results in a clean chipping-free edge.

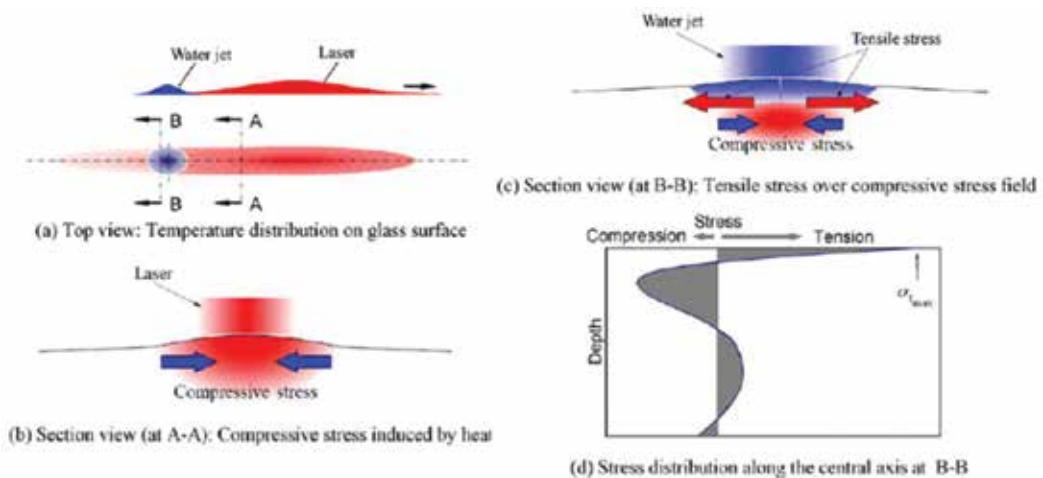


Figure 3. Schematic representation of laser scribe mechanism. (a) Top view: temperature distribution on glass surface. (b) Section view (at A-A): compressive stress induced by heat. (c) Section view (at B-B): tensile stress over compressive stress field. (d) Stress distribution along the central axis at B-B [17].

Although not fully understood, a thermal model was used once again to explain the “stealth dicing” process developed by Hamamatsu [18]. It consists in creating a thin damaged layer inside the material while the surface remains unscathed. It is used for dicing specific microelectronics chips where no debris must be generated and the use of water must be avoided. The authors explain that it is possible to focus the laser beam inside the material when it is partially transparent at the chosen wavelength (1.024 μm wavelength for silicon for instance).

At the focal point the intensity is within the range of 10^8 to 10^9 W/cm². Through heat transfer simulation, it was revealed that the temperature increased and so did the absorption. Mechanical stresses and acoustic waves generated by the temperature raise result in the creation of voids and dislocations in the material structure. The substrate is stuck to a tape. The tape expansion leads to tensile stresses high enough to finally separate the chips.

Other methods are used for more complex processes. In the case of femtosecond lasers, the heating of electrons is decoupled with the lattice. The use of heat transfer equation becomes highly questionable. Different mechanisms can occur depending on the laser intensity. Ionization of the target occurs leaving a mix of charged species repelling each other. Molecular dynamics method is fit to study this kind of phenomenon because it directly studies the movement of atoms and molecules based on Newton equations of motion [19]. However, in this short literature review, we have seen that the thermodynamic and thermo-mechanical phenomena are well suited to describe the dynamics of a laser process. This is also true for ultrashort pulsed laser in some cases. Indeed, depending on the objective, two-temperature model can be implemented for processes where the electron temperature remains low ($<10^4$ K). An example of such model is proposed in the following section.

2.3. Application: two-temperature model for picosecond laser formation of LIPSS on copper film

2.3.1. Context of the study and presentation of the heat transfer model

The FEM package COMSOL Multiphysics was used to compare the difference between nanosecond and picosecond pulses while modeling laser-copper interaction. The objective here was to qualitatively identify the role of thermal phenomena during the formation of LIPSS (Laser Induced Periodic Surface Structure) on copper by the irradiation of an ultraviolet (266 nm, fourth harmonic) picosecond laser (40 ps). It is an original simulation study that falls within the framework of a former PhD investigation [20]. Indeed, the mechanism of formation of LIPSS is investigated since the 70s and is still under debate. Several mechanisms were proposed and it appeared that the nature of LIPSS and its formation depend on the pulse duration, the wavelength, the material property and state (bulk, film, surface roughness...). While thermal phenomena could be part of the mechanism of LIPSS formation for nanosecond lasers and nonresonant mechanism associated with optical phenomena are responsible for their formation with femtosecond lasers, it is less clear with picosecond lasers [20].

As stated in Section 2.1, the electron heating is decoupled from the lattice heating as soon as the pulse duration is lower than the characteristic time transfer (3 ps for copper). The pulse duration is only one order higher than the electron-lattice time transfer. Therefore, the two-temperature model should be applied in this case (Eqs. (7) and (8)), where electron and lattice are linked together by a coupling parameter $g(T_e)$ (Eq. (10)).

$$C_e(T_e) \frac{\partial T_e}{\partial t} = \nabla(k_e(T_e, T_l) \nabla T_e) - g(T_e)(T_e - T_l) + Q \text{ (heat transfer equation for electrons)} \quad (7)$$

$$C_1(T_1) \frac{\partial T_1}{\partial t} = k_1 \nabla^2 T_1 + g(T_e)(T_e - T_1) \quad \text{(heat transfer equation for the lattice)} \quad (8)$$

$$k_e = k'_e T_e, \quad C_e = C'_e T_e \quad \text{(for low } T_e) \quad (9)$$

$$g(T_e) = \frac{C_e}{\tau_{el}} \quad \text{(electron-phonon coupling parameter)} \quad (10)$$

$$Q = \frac{A \times \alpha \times 2 \times F \times \sqrt{\ln(2)}}{\tau \times \sqrt{\pi}} \times \exp\left(-4 \times \ln(2) \times \left(\frac{t - 3\tau}{\tau}\right)^2\right) * \exp(-\alpha \times x) \quad (11)$$

The subscripts “e” and “l” denote, respectively, the electron and the lattice. T is the temperature (K), A is the optical absorption, α is the linear absorption coefficient (1/m), τ is the pulse duration (s), F is the fluence (J/cm²), x is the depth variable (m), C is the thermal heat capacity, k is the thermal heat conductivity (W/m/K) and Q (Eq. (11)) is the heat source (W.m⁻³). C'_e and k'_e are, respectively, the derivative of electron heat capacity (mJ/K²/cm³) and the derivative of electron thermal conductivity (W/K²/m). The material properties used in this investigation are summarized in **Table 1** and were obtained from Hallo et al. [21]:

| | |
|---------------------------------------------------------------------------------|-----------------------|
| Density (kg.m ⁻³) | 8960 |
| Number of electrons per atom Z | 1 |
| Optical penetration depth l_s (m) | 12.5×10^{-9} |
| lattice heat capacity C_l (J/K/m ³) | 395 |
| Derivative of electron heat capacity C'_e (J/K ² /m ³) | 70 |
| Lattice thermal heat conductivity k_l (W/m/K) | 390 |
| Derivative of electron heat conductivity k'_e (W/K ² /m) | 1.34 |
| Electron-lattice exchange rate g (W/K/m ³) | 34×10^{15} |
| Melting temperature (K) | 1360 |

Table 1. Material properties of copper.

Copper films with thicknesses of 0.2, 0.5, and 1 μm were deposited on silicon or glass (not considered in this model) substrate by cathodic magnetron sputtering technique. The laser beam was supposed to have a perfect Gaussian spatial distribution and is represented as heat source Q . Thermal losses due to convection or radiation were neglected but can be taken into account as suggested in Ref. [22], especially for longer pulse duration. The optical absorption coefficient and the thermal properties were fixed. Considering the optical penetration depth

and the pulse duration, the mesh size of the model and the time step need to be very small. The mesh size was arbitrarily set at 5 nm (optical penetration depth of 12 nm) and the time step was set according to the Neumann criterion (Eq. (12)):

$$\Delta t < \Delta z^2 \left[\frac{C(T)}{k(T)} \right]_{\min} \quad (12)$$

If the time step is close enough to the minimum requirement, COMSOL will adjust it automatically according to convergence plots. The mesh size is more important as it is fixed except if adaptive remeshing option is set. It requires a considerable effort for a quad core computer to model this. Fortunately, the spot size is three orders of magnitude bigger than the optical penetration depth. In this case, we can reduce the model to a one-dimensional problem and analyze only the temperature evolution in depth.

2.3.2. Results and discussions

The single-shot ablation threshold was determined to be around 190 mJ/cm² by the experiment [20]. The model evaluated the surface peak temperature at 1310 K for 200 nm thick film and 1263 K for 1 μm thick film (**Figure 4**) when a laser fluence of 190 mJ/cm² is applied. The relaxation is also steeper with a thickness of 1 μm (**Figure 4**) for the pulse duration of 42 ps. The surface peak temperature is higher with a thickness of 0.2 μm and pulse duration of 10 ns. Heat continuity was assumed in this model as there is no information about the interface quality, but it can potentially have an effect on the film temperature especially in the case of nanosecond pulse where the heat penetration depth is around 1 μm. This could cause damage at the copper-substrate interface (delamination). The interface could have a low transmittance and if the substrate is an insulator (glass for instance), the heat could be confined in the layer and the temperature should be higher. This might be the reason why the melting temperature is not reached in the model with a fluence of 190 mJ/cm². To be thorough, the interface between the film and the substrate should be modeled as the heat transfer continuity depends on this interface quality. However, with picosecond pulse duration, the heat penetration depth is two orders of magnitude lower than 1 μm but only one order of magnitude lower for 0.2 μm thick film. Thus, the heat transfer continuity might be influent in the case of 0.2 μm thick film but not for 1 μm thick film (**Figure 4**). Also, the material properties were fixed and they are thermo-dependent in reality, especially when a phase change is involved. Given the values observed for the thermal conductivity, the thermal heat capacity in reference [23], and the fact that the model does not go above the melting point, it was a reasonable assumption, but it might explain the small difference between the model and the experiment. It should be noted that the ablation threshold is evaluated with an error of ±20 mJ/cm². The underestimation of the temperature could be due to the absorption as well. A linear absorption coefficient of 0.66 is taken but it could vary because of the ionization of the target [24]. Besides, the properties might be different between the bulk material and thin film. This analysis shows the importance of the initial conditions and simplification hypotheses in a simulation.

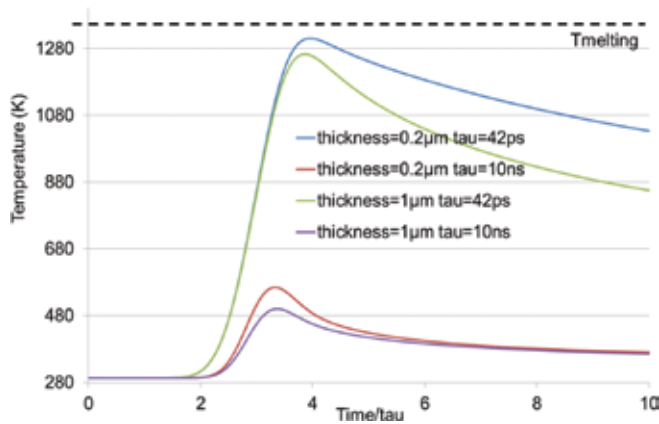


Figure 4. Lattice surface temperature for different copper thicknesses (0.2 and 1 μm) and different pulse duration (10 ns and 42 ps). The fluence F was set at $190 \text{ mJ}/\text{cm}^2$. The time is divided by the respective pulse duration τ in order to have the same scale of observation on the x -axis.

The model was tested with pulse duration of 10 ns. It is observed on **Figure 5** that the electron and lattice temperatures are almost identical. It confirms that a one-temperature model is sufficient for nanosecond pulse. For the picosecond model, the electron temperature (3215 K)

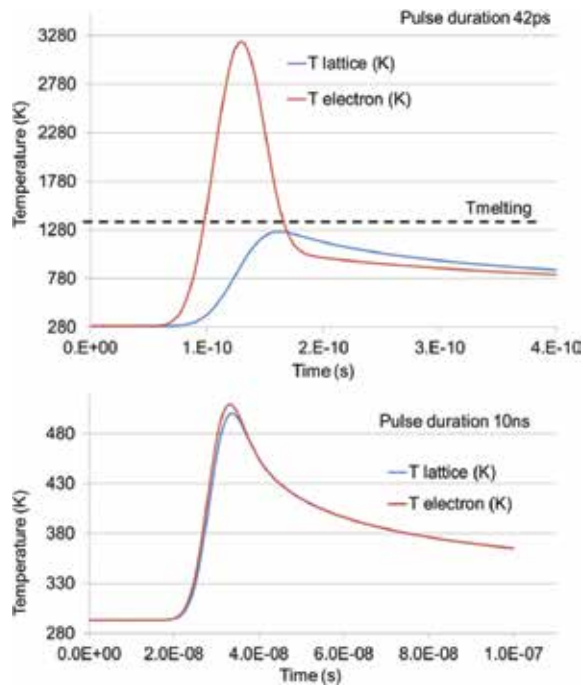


Figure 5. Electron and lattice surface temperature for pulse duration of 42 ps (top) and 10 ns (bottom) on a $1 \mu\text{m}$ thick copper target.

is higher than the lattice temperature (1263 K) and there is a delay of the same order as the pulse duration between the two temperatures. It is conformant with the theory which explains that the electrons transfer heat to the lattice during the pulse for the nanosecond regime and it is not the case for the ultrashort regime (especially <500 fs). Here, we have an intermediate regime where the lattice is heated up after the pulse by the electron-lattice heat transfer. The melting point is almost reached. The temperature might be underestimated because of approximations and work hypotheses mentioned earlier. Nevertheless, this model tends to confirm the implication of thermal effects in the formation of LIPPS in the picosecond regime.

This was a single-shot investigation. The damage threshold can be lowered by an accumulation/incubation effect. It could be interesting to study the thermal implication and the effect of the number of pulses on the delamination of the films. Working under the single-shot ablation threshold with multiple pulses allows a better control of the formation of LIPSS. This is of interest for industrial applications (super hydrophobic surfaces for instance). However, the pulse duration is 9 orders smaller than the pulse repetition rate (40 ps against 10 Hz). The time step could be modulated so that it is short during laser irradiation and longer during relaxation but it would still be difficult to investigate the incubation effect for 1000 pulses at low fluences without the use of a super calculator.

In conclusion, this example shows that COMSOL was able to provide valuable qualitative information about a laser machining mechanism. This model could be improved by lifting the simplifications hypothesis one by one (convection/radiation losses [22], interfaces between solids [25], ionization [26], thermo-dependent properties [27], etc.). Also, with more data (material properties, experimental conditions) it would be possible to have reliable quantitative information at the expense of more computational power. It should be noted that this method is limited to a nonphase change model and other numerical approaches such as Molecular Dynamic mentioned earlier would be more appropriate otherwise. Overall, Section 2 mentioned how to model situations to better understand the complex physical phenomena involved in a process. The next section presents a more applied approach where direct answers regarding the parameters are desired for process prediction and optimization: the Design Of Experiment.

3. The Design Of Experiment methodology

3.1. Introduction

The Design Of Experiment methodology is based on statistical analysis and provides a semiempirical model in a similar way than limited development. Indeed, a response (laser hole drilling depth, for instance) can be described by a polynomial function of several parameters in a restricted domain through multilinear regression. Opposed to the Change One Separate factor at a Time (COST) method, DOE saves time and resources (human, machine, costs, sample, etc.) and is more relevant when parameters have a coupled effect on the response. It is a powerful tool to rule out noninfluential parameters (screening), describe, test the robustness or even optimize a process with a minimum of experimental trials. It is widely used in the

industry to develop new products/process or improve existing ones, improve the quality, reduce the production costs, or the impact on the environment and even evaluate the influence of perturbations on a process (temperature, humidity, etc.) [28, 29].

The following sections propose to explore the use of this method in laser-based applications and to discuss the study of dicing silicon carbide substrates in the microelectronics industry.

3.2. The use of Design Of Experiment in the literature

The following paragraph aims at explaining the key steps and objectives of the Design Of Experiment methodology and cannot be taken as a full course on the subject. A literature review reveals that many authors have used Taguchi tables or the more conventional Response Surface Methodology (RSM). It is important to note that several strategies exist and they must be used depending on the objective of the researcher and the means/costs involved. The choice of strategy is strongly dependent on the researcher's experience and knowledge, especially when it comes to defining the control parameters, identifying the noise parameters (the one we are submitted to), the response he wants to characterize/measure, and the range of variation of the parameters (domain of study). Once these steps have been completed, whatever the employed strategy, it needs to be addressed with great care and in a sequential manner.

3.2.1. The screening

The parameters are coded between -1 (minimum value) and $+1$ (maximum value) so that the scale of variation becomes the same between the parameters and it is easier to make a hierarchy of their degree of influence. In RSM, the first step is the analysis of the center of the domain. All parameters are set at 0 (average value) in their coded form. The experiment is replicated three times. If the value is two orders of magnitude larger than the standard error, it is possible to carry on the study of the response. It means that the response obtained is not due to perturbation/noise. Otherwise, there might be a problem with the measurement tools and most likely that the domain of study is not large enough. It must be noted that the number of replication of the center point depends on the number of parameters and levels and needs to be increased when a quadratic model is envisaged.

The following step, the screening, is crucial and can already provide significant information such as: determining which parameters are influent and create a hierarchy, postulating a linear model without interaction, providing a predictive model (qualitatively), and determining if the domain was established properly. In some cases, it is already noticeable that interactions between parameters are influent and that nonlinearity is expected. Remember, if the objective was to identify among a lot of parameters which one were the most significant, then there is no need to carry on. A screening postulates a linear model without interaction.

A proper way to conduct the screening is to use the Hadamard matrices. These are square matrices (H2, H4, H8, H16, etc.) and correspond to a system of equations. With three parameters for instance, H4 is recommended as three equations are required to solve the three unknown parameters and one degree of freedom is available (for the average value). With four parameters, H8 is recommended because H5 does not exist. The four remaining trials are not

lost since Hadamard matrices are contained into full factorial or composite designs which are used to obtain, respectively, a linear model with interactions and a quadratic model.

3.2.2. Prediction and optimization

For prediction or optimization objectives, a full factorial design (linear model + interaction) or a composite design (quadratic or cubic model) is carried on to have a relevant predictive model that will allow setting the parameters values according to the desired response. When a nonlinear model is involved, an optimization step is possible. It is even more useful when several responses are studied and that a compromise must be found. A function called “desirability function” is used especially to optimize multiple responses simultaneously according to the target of the scientist. Each response Y_i is transformed into a dimensionless factor bounded by $0 < D_i < 1$ where a higher “ D_i ” indicates a more desirable response value. Three cases arise. “Nominal-the best” case is when the scientist desires to reach a certain response value. “Larger-the best” is when the scientist wants to maximize a response value (laser welding depth of penetration for instance at the highest possible speed) and the “smaller-the better” case is when he wants to minimize a response (HAZ for instance). That desirability function is usually treated with statistical software according to the scientist’s objective (minimize, maximize, targeted value). Ref. [30] describes a good example of prediction and optimization of laser butt welding. The bead width, depth of penetration, and the tensile strength of the joint are analyzed. The desirability function is combined with the use of Taguchi tables in order to optimize the parameters (beam power, travel speed, and focal position) and improve the quality of the weld. In this chapter, the quality of the weld is optimal when the bead width is minimized and the tensile strength and depth of penetration are maximized.

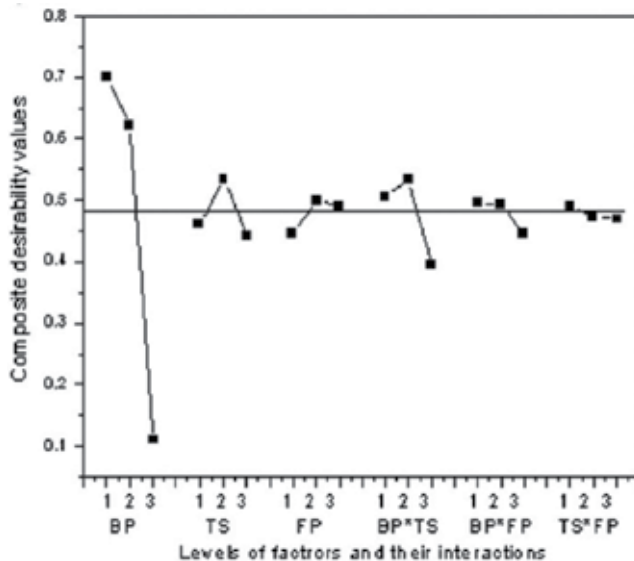


Figure 6. Factor effects on composite desirability values for helium gas [30].

Then, the desirability function is set accordingly. For this configuration, the laser beam power was found to be the most significant parameter. The interaction effects between the beam power and travel speed, the travel speed, and the focal position were found to be significant as well when using helium shielding gas (Figure 6). The interaction effect between beam power and travel speed was found to be most influent followed by the beam power, the travel speed and the focal position when other gases were used.

In another example, the authors in Ref. [31] wanted to dice sapphire substrates used in the fabrication of microelectronics chips with a Nd:YAG nanosecond laser (second harmonic 532 nm). They aimed at a depth equivalent to 1/3–1/4 of the wafer thickness (108–148 μm in this case) to be able to subsequently break it and separate the dies. In the meantime, they must choose carefully the laser parameters in order to minimize the groove width because of economical and throughput reason. The studied parameters were the pulse energy (*A*), the scanning velocity (*B*), and the number of passes (*C*). It was found that *A*, *B*, and *C* were influent on the depth as well as the interaction terms *AB*, *AC*, *BC*, and the quadratic terms *A*² and *B*². The effects of pulse energy and scanning times have slight and nearly equal effects while speed was the dominant parameter especially when the laser is scanned several times with high pulse energy. For the width, the dominant parameter was the pulse energy. A combination of low

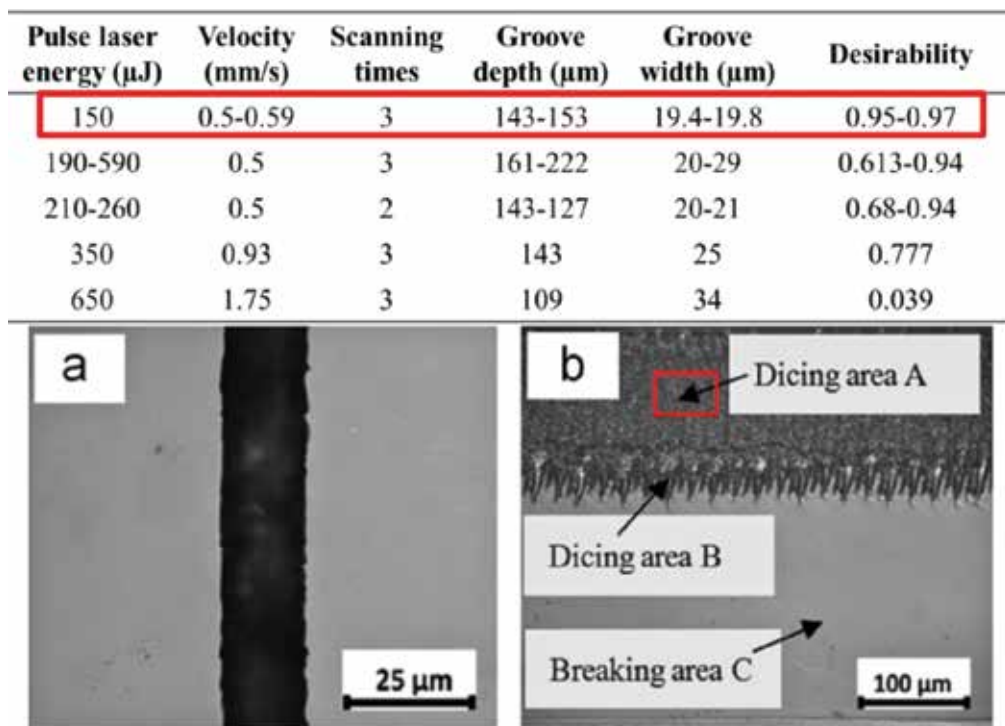


Figure 7. Desirability function analysis and results obtained with optimal parameters. (a) Surface view of laser scribed sapphire, (b) wall section view [31].

scanning velocity (0.5–0.59 mm/s), low pulse energy (150 μJ /pulse), and multiple passes (3) was found based on desirability analysis (**Figure 7**) to obtain deep (148 μm) and narrow grooves (19 μm) (**Figure 7a and b**).

In this example [31] and others [12, 32], Box Benhken Designs (BBD) were used. They are an alternative to composite designs because they contain fewer experiments than the latter. However, there might be a loss of accuracy in the final model; they do not contain the screening and a nonlinear model is postulated from the start. In the chapters mentioned above, it is suggested that parametric studies were performed before doing the BBD. Then the authors knew the model would be nonlinear. Overall, the risk of using BBD must be assessed carefully.

A problem of laser welding of AISI304 stainless steel is presented in [12]. The depth of penetration of the weld and the bead width characterize the geometry and are related to the mechanical quality of the weld. These two responses are studied according to the beam power, the welding speed, and the beam angle using a BBD. It was found that the beam power was the most significant parameter followed by the welding speed. This is conformant with Ref. [30] mentioned earlier. With an optimal combination of parameters 1250 W, 750 mm/min, and a beam angle of 90° , depth of penetration of 1.5 mm and beam width of 1.3 mm were achieved. The results were compared to finite element simulation and were discussed in Section 2.2.

In Ref. [32], BBD was used to predict the geometry (depth and width) of CO_2 laser-machined micro-channel in glass. Three different models using Artificial Neural Network (ANN) were implemented through Labview[®]. It was found that one of them gave a better prediction precision than DOE and the two others had a greater average percentage error. Overall, the ANN strategy was deemed useful for prediction and laser parameters optimization. It was found that the laser beam power had a positive effect on the channel width and depth increase. The pulse repetition rate had a negative effect on both responses. The traverse speed had a negligible effect on the channel width and tended to decrease the channel depth when increasing.

3.2.3. Prediction and robustness

The study of the robustness is another objective and is dear to the industrials for better process control and repeatability. It can be performed through the analysis of the error (for each experiment) as a response while carrying on RSM. Taguchi method is a particular case of the Design Of Experiment and is relevant for robustness study. The tables of Taguchi are mostly fractional designs. In Taguchi methodology, the signal to noise (S/N) ratio is analyzed according to the following equation:

$$S/N_i = -10 \log \left[\frac{1}{n} \sum_{i=1}^n y_i^2 \right] \quad (13)$$

$$S/N_i = -10 \log \left[\frac{1}{n} \sum_{i=1}^n \frac{1}{y_i} \right] \quad (14)$$

$$S/N = -10 \log \left[\frac{1}{n} \sum_{i=1}^n (y_i - m)^2 \right] \quad (15)$$

where n is the number of trials for each experiment, y_i is the response of the i th experiment, and m is the target the scientist wants to reach. It allows control and the reduction of variability of the response. The “smaller-the better-characteristic” (Eq. (13)) is used when the scientist wants to minimize a response as opposed to the “larger-the better characteristic” (Eq. (14)). The “nominal-the-best” characteristic (Eq. (15)) is about reaching a specified target. It is not the same as the desirability function (Section 3.2.2) since this is an analysis of the signal-to-noise ratio and this is what makes the Taguchi method more relevant for robustness study.

The methodology is a bit different than RSM [30]: (1) identify the control factors and the interactions, (2) identify the levels of each factors, (3) select the appropriate orthogonal array (OA), (4) assign the factors/interactions to the columns of the OA, (5) conduct the experiments, (6) analyze the data and determine the optimal levels, (7) perform the confirmation experiments. The two first steps are already tricky and imply that the researcher must have a prerequisite knowledge or have performed earlier experiments to guide him. For steps 3 and 4, the researcher has to choose the orthogonal array and how to fill the columns, thanks to steps 1 and 2 and thanks to the “interaction graphs.” The Taguchi tables are indeed limited to a certain type of model with a restricted number of parameters and levels. They have to be filled according to the “interaction graphs.” They show the main factors and the interaction that are possible to study for each Taguchi table. These graphs contain other criteria as well: they show how difficult it is to change the level of parameters [33]. For processes where the temperature is a key factor, it takes more time to cool down an oven than to heat it for instance. An experiment in this case can have an effect on the following one. Therefore, the sequence of experiment must be chosen carefully. Taguchi method has been successfully used in numerous studies [34, 35].

After each batch of experiments, the Analysis Of Variance (ANOVA), the analysis of multi-linear regression coefficient and the study of residuals must be carried on. These are statistical means to validate the models. Once the final model is found to be statistically adequate, new experiments (not included in the original design) must be executed and compared to the model for its final validation. Another objective of the work cited as Ref. [32] was to compare DOE and ANN methods and show the interest in developing new modeling techniques with the same robustness than DOE while being more easily or successfully applied. This should be kept in mind as the way to go for future simulation method development. The overall Design Of Experiment methodology is summarized by **Figure 8**.

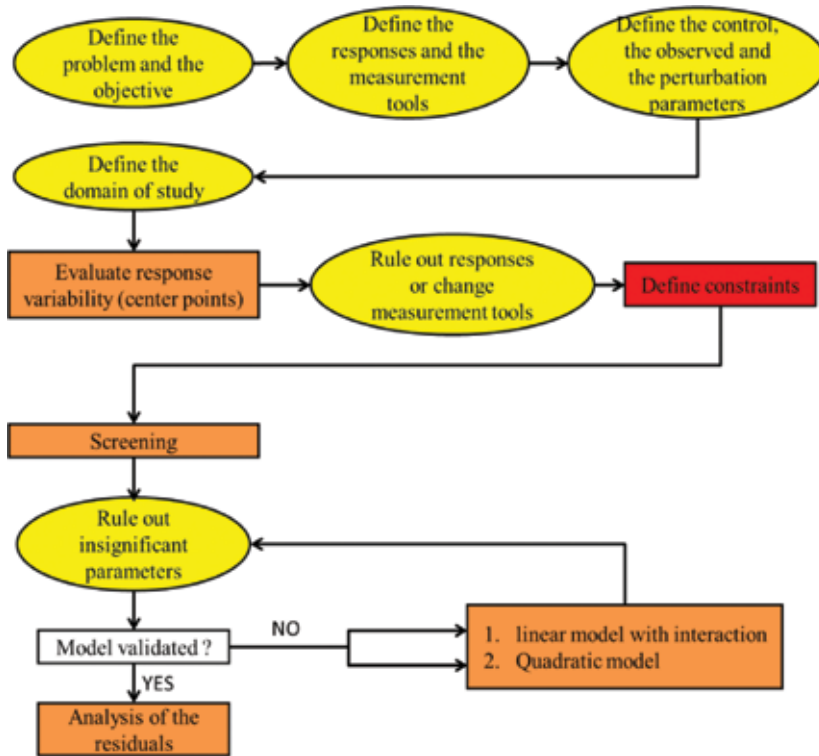


Figure 8. Response surface methodology diagram. Yellow designates the analysis and decisions depending on the researcher's experience, squares designate the experimental work, and the red one designates a turning point where a lot of information is gathered and will decide on the next steps.

3.3. Application: optimization of laser parameters for dicing silicon carbide substrate

3.3.1. RSM study

The following study is extracted from Ref. [36]. In the microelectronics industry, laser is used to replace the conventional method of blade dicing for hard and chemically inert substrates. Laser is used to scribe and then break the substrate in order to separate electronic chips. A Diode Pumped Solid State (DPSS) Nd:YAG laser operating at a wavelength of 355 nm (3rd harmonic), a repetition rate of 40 kHz with a pulse duration around 90 ns, and a spot size around 5 μm is used. The laser source is embedded in an enclosed station as it is destined for production and is operating in white room environment. The substrate of interest is a three inches diameter silicon carbide wafer and is 360 μm thick. The scribe and break method requires a scribing depth of one fourth to one third of the wafer thickness. However, the breaking step becomes difficult for hard substrates such as SiC and because the breaking efficiency depends on the leverage (dies size). The groove needs to go deeper and the objective is to optimize this depth according to the laser parameters: pulse energy (A), number of passes (B), defocus (C), and scanning speed (D). As seen in Section 3.2, other parameters are influent on

a laser process but these are the main parameters that an operator can customize on this station. The parameters and their values are reported in **Table 2**.

| Parameter (Pi) | Identifier | Level -1 (low) | Level 1 (high) | Level 0 (average) | ΔP_i |
|---------------------------------------|------------|----------------|----------------|-------------------|--------------|
| Energy ($\mu\text{J}/\text{pulse}$) | A | 30 | 140 | 85 | 110 |
| Passes | B | 1 | 5 | 3 | 4 |
| Defocus (μm) | C | -15 | -65 | -40 | -50 |
| Speed (mm/s) | D | 10 | 48 | 29 | 38 |

Table 2. Parameter values, identifiers, and study domain.

Following the procedure illustrated by **Figure 8**, the experiment performed at the center of the domain is replicated seven times (in italic in **Table 3**) and reveals that the response can be studied because the mean response value (157.9 μm) is two orders greater than the standard deviation (1.97). In other words, the response obtained is due to the parameters and not due to noise factors.

| Sequence | Energy (A) | Passes (B) | Defocus (C) | Speed (D) | Depth (Y) |
|----------|------------|------------|-------------|-----------|-----------|
| 1 | -1 | -1 | -1 | -1 | 73.8 |
| 2 | 1 | -1 | -1 | -1 | 210.8 |
| 3 | -1 | 1 | -1 | -1 | 101 |
| 4 | 1 | 1 | -1 | -1 | 286.2 |
| 5 | -1 | -1 | 1 | -1 | 72 |
| 6 | 1 | -1 | 1 | -1 | 181.2 |
| 7 | -1 | 1 | 1 | -1 | 100 |
| 8 | 1 | 1 | 1 | -1 | 261 |
| 9 | -1 | -1 | -1 | 1 | 30 |
| 10 | 1 | -1 | -1 | 1 | 127.2 |
| 11 | -1 | 1 | -1 | 1 | 65 |
| 12 | 1 | 1 | -1 | 1 | 180 |
| 13 | -1 | -1 | 1 | 1 | 47.2 |
| 14 | 1 | -1 | 1 | 1 | 122 |
| 15 | -1 | 1 | 1 | 1 | 68.4 |
| 16 | 1 | 1 | 1 | 1 | 165.8 |
| 17 | $-\alpha$ | 0 | 0 | 0 | 85.6 |
| 18 | A | 0 | 0 | 0 | 189.6 |
| 19 | 0 | $-\alpha$ | 0 | 0 | 124.4 |

| Sequence | Energy (A) | Passes (B) | Defocus (C) | Speed (D) | Depth (Y) |
|----------|------------|------------|-------------|-----------|-----------|
| 20 | 0 | α | 0 | 0 | 168.6 |
| 21 | 0 | 0 | $-\alpha$ | 0 | 156.4 |
| 22 | 0 | 0 | α | 0 | 143.2 |
| 23 | 0 | 0 | 0 | $-\alpha$ | 201.6 |
| 24 | 0 | 0 | 0 | α | 123.2 |
| 25 | 0 | 0 | 0 | 0 | 158.8 |
| 26 | 0 | 0 | 0 | 0 | 158.6 |
| 27 | 0 | 0 | 0 | 0 | 158.4 |
| 28 | 0 | 0 | 0 | 0 | 159 |
| 29 | 0 | 0 | 0 | 0 | 156.2 |
| 30 | 0 | 0 | 0 | 0 | 154.4 |
| 31 | 0 | 0 | 0 | 0 | 160.2 |

Table 3. Central composite face-centered in a cube design ($\alpha=1$) and measured response values.

| Source | Sum of squares | Degree of freedom | Mean square | F value | p-Value |
|--------------------|----------------|-------------------|----------------|-----------------|-------------------|
| Model | 40252.44 | 6 | 6708.74 | 2024.44 | <0.0001 |
| A | 28752.02 | 1 | 28752.02 | 8676.25 | <0.0001 |
| B | 2298.42 | 1 | 2298.42 | 693.57 | <0.0001 |
| C | 220.5 | 1 | 220.05 | 66.54 | <0.0001 |
| D | 7176.02 | 1 | 7176.02 | 2165.45 | <0.0001 |
| AD | 1740.5 | 1 | 1740.5 | 525.22 | <0.0001 |
| BD | 64.98 | 1 | 64.98 | 19.61 | <0.0031 |
| Curvature | 2660.03 | 1 | 2660.03 | 802.69 | <0.0001 |
| Residual | 23.20 | 7 | 3.31 | | |
| Lack of fit | 0.02 | 1 | 0.02 | 5.178E-3 | 0.9450 |
| Pure error | 23.18 | 6 | 3.86 | | |
| Cor total | 42935.67 | 14 | | | |

Table 4. ANOVA table for the screening (Hadamard design).

Table 3 shows the full design. The screening is set as a Hadamard H8 (because four factors are involved and H5 does not exist) and is shown in normal font in **Table 3**. The ANOVA results (**Table 4**) are used to determine the relevancy of a linear model. We focus on the regression coefficients and the p -value associated to the lack-of-fit and each parameter. The p -value (Fisher test) must be lower than 0.05 for the item to be declared significant. Thus, in this case, the lack

of fit is not significant. The multilinear regression coefficients are all low and the difference of mean values at the central point for the model and the experiment is greater than the standard deviation. A linear model is obviously not adequate. A linear model taking into account the interactions between parameters will not be adequate either. Indeed, the curvature is deemed significant by the ANOVA. It means that a nonlinear model will be adequate.

| Source | Sum of squares | Degree of freedom | Mean square | F value | p-Value |
|--------------------|----------------|-------------------|--------------|-------------|---------------|
| Model | 1.02E+5 | 16 | 6372.54 | 624.62 | <0.0001 |
| A | 5408.0 | 1 | 5408.0 | 530.07 | <0.0001 |
| B | 9220.82 | 1 | 9220.82 | 903.79 | <0.0001 |
| C | 269.12 | 1 | 269.12 | 26.38 | 0.0002 |
| D | 3073.28 | 1 | 3073.28 | 301.23 | <0.0001 |
| AB | 1232.01 | 1 | 1232.01 | 120.76 | <0.0001 |
| AC | 529.0 | 1 | 529.0 | 51.85 | <0.0001 |
| AD | 2704.0 | 1 | 2704.0 | 265.04 | <0.0001 |
| BD | 207.36 | 1 | 207.36 | 20.32 | 0.0005 |
| CD | 216.09 | 1 | 216.09 | 21.18 | 0.0004 |
| A ² | 845.87 | 1 | 845.87 | 82.91 | <0.0001 |
| B ² | 217.46 | 1 | 217.46 | 21.31 | 0.0004 |
| C ² | 88.93 | 1 | 88.93 | 8.72 | 0.0105 |
| D ² | 118.11 | 1 | 118.11 | 11.58 | 0.0043 |
| ABD | 222.01 | 1 | 222.01 | 21.76 | 0.0004 |
| A ² D | 149.65 | 1 | 149.65 | 14.67 | 0.0018 |
| AB ² | 145.6 | 1 | 145.6 | 14.27 | 0.002 |
| Residual | 142.83 | 14 | 10.2 | | |
| Lack of fit | 119.66 | 8 | 14.96 | 3.87 | 0.0581 |
| Pure error | 23.18 | 6 | 3.86 | | |
| Cor total | | 30 | | | |

Table 5. ANOVA table for the cubic model.

A central composite face-centered in a cube design was chosen (**Table 3**) to model a quadratic, possibly a reduced cubic model. A third parameter α is introduced in a central composite design. Its value depends on the number of parameters and levels and is chosen to cope with the statistical degradation of the accuracy of the model. Indeed, nonlinear models require the use of three levels which make 81 experiments to execute for four parameters (3^4). The use of this third value α allows decreasing the number of experiments compared to a full design while keeping a certain statistical accuracy (although not as good as a full design).

Finally, the ANOVA results (**Table 5**) reveal that the model is significant and the lack-of-fit is not (p -value close to 0.05). All coefficients shown in the ANOVA table are significant; the others are not, hence the term of “reduced” cubic model. The multilinear regression coefficients are close to 1 ($R^2 = 0.9986$, R^2 adjusted = 0.997, R^2 predicted = 0.9805). The reduced cubic model is thus significant and the final mathematical equation (Eq. (16)) in terms of coded factors is given using the least-squares method.

$$Y = 156.89 + 52A + 22.63B - 3.87C - 39.2D + 8.78AB - 5.75AC - 13AD - 3.6BD + 3.68CD - 18.05A^2 - 9.15B^2 - 5.85C^2 + 6.75D^2 - 3.73ABD + 9.17A^2D + 9.05AB^2 \quad (16)$$

The model is determined to be statistically adequate. The study of the residuals did not reveal major inconstancies. It is necessary to check if the model is scientifically adequate and if it can predict response values with additional experiments.

3.3.2. Experimental validation

From the response equation (Eq. (16)), it is clear that the pulse energy (A) and the scanning speed (D) are the most influent parameters on the scribing depth. Heating a target via laser irradiation depends on the amount of energy brought to the target and the interaction duration. This is why they are the most dominant factors and why the interaction term AD appears in the equation. Square terms coefficient A^2 and D^2 are conformant with theory as well. Indeed, the depth increases with increasing energy input until saturation. It is the classical logarithm trend observed in the literature [37]. The scribing depth also decreases with increasing speed until saturation. Interaction terms such as AC (evaluation of the fluence, Eqs. (18) and (19)), AD (effect of fluence over time), and CD (laser/material interaction over time) appear naturally in the response equation because they are linked by Eqs. (17)–(19):

$$F = \frac{E}{\pi \times \omega(z)^2} = \frac{A}{\pi \times \omega(C)^2} \quad (17)$$

$$O = 1 - \frac{v}{\omega(z) \times f} = 1 - \frac{D}{\omega(C) \times f} \quad (18)$$

$$\omega(z) = \omega_0 \sqrt{1 + \left(\frac{M^2 \lambda z}{\pi \omega_0^2} \right)^2} = \omega_0 \sqrt{1 + \left(\frac{M^2 \lambda C}{\pi \omega_0^2} \right)^2} \quad (19)$$

where z is the defocus (m), O is the overlap ratio, f is the repetition rate (Hz), v is the scanning speed (mm/s), λ is the wavelength (nm) and ω_0 (cm) is the spot radius at the focal point. The effect of the number of passes B varied depending on the delay between two passes and thus on the scanning speed. The effect saturated around three passes for pulse energies below 85

μJ and tended to saturate around five passes above this energy threshold. The number of scans effect saturates as the aspect ratio (depth/width) increases because there is less margin for debris ejection. Debris disturbs the beam propagation at the bottom of the trench and successive passes become less effective. This inconvenience can be balanced depending on the pulse energy and the scanning speed because they rule the laser-material interaction efficiency. This is why interaction terms between the number of passes (B), the pulse energy (A), and the scanning speed (D) appear in the response equation.

Additional experiments were performed and compared to the predicted values given by the model. A reasonable correspondence was found between predicted and experimental values as observed in **Figure 9**.

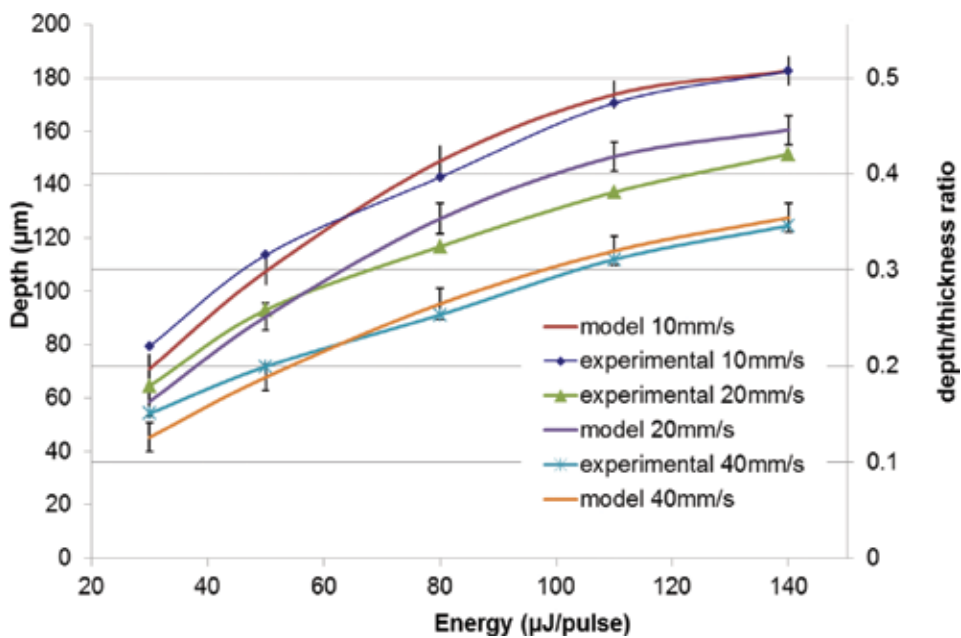


Figure 9. Graph showing the variation of depth versus the energy at different scanning speeds. The frequency was fixed at 40 kHz.

This model was successfully used to determine optimal parameters for an objective of 180 μm deep scribe in silicon carbide substrate.

4. Conclusion

Whether it is Finite Element Methods, Monte Carlo or Molecular Dynamics, numerical simulation gives the opportunity to better comprehend the physics of laser-material interaction and in many cases to predict results and optimize the parameters for laser processing. In this chapter, numerical simulation was proven to be valuable to both fundamental science and

laser applications in the industry. Computer calculation improvement makes it possible to model complex problems when multiphysical phenomena are coupled and allowed important achievements in the field of laser processing. Simplification assumptions are still required but with time and research efforts, models will become more and more realistic giving the possibility of getting a snapshot inside complex physical mechanisms that cannot be observed through experimental means.

Author details

Guillaume Savriama* and Nadjib Semmar

*Address all correspondence to: guillaume.savriama@gmail.com

GREMI UMR 7344, CNRS/Université d'Orléans, Orléans, France

References

- [1] A. Otto, H. Koch, K.-H. Leitz & M. Schmidt, Numerical simulations—a versatile approach for better understanding dynamics in laser material processing, *Physics Procedia* 12, 11–20 (2011).
- [2] M.J. Kim & J. Zhang, Finite element analysis of evaporative cutting with a moving high energy pulsed laser, *Applied Mathematical Modelling* 25, 203–220 (2001).
- [3] H. Karbasi, *COMSOL Assisted Simulation of Laser Engraving*, Proceedings of the Comsol Conference, Boston (2010), available from https://www.comsol.com/paper/download/62352/karbasi_paper.pdf.
- [4] K. Salonitis, D. Drougas & G. Chryssolouris, Finite element modelling of penetration laser welding of sandwich materials, *Physics Procedia* 5, 325–335 (2010).
- [5] M. Darif & N. Semmar, *Numerical Simulation of Si Nanosecond Laser Annealing by COMSOL Multiphysics*, Proceedings of the Comsol Conference, Hannover (2008), available from <https://www.comsol.com/paper/download/37728/Darif.pdf>.
- [6] N. Semmar & C. Boulmer-Leborgne, Metallic thin films heated by pulsed lasers: Numerical simulation of the thermal field and the melting kinetics, *Journal de Physique IV* 120, 413–420 (2004).
- [7] E.G. Gamaly, A.V. Rode, B.Luther-Davies & V.T. Tikhonchuk, Ablation of solids by femtosecond lasers: ablation mechanism and ablation thresholds for metals and dielectrics, *Physics of Plasmas* 9, 949–952 (2002).

- [8] B.C. Stuart, M.D. Feit, S. Herman, A.M. Rubenchik, B.W. Shore & M.D. Perry, Nano-second-to-femtosecond laser-induced breakdown in dielectrics, *Physical Review B* 53, 1749–1761 (1996).
- [9] E. Carpenne, D. Höche & P. Schaaf, Fundamentals of laser material interactions. In *Laser Processing of Materials: Fundamentals, Applications and Developments*, P. Schaff editor, Springer Series in Materials Science 139 (2010), p. 39.
- [10] S.M. Eaton, H. Zhang & P.R. Herman, Heat accumulation effects in femtosecond laser-written waveguides with variable repetition rate, *Optics Express* 13, 4708–4716 (2005).
- [11] I. Miyamoto, K. Cvecek & M. Schmidt, Crack-free conditions in welding of glass by ultrashort laser pulse, *Optics Express* 21, 14291–14302 (2013).
- [12] K.R. Balasubramanian, N. Siva Shanmugam, G. Buvanashakaran & K. Sankaranarasamy, Numerical and experimental investigation of laser beam welding of AISI 304 stainless steel sheet, *Advances in Production Engineering and Management* 3, 93–105 (2008).
- [13] H. Koch, K.-H. Leitz, A. Otto & M. Schmidt, Laser deep penetration welding simulation based on a wavelength dependent absorption model, *Physics Procedia* 5, 309–315 (2010).
- [14] N. Pierron, P. Sallamand & S. Mattei, *Numerical Modelling of Molten Pool Formation During an Interaction of a Pulse Laser (Nd:YAG) with an Aluminum Sheet*, Proceedings of the COMSOL Multiphysics user's conference, Paris (2005), available from https://www.researchgate.net/publication/266180484_Numerical_modeling_of_molten_pool_formation_during_an_interaction_of_a_pulse_laser_NdYAG_with_an_aluminum_sheet.
- [15] M. Courtois, M. Carin, P. Le Masson & S. Gaeid, *Keyhole Formation during Spot Laser Welding. Heat and Fluid Flow Modeling in a 2D Axisymmetric Configuration*, Proceedings of the COMSOL Multiphysics user's Conference, Milan (2012) available from https://www.comsol.com/paper/download/151897/courtois_paper.pdf.
- [16] J.J. Radice, P.J., Joyce, A.C. Tresansky, R.J. Watkins, *A COMSOL Model of Damage Evolution due to High Energy Laser Irradiation of Partially Absorptive Materials*, Proceedings of the COMSOL Multiphysics user's conference, Boston (2012) available from https://www.comsol.it/paper/download/152671/joyce_paper.pdf.
- [17] K. Yamamoto, N. Hasaka, H. Morita & E. Ohmura, Influence of glass substrate thickness in laser scribing of glass, *Precision Engineering* 34, 55–61 (2010).
- [18] M. Kumagai et al., Analysis of processing mechanism in stealth dicing ultra-thin silicon wafer, *Journal of Advanced Mechanical Design, Systems, and Manufacturing* 2, 540–549 (2008).
- [19] X. Wang & X. Xu, Molecular dynamics simulation of heat transfer and phase change during laser material interaction, *ASME Journal of Heat Transfer* 124, 265–274 (2002).

- [20] Thi Trang Dai Huynh, *Etude de la dynamique de formation de nanostructures périodiques sur une couche mince de cuivre induites par impulsions laser nanoseconde et picoseconde à 266 nm*, PhD thesis (2014). <https://tel.archives-ouvertes.fr/tel-01145272/document>
- [21] L. Hallo, O. Riou, C. Stenz & V.T. Tikhonchuk, Infrared emissivity studies of melting thresholds and structural changes of aluminum and copper samples heated by femtosecond laser pulses, *Journal of Physics D: Applied Physics*, 5272-1 5272-10 (2006).
- [22] M. Musella & H.-R. Tschudi, Transient radiative and conductive heat transfer in ceramics subjected to laser heating, *International Journal of Thermophysics* 26, 981–999 (2005).
- [23] J.F. Shackelford & W. Alexander, *Materials Science and Engineering Handbook*. 3rd edition, CRC Press LLC, Boca Raton, 398, pp. 409–410 (2001).
- [24] J. Lopez et al., *Laser Micro Processing of Metal and Silicon using 100 kHz and 2 MHz Ultrafast Lasers*, ICALEO 2009 Orlando Florida, Laser Institute of America, paper M308 (2009).
- [25] X. Zhang, P.Z. Cong & M. Fujii, A study of thermal contact resistance at the interface of two solids, *International Journal of Thermophysics* 27, 880–895 (2006).
- [26] A. Gurizzan & P. Villorosi, Ablation model for semiconductors and dielectrics under ultrafast laser pulses for solar cells micromachining, *European Physical Journal Plus* 130, 16–25 (2015).
- [27] J. Xie & A. Kar, Mathematical modeling of melting during laser materials processing, *Journal of Applied Physics* 81, 3015–3022 (1997).
- [28] D.R. Cox & N. Reid, *The Theory of the Design of Experiments*, CRC Press LLC, Boca Raton (2000).
- [29] A. Kr. Dubey & V. Yadava, Experimental study of Nd:YAG laser beam machining-an overview, *Journal of Material Processing Technology* 195, 15–26 (2008).
- [30] P. Sathiya, M.Y. AbdulJaleel, D. Katherasan & B. Shanmugarajan, Optimization of laser butt welding parameters with multiple performance characteristics, *Optics and Laser Technology* 43, 660–673 (2011).
- [31] X. Xie et al., Modeling and optimization of pulsed green laser dicing of sapphire using response surface methodology, *Optics & Laser Technology* 45, 125–131 (2013).
- [32] S.M. Karazi, A. Issa & D. Brabazon, Comparison of ANN and DoE for the prediction of laser-machined micro-channel dimensions, *Optics and Lasers in Engineering* 47, 956–964 (2009).
- [33] G. Taguchi & S. Kinoshi, *Orthogonal Arrays and Linear Graphs*, ASI Press, Dearborn, MI (1987).

- [34] T. Canel, A. Ugur Kaya & B. Celik, Parameter optimization of nanosecond laser for microdrilling on PVC by Taguchi method, *Optics and Laser Technology* 44, 2347–2353 (2012).
- [35] Y.H. Chen, S.C. Tam, W.L. Chen & H.Y. Zheng, Application of Taguchi method in the optimization of laser micro-engraving of photomasks, *International Journal of Materials & Product Technology* 11, 333–344 (1996).
- [36] G. Savriama, F. Baillet, L. Barreau, C. Boulmer-Leborgne & N. Semmar, Optimization of diode pumped solid state ultraviolet laser dicing of silicon carbide chips using the design of experiment methodology, *Journal of Laser Applications* 27, 032009-1 032009-9 (2015).
- [37] S. Gupta, B. Pecholt & P. Molian, Excimer laser ablation of single crystal 4H-SiC and 6H-SiC wafers, *Journal of Material Sciences* 46, 196–206 (2011).

Mathematical Modeling for Nanofluids Simulation: A Review of the Latest Works

Mohammad Reza Safaei, AminHossein Jahanbin,
Ali Kianifar, Samira Gharehkhani,
Akeel Shebeeb Kherbeet, Marjan Goodarzi and
Mahidzal Dahari

Additional information is available at the end of the chapter

<http://dx.doi.org/10.5772/64154>

Abstract

Exploiting nanofluids in thermal systems is growing day by day. Nanofluids having ultrafine solid particles promise new working fluids for application in energy devices. Many studies have been conducted on thermophysical properties as well as heat and fluid flow characteristics of nanofluids in various systems to discover their advantages compared to conventional working fluids. The main aim of this study is to present the latest developments and progress in the mathematical modeling of nanofluids flow. For this purpose, a comprehensive review of different nanofluid computational fluid dynamics (CFD) approaches is carried out. This study provides detailed information about the commonly used formulations as well as techniques for mathematical modeling of nanofluids. In addition, advantages and disadvantages of each method are rendered to find the most appropriate approach, which can give valid results.

Keywords: nanofluid, CFD, numerical simulation, mathematical modeling, single- and two-phase methods

1. Introduction

In general, the assessment of the thermal performance of a system through numerical simulations is much affordable compared to experimental studies with high expenses of material and

equipment. The significance of a numerical study is highlighted when a nanofluid is utilized as the working fluid. High costs for the production of nanofluids and difficulties in preparing stable nanofluids are the main barriers to perform experiments with nanofluids. Therefore, numerical modeling of nanofluids, where a suitable approach is selected to simulate the flow, could be the best solution for problems involved with nanoparticle suspensions.

However, in spite of considerable developments in computing power and methods, literature review reveals that there is no comprehensive study to conclude the best technique for the modeling of nanofluids. In particular, due to the ultrafine size of nanoparticles, the governing terms in multiphase models are still not entirely identified. In the present work, latest studies on numerical simulations of nanofluid flow are reviewed with a particular focus on different multiphase schemes.

2. Numerical methods for nanofluids' flow simulation

Nanofluid computational fluid dynamic (CFD) modeling can be classified into two main groups: single-phase and two-phase models. However, there are few other models that may not be included in these categories, such as Lattice-Boltzmann method (LBM). Moreover, different numerical approaches have been employed to solve models mentioned above to predict thermal and hydraulic characteristics of nanofluids flow. Finite volume method (FVM) and finite element method (FEM) are two main approaches for solving the governing equations of nanofluid problems. However, finite difference method (FDM), control volume-based finite element method, and some novel numerical approaches such as homotopy analysis method (HAM) and smoothed particle hydrodynamics (SPH) methods have also been utilized in the previous studies. In this study, a comprehensive review of various numerical methods for the simulation of nanofluids is accomplished.

2.1. Single-phase approaches

Although suspension of a nanofluid is inherently a two-phase fluid, if some proper assumptions are made, it can be considered as a homogeneous liquid. Due to the existence of ultrafine nanoparticles, it is assumed that these particles can be easily dispersed in the host fluid. For this purpose, both the nanoparticles and base fluid are considered to be in thermal balance without any slip between their molecules. Therefore, under such assumptions, in many studies, nanofluids have been assumed as a single-phase fluid.

2.1.1. Conventional single-phase model

Mass, momentum, and energy equations, which are used for conventional liquids, could also be applied to single-phase flow with the above assumptions. In this case, only thermophysical properties of nanofluids should be determined. Therefore, the governing equations in the steady state can be expressed as below [1]:

Conservation of mass:

$$\nabla \cdot (\rho_{eff} \vec{u}) = 0 \quad (1)$$

Conservation of momentum:

$$\nabla \cdot (\rho_{eff} \vec{u} \vec{u}) = -\nabla P + \nabla \cdot (\mu_{eff} \nabla \vec{u}) - (\rho\beta)_{eff} (T - T_0) g \quad (2)$$

Conservation of energy:

$$\nabla \cdot ((\rho c_p)_{eff} \vec{u} T) = \nabla \cdot (k_{eff} \nabla T) \quad (3)$$

There are numerous publications simulating nanofluids characteristics as a single-phase fluid. Mixed convection heat transfer in a T-shaped lid-driven cavity was examined numerically by Mojumder et al. [2]. A residual FEM model was applied for the numerical simulation. They validated their simulation code against data of Abu-Nada, Chamkha [3]. The results revealed that higher Grashof number causes rise in the heat transfer rate.

Turbulent nanofluid flow for different nanoparticles such as alumina, cupric oxide, and titania was investigated by Rostamani et al. [4] at various concentrations in a long horizontal duct under constant heat flux. They employed the control volume approach and temperature-dependent thermophysical properties. It was found that increasing the number of dispersed nanoparticles in base fluid increases the pumping power and heat transfer rate. In addition, the predicted Nusselt numbers in some cases demonstrated good agreements to the obtained results by Pak, Cho [5], and Maiga et al. [6] correlations.

Abu-Nada [7] considered the Rayleigh-Benard-free convection heat transfer in CuO-water nanofluids using FVM, where the effect of temperature-dependent properties was the primary objective. The obtained results by temperature-dependent models were also compared with classic models (Maxwell-Garnett (MG) and Brinkman). Results displayed that for $Ra > 10^3$, the effect of temperature on fluid flow and heat transfer was insignificant due to the presence of high viscosity, which was caused by the nanoparticles volume fraction.

Bouhaleb and Abbassi [8] employed Control Volume-Finite Element method to study the free convection in an inclined cavity. They solved the free convection problem using Boussinesq approximation and employing the SIMPLER algorithm for velocity-pressure coupling. The results showed that the variation of inclination angel highlights a hysteresis behavior of the nanofluid flow. Also, increasing the diameter of solid nanoparticles led to a strong decay in heat transfer. Furthermore, they concluded that the efficiency of heat transfer strongly depends on the diameter of nanoparticles, not its concentration in base fluid.

While a considerable number of recent studies on numerical simulation of nanofluids have been employed by FVM [9–11] and FEM [12–14] for their studies, in several studies Finite Difference Method has been used for different applications of nanofluids. For instance, Buddakkagari and Kumar [15] studied laminar-forced convection of a nanofluid over a vertical

cone/plate. The non-dimensional governing equations were solved using FDM model, Crank-Nicolson type. The results illustrated that the Prandtl number affects the boundary layer dramatically. Furthermore, the momentum boundary layer was more affected by higher values of Lewis number. Finally, it was concluded that the boundary layer growth depends on Brownian motion and thermophoresis force.

However, applying the single-phase model for nanofluids has some limitations. For instance, the results obtained from this model were strongly dependent on adopted thermophysical properties and in some cases using the single-phase model may underestimate the Nusselt number, compared to models adopting temperature-dependent properties [16, 17]. The reason behind this could be due to various factors such as gravity, friction forces, Brownian motion, and solid/liquid interface. Ding and Wen [18] showed that the primary assumption of homogeneous fluid is not always acceptable. However, the review of the previous works illustrates that choosing the appropriate thermophysical property correlations in the single-phase method results in a reasonable estimation of nanofluids properties [19, 20]. Therefore, selecting suitable thermophysical properties such as variable properties, and considering the chaotic movement of nanoparticles (dispersion model) may compensate, to some extent, the limitations of single-phase model.

2.1.2. Thermal dispersion model

Brownian and gravity forces, the friction force between the base fluid and nanoparticles, sedimentation, and dispersion may coexist in a nanofluid flow. In fact, slip motion between liquid molecules and solid particles is not negligible, and the random movement of nanoparticles ameliorates the thermal dispersion in nanofluids, which reinforces heat transfer. For the first time, the thermal dispersion model was suggested by Xuan and Roetzel [21]. They assumed that nanoparticles move randomly, causing small chaos in velocity and temperature magnitudes (T' and \vec{u}'). The essential phase averages can be written as [21]:

$$T = \langle T \rangle^f + T' \quad (4)$$

$$\vec{u} = \langle \vec{u} \rangle^f + \vec{u}' \quad (5)$$

where

$$\langle T \rangle^f = \frac{1}{V_f} \int T dV \quad (6)$$

$$\langle \vec{u} \rangle^f = \frac{1}{V_f} \int \vec{u} dV \quad (7)$$

$$\frac{1}{V_f} \int_{V_f} T' dV = 0 \tag{8}$$

By assuming that the boundary layer between the liquid and solid phases is negligible, unsteady-state, energy equation can be written as

$$(\rho c_p)_{nf} \left[\frac{\partial \langle T \rangle^f}{\partial t} + \langle \vec{u} \rangle^f \cdot \nabla \langle T \rangle^f \right] = \nabla \cdot (k_{nf} \nabla \langle T \rangle^f) - (\rho c_p)_{nf} \nabla \cdot \langle \vec{u} T' \rangle^f \tag{9}$$

The thermal dispersion generates a heat flux in the flow that is equal to

$$q_d = (\rho c_p)_{nf} \langle \vec{u} T' \rangle^f = -k_d \cdot \nabla \langle T \rangle^f \tag{10}$$

k_d is the thermal conductivity tensor due to dispersion. Now, Eq. (9) can be rewritten as

$$\frac{\partial \langle T \rangle^f}{\partial t} + \langle \vec{u} \rangle^f \cdot \nabla \langle T \rangle^f = \nabla \cdot \left[(\alpha_{nf} \mathbf{I} + \frac{\mathbf{k}_d}{(\rho c_p)_{nf}}) \cdot \nabla \langle T \rangle^f \right] \tag{11}$$

where α is the thermal diffusivity and \mathbf{I} is the identity tensor. The following form may be applicable for the effective thermal conductivity of nanofluid:

$$k_{eff} = k_{nf} + k_d \tag{12}$$

where k_d refers to the dispersed thermal conductivity coefficient. Despite the fact that this term plays a key role in dispersion model, just a few correlations were proposed in the literature. Xuan and Roetzel [21] with reference to some publications in porous media [22, 23] proposed the following forms:

$$k_d = C^* (\rho c_p)_{nf} u R, \quad k_d = C_d (\rho c_p)_{nf} u R d_p \phi \tag{13}$$

C_d is an unknown constant and R is referred to pipe radius. Khaled and Vafai [24] investigated heat transfer enhancement by considering dispersion effects. They used the following linearized model introduced by Xuan and Roetzel [21] correlations for dispersed thermal conductivity of nanofluids:

$$k_d = C^* (\rho c_p)_{nf} \phi H u_m \tag{14}$$

where H is the half of duct height, u_m is the average bulk velocity, and C^* is an unknown constant. By employing control volume approach, Mojarrad et al. [25] analyzed the heat transfer of α -alumina-water nanofluid in the entrance region of a rounded pipe. They also compared their results with experimental data. The results showed that dispersion model provides reasonable outcomes in spite of its simplicity. Moreover, they suggested a new correlation for radial dispersed thermal conductivity:

$$k_d = C_d (\rho c_p)_{nf} \frac{R\phi}{d_p} \left(\frac{\partial T}{\partial r} \right) \quad (15)$$

By using dispersion model, Zeinali Heris et al. [26, 27] investigated convective heat transfer of different nanofluids. They studied heat transfer augmentation due to nanofluids flow through the tubes with different cross-section geometries. The numerical results were validated against experimental data [28, 29] and good agreement was observed. The results showed that the Nusselt number would enhance with increasing particle loading and decreasing particle size.

Thermal behavior of nanofluids in a cavity was analyzed by Kumar et al. [30]. The dimensionless-governing equations were resolved via semi-explicit FVM solver. The Grashof number, volume concentration, and nanoparticles shape effects on heat transfer rate were assessed. The results showed that the dispersed thermal conductivity is more intensive in the vicinity of walls in comparison with pipe center. Also, it was found that dispersed thermal conductivity and hydraulic diameter of the particles are strongly dependent to each other.

Akbaridoust et al. [31] examined laminar steady-state nanofluid flow through helically shaped tubes, both numerically and experimentally. The governing equations in three-dimensional (3-D) form were solved by finite difference approach, using a FORTRAN code. Dispersion model was modified in order to be applicable for helical tubes. This modification resulted in minimized difference between numerical results and experimental data. The results showed that higher curvature ratios cause more heat transfer rates.

2.2. Two-phase approaches

Due to some factors such as Brownian force, Brownian diffusion, friction force, thermophoresis, and gravity, nanofluids may be considered two-phase fluids by nature. Therefore, the classic theory of solid-liquid mixture can be applied to nanofluids. In such models, nanoparticles and base fluid are considered as two separate phases with different temperatures and velocities. Although two-phase approaches may obtain realistic results, they have high computational cost in comparison to single-phase models. Two-phase approaches can be categorized into two general models: Lagrangian-Eulerian and Eulerian-Eulerian.

2.2.1. Lagrangian-Eulerian model

In the Lagrangian-Eulerian or discrete phase model, the fluid phase is considered as a continuum by solving the N-S equations in time-averaged form, while the dispersed phase was solved by tracking the particles in the Lagrangian frame. Also, in this model, the interaction between fluid and particles presented as a source term in both momentum and energy equations.

Mathematical formulations of the Lagrangian-Eulerian in two-phase model can be written as follows [32]:

Conservation of mass:

$$\nabla \cdot (\rho \vec{u}) = 0 \quad (16)$$

Conservation of momentum:

$$\nabla \cdot (\rho \vec{u} \vec{u}) = -\nabla P + \nabla \cdot (\mu \nabla \vec{u}) + S_m \quad (17)$$

Conservation of energy:

$$\nabla \cdot (\rho c_p \vec{u} T) = \nabla \cdot (k \nabla T) + S_e \quad (18)$$

where S_m and S_e are source/sink terms representing the exchange of momentum and energy between liquid and solid phases. The momentum and energy source/sink terms are defined as [33, 34]

$$s_m = \frac{1}{\delta V} \sum_{np} \vec{F} \quad (19)$$

$$s_e = \frac{1}{\delta V} \sum_{np} Nu_p \pi d_p k_p (T - T_p) \quad (20)$$

where Nu_p can be computed from the Ranz correlation [35]:

$$Nu_p = 2 + 0.6 Re_p^{0.5} Pr^{0.333} \quad (21)$$

In Lagrangian reference frame, the particle motion and energy equations are as follows:

$$m_p \frac{d\vec{u}_p}{dt} = \vec{F}_g + \vec{F}_D + \vec{F}_L + \vec{F}_{Br} + \vec{F}_b \quad (22)$$

$$m_p c_p \frac{dT_p}{dt} = Nu_p \pi d_p k_f (T_f - T_p) \quad (23)$$

In Eq. (22), F stands for various forces including gravity, drag, Saffman's lift, Brownian, and buoyancy, respectively.

Turbulent nanofluid flow in helical tubes was investigated numerically and experimentally by Bahremand et al. [36]. The numerical simulation was performed by both single-phase model and Lagrangian-Eulerian approach in connection with renormalization group (RNG) $k-\epsilon$ model. ANSYS CFX software was used for solving the governing equations. The results indicated that nanofluids with a higher concentration exhibit a greater heat transfer coefficient and pressure drop. Also, it was found that the two-phase model yields more accurate results compared to single-phase model.

Alumina-water nanofluid flow and heat transfer in a long tube with uniform heating at the walls were investigated by Moraveji and Esmaeili [37]. The simulations were conducted in both single- and two-phase methods where the governing equations were solved by FVM. Both temperature-dependent and constant thermophysical properties were considered in the study. The results of the modeling revealed that the temperature-dependent properties are more sensitive to the Reynolds number variations and led to higher values of the Nusselt number. Comparison between single-phase and two-phase (discrete phase) models showed the maximum difference of 11% for the average heat transfer coefficient.

Tahir and Mital [38] studied the laminar-forced convection of Al_2O_3 -water nanofluid in a tube numerically. They analyzed the impacts of the Reynolds number, particle diameter, and volume fraction of the particles in their study. A good agreement was achieved between the simulation and experimental data using discrete phase method. The results of the survey demonstrated that the heat transfer coefficient increased linearly with both the Reynolds number and volume fraction of nanoparticles. However, there was a non-linear parabolic decrease with increasing nanoparticle size. It was concluded that the Reynolds number and volume fraction have the maximum and the minimum effects on heat transfer coefficient, respectively.

A comprehensive simulation of turbulent-forced convection for Cu-water was carried out by Behroyan et al. [39]. The Reynolds number of the flow was chosen between 10,000 and 25,000, where the volume fraction of copper nanoparticles was taken in the range of 0.0–2.0%. Two single-phase models (Newtonian and non-Newtonian) and three two-phase models were employed in this study. The ANSYS commercial CFD package was utilized to solve the governing equations. The obtained results showed that the Newtonian single-phase method as well as discrete phase method is in better agreement with experimental data, compared to other numerical approaches.

The present literature survey reveals that using Lagrangian-Eulerian approach for modeling the heat transfer of nanofluids is in early stages. Therefore, more studies are required to be conducted to determine the capability of the Lagrangian-Eulerian model, especially in turbulent regime [40]. Also, in some other studies such as Safaei et al. [32] and Xu et al. [41], it is emphasized that Lagrangian-Eulerian is a suitable model just for low concentration two-phase suspensions ($\varphi < 1\%$). Moreover, it was mentioned that this model needs extremely high computational time due to a large amount of calculation.

2.2.2. Eulerian-Eulerian model

The other important branch of two-phase models is the Eulerian-Eulerian model. Since the Eulerian-Eulerian model is suitable for mixtures with a high amount of particles, applying this model to nanofluids consisting of an extremely large number of nanoparticles is recommended. The main models of Eulerian-Eulerian available in the literature are three models including Mixture, Eulerian, and VOF (volume of fluid).

2.2.2.1. Volume of fluid model

In the VOF model, the volume fractions of all phases are obtained for the entire domain of study, by solving the continuity equation for the secondary phases. A single set of momentum equations is solved for all the phases to find the velocity components. The sum of all employed phases' volume fractions is equal to unity. Accordingly, the primary phase volume fraction magnitude is achieved. In addition, all the physical properties are calculated by using an average weighted of different phases according to their volume fraction on each control volume. Finally, a shared temperature is calculated from a single energy equation [42].

Mass conservation for VOF model can be expressed as

$$\nabla \cdot (\varphi_z \rho_z \vec{u}_z) = 0 \quad (24)$$

where $\sum_{z=1}^n \varphi_z = 1$ and all properties are computed such as $N = \sum_{z=1}^n \varphi_z N_z$.

In this model, Eqs. (2) and (3) are used as momentum and energy equations.

According to literature, a few studies have been done on using the VOF model for the simulation of nanofluids. Akbari et al. [43] studied turbulent-forced convective heat transfer of Al_2O_3 -water as well as Cu-water nanofluids inside a horizontal tube under uniform heat flux. The governing equations were solved implementing different numerical approaches, for example, single-phase, VOF, mixture, and Eulerian models, using FLUENT software. The results showed that the thermal field forecasting by multiphase models was different from the results of experimental data and single-phase approach. However, single-phase and two-phase models predicted almost same hydrodynamic results. It was concluded that unlike the results of previous studies [17, 44], two-phase models overestimate the thermal field. Under similar conditions, however, Hejzian et al. [45] found different results when investigating the

turbulent convection of TiO_2 -water nanofluid in a horizontal tube using FVM method. The results of this study showed that the mixture and VOF models are more appropriate to predict the heat transfer field, compared to single-phase model.

Turbulent heat transfer of nanofluids flow through a mini-channel heat sink was analyzed by Naphon and Nakharintr [46]. The k - ϵ turbulence model with single-phase, mixture, and VOF approaches was employed to analyze the heat transfer and flow characteristics. Also, some experiments conducted to verify the predicted results and reasonable agreements were achieved. It was concluded that the single-phase model cannot predict the Nusselt number with accuracy as good as mixture and VOF models because the impacts of Brownian motion and non-uniform distribution of nano-particles in the solution domain are not considered in the single-phase model. In addition, under similar conditions, VOF and mixture models present more appropriate results compared to the single-phase model.

Hanafizadeh et al. [47] carried out a study to compare single and two-phase approaches for Fe_3O_4 -water nanofluid in both developing and fully developed regions in a circular tube under constant heat flux. The study was conducted for 0.5–2 vol. % and $300 \leq \text{Re} \leq 1200$. The results showed that higher values of both Reynolds number and volume fraction would augment the average heat transfer coefficient, while just increasing the number of dispersed nanoparticles does not have a considerable impact on heat transfer enhancement. Also, in the fully developed region, a higher number of dispersed nanoparticles in base fluid would reduce the error of studied numerical methods. On the other hand, in developing region of a tube and for low Reynolds numbers, increase in nanofluid volume fraction would decrease the accuracy of numerical methods, while this trend was reversed for moderate and high Reynolds numbers.

In total, since a limited number of studies have used this numerical approach, further studies are needed to evaluate the capability of the VOF model.

2.2.2.2. Mixture model

The mixture model is one of the most popular methods for modeling of multiphase slurry flows. The main feature of this approach is that only one set of velocity elements is solved for the mixture momentum conservation equations. The velocities of dispersed phases are extracted from the algebraic formulations [48]. Moreover, since the primary phase affects the secondary phase through drag force and turbulence, the effect of secondary phase on the primary phase could be found through mean momentum reduction and turbulence. The basic assumptions of mixture model are as follows [49, 50]:

- All phases share a single pressure.
- The interaction between different dispersed phases is assumed to be negligible.
- Nanoparticles in the secondarily dispersed phase are spherical in shape, with a uniform size.
- The concentration of the secondarily dispersed phases is solved by a scalar equation, considering the correction made by phase slip.

The governing equations of the nanofluids' mixture model can be written as follows [51]:

Continuity:

$$\frac{\partial}{\partial t}(\rho_m) + \nabla \cdot (\rho_m \vec{u}_m) = 0 \quad (25)$$

where

$$\vec{u}_m = \frac{\sum_{Z=1}^n \varphi_Z \rho_Z \vec{u}_Z}{\rho_m} = \vec{u}_Z \quad (26)$$

and

$$\rho_m = \sum_{Z=1}^n \varphi_Z \rho_Z \quad (27)$$

Momentum:

$$\frac{\partial}{\partial t}(\rho_m \vec{u}_m) + \nabla \cdot (\rho_m \vec{u}_m \vec{u}_m) = -\nabla P_m + \nabla \cdot [\mu_m (\nabla \vec{u}_m + \nabla \vec{u}_m^T)] + \rho_m \beta_m (T - T_0) \mathbf{g} \quad (28)$$

where

$$\mu_m = \sum_{Z=1}^n \varphi_Z \mu_Z \quad (29)$$

Energy:

$$\frac{\partial}{\partial t} \rho_m h_m + \nabla \cdot (\rho_m h_m \vec{u}_m) + \nabla \cdot (P \vec{u}_m) = \nabla \cdot (k_m \nabla T) \quad (30)$$

where

$$\rho_m h_m = \sum_{Z=1}^n (\varphi_Z \rho_Z h_Z) \quad (31)$$

and

$$k_m = \sum_{Z=1}^n \varphi_Z (k_Z) \quad (32)$$

As a pioneer, Behzadmehr et al. [44] employed single-phase approach as well as two-phase mixture model to study the turbulent heat transfer of copper-water nanofluid inside a circular tube. The results of their study revealed that the obtained results from mixture model are much closer to experimental data, compared to the results of single-phase model. In a similar study, Bianco et al. [52] analyzed the steady-state turbulent convection heat transfer of Al_2O_3 -water nanofluid in a circular tube under constant heat flux. FLUENT commercial software was used to solve the governing equations. The results showed that single-phase and mixture models give approximately the same results at low concentrations (i.e., $\varphi = 1\%$), while for higher concentrations, the difference between two models is considerable.

Shariat et al. simulated alumina-water nanofluid in an elliptic tube [53]. The impacts of nanoparticles mean diameter and buoyancy force on the nanofluid flow behaviors were investigated in that study. The three-dimensional equations of the mixture model were solved by using FVM. The results showed that at a specified value of Reynolds and Richardson numbers, an increase in nanoparticles size diminishes the Nusselt number while it does not have a remarkable effect on the friction factor. A non-linear relation between the nanoparticles size and heat transfer characteristics of nanofluid was also observed.

Laminar-free convection heat transfer of alumina-water nanofluid inside a cavity was studied by Corcione et al. [54]. The governing equations were solved by a CFD code based on a two-phase mixture model. Temperature-dependent effective properties considering the Brownian motion and thermophoresis were employed and different nanoparticles volume fractions were analyzed. It was found that the heat transfer trend reached a peak value at maximum particle loading. Using these results, new correlations were developed for different parameters such as the optimal particle loading and a maximum value of the heat transfer augmentation.

Goodarzi et al. [51] investigated both laminar and turbulent mixed convection of Cu-water nanofluid inside a rectangular shallow cavity. The upper movable lid of the cavity was considered at a lower temperature, compared to the bottom wall. FLUENT commercial code was utilized to solve the problem, along with some modifications in governing equations by developing user-defined function (UDF) codes. The results showed that the impact of the volume fraction on turbulent kinetic energy, turbulence intensity, skin friction, and wall shear stress is insignificant. However, under similar conditions, lower Richardson number leads to higher wall shear stress and turbulence kinetics energy.

The single- and two-phase models were employed by Naphon and Nakharintr [55] to investigate the 3-D laminar convection heat transfer of nanofluids inside a mini-channel heat sink. Some experiments were also carried out for validation purpose. The research outcomes demonstrated that two-phase mixture model is in better agreement with experimental results, compared to single-phase model.

Recently, Siavashi et al. [56] investigated the application of nanofluids and porous media to enhance the heat transfer inside an annular pipe. The simulation was conducted to investigate the effects of different parameters such as the Darcy and Reynolds numbers as well as porous medium radius and its position on heat transfer enhancement, heat loss, and entropy generation. Two-phase mixture model along with Darcy-Brinkman-Forchheimer equation was employed for nanofluid flow simulation in porous media. A FVM code was developed to solve the governing equations. The results showed that the geometry, nanoparticle concentration, and magnitude of the Reynolds number have considerable effects on both the performance and entropy generation numbers.

By reviewing the literature, it can be seen that among different multiphase approaches, the mixture model is the most popular model for nanofluids modeling. This popularity can be due to some facts such as accuracy, simplicity in both theory and implementation, and low computational cost. However, for using this model there are some limitations and requirements, which were addressed in detail by Moraveji and Ardehali [49], Bahiraei [50], and Goodarzi et al. [51].

2.2.2.3. Eulerian model

In this model, pressure is assumed to be equal for all the phases, while other governing equations are solved separately for primary and secondary phases. The volume of the two phases is estimated by integrating the volume fraction on solution domain, where the aggregate of volume fractions totality becomes one [50]. The Eulerian model corresponding equations can be expressed as follows [42]:

Continuity:

$$\nabla \cdot (\varphi_z \rho_z \vec{u}_z) = 0 \tag{33}$$

where $\vec{u}_z = \int_V \varphi_z dv$, $\sum_{z=1}^n \varphi_z = 1$.

Conservation of momentum (z^{th} phase):

$$\nabla \cdot (\varphi_z \rho_z \vec{u}_z \vec{u}_z) = \sum_{p=1}^n \vec{R}_{pz} + F_{\text{lift}_z} + \varphi_z \nabla \cdot (\mu_z \nabla \vec{u}) + \varphi_z \rho_z \vec{g} - \varphi_z \nabla P \tag{34}$$

where $\sum_{p=1}^n \vec{R}_{pz} = \sum_{p=1}^n S_{pz} (\vec{u}_p - \vec{u}_z)$ denotes the interaction force between phases, $S_{pz} = (\varphi_z \varphi_p \rho_p f) / \tau_p$, $\tau_p = (\rho_p d_p^2) / (18 \mu_z)$, and f indicates the drag friction, which is computed by Schiller and Naumann [57] recommendation:

$$f = \frac{C_D Re_p}{24} \quad (35)$$

where

$$C_D = \begin{cases} \frac{24(1 + 0.15 Re_p^{0.687})}{Re_p} & Re \leq 1000 \\ 0.44 & Re > 1000 \end{cases} \quad (36)$$

The nanoparticle Reynolds number (Re_p) in Eq. (36) and lift force in Eq. (34) [58] are, however, based on particle-fluid relative velocity, which is extremely small for nanoparticles.

$$Re_p = \frac{\rho_f |\vec{u}_p - \vec{u}_z| d_p}{\mu_z} \cong 0 \quad (37)$$

$$F_{lift,z} = -\frac{1}{2} \rho_z \varphi_z (\vec{u}_p - \vec{u}_z) \times (\nabla \times \vec{u}_z) \cong 0 \quad (38)$$

Considering Eq. (37), the first two terms on the right side of Eq. (34) should be ignored.

Conservation of energy:

$$\nabla \cdot (\varphi_z \rho_z \vec{u}_z h_z) = -\nabla \cdot (k_z \nabla T_z) - \tau_q : \nabla \vec{u}_z + \sum_{p=1}^n \vec{Q}_{pz} \quad (39)$$

Where $\vec{Q}_{pz} = h (\vec{u}_p - \vec{u}_z)$ is the heat exchange coefficient and $h = \frac{6k_q \varphi_q \varphi_p N u_p}{d_p^2}$. Also, $N u_p$ is calculated from Eq. (21).

Kalteh et al. [59] investigated the laminar-forced convection heat transfer of Cu-water nanofluid inside a microchannel. The Eulerian model utilized for flow simulation and governing equations was solved by FVM. The results demonstrated that the nanoparticles are distributed uniformly inside the solution domain. The two-phase model also presented a higher heat transfer augmentation compared to the single-phase model.

Laminar- and turbulent-forced convection of nanofluids inside small tubes were investigated by Chen et al. [60]. The multiphase flow was simulated using both mixture and Eulerian models and the results were compared with experimental data as well as the correlations from the literature. The obtained results for two models were quite similar, although mixture approach results showed better agreement with experimental results.

Thermal behavior and nanofluid flow at the entrance region of a pipe under constant heat flux were modeled by Göktepe et al. [61]. The results demonstrated that two-phase models predict heat transfer coefficient and friction factor with a higher accuracy at the entrance region, compared to the single-phase model. The authors also suggested that more suitable relations for nanoparticles are required to enhance the forecast accuracy of the Eulerian model.

Recently, Sadeghi et al. [62] studied nanoparticle aggregation effect on laminar convection heat transfer of alumina-water nanofluid in a circular tube. The Eulerian model was implemented according to nanoclusters Brownian motion and their fractal structure. The governing equations were solved using ANSYS CFX commercial software. The results revealed that nanoparticles size and concentration as well as fractional structure have undeniable effects on heat transfer phenomenon of nanofluid. Also, it was noted that Brownian motion can affect the convective heat transfer of nanofluids significantly.

All in all, it can be concluded that the main advantage of the Eulerian model in comparison to single-phase model is that there is no need to apply effective property models for the nanofluids [59]. However, it may not be as precise as the mixture model [17, 60].

2.3. Other approaches

2.3.1. Lattice-Boltzmann Method

Lately, Lattice-Boltzmann method or Thermal Lattice-Boltzmann method has become an attractive alternative to simulate the nanofluids flow. The gap between microscopic and macroscopic phenomena is removed by employing Lattice-Boltzmann method since it considers molecular dynamics [50]. In Lattice-Boltzmann method, the conservation equations are resolved by the assumption that the nanoparticles are microscopically located in a chain of lattices where their distributions are determined based on Boltzmann method. In the paper of Succi [63], microscopic interaction between the nanoparticles was numerically modeled utilizing a collision model and microscopic and macroscopic quantities of components were joined together. Also in [64, 65], two more different methods were employed, namely D2Q9 (two-dimensional and 9-velocity) square and D3Q19 (three-dimensional and 19-velocity) cube lattice structures. In Lattice-Boltzmann method, it is easy to deal with the complex boundaries; also, the other advantages of this method include physical representation of microscopic interactions and the existence of uniform algorithms to solve the multiphase flows [65].

For the first time, Xuan and Yao [66] proposed LBM for simulating flow and energy transport of the nanofluids. After this study, the use of this method was rapidly increased. Considering interaction forces such as Brownian, gravity-buoyancy, drag, and interaction potential forces between two phases, Qi et al. [67] studied the free convection of nanofluid using a two-phase Lattice-Boltzmann model. It was found that while Brownian, gravity-buoyancy, and interaction potential forces have positive impacts on the augmentation of free convection, drag force has a negative impact.

Karimipour et al. [68] studied laminar-forced convective heat transfer of copper-water nanofluid inside a microchannel using double-population LBM-BGK method. The obtained

results of this study were in a fair agreement with previous studies, which shows that LBM could be utilized to simulate forced convection for the nanofluids flow inside micro-sized configurations.

Recently, by employing a 2-D double multiple-relaxation-time (MRT) thermal Lattice-Boltzmann model, Zhang and Che [69] simulated the magneto-hydrodynamic (MHD) flow and heat transfer of copper water in an inclined cavity with four heat sources. The governing equations were solved using D2Q9- and D2Q5-MRT models, which was validated by previous investigations. The results showed that the inclination angle has a considerable effect on flow fields, the temperature patterns, and the local Nusselt number distributions. Moreover, it was concluded that MRT Lattice-Boltzmann method is competent for solving heat transfer of nanofluids in enclosures affected by a magnetic field.

In the end, LBM has been widely used for natural, forced, and mixed convection of nanofluids, which can be found in details [70, 71]. The results of this model have higher accuracy than the results of conventional CFD approaches. However, it seems that more research may be needed in order to find out to what extent LBM is applicable in the simulation of nanofluids flow and characteristics.

2.3.2. Non-homogeneous two-component model (Buongiorno model)

Buongiorno [72] investigated the effects of seven different slip mechanisms between the base fluid and nanoparticles: gravity, thermophoresis, Brownian diffusion, inertia, Magnus effect, fluid drainage and diffusiophoresis, in the absence of turbulent effects. It was demonstrated that thermophoresis and Brownian diffusion are the most influential mechanisms on nanofluids flow and heat transfer, which can affect nanoparticle concentration variations. Under such conditions, the four coupled governing equations were proposed as follows [73, 74]:

Conservation of mass:

$$\nabla \cdot (\rho_{nf} \vec{u}) = 0 \quad (40)$$

Conservation of momentum:

$$\nabla \cdot (\rho_{nf} \vec{u} \vec{u}) = -\nabla P + \nabla \cdot (\mu_{nf} \nabla \vec{u}) \quad (41)$$

Conservation of energy:

$$\nabla \cdot ((\rho c_p)_{nf} \vec{u} T) = \nabla \cdot (k_{nf} \nabla T) - c_{p, np} \vec{J}_{np} \cdot \nabla T \quad (42)$$

Conservation of nanoparticles:

$$\vec{u} \cdot \nabla \varphi = -\frac{1}{\rho_{np}} \nabla \cdot \vec{J}_{np} \quad (43)$$

where \vec{J}_{np} is nanoparticles flux and is defined as

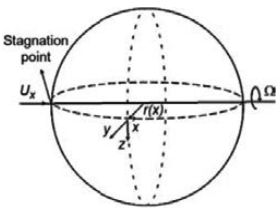
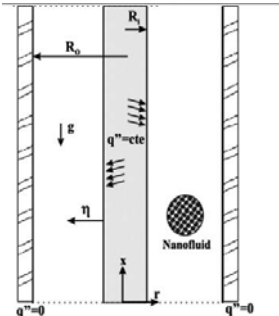
$$\vec{J}_{np} = \vec{J}_{np_{Br}} + \vec{J}_{np_T} \quad (44)$$

The aforementioned terms can be calculated as follows [75]:

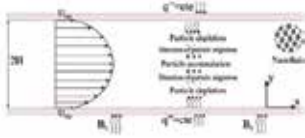
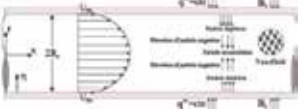
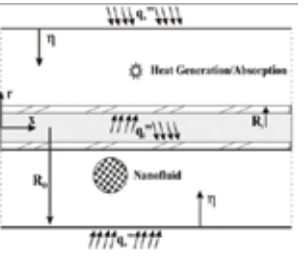
$$\vec{J}_{np_{Br}} = \frac{k_{Br} T}{3\pi\mu_f d_{np}} \quad (45)$$

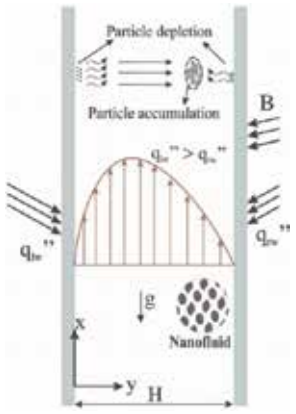
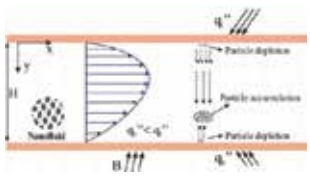
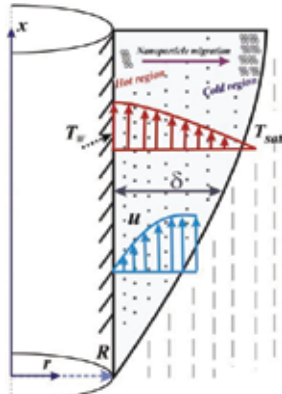
$$\vec{J}_{np_T} = 0.26 \left(\frac{k_f}{2k_f + k_{np}} \frac{\mu_f}{\rho_f} \varphi \right) \quad (46)$$

where D represents the diffusion coefficient.

| Authors | Geometry of study | Type of nanofluid | Properties | Remarks |
|----------------------|-------------------------------------------------------------------------------------|-----------------------------------------------------------------------------|----------------------------------------------------------------------------------------------------|--------------------------------------------------------------------------------------------------------------------------------------------------------------------------------------------------------------------------------------------------------------------------------------------|
| Malvandi [79] |  | Non-homogeneous mixtures | $1 \text{ nm} \leq d_p \leq 100 \text{ nm}$ $0 \leq \phi \leq 0.2$ | Increasing the thermophoresis is found to decrease heat transfer and concentration rates. This decrease suppresses for higher thermophoresis number. In addition, it was observed that unlike the heat transfer rate, a rise in Brownian motion leads to an increase in concentration rate |
| Malvandi et al. [80] |  | Al ₂ O ₃ and TiO ₂ /water-based nanofluids | $1 \text{ nm} \leq d_p \leq 100 \text{ nm}$ $0 \leq \phi \leq 0.1$ $0.1 \leq N_{BT} \leq 10$ | The buoyancy has negative effect on the efficiency of nanoparticle inclusion; however, slip velocity at the surface enhances both the heat transfer rate and the efficiency |

| Authors | Geometry of study | Type of nanofluid | Properties | Remarks |
|----------------------|-------------------|-------------------------------------------------|-------------------------------------------------------------------------------------------------------------------------|-------------------------------------------------------------------------------------------------------------------------------------------------------------------------------------------------------------------------------------------------------------------------------------------------------------------------------------------------------------------------------------------------------------------|
| Malvandi, Ganji [81] | | Al ₂ O ₃ /water nanofluid | $1\text{ nm} \leq d_p \leq 100\text{ nm}$ $0 \leq \phi \leq 0.1$ $0.1 \leq N_{BT} \leq 10$ $0 \leq Ha \leq 10$ | The heat transfer rate is enhanced by the presence of the magnetic field especially for the smaller nanoparticles. Moreover, as the magnetic field strength (Ha) intensifies, the peak of the velocity profile near the walls is increased; however, the peak of the velocity profile at the core region is decreased. |
| Malvandi, Ganji [82] | | Al ₂ O ₃ /water nanofluid | $1\text{ nm} \leq d_p \leq 100\text{ nm}$ $0 \leq \phi \leq 0.1$ $4 \leq N_{BT} \leq 10$ | The concentration of nanoparticles is higher near the cold wall (nanoparticles accumulation), while it is lower near the adiabatic wall (nanoparticles depletion). Also, there is an optimum value for the bulk mean of nanoparticle volume fraction in which the heat transfer rate is maximum. This optimum value decreases for smaller nanoparticles. |
| Malvandi et al. [83] | | Al ₂ O ₃ /water nanofluid | $1\text{ nm} \leq d_p \leq 100\text{ nm}$ $0 \leq \phi \leq 0.1$ $0.1 \leq N_{BT} \leq 10$ $0 \leq Ha \leq 15$ | In the presence of the magnetic field, the velocity gradients near the wall grow, which increases the slip velocity at boundaries and thus the heat transfer rate intensifies. What is more? Increasing Ha (intensifying the magnetic field) leads to an increase in the Lorentz force (a retarding force to the transport phenomena), which tends to resist the fluid flow and thus reduces the flow's velocity. |

| Authors | Geometry of study | Type of nanofluid | Properties | Remarks |
|----------------------|-------------------------------------------------------------------------------------|-------------------------------------------------|---------------------------------------------------------------------------------------------------------------------------|--------------------------------------------------------------------------------------------------------------------------------------------------------------------------------------------------------------------------------------------------------------------------------------------------------------------------------------------------------------------------------------------------------------------------------|
| Malvandi, Ganji [84] |  | Al ₂ O ₃ /water nanofluid | $1 \text{ nm} \leq d_p \leq 100 \text{ nm}$ $0 \leq \phi \leq 0.1$ $0.2 \leq N_{BT} \leq 10$ $0 \leq Ha \leq 10$ | <p>Obtained results indicated that nanoparticles move from the heated walls (nanoparticles depletion) toward the core region of the channel (nanoparticles accumulation) and construct a non-uniform nanoparticle distribution.</p> <p>Moreover, in the presence of the magnetic field, the near-wall velocity gradients increase, enhancing the slip velocity and thus the heat transfer rate and pressure drop increase.</p> |
| Malvandi, Ganji [85] |  | Al ₂ O ₃ /water nanofluid | $1 \text{ nm} \leq d_p \leq 100 \text{ nm}$ $0 \leq \phi \leq 0.1$ $0.2 \leq N_{BT} \leq 10$ $0 \leq Ha \leq 10$ | <p>Nanoparticles concentration is higher in the core region of the microchannel (nanoparticles accumulation) while taking its minimum values closer to the heated wall (nanoparticles depletion). That is to say, nanoparticles move from the heated wall toward the core region and construct a non-uniform nanoparticle distribution.</p> |
| Moshizi et al. [86] |  | Al ₂ O ₃ /water nanofluid | $1 \text{ nm} \leq d_p \leq 100 \text{ nm}$ $0 \leq \phi \leq 0.1$ $0.2 \leq N_{BT} \leq 10$ | <p>In the case of heat absorption, by imposing heatflux at both walls, the dimensional temperature profile becomes to be more uniform. The variations on the heat transfer coefficient enhancement in the case of heat absorption are smaller than in the case of heat generation, for a moderate range of NBT.</p> <p>Furthermore, the heat absorption boosts the pressure drops of nanofluid.</p> |

| Authors | Geometry of study | Type of nanofluid | Properties | Remarks |
|----------------------|-----------------------------------------------------------------------------------------------------------------------------------------------------------------------------------------------------------------------------------------------------------------------------------------------------------------------------------------------------------------------------------------------------------------------------------------------------------|-----------------------------------------------------------------------------|-------------------------------------------------------------------------------------------------------------------------|---------------------------------------------------------------------------------------------------------------------------------------------------------------------------------------------------------------------------------------------------------------------------------------------------------------------------------|
| Malvandi, Ganji [87] |  <p>The diagram shows a vertical channel of height H. Heat flux q_w'' is applied from both sides. A velocity profile u is shown as a downward curve. Nanoparticles are shown with arrows indicating 'Particle depletion' near the walls and 'Particle accumulation' in the center. A coordinate system (x, y) is shown at the bottom left.</p> | Al ₂ O ₃ /water nanofluid | $1\text{ nm} \leq d_p \leq 100\text{ nm}$ $0 \leq \phi \leq 0.1$ $0.2 \leq N_{BT} \leq 10$ $0 \leq Ha \leq 10$ | It is shown that nanoparticles eject themselves from the heated walls, construct a depleted region, and accumulate in the core region, but they are more likely to accumulate toward the wall with the lower heat flux. |
| Malvandi et al. [88] |  <p>The diagram shows a channel with heat flux q_w'' applied from both sides. A velocity profile u is shown. Nanoparticles are shown with arrows indicating 'Particle depletion' near the walls and 'Particle accumulation' in the center. A coordinate system (x, y) is shown at the bottom left.</p> | Al ₂ O ₃ /water nanofluid | $1\text{ nm} \leq d_p \leq 100\text{ nm}$ $0 \leq \phi \leq 0.1$ $0.2 \leq N_{BT} \leq 10$ $0 \leq Ha \leq 10$ | The non-uniform nanoparticle distribution makes the velocities move toward the wall with the higher heat flux and enhances the heat transfer rate there. In addition, it is shown that the advantage of nanoparticle inclusion is increased in the presence of a magnetic field, though heat transfer enhancement is decreased. |
| Malvandi et al. [89] |  <p>The diagram shows a curved channel with radius R. A temperature profile T is shown as a red curve, and a velocity profile u is shown as a blue curve. The channel is divided into 'Hot region' and 'Cold region'. A coordinate system (x, r) is shown at the bottom left.</p> | Al ₂ O ₃ and TiO ₂ /water-based nanofluids | $1\text{ nm} \leq d_p \leq 100\text{ nm}$ $0 \leq \phi \leq 0.06$ $0.2 \leq N_{BT} \leq 10$ | The heat transfer enhancement of titania-water nanofluids is completely insignificant relative to such enhancement for alumina-water nanofluid. Therefore, alumina-water nanofluid exhibits a better performance compared to titania-water nanofluids. |

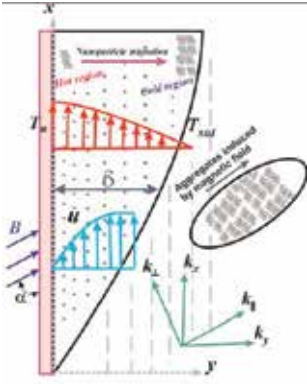
| Authors | Geometry of study | Type of nanofluid | Properties | Remarks |
|---------------|------------------------------------------------------------------------------------------------------------------------------------------------------------------------------------------------------------------------------------------------------------------------------------------------------------------------------------------------------------|-------------------------------------------------|-----------------------------------------------------------------------------------------------------------------------------------------------------------|---------------------------------------------------------------------------------------------------------------------------------------------------------------------------------------------------------------------------------------------------------|
| Malvandi [90] |  <p>The diagram illustrates a vertical annular pipe with a coordinate system (x, y). It shows temperature profiles (red and blue) and a magnetic field vector B. A region of nanoparticle migration is highlighted with a circular inset showing a grid of particles.</p> | Fe ₃ O ₄ -water nanofluid | $1\text{ nm} \leq d_p \leq 100\text{ nm}$ $0 \leq \phi \leq 0.06$ $0.2 \leq N_{BT} \leq 10$ $0 \leq Ha \leq 5$ $45^\circ < \alpha < 90^\circ$ | A closed-form expression for the distribution of nanoparticle volume fraction has been obtained. It has been shown that the heat transfer rate is improved further when an external magnetic field exerts in the direction of the temperature gradient. |

Table 1. Some recent studies on modified Buongiorno model.

Sheikhzadeh et al. [76] studied the effects of Brownian motion, thermophoresis, and Dufour (transport model) on laminar-free convection heat transfer of alumina-water nanofluid flow in a square enclosure. Variable thermophysical properties utilized for fluid characterization and the governing equations were discretized using FVM. The results illustrated that the Dufour effect on heat transfer is not significant. In addition, a comparison between experimental data and numerical results revealed that the transport model is in better agreement with experimental results, compared to single-phase model.

Using the same method, Bahiraei et al. [77] studied the laminar convection heat transfer of alumina-water nanofluid inside a circular tube, considering particle migration effects. The results showed that with the Reynolds number or volume fraction augmentation, the average heat transfer coefficient enhances. In addition, it was reported that by considering the particle migration effect, higher heat transfer coefficient would be achieved.

Using modified Buongiorno model, Malvandi et al. [78] investigated MHD mixed convection heat transfer for Al₂O₃-water nanofluid inside a vertical annular pipe. The governing equations reduced to two-point O.D.E.s, which were solved by means of the Runge-Kutta-Fehlberg scheme. The obtained results indicated that the excellence of using nanofluids for heat transfer enhancement purpose is diminished by the presence of a magnetic field. Moreover, it was noted that the imposed thermal asymmetry may change the direction of nanoparticle migration, and, hence, alters the velocity, temperature, and nanoparticle concentration profiles.

Table 1 shows some new works on modified Buongiorno model.

2.3.3. Other approaches

In some other studies, novel numerical approaches have been employed to solve the governing equations of nanofluids. SPH method has been used by Mansour and Bakier [91] to study free convection within an enclosed cavity filled with Al₂O₃ nanoparticles. The left and right walls

of the cavity had a complex-wavy geometry while upper and lower walls were both flat and insulated. Complex-wavy walls were modeled as the superposition of two sinusoidal functions. The results revealed that heat transfer performance may be optimized by tuning the wavy-surface geometry parameter in accordance with the Rayleigh number. Using optimal homotopy analysis method (OHAM), Nadeem et al. [92] examined 2-D stagnation point flow of a non-Newtonian Casson nanofluid over a convective-stretching surface. The governing non-linear partial differential equations were converted into non-linear ordinary differential equations and solved analytically using OHAM. The results showed that heat transfer rate is an increasing function of the stretching parameter, Prandtl and Biot numbers and it decreases with an increase in non-Newtonian parameter, Brownian motion, and thermophoresis.

The laminar axisymmetric flow of a nanofluid over a non-linearly stretching sheet was studied by Mustafa et al. [93], both numerically and analytically. The simultaneous effects of Brownian motion and thermophoretic diffusion of nanoparticles were taken into account. The numerical solution was computed by employing implicit finite difference scheme known as Keller-Box method. The results obtained from both solutions were in excellent agreement with each other. The results demonstrated that the effect of Brownian motion on fluid temperature and wall heat transfer rate is insignificant. Moreover, it was reported that increases in Schmidt number lead to a thinner nanoparticle volume fraction boundary layer.

3. Conclusion

A comprehensive review of popular methods in the simulation of the nanofluids was carried out. Different CFD approaches including single-phase, multiphase, and other methods were reviewed. For each model, the governing equations and recent literature were studied.

Conventional single-phase model was the most common method to study the convective heat transfer of nanofluids. This can be due to the fact that this model simplifies the simulation and in comparison to other models has the lowest computational cost. However, the results obtained from this model may have some deviation from the experimental data. For instance, it was reported in many studies that homogeneous model underestimates the heat transfer coefficient and Nusselt number, when compared to the dispersion and two-phase models. However, it was also revealed that using the temperature-dependent thermophysical properties in homogeneous model can lead to more realistic results. On the other hand, dispersion model for both constant and temperature-dependent properties showed promising results, compared with experimental data. This model requires less computational time compared to two-phase model. In addition, the model takes into account thermal dispersion effect, which leads to more reliable results in comparison with the homogeneous model.

Nanofluids are inherently multiphase fluids; therefore, employing two-phase model taking into account the slip velocity, Brownian motion, thermophoresis, and so forth, can lead to more appropriate results. Most of the publications confirmed that different two-phase models predict more accurate results than the homogeneous model. Also, higher values of the heat transfer coefficient were reported for two-phase models, compared to conventional single-

phase model. A vast number of studies utilized the mixture and Eulerian models, and to smaller extent VOF and Lagrangian-Eulerian models. Some publications noted that among all two-phase models, mixture model predicts more precise results compared with experimental data. However, this model has some limitation and cannot be applied in some cases. On the other hand, since VOF and Lagrangian-Eulerian models are employed less than other two-phase models, it seems that further research might be needed to assess their precision in nanofluids simulation.

In the end, LBM and non-homogeneous two-component models are rather novel approaches, used in several cases. The results predicted by these approaches showed a promising accordance with the results obtained from previous studies. Moreover, according to literature, these methods may present some well-known advantages in the modeling of nanofluids. Obviously, more attempts should be made to find the flow characteristics of nanofluids in various systems and in the presence of different modes of heat transfer in order to examine the aforementioned approaches.

Acknowledgements

The authors gratefully acknowledge High Impact Research Grant UM.C/HIR/MOHE/ENG/23 and the Faculty of Engineering, University of Malaya, Malaysia, for support in conducting this research work.

Nomenclature

| | |
|-----------|--------------------------------------------|
| d | Diameter (m) |
| C_D | Drag coefficient |
| V | volume (m^3) |
| F | Force ($kg\ m/s^2$) |
| m | mass (kg) |
| u, v | Flow velocity in x - y direction (m/s) |
| P | Fluid pressure (Pa) |
| \vec{g} | Gravity acceleration (m/s^2) |
| C_p | Heat capacity (J/kg K) |
| Nu | Nusselt number |
| Re | Reynolds number |
| h | Sensible enthalpy (J/Kg) |
| T | Temperature (K) |

| | |
|-----|------------------------------------------------|
| k | Thermal conductivity (W/m K) |
| t | Time (s) |
| u | Velocity components in x, y directions (m/s) |

Greek symbols

| | |
|----------|-----------------------------------------------|
| α | thermal diffusivity (m^2/s) |
| ρ | Density (kg/m^3) |
| μ | Dynamic viscosity (Pa s) |
| ϕ | Nanoparticle volume fraction |
| β | Thermal expansion coefficient (1/K) |

Super- and Subscripts

| | |
|------|-----------------|
| Br | Brownian motion |
| eff | Effective |
| f | Fluid |
| Z, q | Indices |
| np | nanoparticle |
| m | Mixture |
| nf | Nanofluid |
| p | Particle |
| T | Thermophoresis |

Author details

Mohammad Reza Safaei^{1*}, AminHossein Jahanbin², Ali Kianifar³, Samira Gharehkhani¹, Akeel Shebeeb Kherbeet⁴, Marjan Goodarzi⁵ and Mahidzal Dahari⁶

*Address all correspondence to: cfid_safaei@um.edu.my; cfid_safaei@yahoo.com

1 Department of Mechanical Engineering, Faculty of Engineering, University of Malaya, Kuala Lumpur, Malaysia

2 Department of Industrial Engineering (DIN), University of Bologna, Bologna, Italy

3 Department of Mechanical Engineering, Engineering Faculty, Ferdowsi University of Mashhad, Mashhad, Iran

4 Department of Mechanical Engineering, KBU International College, Petaling Jaya, Selangor, Malaysia

5 Young Researchers and Elite Club, Mashhad Branch, Islamic Azad University, Mashhad, Iran

6 Department of Electrical Engineering, Faculty of Engineering, University of Malaya, Kuala Lumpur, Malaysia

References

- [1] Yarmand H, Gharehkhani S, Kazi SN, Sadeghinezhad E, Safaei MR. Numerical investigation of heat transfer enhancement in a rectangular heated pipe for turbulent nanofluid. *The Scientific World Journal*. 2014;2014(Article ID 369593):1–9. doi: 10.1155/2014/369593.
- [2] Mojumder S, Sourav S, Sumon S, Mamun M. Combined effect of Reynolds and Grashof numbers on mixed convection in a lid-driven T-shaped cavity filled with water- Al_2O_3 nanofluid. *Journal of Hydrodynamics, Ser B*. 2015;27(5):782–94.
- [3] Abu-Nada E, Chamkha AJ. Mixed convection flow in a lid-driven inclined square enclosure filled with a nanofluid. *European Journal of Mechanics-B/Fluids*. 2010;29(6): 472–82.
- [4] Rostamani M, Hosseinizadeh S, Gorji M, Khodadadi J. Numerical study of turbulent forced convection flow of nanofluids in a long horizontal duct considering variable properties. *International Communications in Heat and Mass Transfer*. 2010;37(10): 1426–31.
- [5] Pak BC, Cho YI. Hydrodynamic and heat transfer study of dispersed fluids with submicron metallic oxide particles. *Experimental Heat Transfer an International Journal*. 1998;11(2):151–70.
- [6] Maiga SEB, Palm SJ, Nguyen CT, Roy G, Galanis N. Heat transfer enhancement by using nanofluids in forced convection flows. *International Journal of Heat and Fluid Flow*. 2005;26(4):530–46.
- [7] Abu-Nada E. Rayleigh-Bénard convection in nanofluids: effect of temperature dependent properties. *International Journal of Thermal Sciences*. 2011;50(9):1720–30.
- [8] Bouhaleb M, Abbassi H. Numerical Investigation Of Heat Transfer By CuO–Water Nanofluid In Rectangular Enclosures. *Heat Transfer Engineering*. 2016;37(1):13–23.

- [9] Togun H, Safaei MR, Sadri R, Kazi SN, Badarudin A, Hooman K et al. Numerical simulation of laminar to turbulent nanofluid flow and heat transfer over a backward-facing step. *Applied Mathematics and Computation*. 2014;239:153–70.
- [10] Yarmand H, Ahmadi G, Gharehkhani S, Kazi SN, Safaei MR, Alehashem MS et al. Entropy generation during turbulent flow of zirconia-water and other nanofluids in a square cross section tube with a constant heat flux. *Entropy*. 2014;16(11):6116–32.
- [11] Togun H, Ahmadi G, Abdulrazzaq T, Shkarah AJ, Kazi S, Badarudin A et al. Thermal performance of nanofluid in ducts with double forward-facing steps. *Journal of the Taiwan Institute of Chemical Engineers*. 2015;47:28–42.
- [12] Selimefendigil F, Öztop HF, Chamkha AJ. Fluid-structure-magnetic field interaction in a nanofluid filled lid-driven cavity with flexible side wall. *European Journal of Mechanics – B/Fluids*. doi:<http://dx.doi.org/10.1016/j.euromechflu.2016.03.009>.
- [13] Selimefendigil F, Öztop HF. Conjugate natural convection in a cavity with a conductive partition and filled with different nanofluids on different sides of the partition. *Journal of Molecular Liquids*. 2016;216:67–77. doi:<http://dx.doi.org/10.1016/j.molliq.2015.12.102>.
- [14] Selimefendigil F, Öztop HF, Chamkha AJ. Mhd mixed convection and entropy generation of nanofluid filled lid driven cavity under the influence of inclined magnetic fields imposed to its upper and lower diagonal triangular domains. *Journal of Magnetism and Magnetic Materials*. 2016;406:266–81. doi:<http://dx.doi.org/10.1016/j.jmmm.2016.01.039>.
- [15] Buddakkagari V, Kumar M. Transient boundary layer laminar free convective flow of a nanofluid over a vertical cone/plate. *International Journal of Applied and Computational Mathematics*. 2015;1(3):427–48.
- [16] Jahanbin AH, Javaherdeh K. Numerical investigation of CuO nanoparticles effect on forced convective heat transfer inside a mini-channel: comparison of different approaches. *Life Science Journal*. 2013;10(8s):183–189.
- [17] Lotfi R, Saboohi Y, Rashidi A. Numerical study of forced convective heat transfer of nanofluids: comparison of different approaches. *International Communications in Heat and Mass Transfer*. 2010;37(1):74–8.
- [18] Ding Y, Wen D. Particle migration in a flow of nanoparticle suspensions. *Powder Technology*. 2005;149(2):84–92.
- [19] Nikkhah Z, Karimipour A, Safaei MR, Forghani-Tehrani P, Goodarzi M, Dahari M et al. Forced convective heat transfer of water/functionalized multi-walled carbon nanotube nanofluids in a microchannel with oscillating heat flux and slip boundary condition. *International Communications in Heat and Mass Transfer*. 2015;68:69–77.

- [20] Safaei M, Togun H, Vafai K, Kazi S, Badarudin A. Investigation of heat transfer enhancement in a forward-facing contracting channel using FMWCNT nanofluids. *Numerical Heat Transfer, Part A: Applications*. 2014;66(12):1321–40.
- [21] Xuan Y, Roetzel W. Conceptions for heat transfer correlation of nanofluids. *International Journal of heat and Mass transfer*. 2000;43(19):3701–7.
- [22] Plumb O, editor. The effect of thermal dispersion on heat transfer in packed bed boundary layers. *ASME/JSME Thermal Engineering Joint Conference*; 1983.
- [23] Hunt M, Tien C. Effects of thermal dispersion on forced convection in fibrous media. *International Journal of Heat and Mass Transfer*. 1988;31(2):301–9.
- [24] Khaled A-R, Vafai K. Heat transfer enhancement through control of thermal dispersion effects. *International Journal of Heat and Mass Transfer*. 2005;48(11):2172–85.
- [25] Mojarrad MS, Keshavarz A, Shokouhi A. Nanofluids thermal behavior analysis using a new dispersion model along with single-phase. *Heat and Mass Transfer*. 2013;49(9):1333–43.
- [26] Zeinali Heris S, Noie SH, Talaii E, Sargolzaei J. Numerical investigation of Al₂O₃/water nanofluid laminar convective heat transfer through triangular ducts. *Nanoscale Research Letters*. 2011;6(1):1.
- [27] Zeinali Heris S, Kazemi-Beydokhti A, Noie S, Rezvan S. Numerical study on convective heat transfer of Al₂O₃/water, CuO/water and Cu/water nanofluids through square cross-section duct in laminar flow. *Engineering Applications of Computational Fluid Mechanics*. 2012;6(1):1–14.
- [28] Heris SZ, Etemad SG, Esfahany MN. Experimental investigation of oxide nanofluids laminar flow convective heat transfer. *International Communications in Heat and Mass Transfer*. 2006;33(4):529–35.
- [29] Zeinali Heris S, Esfahany MN, Etemad SG. Experimental investigation of convective heat transfer of Al₂O₃/water nanofluid in circular tube. *International Journal of Heat and Fluid Flow*. 2007;28(2):203–10.
- [30] Kumar S, Prasad SK, Banerjee J. Analysis of flow and thermal field in nanofluid using a single phase thermal dispersion model. *Applied Mathematical Modelling*. 2010;34(3):573–92.
- [31] Akbaridoust F, Rakhsha M, Abbassi A, Saffar-Avval M. Experimental and numerical investigation of nanofluid heat transfer in helically coiled tubes at constant wall temperature using dispersion model. *International Journal of Heat and Mass Transfer*. 2013;58(1):480–91.
- [32] Safaei M, Mahian O, Garoosi F, Hooman K, Karimipour A, Kazi S et al. Investigation of micro-and nanosized particle erosion in a 90° pipe bend using a two-phase discrete

- phase model. *The Scientific World Journal*. 2014;2014(Article ID 740578):1–12. doi: 10.1155/2014/740578.
- [33] Minkowycz W, Sparrow EM, Murthy J. *Handbook of numerical heat transfer*. Wiley Online Library; New York 1988.
- [34] Mirzaei M, Saffar Avval M, Naderan H. Heat transfer investigation of laminar developing flow of nanofluids in a microchannel based on Eulerian–Lagrangian approach. *The Canadian Journal of Chemical Engineering*. 2014;92(6):1139–49.
- [35] Oosthuizen PH, Carscallen WE. *Introduction to compressible fluid flow*. Boca Raton, FL: CRC Press; 2013.
- [36] Bahremand H, Abbassi A, Saffar-Avval M. Experimental and numerical investigation of turbulent nanofluid flow in helically coiled tubes under constant wall heat flux using Eulerian–Lagrangian approach. *Powder Technology*. 2015;269:93–100.
- [37] Moraveji MK, Esmaeili E. Comparison between single-phase and two-phases CFD modeling of laminar forced convection flow of nanofluids in a circular tube under constant heat flux. *International Communications in Heat and Mass Transfer*. 2012;39(8):1297–302.
- [38] Tahir S, Mital M. Numerical investigation of laminar nanofluid developing flow and heat transfer in a circular channel. *Applied Thermal Engineering*. 2012;39:8–14.
- [39] Behroyan I, Ganesan P, He S, Sivasankaran S. Turbulent forced convection of Cu–water nanofluid: CFD model comparison. *International Communications in Heat and Mass Transfer*. 2015;67:163–72.
- [40] Vanaki SM, Ganesan P, Mohammed H. Numerical study of convective heat transfer of nanofluids: a review. *Renewable and Sustainable Energy Reviews*. 2016;54:1212–39.
- [41] Xu P, Wu Z, Mujumdar A, Yu B. Innovative hydrocyclone inlet designs to reduce erosion-induced wear in mineral dewatering processes. *Drying Technology*. 2009;27(2): 201–11.
- [42] Akbari M, Galanis N, Behzadmehr A. Comparative analysis of single and two-phase models for Cfd studies of nanofluid heat transfer. *International Journal of Thermal Sciences*. 2011;50(8):1343–54.
- [43] Akbari M, Galanis N, Behzadmehr A. Comparative assessment of single and two-phase models for numerical studies of nanofluid turbulent forced convection. *International Journal of Heat and Fluid Flow*. 2012;37:136–46.
- [44] Behzadmehr A, Saffar-Avval M, Galanis N. Prediction of turbulent forced convection of a nanofluid in a tube with uniform heat flux using a two phase approach. *International Journal of Heat and Fluid Flow*. 2007;28(2):211–9.

- [45] Hejazian M, Moraveji MK, Beheshti A. Comparative numerical investigation on TiO₂/water nanofluid turbulent flow by implementation of single phase and two phase approaches. *Numerical Heat Transfer, Part A: Applications*. 2014;66(3):330–48.
- [46] Naphon P, Nakharintr L. Turbulent two phase approach model for the nanofluids heat transfer analysis flowing through the minichannel heat sinks. *International Journal of Heat and Mass Transfer*. 2015;82:388–95.
- [47] Hanafizadeh P, Ashjaee M, Goharkhah M, Montazeri K, Akram M. The comparative study of single and two-phase models for magnetite nanofluid forced convection in a tube. *International Communications in Heat and Mass Transfer*. 2015;65:58–70.
- [48] El-Batsh H, Doheim M, Hassan A. On the application of mixture model for two-phase flow induced corrosion in a complex pipeline configuration. *Applied Mathematical Modelling*. 2012;36(11):5686–99.
- [49] Moraveji MK, Ardehali RM. Cfd modeling (comparing single and two-phase approaches) on thermal performance of Al₂O₃/water nanofluid in mini-channel heat sink. *International Communications in Heat and Mass Transfer*. 2013;44:157–64.
- [50] Bahiraei M. A comprehensive review on different numerical approaches for simulation in nanofluids: traditional and novel techniques. *Journal of Dispersion Science and Technology*. 2014;35(7):984–96.
- [51] Goodarzi M, Safaei M, Vafai K, Ahmadi G, Dahari M, Kazi S et al. Investigation of nanofluid mixed convection in a shallow cavity using a two-phase mixture model. *International Journal of Thermal Sciences*. 2014;75:204–20.
- [52] Bianco V, Manca O, Nardini S. Numerical investigation on nanofluids turbulent convection heat transfer inside a circular tube. *International Journal of Thermal Sciences*. 2011;50(3):341–9.
- [53] Shariat M, Moghari RM, Akbarinia A, Rafee R, Sajjadi S. Impact of nanoparticle mean diameter and the buoyancy force on laminar mixed convection nanofluid flow in an elliptic duct employing two phase mixture model. *International Communications in Heat and Mass Transfer*. 2014;50:15–24.
- [54] Corcione M, Cianfrini M, Quintino A. Two-phase mixture modeling of natural convection of nanofluids with temperature-dependent properties. *International Journal of Thermal Sciences*. 2013;71:182–95.
- [55] Naphon P, Nakharintr L. Numerical investigation of laminar heat transfer of nanofluid-cooled mini-rectangular fin heat sinks. *Journal of Engineering Physics and Thermophysics*. 2015;88(3):666–75.
- [56] Siavashi M, Bahrami HRT, Saffari H. Numerical investigation of flow characteristics, heat transfer and entropy generation of nanofluid flow inside an annular pipe partially or completely filled with porous media using two-phase mixture model. *Energy*. 2015;93:2451–66.

- [57] Schiller L, Naumann Z. A drag coefficient correlation. *Vdi Zeitung*. 1935;77(318):51.
- [58] Drew D, Lahey R. Analytical modeling of multiphase flow. In: *Particulate two-phase flow*. Butterworth–Heinemann Boston 1993:509–66.
- [59] Kalteh M, Abbassi A, Saffar-Avval M, Harting J. Eulerian–Eulerian two-phase numerical simulation of nanofluid laminar forced convection in a microchannel. *International journal of heat and fluid flow*. 2011;32(1):107–16.
- [60] Chen Y-j, Li Y-y, Liu Z-h. Numerical simulations of forced convection heat transfer and flow characteristics of nanofluids in small tubes using two-phase models. *International Journal of Heat and Mass Transfer*. 2014;78:993–1003.
- [61] Göktepe S, Atalık K, Ertürk H. Comparison of single and two-phase models for nanofluid convection at the entrance of a uniformly heated tube. *International Journal of Thermal Sciences*. 2014;80:83–92.
- [62] Sadeghi R, Haghshenasfard M, Etemad SG, Keshavarzi E. Theoretical investigation of nanoparticles aggregation effect on water-alumina laminar convective heat transfer. *International Communications in Heat and Mass Transfer*. 2016;72:57–63.
- [63] Succi S. Lattice Boltzmann equation: failure or success? *Physica A: Statistical Mechanics and its Applications*. 1997;240(1):221–8.
- [64] Karimipour A, Esfe MH, Safaei MR, Semiromi DT, Jafari S, Kazi S. Mixed convection of copper–water nanofluid in a shallow inclined lid driven cavity using the Lattice Boltzmann method. *Physica A: Statistical Mechanics and its Applications*. 2014;402:150–68.
- [65] Zhang J. Lattice Boltzmann method for microfluidics: models and applications. *Microfluidics and Nanofluidics*. 2011;10(1):1–28.
- [66] Xuan Y, Yao Z. Lattice Boltzmann model for nanofluids. *Heat and mass transfer*. 2005;41(3):199–205.
- [67] Qi C, He Y, Yan S, Tian F, Hu Y. Numerical simulation of natural convection in a square enclosure filled with nanofluid using the two-phase Lattice Boltzmann method. *Nanoscale Research Letters*. 2013;8(1):1–16.
- [68] Karimipour A, Nezhad AH, D'Orazio A, Esfe MH, Safaei MR, Shirani E. Simulation of copper–water nanofluid in a microchannel in slip flow regime using the Lattice Boltzmann method. *European Journal of Mechanics-B/Fluids*. 2015;49:89–99.
- [69] Zhang T, Che D. Double Mrt thermal Lattice Boltzmann simulation for MHD natural convection of nanofluids in an inclined cavity with four square heat sources. *International Journal of Heat and Mass Transfer*. 2016;94:87–100.
- [70] Kamyar A, Saidur R, Hasanuzzaman M. Application of computational fluid dynamics (CFD) for nanofluids. *International Journal of Heat and Mass Transfer*. 2012;55(15–16): 4104–15.

- [71] Sidik NAC, Razali SA. Lattice Boltzmann method for convective heat transfer of nanofluids—a review. *Renewable and Sustainable Energy Reviews*. 2014;38:864–75.
- [72] Buongiorno J. Convective transport in nanofluids. *Journal of Heat Transfer*. 2006;128(3):240–50.
- [73] Malvandi A, Ganji D. Effects of nanoparticle migration on water/alumina nanofluid flow inside a horizontal annulus with a moving core. *Journal of Mechanics*. 2015;31(03):291–305.
- [74] Hedayati F, Malvandi A, Kaffash M, Ganji D. Fully developed forced convection of alumina/water nanofluid inside microchannels with asymmetric heating. *Powder Technology*. 2015;269:520–31.
- [75] Malvandi A, Moshizi SA, Ganji DD. Two-component heterogeneous mixed convection of alumina/water nanofluid in microchannels with heat source/sink. *Advanced Powder Technology*. 2016;27(1):245–54. doi:<http://dx.doi.org/10.1016/j.appt.2015.12.009>.
- [76] Sheikhzadeh GA, Dastmalchi M, Khorasanizadeh H. Effects of nanoparticles transport mechanisms on Al_2O_3 –water nanofluid natural convection in a square enclosure. *International Journal of Thermal Sciences*. 2013;66:51–62.
- [77] Bahiraei M, Mostafa Hosseinalipour S, Hangi M. Prediction of convective heat transfer of Al_2O_3 -water nanofluid considering particle migration using neural network. *Engineering Computations*. 2014;31(5):843–63.
- [78] Malvandi A, Safaei M, Kaffash M, Ganji D. Mhd mixed convection in a vertical annulus filled with Al_2O_3 –water nanofluid considering nanoparticle migration. *Journal of Magnetism and Magnetic Materials*. 2015;382:296–306.
- [79] Malvandi A. The unsteady flow of a nanofluid in the stagnation point region of a time-dependent rotating sphere. *Thermal Science*. 2015;19(5):1603–12.
- [80] Malvandi A, Moshizi S, Soltani EG, Ganji D. Modified Buongiorno's model for fully developed mixed convection flow of nanofluids in a vertical annular pipe. *Computers & Fluids*. 2014;89:124–32.
- [81] Malvandi A, Ganji DD. Magnetohydrodynamic mixed convective flow of Al_2O_3 –water nanofluid inside a vertical microtube. *Journal of Magnetism and Magnetic Materials*. 2014;369(0):132–41. doi:<http://dx.doi.org/10.1016/j.jmmm.2014.06.037>.
- [82] Malvandi A, Ganji D. Effects of nanoparticle migration on force convection of alumina/water nanofluid in a cooled parallel-plate channel. *Advanced Powder Technology*. 2014;25(4):1369–75.
- [83] Malvandi A, Moshizi SA, Ganji DD. Effect of magnetic fields on heat convection inside a concentric annulus filled with Al_2O_3 –water nanofluid. *Advanced Powder Technology*. doi:<http://dx.doi.org/10.1016/j.appt.2014.07.013> 2016; 25(6):1817-1824..

- [84] Malvandi A, Ganji DD. Magnetic field effect on nanoparticles migration and heat transfer of water/alumina nanofluid in a channel. *Journal of Magnetism and Magnetic Materials*. 2014;362:172–9. doi:<http://dx.doi.org/10.1016/j.jmmm.2014.03.014>.
- [85] Malvandi A, Ganji DD. Brownian motion and thermophoresis effects on slip flow of alumina/water nanofluid inside a circular microchannel in the presence of a magnetic field. *International Journal of Thermal Sciences*. 2014;84:196–206. doi:<http://dx.doi.org/10.1016/j.ijthermalsci.2014.05.013>.
- [86] Moshizi SA, Malvandi A, Ganji DD, Pop I. A two-phase theoretical study of Al_2O_3 -water nanofluid flow inside a concentric pipe with heat generation/absorption. *International Journal of Thermal Sciences*. 2014;84:347–57. doi:<http://dx.doi.org/10.1016/j.ijthermalsci.2014.06.012>.
- [87] Malvandi A, Ganji D. Effects of nanoparticle migration on hydromagnetic mixed convection of alumina/water nanofluid in vertical channels with asymmetric heating. *Physica E: Low-dimensional Systems and Nanostructures*. 2015;66:181–96.
- [88] Malvandi A, Ganji D, Kaffash M. Magnetic field effects on nanoparticle migration and heat transfer of alumina/water nanofluid in a parallel-plate channel with asymmetric heating. *The European Physical Journal Plus*. 2015;130(4):1–21.
- [89] Malvandi A, Heysiattalab S, Ganji D. Thermophoresis and Brownian motion effects on heat transfer enhancement at film boiling of nanofluids over a vertical cylinder. *Journal of Molecular Liquids*. 2016;216:503–9.
- [90] Malvandi A. Film boiling of magnetic nanofluids (MNFs) over a vertical plate in presence of a uniform variable-directional magnetic field. *Journal of Magnetism and Magnetic Materials*. 2016;406:95–102.
- [91] Mansour M, Bakier M. Free convection heat transfer in complex-wavy-wall enclosed cavity filled with nanofluid. *International Communications in Heat and Mass Transfer*. 2013;44:108–15.
- [92] Nadeem S, Mehmood R, Akbar NS. Optimized analytical solution for oblique flow of a casson-nano fluid with convective boundary conditions. *International Journal of Thermal Sciences*. 2014;78:90–100.
- [93] Mustafa M, Khan JA, Hayat T, Alsaedi A. Analytical and numerical solutions for axisymmetric flow of nanofluid due to non-linearly stretching sheet. *International Journal of Non-Linear Mechanics*. 2015;71:22–9.

Application of Phase-Field Method to the Analysis of Phase Decomposition of Alloys

Erika O. Avila-Davila, Victor M. Lopez-Hirata and
Maribel L. Saucedo-Muñoz

Additional information is available at the end of the chapter

<http://dx.doi.org/10.5772/64153>

Abstract

This chapter is focused on the application of the phase-field method to the analysis of phase decomposition during the isothermal aging of alloys. The phase-field method is based on a numerical solution of either the nonlinear Cahn-Hilliard equation or the Cahn-Allen equation. These partial differential equations can be solved using the finite difference method among other numerical methods. The phase-field method has been applied to analyze different types of phase transformations in alloys, such as phase decomposition, precipitation, recrystallization, grain growth, solidification of pure metals and alloys, martensitic transformation, ordering reactions, and so on. One of the main advantages of phase-field method is that this method permits to follow the microstructure evolution in two or three dimensions as the time of phase transformations progresses. Thus, the morphology, size, and size distribution could be determined to follow their corresponding growth kinetics. Additionally, the evolution of chemical composition can also be followed during the phase transformations. Furthermore, both Allen-Cahn and Cahn-Hilliard equations can be solved simultaneously to analyze the presence of ordered phases or magnetic domains in alloys.

The formation of phases in alloys usually takes place by nucleation mechanism, growth mechanism, or spinodal decomposition mechanism, which is followed by the coarsening of phases in alloy systems. These three processes can be analyzed using the phase-field method and their results can also be compared with the fundamental theories of phase transformations such as the Cahn-Hilliard spinodal decomposition theory and the Lifshitz-Slyozov-Wagner diffusion-controlled coarsening theory.

Therefore, this chapter first deals with the analysis of phase decomposition during the isothermal aging of hypothetical binary alloys using the nonlinear Cahn-Hilliard equation. To continue, the effect of main parameters, such as the atomic mobility interface energy and alloy composition, on the microstructure evolution and growth kinetics are discussed. To conclude, the application of phase-field method is extended

to the analysis of phase decomposition during isothermal aging of real binary and ternary alloy systems, such as Fe-Cr, Cu-Ni, and Cu-Ni-Fe. A comparison of simulated results with experimental ones is also included.

Keywords: phase field method, phase decomposition, alloys, aging

1. Introduction

In the field of materials science, it is important to analyze different moving free boundary problems in order to understand its effect on the phase transformations that may occur in materials. For instance, the solidification and grain growth, and martensitic transformation are diffusion-controlled and diffusion-less phase transformations, respectively, with this characteristic. One way to overcome this need is the use of the diffuse interface model [1]. Furthermore, the application of the phase-field method to this sort of problem permits the use of the order parameter and phase-field variable which takes into account the composition gradient energy present in a diffuse interface model. For instance [2], the order parameter φ could take values either 0 or 1, which may represent the liquid or solid states, respectively, during the solidification process of a pure metal.

The phase-field method is based on the equations proposed by Cahn-Hilliard [1], Allen-Cahn [2], or Ginzburg-Landau [3]:

$$\frac{\partial c_i(x,t)}{\partial t} = \nabla \cdot \left(\sum_j M_{ij} \nabla \frac{\partial G_{\text{sys}}}{\partial c_i(x,t)} \right) \quad (1)$$

$$\frac{\partial \phi_i(x,t)}{\partial t} = - \sum_j L_{ij} \left(\frac{\partial G_{\text{sys}}}{\partial \phi_i(x,t)} \right) \quad (2)$$

where $c_i(x,t)$ and $\phi_i(x,t)$ correspond to the field variable, for instance, concentration and order parameter as a function of position x and time t . M_{ij} and L_{ij} are the mobility. The free energy of a given system may include, for instance, the following terms [4]:

$$G_{\text{sys}} = F_c + F_{\text{grad}} + F_{\text{str}} + F_{\text{mag}} + F_{\text{ele}} \quad (3)$$

F_c is the local free energy, F_{grad} the compositional gradient energy, F_{str} the elastic strain energy, and F_{mag} and F_{ele} the energies corresponding to magnetic and electric effects, respectively.

The composition gradient energy can be defined, for instance, for the field variable, concentration c , by the following mathematical expression [1]:

$$F_{grad} = \frac{1}{2} \int_r k (\nabla c)^2 dr \quad (4)$$

where κ is the gradient energy coefficient.

One of the main advantages of phase-field method is that this method permits to follow the microstructure evolution in two or three dimensions as the time of phase transformations progresses. Thus, the morphology, size, and size distribution could be determined to follow their corresponding growth kinetics. Additionally, the evolution of chemical composition can also be followed during the phase transformations.

To solve either of the partial differential equations, Eqs (1) or (2), several numerical methods have been used such as finite difference method, difference volume method, and finite element method [5]. The use of explicit finite difference method is simple and good alternative to solve this type of differential equations. For instance, the finite difference method can be used to solve a simple partial differential equation such as the simplified one-dimension equation of the second Fick's law:

$$\frac{\partial c}{\partial t} = D \frac{\partial^2 c}{\partial x^2} \quad (5)$$

where D is the diffusion coefficient. The finite difference solution can be approximated as follows [6]:

$$\frac{c_i^{t+1} - c_i^t}{\Delta t} = D \frac{c_{i+1}^t - 2c_i^t + c_{i-1}^t}{\Delta x^2} \quad (6)$$

where t indicates the time and $t + 1$ is equal to $t + \Delta t$ being Δt the time step. The spacing between two nodes is Δx , the distance step. The node number corresponds to i . c_i^{t+1} indicates the calculated concentration for the node i in the next time step, $t + \Delta t$ and c_i^t that of the previous time t .

This chapter is mainly focused on the application to the phase decomposition by the spinodal decomposition mechanism during the isothermal aging of hypothetical binary alloys using the nonlinear Cahn-Hilliard equation [7]. The effect of main parameters such as the atomic mobility of alloy and elastic-strain energy on the microstructure evolution and growth kinetics is analyzed. To conclude, the application of phase-field method is extended to the analysis of spinodal decomposition during isothermal aging of real binary and ternary alloy systems, such as Cu-Ni, Fe-Cr, and Cu-Ni-Fe. A comparison of simulated results with experimental ones is also included.

2. Phase decomposition in alloys

The formation of phases in alloys usually takes place by nucleation mechanism, growth mechanism, or spinodal decomposition mechanism, which is followed by the coarsening of phases in alloy systems. These three processes can be analyzed using the phase-field method, and their results can also be compared with the fundamental theories of phase transformations such as the Cahn-Hilliard spinodal decomposition theory [4] and the Lifshitz-Slyozov-Wagner (LSW) diffusion-controlled coarsening theory [8]. The phase decomposition that takes place by the spinodal decomposition mechanism is distinguished from the phase separation that occurs by nucleation and growth mechanism by the formation of an initial composition modulation, which shows an increase in the modulation amplitude with time. In contrast, the phase formation by nucleation and growth predicts that the formed phase has a composition very close to the equilibrium one from the start to the finish of phase transformation [9]. Besides, the spinodal decomposition is usually associated with the presence of a miscibility gap in the equilibrium phase diagram, as shown in **Figure 1**. The miscibility gap is the equilibrium line and there is only one α phase for compositions and temperatures above this line, whereas a mixture of two phases, α_1 and α_2 , is present inside the miscibility gap. This figure also shows the existence of the chemical spinodal located within the miscibility gap. A supersaturated α_{ss} phase is expected to decompose spinodally into a mixture of A-rich α_1 and B-rich α_2 phases for an alloy composition after heating at a temperature higher than that of the miscibility gap and then quenching and heating or aging at a temperature lower than the chemical spinodal. The miscibility gap in **Figure 1** is usually related to the plot of free energy versus composition shown in **Figure 2**. This figure shows the free energy curve shape changes as the temperature decreases. This type of curve is known as the spinodal curve, and it indicates that any alloy composition is in unstable state and thus it is expected to decompose into a mixture of A-rich α_1 and B-rich α_2 phases. The minimum and saddle points at each temperature of the spinodal curve correspond to the equilibrium and chemical spinodal shown in **Figure 1**.

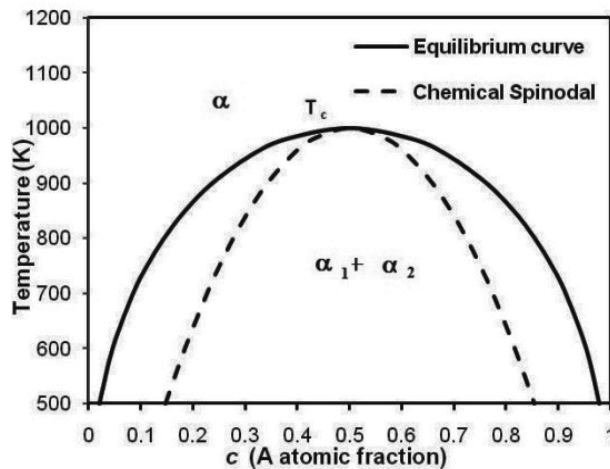


Figure 1. Miscibility gap in a hypothetical A-B phase diagram.

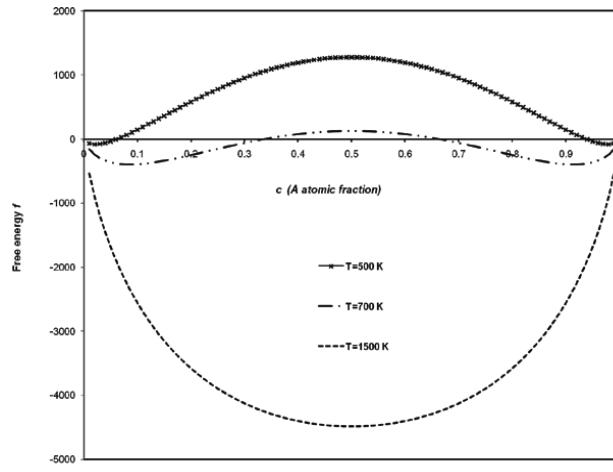


Figure 2. Plot of free energy versus composition for the miscibility gap in **Figure 1**.

The Cahn-Hilliard theory of spinodal decomposition [4] was developed by the modification of the second Fick’s law equation in order to allow only the growth of the modulation amplitude in composition with a wavelength larger than a critical value. Furthermore, the nonlinear Cahn-Hilliard equation, used in the simulations of this work, has its origin in this theory.

3. Simulation of hypothetic binary alloys

In the numerical simulation of the phase decomposition for a hypothetic A-B binary alloy, the nonlinear Cahn-Hilliard equation [7] can be rewritten as follows:

$$\frac{\partial c_i(x,t)}{\partial t} = M_i \nabla^2 \left(\frac{\partial f_o(c)}{\partial c_i} - K_i \nabla^2 c_i \right) \quad (7)$$

The local chemical free energy $f_o(c)$ was assumed to follow the following equation [10]:

$$f_o = -(c - 0.5)^2 + 2.5(c - 0.5)^4 \quad (8)$$

This equation represents a spinodal curve similar to those shown in **Figure 2**. In the first case of simulation, the mobility M_i was considered to be constant and equal to 1, and the composition c is equal to 0.4. The calculated concentration profiles for different times are shown in **Figure 3**. The initial modulation amplitude increases with time which confirms that the phase decomposition occurs by the spinodal decomposition mechanism [4]. Besides, the initial composition modulation forms a mixture of A-rich α_1 and B-rich α_2 phases as a result of heating

at a temperature with mobility M_i equal to 1. An advantage of the phase-field method is that the microstructure evolution can be obtained by plotting the concentration in two dimensions. **Figure 4** shows the calculated microstructures as a function of time. The black and white zones correspond to the A-rich α_1 and B-rich α_2 phases, respectively. The morphology of the decomposed phases is irregular and interconnected as predicted by the Cahn-Hilliard theory of spinodal decomposition [4]. The coarsening process of the decomposed phases is also observed for the longer times.

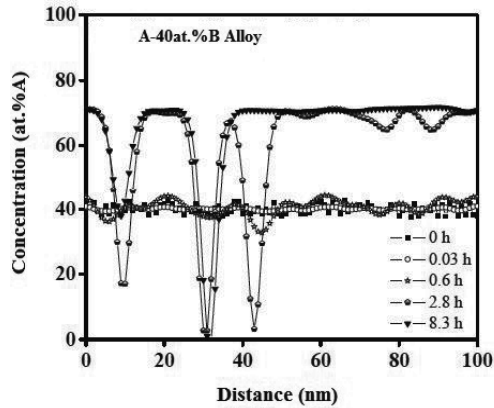


Figure 3. Concentration profiles for the numerical simulation of $M_i = 1$ and $c = 0.4$.

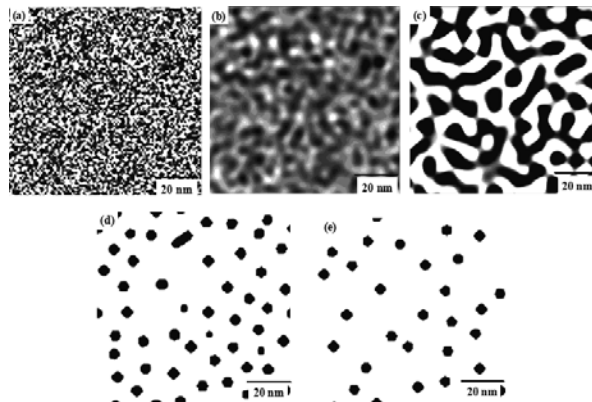


Figure 4. Microstructure evolution for $M_i = 1$ and $c = 0.4$ for (a) 0 h, (b) 0.03 h, (c) 0.6 h, (d) 2.8 h, and (e) 6.3 h.

In the second example, the mobility M_i was not constant and defined with the following equation:

$$M_i = 1 - \alpha c^2 \quad (9)$$

where $\alpha = 1$ and the nonlinear Cahn-Hilliard equation was modified as follows:

$$\frac{\partial c_i(x,t)}{\partial t} = \nabla \left[M_i \nabla \left(\frac{\partial f_0(c)}{\partial c_i} - K_i \nabla^2 c_i \right) \right] \quad (10)$$

The numerical solution of the former partial differential equation conducted to the following concentration profiles (**Figure 5**). The same characteristics described in the previous example are also observed for this case. However, the amplitude of the composition modulation for this case increases faster with time than that for the former case. The microstructure evolution for this case is different from the one shown for the previous case (**Figure 6**). That is, the decomposed phases form a lamellar structure instead of the irregular and interconnected morphology of the previous case. This may be attributed to the variable mobility of the decomposed phases [4].

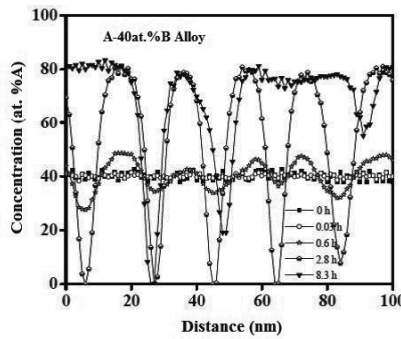


Figure 5. Concentration profiles for the numerical simulation of variable M_i and $c = 0.4$.

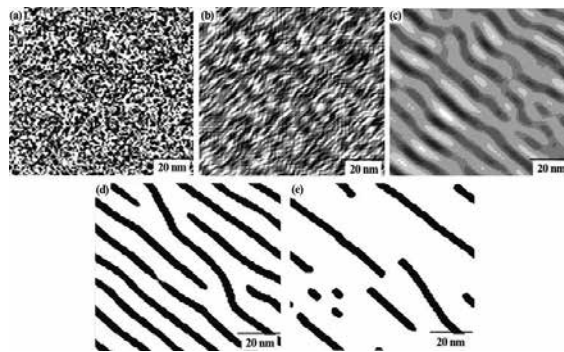


Figure 6. Microstructure evolution for variable M_i and $c = 0.4$ for (a) 0 h, (b) 0.03 h, (c) 0.6 h, (d) 2.8 h, and (e) 6.3 h.

To complete the numerical simulation of hypothetical binary alloys, the next case includes the presence of an isotropic elastic-strain energy f_{el} with a value equal to 1 and M_i equal to 1. The nonlinear Cahn-Hilliard equation was modified as follows:

$$\frac{\partial c_i(x,t)}{\partial t} = M_i \nabla^2 \left(\frac{\partial f_o(c)}{\partial c_i} + \frac{\partial f_{el}}{\partial c_i} - K_i \nabla^2 c_i \right) \quad (11)$$

Figure 7 illustrates the concentration profiles for this case and the same characteristics, observed in the others, are also present. That is, the modulation amplitude increases with time. Besides, a mixture of A-rich α_1 and B-rich α_2 phases is formed after aging. The microstructure evolution is similar to that of the first case for short times. That is, the morphology of the decomposed phases is irregular and interconnected, which is known as percolated structure [4] (**Figure 8**). Nevertheless, one of the decomposed phases takes a cuboid shape for the longest times, which is attributed to the isotropic elastic-stain energy [9].

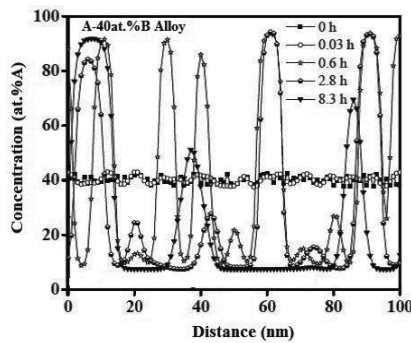


Figure 7. Concentration profiles for the numerical simulation of $f_{el} = 1$ and $c = 0.4$.

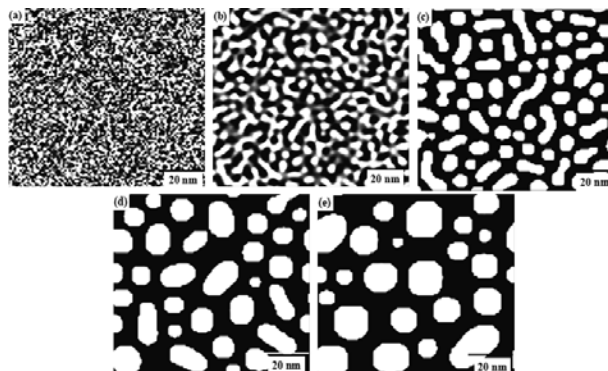


Figure 8. Microstructure evolution for $f_{el} = 1$ and $c = 0.4$ for (a) 0 h, (b) 0.03, (c) 0.6 h, (d) 2.8 h, and (e) 6.3 h.

4. Simulation in real binary alloys

In the next part of this chapter, the numerical simulation of the phased decompositions of Cu-Ni and Fe-Cr alloys after aging at different temperatures for different times is shown. Simulated results are compared to the experimental ones. To begin, the Cu-Ni alloys are widely used in different industrial applications. The equilibrium phase diagram is shown in **Figure 9**. This diagram has a miscibility gap located at temperatures lower than 350°C [11]. Thus, a supersaturated solid solution, formed by heating above 350°C and then quenching, is expected to decompose spinodally into a mixture of Cu-rich and Ni-rich phases after aging at a temperature lower than 350°C. Nevertheless, the growth kinetics of spinodal decomposition is very slow due to the low atomic diffusivity at these temperatures [7]. Thus, the application of the phase-field method to analyze the spinodal decomposition seems to be a good alternative because of the slow kinetics.

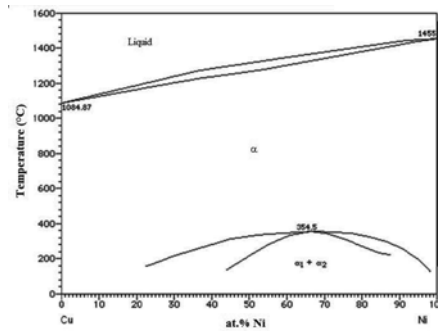


Figure 9. Equilibrium Cu-Ni phase diagram [11].

The nonlinear Cahn-Hilliard equation, Eq. (7), was solved to analyze the phase decomposition in these alloys. The local energy f_o was defined using the regular solution model as follows [7]:

$$f_o = f_{Cu} c_{Cu} + f_{Ni} c_{Ni} + \Omega_{Cu-Ni} c_{Cu} c_{Ni} + RT(c_{Cu} \ln c_{Cu} + c_{Ni} \ln c_{Ni}) \quad (12)$$

where R is the gas constant, T is the absolute temperature. f_{Cu} and f_{Ni} are the molar free energy of pure Cu and Ni, respectively, and Ω_{Cu-Ni} is the interaction parameter. The atomic mobility M_i is related to the interdiffusion coefficient \bar{D}_i as follows:

$$\bar{D}_i = M_i \left(\frac{\partial^2 f_o}{\partial c_i^2} \right) \quad (13)$$

The interdiffusion coefficient \bar{D}_i was assumed to be defined as follows [4]:

$$\bar{D}_i = D_{Ni}c_{Cu} + (1 - c_{Cu})D_{Cu} \quad (14)$$

The gradient energy coefficient K was determined as proposed by reference [4]:

$$K = \left(\frac{2}{3}\right) h_{0.5}^M r_0^2 \quad (15)$$

where $h_{0.5}^M$ is the mixing heat per unit volume at $c = 0.5$ and r_0 is the nearest neighbor distance. The heat of mixing h^M was determined according to the next equation [4]:

$$h^M = c_{Cu}c_{Ni}\Omega_{Cu-Ni} \quad (16)$$

The thermodynamic, diffusion, crystal lattice, and elastic parameters for the microstructure simulation were obtained from the literature [12–15] and these are shown in **Table 1**. The effect of coherency elastic-strain energy was considered to be present during the phase decomposition of Cu-Ni alloys in spite of the similar lattice parameters of copper and nickel [13]. This elastic-strain energy was introduced into Eq. (7), according to the simple definition proposed by Hilliard [4]:

| Parameter | Ni-Cu alloys | |
|-------------------------------------------------------------------|---------------------------------------------------------------------------|---------------------------------|
| Crystal lattice parameter a (nm) [13] | 0.360 | |
| η (nm) [13] | 0.0016 | |
| Ω_{Cu-Ni} (J mol ⁻¹) [12] | (8366.0 + 2.802T) + (-4359.6 + 1.812T)(c _{Cu} -c _{Ni}) | |
| Diffusion coefficient D (cm ² s ⁻¹) [14] | Cu 1.5–2.3 exp (-230,000–260,000 J mol ⁻¹)/RT | |
| | Ni 17–35 exp (-270,000–300,000 J mol ⁻¹)/RT | |
| c_{ij} (J m ⁻³) | $c_{11} = 16.84 \times 10^{10}$ | $c_{11} = 24.65 \times 10^{10}$ |
| Cu/Ni [15] | $c_{12} = 12.14 \times 10^{10}$ | $c_{44} = 12.47 \times 10^{10}$ |
| | $c_{44} = 7.54 \times 10^{10}$ | |

Table 1. Values of lattice, diffusion, thermodynamic and elastic constants.

$$f_{el} = A \int \eta^2 Y (c - c_0)^2 dx \quad (17)$$

where A is the cross-sectional area and Y is an elastic constant defined by the elastic stiffness constants, c_{11} , c_{12} , and c_{44} , for the Cu-rich and Ni-rich phases. The parameter η is equal to $\ln a/dc$. In the case of fcc metals, the elastic energy will be a minimum for the <100> crystallographic directions, and thus the Y value can be assumed similar to that corresponding to an isotropic material [4]:

$$Y_{\langle 100 \rangle} = c_{11} + c_{12} - 2 \left(\frac{c_{12}^2}{c_{11}} \right) \quad (18)$$

The elastic constants, c_{ij} , were calculated as follows:

$$c_{ij} = c_{ij}^{Cu} c_{Cu} + c_{ij}^{Ni} (1 - c_{Cu}) \quad (19)$$

Considering the elastic strain energy, f_{el} , Eq. (7) was rewritten as Eq. (11).

The microstructural simulation was carried out using the finite difference method with 101×101 points square grid with a mesh size of 0.25 nm and a time-step size of 10 s. The simulations were performed for the Ni-30at.% Cu alloy at temperatures between 250 and 322°C for different times.

Figure 10 shows the numerically calculated plots of Cu concentration versus distance for the Ni-30at.%Cu alloy solution treated (0 h) and aged at 300°C for different times. There is an increase in the modulation amplitude with aging time. The increase in amplitude at this temperature confirms that the phase decomposition occurs spinodally in this alloy. The long simulated aging times also confirm that the growth kinetics of phase decomposition is very slow in this alloy system.

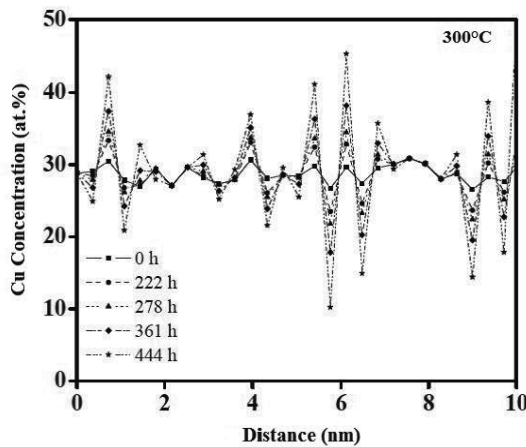


Figure 10. Ni-30at.%Cu alloy aged at 300°C.

The simulated microstructures of the Ni-30at.%Cu alloy aged at 300°C for 0, 222, 278, 361, and 444 h are shown in **Figure 11 (a–e)**, respectively. The black and white regions correspond to the Cu-rich and Ni-rich phases, respectively. It can be seen that the morphology of the decomposed phases is irregular and interconnected. The volume fraction of the Ni-rich phase increased with aging time.

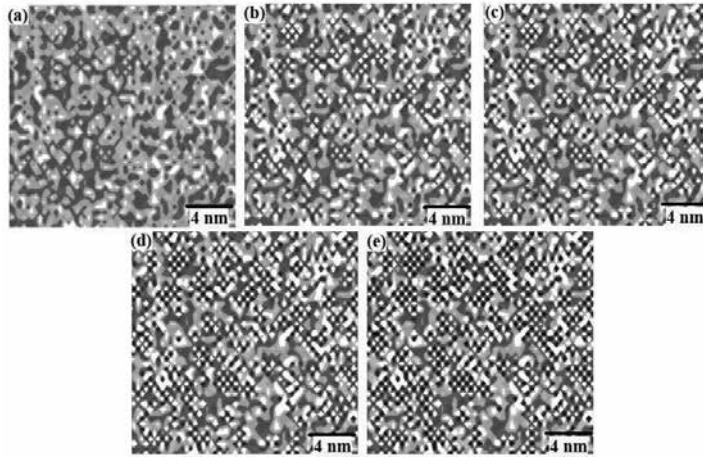


Figure 11. Microstructure evolution of Ni-30at.%Cu alloy aged at 300°C for (a) 0 h, (b) 222 h, (c) 278 h, (d) 361 h, and (e) 444 h.

The experimental Ne-gas field ion microscopy (FIM) images of the Ni-30at.%Cu alloy aged at 300°C for 500 h is shown in **Figure 12**. There is a good agreement between the calculated and experimental morphologies of the decomposed phases.

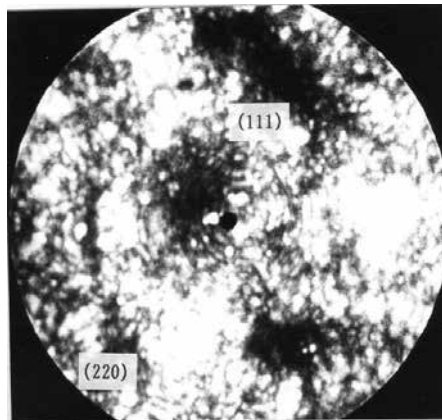


Figure 12. Ne FIM image of the Ni-30at.%Cu alloy aged at 300°C for 500 h.

In the next paragraphs, a second example about the numerical simulation of real alloys is presented. The Fe-Cr alloys are a very important alloy system since this is used as the basis for different industrial alloys, such as the family of stainless steels. The Fe-Cr equilibrium phase diagram [11] also shows a miscibility gap found at temperatures lower than 500°C (**Figure 13**). Thus, the phase decomposition of the supersaturated solid solution into a mixture of Cr-rich and Fe-rich phases is also expected as a result of aging at temperatures lower than 500°C.

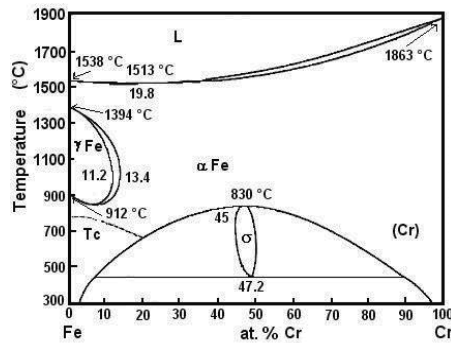


Figure 13. Equilibrium Fe-Cr phase diagram [11].

The phase decomposition simulation was based on a numerical solution of the nonlinear Cahn-Hilliard equation, Eq. (7). The formulation for this case is very similar to that described previously for the numerical simulation of the phase decomposition in Ni-Cu alloys.

The crystal lattice, thermodynamic, diffusion, and elastic constants for the microstructural simulation in Fe-Cr alloys were taken from references [13–16] and these parameters are shown in **Table 2**. The simulation of phase decomposition was pursued using the explicit finite difference method with 101×101 and 201×201 points square grids with a mesh size of 0.1 and 0.25 nm and a time-step size up to 10 s. The numerical simulation was performed for the Fe-40at.%Cr alloy aged at 470°C for times from 0 to 1000 h. It is important to mention that the initial composition modulation corresponding to the solution-treated sample was calculated using a random number generator.

| Parameter | Values |
|-------------------------------------------------------------------|--------------------------------------------------------------------------------------------------------------------------|
| Crystal lattice parameter a (nm) [13] | 0.2866 |
| η (nm) [13] | 0.00614 |
| $\Omega_{\text{Fe-Cr}}$ (J mol ⁻¹) [16] | (18600.0 + 0.1T) |
| Diffusion coefficient D (cm ² s ⁻¹) [16] | $D_{\text{Fe}} = 1.2 \exp(-294,000 \text{ J mol}^{-1})/RT$ $D_{\text{Cr}} = 0.2 \exp(-308,000 \text{ J mol}^{-1})/RT$ |
| c_{ij} (J m ⁻³) [15] | |
| Fe | $c_{11} = 23.10 \times 10^{10}$ $c_{12} = 13.54 \times 10^{10}$ $c_{44} = 11.78 \times 10^{10}$ |
| Cr | $c_{11} = 35.00 \times 10^{10}$ $c_{12} = 67.80 \times 10^{10}$ $c_{44} = 10.08 \times 10^{10}$ |

Table 2. Lattice, diffusion, elastic, and thermodynamic parameters.

The plots of Cr concentration versus distance, concentration profiles, for the Fe-40at.%Cr alloy aged at 470°C for different times are shown in **Figure 14**. These concentration profiles indicate clearly that the supersaturated solid solution decomposed spinodally into a mix of Cr-rich and Fe-rich phases since the modulation amplitude increases as the aging time increases.

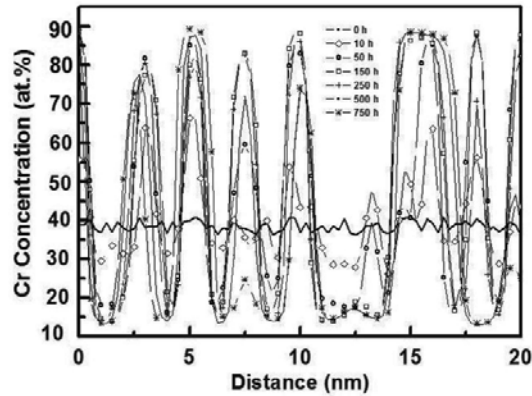


Figure 14. Concentration profiles of Fe-40at.%Cr alloy aged at 470°C.

Figure 15 shows the simulated microstructural evolution of the phase decomposition in the Fe-40-at.%Cr alloy aged at 470°C for times from 10 to 750 h. The white and gray zones represent the Fe-rich and Cr-rich phases, respectively. It can be observed and irregular and interconnected morphology of the decomposed phases in the alloy aged for times up to 10 h. This morphological characteristic is known as percolated structure, and it has been commonly observed to occur during the early stages of aging in the spinodally decomposed alloys. The HR-TEM micrographs of this alloy aged at 470°C for 250 h shows clearly the presence of spheres corresponding to the Cr-rich phases imbedded in the ferrite phase matrix (Figure 16). The decomposed phases present a coherent interface. This shape of decomposed Cr-rich phase is in good agreement with the simulated microstructure (Figure 15(e) and (f)) [17].

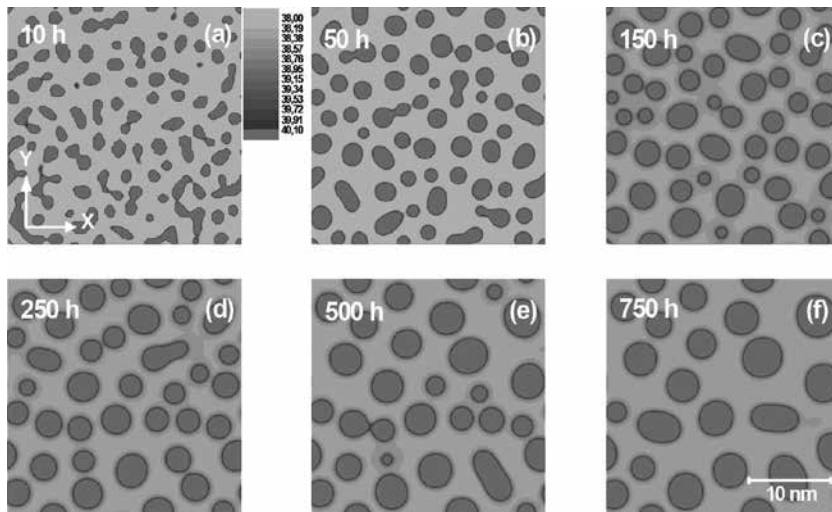


Figure 15. Microstructure evolution of Fe-40at.%Cr alloy aged at 470°C.

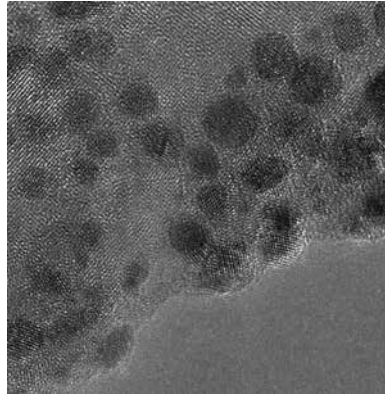


Figure 16. HR-TEM micrograph of Fe-40at.%Cr alloy aged at 470°C for 250 h.

5. Simulation in real ternary alloys

The numerical simulation of phase decomposition of ternary alloys can be also conducted using the phase-field method. The equilibrium Cu-Ni-Fe phase diagram [18] is shown in **Figure 17** at different temperatures. The presence of a miscibility gap is evident and thus the phase decomposition can also be simulated by the phase-field method.

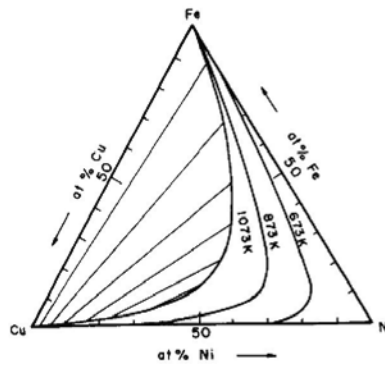


Figure 17. Equilibrium Cu-Ni-Fe phase diagram [16].

The Cahn-Hilliard nonlinear equation for a multicomponent system with a constant mobility can be used for the present simulation, Eq. (7).

The local free energy f_0 was defined using the regular solution model as follows [19]:

$$f_o = f_{Cu} c_{Cu} + f_{Ni} c_{Ni} + f_{Fe} c_{Fe} + \Omega_{Cu-Ni} c_{Cu} c_{Ni} + \Omega_{Cu-Fe} c_{Cu} c_{Fe} + \Omega_{Ni-Fe} c_{Ni} c_{Fe} +$$

$$\Omega_{Cu-Ni-Fe} c_{Cu} c_{Ni} c_{Fe} + RT(c_{Cu} \ln c_{Cu} + c_{Ni} \ln c_{Ni} + c_{Fe} \ln c_{Fe}) \quad (20)$$

where R is the gas constant, T is the absolute temperature, f_{Cu} , f_{Ni} and f_{Fe} correspond to the molar free energy of pure Cu, Ni, and Fe, respectively, and Ω_{Cu-Ni} , Ω_{Cu-Fe} , Ω_{Ni-Fe} and $\Omega_{Cu-Ni-Fe}$ represent the interaction parameters. All these thermodynamic constants are shown in **Table 3**.

| Parameter | Cu-Ni-Fe alloys | |
|-------------------------------------------------------------------|-------------------------------------------------------------------------------------------------------------|---------------------------------|
| Ω_{Cu-Ni} | $(9534.49+2.839T) + (-424.255-0.629T)(c_{Cu}-c_{Ni})$ | |
| Ω_{Cu-Fe} | $(48206.0 - 8.446T) + (-5918.0 + 5.017T)(c_{Cu}-c_{Fe})$ | |
| Ω_{Ni-Fe} | $(-18298.8 + 5.149T) + (14313.6 - 7.659T)(c_{Ni}-c_{Fe})$ | |
| $\Omega_{Cu-Ni-Fe}$ (J mol ⁻¹) [12] | $-35982.0 - 12.0T$ | |
| f_{Cu} | $-8.65T-22.64T\ln T-3.13\times 10^{-3} T^2-7023.9$ | |
| f_{Ni} | $93.23T-12.54T\ln T+1.23\times 10^{-3} T^2-532.3$ | |
| f_{Fe} (J mol ⁻¹) [12] | $39.0T-26.61T\ln T+1.23\times 10^{-3} T^2-4154.5$ | |
| Diffusion coefficient D (cm ² s ⁻¹) [14] | $D_{Ni} = 17.0 \exp(-279,350 \text{ J mol}^{-1})/RT$ $D_{Fe} = 6.1 \exp(-266,000 \text{ J mol}^{-1})/RT$ | |
| Crystal lattice parameter a (nm) [13] | 0.360 | |
| η (nm) [13] | 0.0016 | |
| c_{ij} (J m ⁻³) | $c_{11} = 16.84 \times 10^{10}$ | $c_{11} = 24.65 \times 10^{10}$ |
| Cu/Ni | $c_{12} = 12.14 \times 10^{10}$ | $c_{12} = 14.73 \times 10^{10}$ |
| [15] | $c_{44} = 7.54 \times 10^{10}$ | $c_{44} = 12.47 \times 10^{10}$ |

Table 3. Values of lattice, diffusion, thermodynamic, and elastic parameters.

The atomic mobility M_i is related to the interdiffusion coefficient \bar{D}_i as follows:

$$\bar{D}_i = M_i \left(\frac{\partial^2 f_0}{\partial c_i^2} \right) \quad (21)$$

The atomic mobility M_i was determined using Eq. (21) and the procedure proposed by Honjo and Saito [19]:

$$M_{Ni} = \frac{D_{Ni}}{2\Omega_{Cu-Ni} + 4RT} \quad (22)$$

$$M_{Fe} = \frac{D_{Fe}}{2\Omega_{Cu-Fe} + 4RT} \quad (23)$$

where D_{Ni} corresponds to the diffusion coefficient in Cu-50at.%Ni alloy and D_{Fe} to the diffusion coefficient of Fe in Cu. The values of D_{Ni} and D_{Fe} are also indicated in **Table 3**.

The gradient energy coefficient K_i was determined as proposed by Hilliard [4]. It was shown in Eq. (15).

Thus, the gradient energy coefficient K_i was defined as follows:

$$K_{Ni} = \frac{1}{12} a^2 \Omega_{Cu-Ni} \quad (24)$$

$$K_{Fe} = \frac{1}{12} a^2 \Omega_{Cu-Fe} \quad (25)$$

where a represents the lattice parameter also given in **Table 3**.

The effect of coherency elastic-strain energy was introduced into Eq. (7), according to the simple definition proposed by Hilliard [4]. It was shown in Eq. (17).

The elastic constant Y was assumed to be determined with the following equation [4]:

$$Y = \frac{1}{2} c_{11} + 2c_{12} \left(3 - \frac{c_{11} + 2c_{12}}{c_{11} + 2c_{12}(2c_{44} - c_{11} + c_{12})(l^2 m^2 + m^2 n^2 + l^2 n^2)} \right) \quad (26)$$

where l , m , and n are the direction cosines.

The elastic constants, c_{ij} were calculated as follows:

$$c_{ij} = c_{ij}^{Cu-rich} c_{Cu} + c_{ij}^{Ni-rich} (1 - c_{Cu}) \quad (27)$$

Considering the elastic strain energy, f_{el} , Eq. (7) can be rewritten for the c_{Ni} and c_{Fe} as follows:

$$\frac{\partial c_{Ni}(x,t)}{\partial t} = M_{Ni} \nabla^2 \left(\frac{\partial f_o(c)}{\partial c_{Ni}} + \frac{\partial f_{el}}{\partial c_{Ni}} - K_{Ni} \nabla^2 c_{Ni} \right) \quad (28)$$

$$\frac{\partial c_{Fe}(x,t)}{\partial t} = M_{Fe} \nabla^2 \left(\frac{\partial f_o(c)}{\partial c_{Fe}} + \frac{\partial f_{el}}{\partial c_{Fe}} - K_{Fe} \nabla^2 c_{Fe} \right) \quad (29)$$

Equations (28) and (29) were solved numerically using the explicit finite difference method with 101×101 points square grid with a mesh size of 0.36 nm and a time-step size up to 10 s. The simulations were performed for the Cu-46at.%Ni-4at.%Fe alloy at temperature of 400°C

for times from 0 to 200 h. This composition was selected for comparison of the morphology and kinetics of the phase decomposition. It is important to mention that the initial composition modulation corresponding to the solution treated sample was calculated using a random-number generator as proposed in reference [19].

Figure 18 shows the calculated concentration profiles of the Cu-46at.%Ni-4at.%Fe alloy aged at 400°C for times from 0 to 200 h. An increase in the amplitude of the composition modulation with aging time can be noticed in both cases. This fact has been associated with the phase decomposition via the spinodal decomposition mechanism [4]. This behavior is also in good agreement with the experimental evidence reported in the literature [18] for the aging of Cu-Ni-Fe alloys. The calculated Cu and Fe concentration profiles are shown in **Figure 19** for the alloys aged at 400°C for 200 h. These plots indicate clearly that the supersaturated solid solution decomposes into two phases: a Cu-Ni-Fe-rich phase with a poor content of Fe and a Ni-Cu-Fe-rich phase with a lower content of Cu and a higher content of Fe. The decomposed Cu-Ni-Fe and Ni-Cu-Fe phases are in agreement with the miscibility gap of the equilibrium Cu-Ni-Fe phase diagram [17].

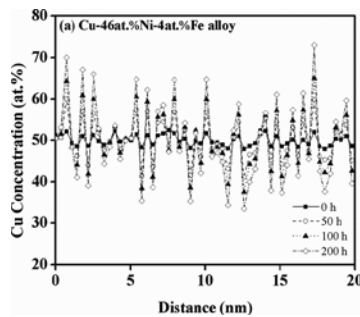


Figure 18. Cu concentration profile of the Cu-46at.%Cu-4at.%Fe alloy aged at 400°C.

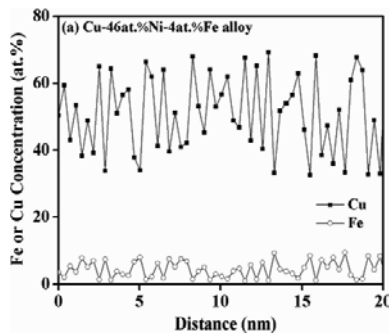


Figure 19. Cu and Fe concentration profile of the Cu-46at.%Cu-4at.%Fe alloy aged at 400°C for 200 h.

The simulated microstructural evolution for the Cu-46at.%Ni-4at.%Fe alloy aged at 400°C for different times is shown in **Figure 20**. The white and black zones correspond to the Ni-Cu-Fe-

rich and Cu-Ni-Fe-rich phases, respectively. The morphology is irregular and interconnected, and it has no preferential alignment in a specific crystallographic direction (**Figure 20(a-c)**). This type of microstructure has been named isotropic [4]. The volume fraction of phases is similar because of the small difference in chemical composition. For higher temperatures, the isotropic morphology at the early stages of aging, as the aging progresses, changes to a cuboid or plate shape, crystallographically aligned along the $\langle 100 \rangle$ directions because of the low coherency-strain energy associated with these directions [9].

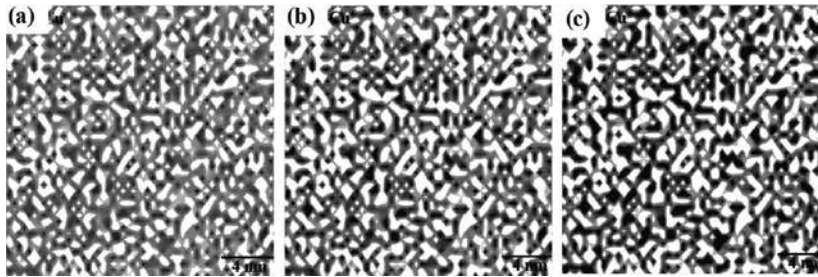


Figure 20. Microstructure evolution of the Cu-46at.%Cu-4at.%Fe alloy aged at 400°C for (a) 50 h, (b) 100 h, and (c) 200 h.

Figure 21 shows the FIM microstructural evolution of the Cu-46at.%Ni-4at.%Fe alloy aged at 400°C for 50 h. FIM image of the solution treated and quenched sample shows the characteristic concentric ring of the (001) plane in both alloys. In the case of the aged samples, brightly imaged zones correspond to the Ni-Cu-Fe-rich phase and dark zones to the Cu-Ni-Fe-rich phase (matrix). The morphology of the decomposed phases was also cuboids or plates aligned in the $\langle 100 \rangle$ directions as the aging progressed.

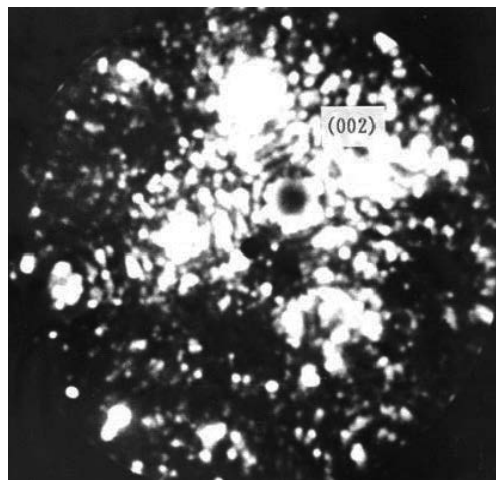


Figure 21. FIM image of the Cu-46at.%Cu-4at.%Fe alloy aged at 400°C for 50 h.

6. Summary

The *phase-field method* for simulation can provide important results, qualitatively and quantitatively, about the microstructural phenomena. This is based on the solution of the Cahn-Hilliard equation and it is a powerful tool to carry out the numerical simulation of the phase decomposition in binary and ternary alloys. The numerical simulation, by mean of the explicit finite difference method, is useful not only to analyze the growth kinetics of phase decomposition but also to determine the morphology of the decomposed phases. Besides, the calculated results show, in general, a good agreement with the experimental results during the aging of these alloys. Additionally, it is interesting to notice that the simulated results enable us to analyze the effect of different parameter such as the atomic mobility and the elastic-strain energy on the growth kinetics and phase morphology of the decomposed phases. Besides, it is important to mention that the numerical simulation permits to analyze the phase decomposition from the early to the late stages of aging which is useful to analyze both the spinodal decomposition and coarsening processes. In the case of the Ni-30at.%Cu alloy, the application of the phase-field method to simulate the microstructural evolution confirmed that the growth kinetics of phase decomposition is very slow in Ni-Cu alloys because of the low atomic diffusive process at temperatures lower than 322°C. However, when a third alloying element, like Fe, is added to this system, the spinodal decomposition process occurs more quickly. Finally, in the case of the Fe-40at.%Cr alloy, it can be clearly observed that the coarsening process of decomposed phases takes place since several concentration fluctuations are grouped in one peak as the aging time progresses.

Acknowledgements

The authors wish to acknowledge financial support from Tecnológico Nacional de México/ Instituto Tecnológico de Pachuca, and SIP-IPN and Conacyt.

Author details

Erika O. Avila-Davila¹, Victor M. Lopez-Hirata^{2*} and Maribel L. Saucedo-Muñoz²

*Address all correspondence to: vlopezhi@prodigy.net.mx

¹ Tecnológico Innstitute of Pachuca, Pachuca de Soto, Hidalgo, Mexico

² National Polytechnic Institute (ESIQIE), Department of Metallurgy and Materials, Mexico City, Mexico

References

- [1] Cahn J.W., Hilliard J.E., Free energy of a nonuniform system I. Interfacial free energy. *J. Chem. Phys.* 1958; 28, 258–267.
- [2] Allen S.M., Cahn J.W., A microscopic theory for antiphase boundary motion and its application to antiphase domain coarsening. *Acta Metal.* 1979; 27, 1085–1095.
- [3] Ginzburg V.L., Landau L.D. On the theory of superconductivity. *Zh. Eksp. Teor. Fiz.* 1950; 20, 1064–1082.
- [4] Hilliard J.E., *Phase transformations*, ASM, 1970.
- [5] Raabe D. *Computational materials science*, Wiley-VCH, 1998.
- [6] Rappaz M., Bellet M., Deville M. *Numerical modelling in materials science and engineering*, Springer, 1998.
- [7] Avila-Davila E.O., Lopez-Hirata V.M., Saucedo-Muñoz M.L., Gonzalez-Velazquez J.L. Microstructural simulation of phase decomposition in Cu-Ni alloys. *J. Alloys Comp.* 2008; 460, 206–212.
- [8] Lifshitz I.M., Slyozov V.V. The kinetics of precipitation from supersaturated solid solution. *J. Phys. Chem. Solids.* 1961; 19, 35–50.
- [9] Kostorz G. *Phase transformations in materials*, Wiley-VCH, 2001.
- [10] Avila-Davila E.O., Lezama-Alvarez S., Saucedo-Muñoz M.L., Lopez-Hirata V.M. Gonzalez-Velazquez J.L., Simulación numérica de la descomposición espinodal en sistemas de aleación hipotéticos A-B y A-B-C. *Revista de Metalurgia.* 2012; 48, 223–236.
- [11] Baker H. *Alloy phase diagrams handbook*, Vol. 3, ASM International, 1992.
- [12] Moser Z., Zakulski W., Spencer P., Hack K. Thermodynamic investigations of solid Cu-Ni and Fe-Ni alloys and calculation of the solid state miscibility gap in the Cu-Fe-Ni system. *CALPHAD.* 1985; 9, 257–269.
- [13] Pearson W.B. *A handbook of lattice spacing and structures of metals and alloys*, ASM International, 1986.
- [14] Mehrer H. *Diffusion in solid metals and alloys*, Springer-Verlag, 1990.
- [15] Dieter G.E. *Mechanical metallurgy*, Mc Graw Hill, 2001.
- [16] Soriano-Vargas O., Avila-Davila E.O., Lopez-Hirata V.M., Dorantes-Rosales H.J., Gonzalez-Velazquez J.L. Spinodal decomposition in an Fe-32 at% Cr alloy during isothermal aging. *Mater. Trans. JIM.* 2009; 50, 1753–1757.
- [17] Lopez-Hirata V.M., Sano N., Sakurai T., Hirano K. A study of phase decomposition in Cu-Ni-Fe alloys. *Acta Metall. Mater.* 1993; 41, 265–271.

- [18] Avila-Davila E.O., Melo-Maximo D.V., Lopez-Hirata V.M., Soriano-Vargas O., Saucedo-Muñoz M.L., Gonzalez-Velazquez J.L. Microstructural simulation in spinodally-decomposed Cu-70 at.%Ni and Cu-46 at.%Ni-4 at.%Fe alloys. *Mater. Characterization*. 2009; 60, 560–567.
- [19] Honjo M., Saito Y. Numerical simulation of phase separation in Fe-Cr binary and Fe-Cr-Mo ternary alloys with use of the Cahn-Hilliard equation. *ISIJ Int.* 2000; 40, 914–919.

Geotechnical Civil Engineering

DEM Simulation Based on Experimental Testing

Dr Šarūnas Skuodis

Additional information is available at the end of the chapter

<http://dx.doi.org/10.5772/63889>

Abstract

The paper examines several key aspects of soil morphology, namely experimental and numerical test validation and compression test result dependency on changing morphology parameters. The present chapter describes investigation of soil morphology parameters influence for numerical compression properties with evaluation of examined sand engineering geological conditions. The main objects of research: morphology parameters investigation with view analysis program and scanning electronic microscope; experimental soil compression testing; numerical soil compression simulation and results validation with experimental ones. The primary purpose of this paper is therefore to investigate the influence of morphology parameters on sand mechanical properties and to determine optimal quantity of spheres for single-particle shape subscription.

Keywords: discrete element method, numerical simulation, compression, morphology, scanning electronic microscope, particles

1. Introduction

The present chapter describes numerical simulation of sand geomaterial with the discrete element method (DEM), based on input data acquired from physical experiments. First of all, sandy soil is composed of different shape and size particles. That means, it is necessary to provide sieving test to determine granulometry curve of investigated sand. After this step, it is used scanning electronic microscope (SEM) to determine main sand particles morphology parameters, namely area, perimeter, form coefficient, angularity, roundness, circularity, and sphericity coefficients, respectively. Next physical experiments level—sand compression with oedometer. Having all this information, it is possible to start numerical DEM modelling of sand compression test.

Granulometric curve and separate particle shape discretization are one of the most relevant existing problems for numerical modelling via DEM. There are no direct recommendations for a single-particle subscription with spheres (single-particle subscription level based on spheres size and quantity). Subscribing soil particles with DEM, it is very important to choose size, shape, and physical properties of modelled particles. It is possible to model realistic size oedometer device without not scaled particles if quantity of modelled particles is small. Modelling of soil which is subscribed with a big quantity of particles is not possible because of the limitations of computer calculation capacity. All simplifications are accepted in order to decrease the calculation time. Another relevant problem, arising from all accepted simplifications, is a very small quantity of the authors working on experimental and numerical testing validation. This fact only proves that there are still a lot of problems related to dispersive systems, which are modelled with DEM.

2. Sand composition and morphology parameters

The investigated area is located in the southern part of Lithuanian continental coastal zone of Baltic Sea, the northern part of Klaipeda city [1]. To the north of the Klaipeda city, only the immediate near-shore contains a sandy strip of Holocene marine sediments (m IV), which occurs in up to 4–5 m of the sea water depth. The material composing the near-shore sediments in the continental coast zone mainly consists of different sand, where prevailing medium coarse and fine sand [2, 3] with admixture of gravel and organic matter [4, 5]. This sand was used for investigations (**Figure 1**). The coordinates of sampling location [1] are 55°46′4.07″, 21°4′39.06″ (WGS).



Figure 1. Location of sand sampling.

The average density of particles (ρ_s) value of marine sands is 2.67 Mg/m³ and varies from 2.65 to 2.71 Mg/m³, respectively. The bulk density of the sand varies from 1.83 to 2.09 Mg/m³, where

average is 1.98 Mg/m^3 . Regardless to the genesis of marine sand and their grain size distribution, the mineral composition consists mainly of quartz. The natural moisture content depends on the degree of saturation of water and ranges from 13.7 to 27.7%. The void ratio (e) in fine sand varies from 0.474 to 0.778, respectively [4–6]. The recent marine sediments (m IV) were formed in the coastal zone; therefore, a distinctive morphological feature of grain shape has high sphericity, where $P = 0.84$ [6]. Investigated sand mineralogical composition determined in reference [7], where basic consistency of the sand is $\sim 85\%$ quarts, $\sim 6\%$ feldspar with remaining contribution of carbonate, mica and some other minerals. The grading curve of investigated soil is given in **Figure 2**.

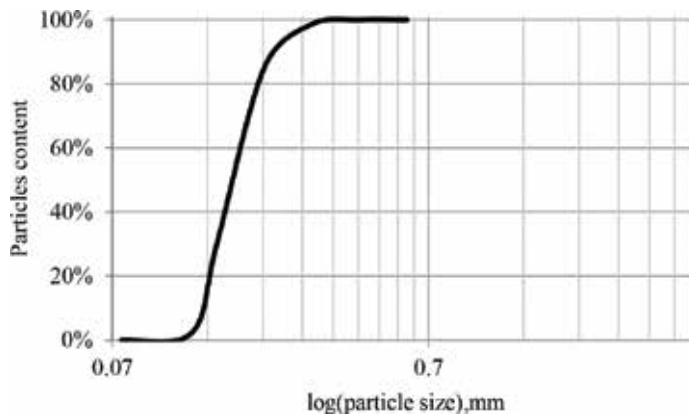


Figure 2. Grading curve of investigated soil sample.

Thirty-three different sand grains corresponding nine sand fractions [8] have been examined, the total number of examined grains being 297. Investigation of grains morphology parameters provided with SEM and view analysis program. Example of investigation process is given in **Figure 3**. Smaller fractions within the 0.0063–0.15 mm are omitted in the panoramic view due to the lack of space in SEM camera. Rest of all fractions was investigated separately.

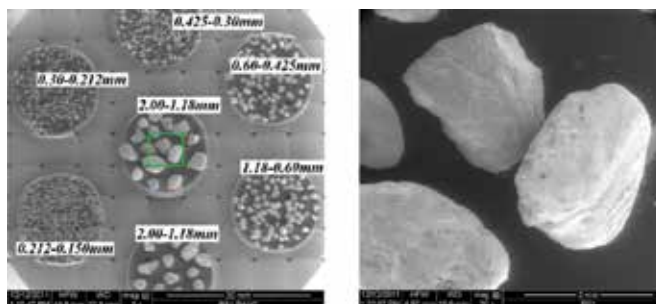


Figure 3. Soil 2D investigation with SEM [1]: pictures of panoramic view (left) and magnification of marked area (right).

The main morphological parameters of investigated sand fractions employed in 2D view analysis [9, 10] include these parameters, namely area (mm^2), equivalent diameter (mm), sphericity, circularity, form coefficient, angularity. Final decision to investigate particles only in 2D was accepted according to literature analysis.

2D and 3D view analysis and determination of grain sphericity results accuracy 5–10% [11, 12]. Due to this fact, it is saved a lot of time which is spent for morphological parameters investigations with SEM and view analysis program. Small results differences between 2D and 3D analysis are due to particle landing on the investigation table with the biggest particle gravity centre (**Figure 4**). Particle stays on investigation table with the biggest stability surface in contact with investigation table [13]. In this case, particles maximum length is in a parallel line with investigation table surface and particles height which is perpendicular for investigation tables is the smallest. Results inaccuracy can be increased if it is investigated mainly flat grains [14].



Figure 4. Flat (on the left hand) and spherical (on the right hand) particle shape.

The analysis of the determined morphological parameters within each fraction shows that the shape of all grains is sufficiently similar—It tests the grains differ principally only in size. The obtained mean 2D morphological parameters of the particles are given in the **Table 1**.

| Morphological parameter | Mean value |
|--------------------------|---------------------------------------------------------------------------------------|
| Area (mm^2) | 0.112 |
| Equivalent diameter (mm) | 0.340 |
| Sphericity | 0.836 |
| Circularity | 0.515 |
| Form coefficient | 0.702 |
| Angularity | 0.410 |
| Particle shape |  |

Table 1. Mean 2D case morphological parameters of investigated sands [15].

The mean shape of investigated sand grain was determined using [16, 17] given solutions for sand shape characterization according to the particle sphericity and roundness. In this case, it is not necessary to use Fourier descriptors [18]. The analysis of the change of morphology

parameters of investigated Baltic Sea soil-type according to the equivalent diameter increment is shown in **Figure 5**.

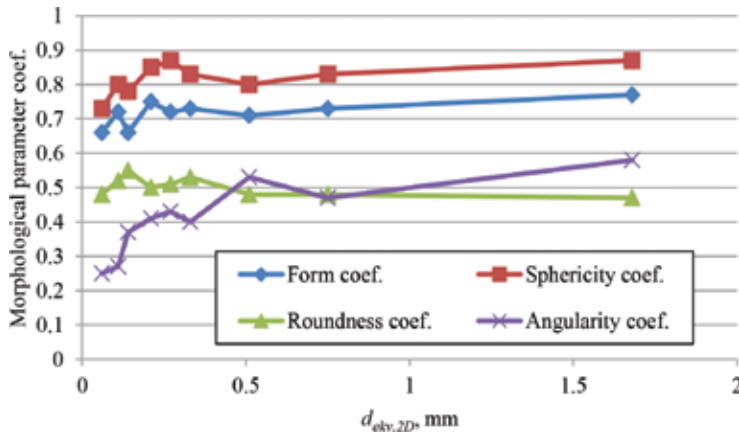


Figure 5. Morphological parameters versus $d_{ekv,2D}$.

3. Experimental sand compression with oedometer

Compression tests were performed using computer controlled (fully automatic) oedometer test device. The same sand soil used for morphology parameters investigation was examined in compression tests with the standard oedometer device (ring height $H=3.39$ cm; ring diameter $D=7.14$ cm). Testing program consists of the study of the influence of vertical stress ramp (Figure 6) on the compression results, the study of crashing of separate particles, and upgrade of testing procedure, respectively.

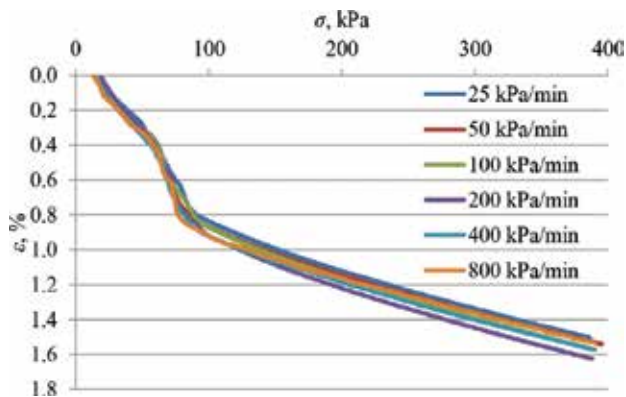


Figure 6. Vertical load ramp influence for soil deformation.

Obtained results, which are presented in **Figure 6**, clearly show that loading ramp is not having any effect for soil deformation. Due to this reason, it was accepted to use 400 kPa/min loading ramp for rest of all tests with oedometer. From this point, it is necessary to check two things before numerical oedometer modelling:

1. Does the examined particles having any crushing effect with used maximum vertical stress 400 kPa on provided oedometer tests.
2. Where are the errors on computer controlled oedometer testing procedure, because in **Figure 6** given results start not from 0 kPa.

The solution for the checking of particles crushing is to provide a series of oedometer tests with different maximum vertical stress. After each test, it is necessary to run sieving test and to check granulometry change. If the granulometry composition is not changing, that means, particles with accepted maximum vertical stress loading are not crushed. Small change of mass after sieving test can be revealed, but this happens due to particles loss during sieving procedure. Normally, particle loss can be up to 1%. Obtained sieving tests results after different maximum loading are given in **Table 2**.

| Sieve size, mm | Particles content, g | | | | |
|-------------------|----------------------|---------|---------|---------|---------|
| | 0 kPa | 200 kPa | 400 kPa | 600 kPa | 800 kPa |
| 2.0–1.18 | 0.000 | 0.000 | 0.000 | 0.000 | 0.000 |
| 1.18–0.6 | 2.145 | 2.003 | 1.999 | 1.864 | 1.816 |
| 0.6–0.425 | 39.593 | 39.234 | 40.478 | 39.298 | 39.053 |
| 0.425–0.3 | 91.319 | 90.727 | 90.984 | 90.466 | 90.640 |
| 0.3–0.212 | 65.780 | 66.430 | 64.859 | 65.803 | 65.380 |
| 0.212–0.150 | 6.188 | 6.217 | 6.206 | 6.185 | 6.190 |
| 0.150–0.125 | 0.297 | 0.306 | 0.318 | 0.347 | 0.359 |
| 0.125–0.075 | 0.121 | 0.153 | 0.204 | 0.324 | 0.358 |
| 0.075–0.063 | 0.026 | 0.023 | 0.026 | 0.030 | 0.031 |
| <0.063 | 0.000 | 0.045 | 0.059 | 0.122 | 0.095 |
| SUM: | 205.469 | 205.138 | 205.133 | 204.439 | 203.922 |

Table 2. Soil sieve test results after different compression steps [19].

Knowing that tested soil particles cannot have crushing effect (the analysis of obtained results revealed that sand particles are not crushed up to 800 kPa maximum vertical loading) makes more simple DEM oedometer test modelling.

The main finding from the compression test procedure is presented in **Figure 7**. Comparison of the standard and improved procedures consists of two different stages. The first comparison stage involves vertical loading values from 0 to 100 kPa. In this stage, the standard test

procedure cannot evaluate immediate settlements [20], since for contact ensurance between porous stone and soil, 10 kPa vertical stress is established. Therefore, **Figure 7** shows results not from 0 kPa.

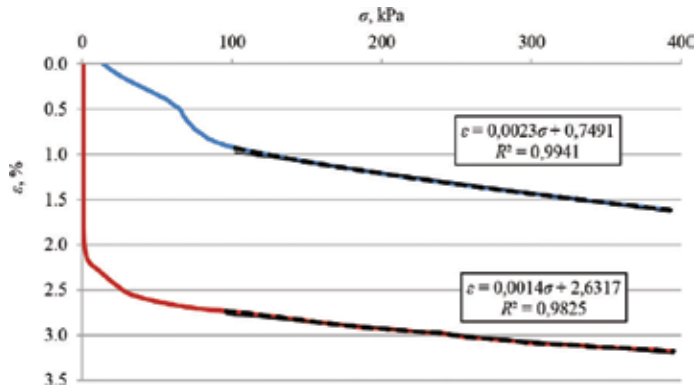


Figure 7. Comparison of soil compression methodologies: blue—standard procedure; red—improved procedure.

The improved testing procedure is better than the standard one, as porous stone is positioned in the calibrated height, selected according to the initial sample height. Performing compression test with the improved testing procedure, it is possible to analyse compression curve from 0 kPa.

The standard and improved testing procedures differ in their obtained compression curves values only, and the character of their vertical strain values remains the same. In the standard procedure, a smaller compressed sample deformation ($\epsilon = 1.6168\%$) is obtained comparing with the improved testing procedure ($\epsilon = 3.1763\%$). The comparison of different compression procedures allow the judicious selection of DEM compression modelling as the preferred methodology since it is an improved testing methodology and allows the analysis of compression results from 0 kPa.

The soil compression curve mostly obtained in literature is given in **Figure 8** [21].

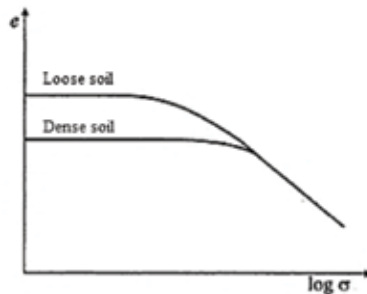


Figure 8. Soil void ratio versus normal stress.

Analysing soil compression curve given in **Figure 8**, it comes obvious that soil density or void ratio for low stress values does not change. Void ratio change is obtained only when soil is loaded with high stress values. Such interpretation of the compression curve is not reliable due to two reasons:

1. In the contact place of porous stone and soil sample, contact settlements occur at the low stress due to not perfect soil surface. Contact settlements ensure good porous stone and soil sample contact between each other.
2. When testing clay soils with large sand or gravel particles, sample surface imperfections occur during soil sample preparation on the sample side, in a contact with the oedometer ring surface. Due to these surface imperfections, the soil sample expands in the horizontal direction during the loading process, and it continues until a sufficient contact with the oedometer ring. This can be considered as an explanation of the appearance of additional sample settlement.

If the soil sample has loading, unloading and reloading steps, **Figure 8** given compression curve is suitable only for the reloading step. Other authors present soil compression curves with vertical loading from 5 to 10 kPa [22–26]. In this case, it is not necessary to show what happens with the soil compression curve when vertical stress is from 0 to 5 or 10 kPa.

4. Numerical simulation of compression test with DEM

Evaluation of the actual compressibility properties via soil compression tests is important for employment of subsequent numerical analysis of stress and strain state of ground subjected by supplement loading (e.g. loads transmitted via foundations from a superstructure, interaction of structure and soil strata, etc.). The confined compression (oedometer) test is approved as a relatively fast and simple laboratory test. It is performed under different conditions, loading paths and durability. Test conditions depend on physical changes in multiphase system of soil, generally related with reorganisation of soil grains, that of initial change of skeleton in cohesive soils and velocity of water filtration for saturated soils. One must note that in some cases the duration of testing procedure for prediction of long-term soil behaviour and in other specific cases is very long [25], thus sometimes taking into account the time and test cost ratio it is not worth even to start the test. On the other hand, one cannot qualitatively explain the variation of soil compression test results, basing on some processing of already known testing and analysis data separately or in concern with view analysis. It is obvious that having not identified the actual physical mechanism for soil grain reorganisation during compression process and its peculiarities, one cannot explain the observed scatter of results under disposal. This mechanism cannot be recorded by applying usual techniques of testing and view analysis but can be simulated applying the relevant DEM techniques (initiated by [27–29]): that of the mathematical models of processes and discrete models for soil grains [1].

The above-mentioned circumstances, as well as the permanently reducing computational costs, the development of numerical techniques and software in the field of multi-scale analysis

(including the particle strata mechanics), initiated a fast development and the applications numerical analysis in the field of the soil behaviour by means of the DEM. Such approach, combined with an experimental analysis for validation and calibration of the mathematical models, is definitely a promising one, allowing to reduce the price and quantity of laboratory tests and a reasonless conservatism in determining the values of mechanical properties of soils in near future.

Numerical simulation via DEM was provided using DEMMAT code [30]. This original program called DEMMAT has been written in Compaq Visual FORTRAN language. The quality of implementation is handled by a physically observable behaviour of interactions: particle–particle, particle–wall, particle–bottom and/or top plate (porous stone), and by the validation with the results obtained from physical experiments. The application of DEM to a system involves the following basic steps [30]:

1. Set-u of initial conditions of the particles and the walls, top and bottom plate (porous stone);
2. Searching for the contacts between particles;
3. Applying interaction laws (calculating forces and moments) to all particle–particle, particle–wall, particle–bottom and/or top plate (porous stone);
4. Applying Newton's second law to determine particle motion. Predicting positions, velocities, accelerations and higher-order time derivatives;
5. Updating the current state of particles and the walls;
6. Assigning a new time $t = t + \Delta t$;
7. If current time is within entire time period ($t \leq T$)—go to the step 2, otherwise go to the next step;
8. Post-processing and visualization.

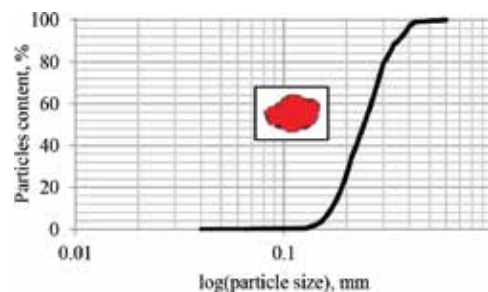


Figure 9. Numerical granulometric composition curve.

More detailed information about used models and parameters in DEM simulation is in references [1, 30].

Numerical DEM simulations are performed with the same granulometric curve as obtained in experimental testing for the Baltic Sea sand. The used numerical granulometric curve with mean experimentally determined particle shape is given in **Figure 9**.

In this study, recalculation of time period is based on reference [31]:

$$T_H = 2.87 \left(\frac{\frac{V_i \rho}{2}}{\frac{R_{min}}{2} \cdot \frac{E_p}{2(1-\nu^2)} \cdot v_{ij}} \right)^{0.2} \tag{1}$$

where E_p – modelled particle deformation modulus, MPa; ν – loading velocity, m/s²; v_{ij} – initial particle velocity, m/s; ρ – particle density, kg/m³; R_{min} – smallest modelled particle radius, m.

Seeking to increase the calculation accuracy, it is necessary to re-calculate the time period, thereby obtaining the real-time period for computation:

$$\Delta t = \frac{T_H}{10} \tag{2}$$

Particles position and contact forces change according to Δt are given in **Figure 10**.

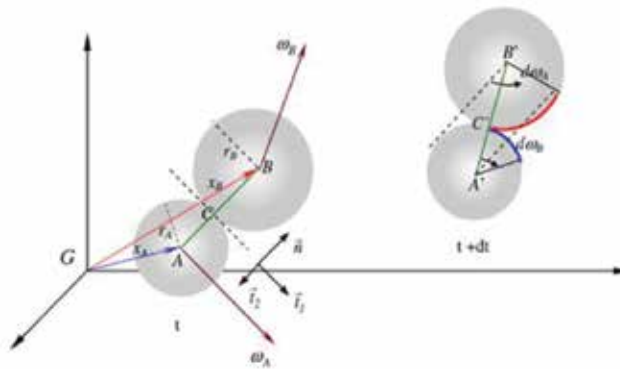


Figure 10. Particles positions and contacts recalculation at time t and $t + dt$ [32].

The test process and parameters for simulations are presented in **Table 3**. The actual Young's modulus $E_{oed} = 200$ GPa for oedometer volume parts is employed for simulations with Poisson's ratio $\nu = 0.3$ and density $\rho = 7850$ kg/m³, and simulated oedometer height $H = 0.00484$ m and diameter $D = 0.0102$ m. During simulations reached maximum strain was 1.76% (as in the experimental testing). Accepted simulated particles Poisson's ratio $\nu = 0.17$, oedometer walls Poisson's ratio $\nu = 0.3$.

| Quantity | Symbol | Unit | Numerical simulation | Literature overview | References |
|---------------------------------------------------------------|------------|-------------------|-------------------------|---------------------------------------------------------------------------------------------------------------------------|--------------------------------------|
| Solid particle density | ρ_s | kg/m ³ | 2,650,000 | 2600; 2650; 2340; 2500; 2730; 2650 × 10 ⁹ | [33–38] |
| Particles Young's modulus | E_p | MPa | 78,000 | 4.61; 26,600; 300; 568–2400; 3000–30,000; 4000–75,000; 63.9–120.3; 70,000 | [34, 35, 30, 39–41, 32, 38] |
| Particles number | N | – | 46,095 | 2658; 6000; 205–1915; 4150; 10,000; 1 | [33, 42–46] |
| Friction coefficient between particles | M | – | 0.84 | 0.5; 0.5; 0.25; 0.6; 0.1–0.9; 0.5; 0.7; 0.66; 0.5 | [33, 47, 36, 44, 48, 49, 37, 50, 51] |
| Friction coefficient between particles and walls/porous stone | M | – | 0.3 | 0; 0; 1.0; 0.5; 0.5; 0 | [33, 36, 44, 49, 37, 51] |
| Rolling friction | μ_r | – | 0.04 | 1.6 × 10 ⁻⁵ ; 0.15; 0.01; 0.05 | [44, 52, 48, 53] |
| Time step | Δt | s | 2 × 10 ⁻⁷ | 1 × 10 ⁻⁷ ; 1.25 × 10 ⁻⁶ ; 2.02 × 10 ⁻⁸ ; 4.44 × 10 ⁻⁸ ; 1 × 10 ⁻⁴ | [33, 44, 54, 55] |
| Loading velocity | V | m/s | 4.84 × 10 ⁻³ | 0.1; 5 × 10 ² %; 0.1 [*] × 10 ⁻⁴ ε/s | [56, 49] |

*Note: Literature overview values correspond references sequence number.

Table 3. Test model data.



Figure 11. Modelled oedometer compression test separation into quarters [1].

All DEM numerical simulation calculations ran on cluster due to faster calculation process. In this case, it is possible to separate modelled oedometer into four quarters where each quarter is calculated by separate computer (**Figure 11**). In DEM simulations, parallel calculations of clusters are widely applied. Using these clusters, it is possible to calculate much bigger simulations in the same period of time, as with a single computer. Nevertheless, applications of clusters in DEM simulations do not provide enough calculation capacity. More detailed explanation of calculations with DEM is presented in Refs. [1, 30].

Used modelled particles shapes in numerical simulations have three shapes: ideal sphere, particle recreated from two spheres and particle recreated from three spheres (**Figure 12**). Recreation of particles shapes is based on experimental testing results obtained from morphology parameters determination part.

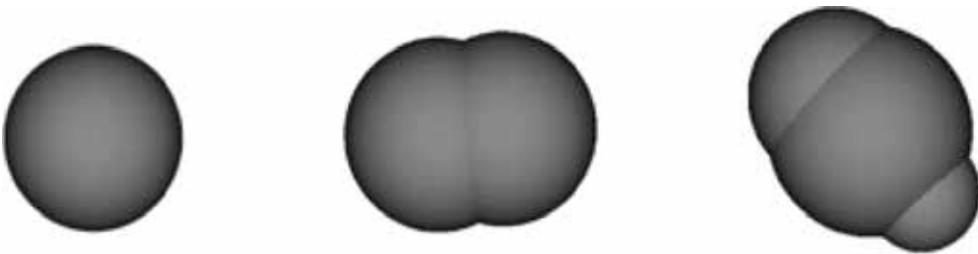


Figure 12. Recreation of particles shapes.

Providing DEM numerical simulations with different recreated particles shapes, it is possible to obtain particle shape influence for compression results. The analysis of influence of simulated particles shape on compression results is presented in **Figure 13**.

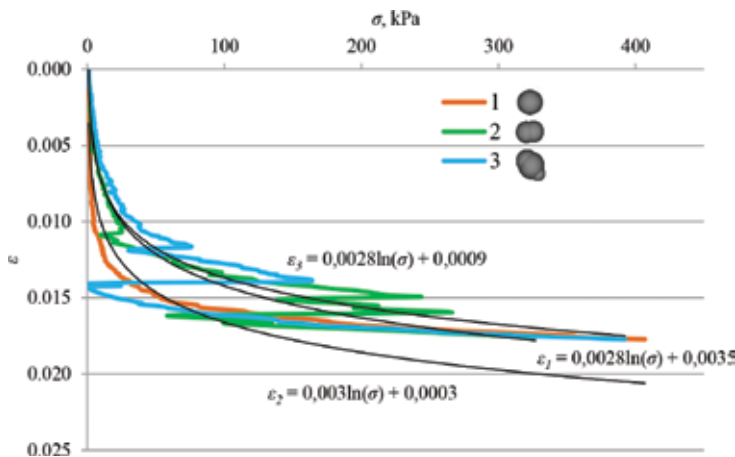


Figure 13. Comparison of compression results with different particle shape: 1—particle recreated from sphere; 2—particle recreated from two spheres; 3—particle recreated from three different sizes spheres.

Analyzing **Figure 13**, it is evident that the compression curve which is obtained from the simulations with ideal sphere particles has a smooth curve. With increasingly complex particle shapes, stress jumps arise in the numerical simulation. These stress jumps appear due to faster particles repositioning than porous stone compression velocity. To increase porous stone velocity is not recommended, because it is possible to have not a static but dynamic modelling effect.

5. Comparison of experimental and numerical simulation tests

Reliability and accuracy of numerical DEM modelling of sand soil behaviour depend on the modelled soil and discretization level of particles. In this research work, the same numerical granulometric curve as obtained experimentally was used (**Figure 14**).

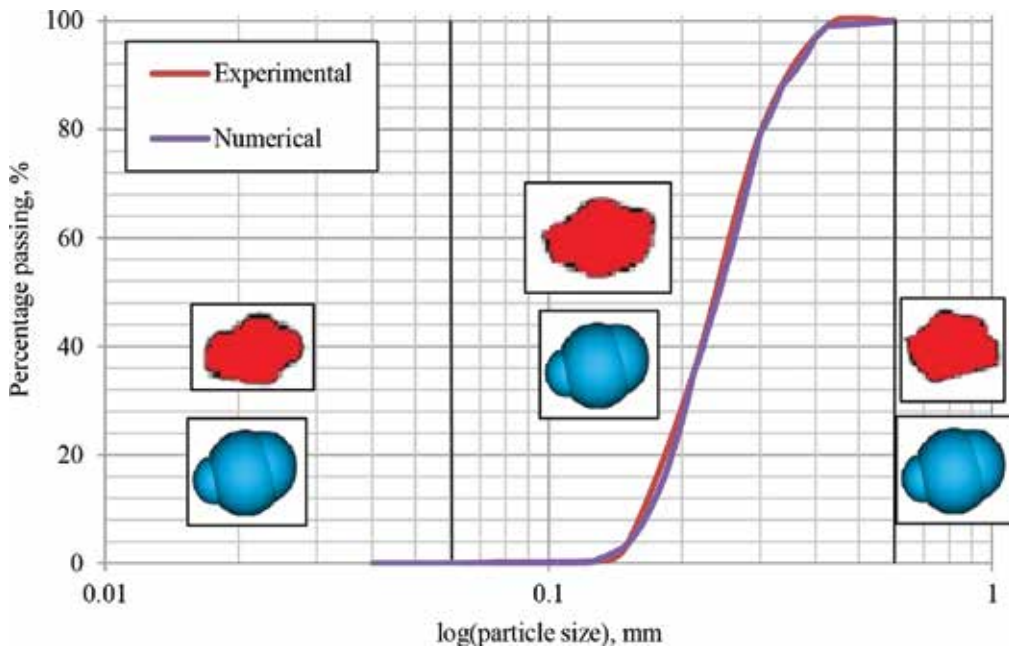


Figure 14. Numerical and experimental granulometric curves.

The analysis of obtained experimental and numerical morphology parameters is given in **Figure 15**. Comparison of results revealed that to recreate morphology parameters, involvement of different quantity of spheres for single-particle subscription is necessary: 8–11 spheres for form coefficient, 7–11 spheres for sphericity, 8–12 spheres for circularity, 3–4 spheres for angularity, respectively. Analysing angularity recreation with different quantity of spheres, the angularity coefficient decreases when more than seven spheres are used for single-particle subscription.

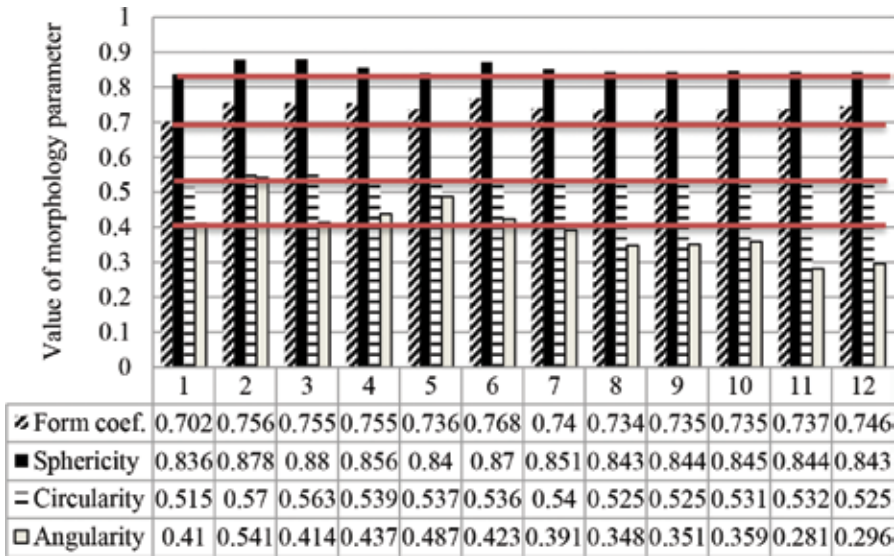


Figure 15. Comparison of morphology parameters: 1—experimental data; 2–12—spheres quantity of recreated numerical particle shapes.

Validation of experimental and numerical ($E_p = 78 \text{ GPa}$ and $\rho_s = 2,650,000 \text{ kg/m}^3$) compression results is presented in **Figure 16**. One can note that used high modelled particles density increases calculation speed and does not have any effect for contact mechanics due to the first Newton law of motion.

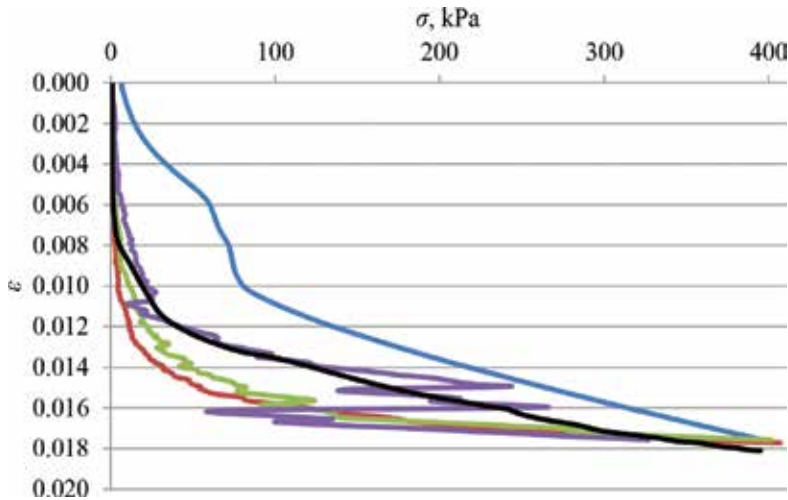


Figure 16. Comparison of compression results: blue—standard experiment; red—numerical experiment (one sphere); green—numerical experiment (two spheres); purple—numerical experiment (three spheres); black—improved experiment.

The analysis of compression results revealed (**Figure 16**) that the increased spheres quantity for single-particle discretization lead the numerical compression curve to the experimental one. For a more qualitative match of experimental and numerical curves, it is better to use the improved experimental compression curve which is closer to the numerical results. In this case, the curves of numerical and improved experimental results get closer to each other. Usually, only numerical tests are corrected with non-normal coefficients to get the same result curve as in the experiment. In this case, it was improved experimental test to get experimental compression curve more closely to numerical one. This effect was obtained realising the same compression procedure in experiments and in numerical simulations.

6. Concluding remarks

This research work presents an experimental investigation of morphology parameters of sand particles, experimental oedometer tests, numerical DEM modelling of oedometer tests, and comparison of experimental and numerical tests. Based on experimental and numerical testing findings, the influence of morphology parameters on mechanical properties of soil is analysed. It is obvious that this research work represents only one soil type (sand). For other soil types as clay, silt, etc., it is not possible to apply obtained results. Nevertheless, the main idea of this research work shows the importance of results validation between experimental and numerical ones. Only comparing results, it is possible to choose the same testing procedure in experimental and numerical simulation. Provided numerical simulations in this research work still are not perfect and needs to be improved. For example, stress jumps, which appear in numerical simulations, are doubtful. The explanation of the stress jumps simple—it is necessary to simulate a bigger particles quantity. In this case, particles for repositioning have not so much space and do not appear big stress jumps. Another way to get smooth and nice numerical simulations compression curve (as in experiment)—simulate particles as ideal spheres. This is what the author wants to show for the readers.

Nowadays simulations oriented on two main things:

- Simulate test as simple as just it is possible and accept so far not real particle shape, physical and mechanical properties, but to have smooth compression curve as in experiment. In this case, it would be not possible to use the same input data in DEM program if the modelled soil or soil particles shape would change;
- Simulate test as just it is possible with more natural and close to reality parameters. This would make calculations very difficult and calculation time increased. But if the soil or soil particles shape would be changed, it would be possible to run calculations without any change of physical and mechanical properties (just make some changes for modelled particle shape).

In both cases, it is recommended to check the numerical simulations with experimental ones. The influence of the above-mentioned factors, contributing the accuracy of numerical modelling is a future trend.

Author details

Dr Šarūnas Skuodis

Address all correspondence to: sarunas.skuodis@vgtu.lt

Director of Civil Engineering Research Centre, Vilnius Gediminas Technical University (VGTU), Lithuania

References

- [1] Skuodis Š, Markauskas D, Norkus A, Žaržojus G, Dirgeliene N. Testing and numerical simulation of Holocene marine sand uniaxial compression at Lithuanian coast. *Baltica*. 2014;27(1):33–44. doi:10.5200/baltica.2014.27.04.
- [2] Repečka M. Quarternary sediments on the bottom surface of the south-eastern Baltic Sea. *Baltica Special Publication*. 1999;12:93–98.
- [3] Gulbinskas S, Trimonis E. Distribution and composition of bottom sediments on the underwater slope at the Lithuanian coast of the Baltic Sea. *Baltica Special Publication*. 1999;12:32–37.
- [4] Gadeikis S, Repečka M. Geotechnical properties of the Baltic Sea bottom sediments (Lithuanian near shore zone). *Baltica Special Publication*. 1999;12:11–14.
- [5] Dundulis K, Gadeikis S, Gadeikyte S, Račkauskas V. Sand soils of Lithuanian coastal area and their geotechnical properties. *Geologija*. 2006;53:47–51.
- [6] Dundulis K, Gadeikis S, Ignatavičius V. Quaternary deposits engineering geological conditions formation. Lithuanian entrains change and resources. *Spec. Litosfera issue*. 2004(2004):318–331.
- [7] Amšiejus J, Dirgeliene N, Norkus A. Analysis of methods for evaluation of soil shear strength parameters. In the 10th International Conference Modern Building Materials, Structures and Techniques; 19–21 May 2010; Vilnius, Lithuania; 2010. p. 1077–1082.
- [8] LST EN ISO 14688-1:2007. Geotechnical investigation and testing - Identification and classification of soil - Part 1: Identification and description (ISO 14688-1:2002). Lithuanian stadartization department; 2007. 14 p.
- [9] Kavrus A, Skuodis Š. Investigation of morphological parameters for sand soil. In 15th Conference of Young Lithuanian Scientists “Science—the Future of Lithuania”; 20–24 May 2012; Vilnius, Technika; 2012. p. 1–8.
- [10] Prušinskiene S. Peculiarities of sandy soils and their investigations methods. Vilnius, Technika; 2012. 183 p. doi:10.3846/1314-5

- [11] Krumbein W C. Measurement and geologic significance of shape and roundness of sedimentary particles. *Journal of Sedimentary Petrology*. 1941;11:64–72.
- [12] Riley NA. Projektion sphericity. *Journal of Sedimentary Petrology* 1941;11: 94–97.
- [13] Fedaa J. *Mechanics of particulate materials—the principles*. Elsevier, Academia; 1982. 447 p.
- [14] Cavarreta I. *The influence of particle characteristics on the engineering behaviour of granular materials [thesis]*. London, London Imperial College; 2009.
- [15] Šlečkuvienė A, Skuodis Š. Influence of sand grains morphological parameters for deformation properties, In 16th Conference of Young Lithuanian Scientists “Science—the Future of Lithuania”; 20–22 March 2013; Vilnius, Technika; 2013. p. 1–7.
- [16] Krumbein WC, Sloss L. *Stratigraphy and Sedimentation. A series of books in geology*. San Francisco, W. H. Freeman and Co; 1951. 497 p.
- [17] Cho G, Dodds J, Santamarina J. Particle shape effects on packing density, stiffness and strength: natural and crushed sands. *Journal of Geotechnical and Geoenvironmental Engineering*. 2006;132(5):591–602.
- [18] Mollon G, Zhao J. Generating realistic 3D sand particles using Fourier descriptors. *Granular Matter*. 2013;15(1):95–108.
- [19] Skuodis Š, Kavrus A. Particle shape evaluation before and after compression. *Science – Future of Lithuania*. 2012;4(4):340–345. doi:10.3846/mla.2012.53
- [20] Skuodis Š, Amšiejus J. Investigation into compressibility of different types of sand fractions using a oedometer. *Engineering Structures and Technologies*. 2011;3(1):16–22. doi:10.3846/skt.2011.02
- [21] Uygur E, Doven AG. 2006. Monotonic and cyclic oedometer tests on sand at high stress levels. *Granular Matter*. 2006;8(2006):19–26.
- [22] Sohby EM, Mazen O, Aboushook M. Advancement in oedometer testing of unsaturated soils. In *International Conference on Advanced Experimental Unsaturated Soil Mechanics, EXPERUS 2005*. Teronto, Italy; 2005. p. 1–6.
- [23] Lupogo K. Effect of fines mineralogy on the oedometric compressional behaviour of sandy soils. *Journal of Civil Engineering and Construction Technology*. 2013;4(7):232–238.
- [24] Comina C, Fotti S, Musso G, Romero E. EIT Oedometer: An advanced cell to monitor spatial and time variability in soil with electrical and seismic measurements. *Geotechnical Testing Journal*. 2008;31(5):1–9.
- [25] Tong F, Yin JH. Nonlinear creep and swelling behaviour of bentonite mixed with different sand contents under oedometric condition. *Marine Georesources & Geotechnology*. 2011;29(4):346–363.

- [26] Shipton B, Coop MR. On the compression behaviour of reconstituted soils. *Soils and Foundations*. 2012;52(4):668–681.
- [27] Cundall PA, Strack ODL. A discrete numerical model for granular assemblies. *Geotechnique*. 1979;29:47–65.
- [28] Williams J R, Hocking G, Mustoe GGW. The theoretical basis of the discrete element method. Numeta 1985, Numerical methods of engineering, Theory and applications, A. A. Balkema, Rotterdam, January (1985).
- [29] Pande G, Beer G, Williams JR. Numerical modeling in rock mechanics, New York, John Wiley and Sons (1990).
- [30] Balevičius R, Džiugys A, Kačianauskas R. Discrete element method and its application to the analysis of penetration into granular media. *Journal of Civil Engineering and Management*. 2004;10(1):3–14.
- [31] Hertz H. The contact of solid elastic bodies, *Journal für die Reine und Angewandte Mathematik*. 1882;92:156–171.
- [32] Belheine N, Plassiard J, Donze F, Darve F, Seridi A. Numerical simulation of drained triaxial test using 3D discrete element modeling. *Computers and Geotechnics*. 2009;36(1):320–331.
- [33] Markauskas D, Kačianauskas R. Compacting of particles for biaxial compression test by the discrete element method. *Journal of Civil Engineering and Management*. 2006;12(2):153–161.
- [34] Tumonis L, Kačianauskas R, Norkus A, Žilionienė D. Comparison study of spherical and multi-spherical particles under cyclic uniaxial compression. *Journal of Civil Engineering and Management*. 2012;18(4):537–545.
- [35] Latham JP, Mindel J, Xiang J, Guises R, Garcia X, Pain C, Gorman G, Piggot M, Munjiza A. Coupled FEMDEM/Fluids for coastal engineers with special reference to armour stability and breakage. *Geomechanics and Geoengineering: An International Journal*. 2009;4(1):39–53.
- [36] Kim BS, Park SW, Kato S. DEM simulation of collapse behaviours of unsaturated granular materials under general stress states. *Computers and Geotechnics*. 2012;42(2012):52–61.
- [37] Thongmune S, Matsumoto T, Kobayashi S, Kitiyodom P, Kurosawa K. Experimental and numerical studies on push-up load tests for sand plugs in a steel pipe pile. *Soils and Foundations*. 2011;51(5):959–974.
- [38] Macaro G, Uti S. DEM triaxial tests of a seabed sand. In *Discrete Element Modeling of Particulate Media: Proceedings of the International Symposium on Discrete Element Modeling of Particulate Media*. Royal Society of Chemistry, Sp. Pub. University of Birmingham, Birmingham, 2012;339:203–211.

- [39] Geng Y, Yu HS, McDowell GR. Discrete element modeling of cavity expansion and pressuremeter test. *Geomechanics and Geoengineering: An International Journal*. 2013;8(3):179–190.
- [40] Widuliński L, Kozicki J, Tejchman J. Numerical simulations of triaxial test with sand using DEM. *Archives of Hydro–Engineering and Environmental Mechanics*. 2009;56(3–4):149–171.
- [41] Cavarretta I, O'Sullivan C, Ibrahim E, Lings M, Hamlin S. Characterization of artificial spherical particles for DEM validation studies. *Particuology*. 2012;10(2012):209–220.
- [42] Wu J, Collop A, McDowell G. Discrete element modelling of monotonic compression tests in an idealised asphalt mixture. *Road Materials and Pavement Design*. 2009;10(1): 211–232.
- [43] Xu Y, Kafui K D, Thornton C, Lian G. Effects of material properties on granular flow in a silo using DEM simulation. *Particulate Science Technology: An International Journal*. 2002;20(2):109–124.
- [44] Nakashima H, Shioji Y, Kobayashi T, Aoki S, Shimizu H, Miyasaka J, Ohdi K. Determining the angle of repose of sand under low-gravity conditions using discrete element method. *Journal of Terramechanics*. 2011;48(2011):17–26.
- [45] Modenese C, Utili S, Houlsby GT. A numerical investigation of quasi-static conditions for granular media. In *Proceedings of the International Symposium on Discrete Element Modelling of Particulate Media*. University of Birmingham, Birmingham, 2012. p. 187–195.
- [46] Jasevičius R, Tomas J, Kačianauskas R. Simulation of ultrafine silica particle on substrate. *Particulate Science and Technology: An International Journal*. 2011;29(2): 107–126.
- [47] Cheng YP, Nakata Y, Bolton MD. Discrete element simulation of crushable soil. *Géotechnique*. 2003;53(7):633–641.
- [48] Wiącek J, Molenda M, Horabik J, Ooi JY. Influence of grain shape and intergranular friction on material behaviour in uniaxial compression: Experimental and DEM modeling. *Powder Technology*. 2012;217(2012):435–442.
- [49] Bagherzadeh–Khalkali A, Mirghasemi AA, Mohammadi S. Micromechanics of breakage in sharp-edge particles using combined DEM and FEM. *Particuology*. 2008;6(2008):347–361.
- [50] Longmore JP, Marais P, Kuttel MM. Towards realistic and interactive sand simulation: A GPU-based framework. *Powder Technology*. 2013;235(2013):983–1000.
- [51] Minh NH, Cheng YP. Strong force network of granular mixtures under one-dimensional compression. In *Proceedings of the International Symposium on Discrete*

- Element Modelling of Particulate Media. University of Birmingham, Birmingham, 2012; p. 227–235.
- [52] Widuliński L, Tejchman J, Kozicki J, Leśniewska D. Discrete simulations of shear zone patterning in sand in earth pressure problems of retaining wall. *International Journal of Solids and Structures*. 2011;48(2011):1191–1209.
- [53] Pocius G, Balevičius R. Simulation of poly- and monodispersed granular material. Part I: Structure characteristics. *Engineering Structures and Technologies*. 2012;4(1):16–28.
- [54] Liu Y, You Z, Zhao Y. Three-dimensional discrete element modeling of asphalt concrete: Size effects of elements. *Construction and Building Materials*. 2012;37(2012):775–782.
- [55] Li LQ, Jiang MJ, Shen ZF. Verification of the double slip and rotation rate model for elliptical granular flow using the distinct element method. In *Proceedings of the International Symposium on Discrete Element Modeling of Particulate Media*. University of Birmingham, Birmingham, 2012; p. 236–244.
- [56] McDowell GR, Collop AC, Wu JW. A dimensional analysis of scaling viscosity and velocity in DEM of constant strain rate tests on asphalt. *Geomechanics and Geoen지니어ing: An International Journal*. 2009;4(2):171–174.

Chemical Engineering

Impact of Fluid Flow on Free Radical Polymerization in a Batch Reactor

Gerardo M. Pineda-Torres, Cecilia Durán-Valencia,
Fernando Barragán-Aroche and
Simon López-Ramírez

Additional information is available at the end of the chapter

<http://dx.doi.org/10.5772/64156>

Abstract

In this work, the mixing process on a batch reactor is analyzed for the thermal synthesis of poly(acrylamide-co-sodium 2-acrylamide-2-methylpropane sulfonate) initiated by ammonium persulfate. The analysis is achieved by using tracer technology and computational fluid dynamics (CFD). ANSYS Fluent® software is used for numerical simulations. By studying the mixing time in the reactor, the injection point and the stirring speed are determined so that the kinetics of copolymerization is improved.

The kinetics of copolymerization is studied qualitatively based on the solution of the inverse rheokinetic problem. The progress of co-polymerization was registered with a Rheometer Anton Paar MCR 301®. The copolymers synthesized were characterized by capillary viscometry, infrared spectroscopy, calorimetry, and rheology.

Keywords: CFD, rheokinetics, rheology, batch reactor, polymerization

1. Introduction

Modeling of chemical reactors attempts to solve both conservation (mass, energy, and momentum) and chemical kinetics equations [1]. The complexity of the mathematics involved can be drastically reduced by considering that convection dominates the diffusion, by assuming a unidimensional scenario or by simplifying the momentum transport equations [2]. Nevertheless, these assumptions may oversimplify the mathematical model by neglecting mixing problems. Mixing plays a fundamental role in reaction engineering. For instance, the

kinetics, the molecular weight, and the composition of polymers can be altered due to local concentration gradients as a consequence of bad mixing [3].

In this study, a batch chemical reactor is analyzed. This type of reactor is defined as a closed and spatially uniform system where the chemical species are transformed only as a function of time. The transformation of chemical species can be quantified by following any physico-chemical property associated with either reagents or products. During free radical polymerizations, the viscosity of the medium increases dramatically while products are formed [4]. The kinetics of polymerization can be followed from the change of viscosity.

Rapid computational development has made the numerical analysis of phenomena associated with stirred tanks easier [5]. For example, through CFD, Patel [6] studied the mixing process on a continuous stirred tank reactor and how the thermal polymerization of styrene is affected.

Computational analysis in stirred reactors has to consider at least two models: one for turbulence and the other for stirring. The turbulence model describes the random and chaotic movement of a fluid [7], while the stirring model describes the displacement of the fluid as a consequence of the local movement of mechanical parts.

The study of batch reactors with a tracer is the basis for understanding flow behavior [8]. Tracer evolution curves allow to identify regions with turbulence, dead zones, recirculation cycles, closed circuits, or even to determine the mixing time of the reactor [9, 10].

In this work, a tracer test was used to validate a mathematical model. The mixing process was analyzed by using both the experimental and simulated behavior of the tracer. The experimental kinetics of polymerization was obtained by a multiparametric nonlinear regression of viscosity-time data.

2. Problem definition

The uses of polyacrylamide have been extended to different applications in the oil industry, such as water conformance, fracking, and enhanced oil recovery (EOR) processes.

In EOR applications, acrylamide (AAM) polymers are dispersed in water to increase their viscosity. However, at high temperatures the viscosity of AAM polymer decreases due to hydrolysis [11]. This can be mitigated by using co-monomers such as sodium 2-acrylamido-2-methylpropane sulfonate (AMPSNa) [12]. This sodium sulfonate monomer is well known because it confers stability to the polymer against divalent cations and high temperatures (above 90°C). In view of the benefits, it is necessary to develop a process for the synthesis of the AAM-AMPSNa copolymer that guarantees product quality and synthesis reproducibility in order to properly design the polymer. The next sections will be focused on studying the relation between the mixing time and the mixing process during the synthesis of copolymer in a batch reactor.

3. Rheokinetics and inverse problem

The kinetics of polymerization was analyzed through the evolution of rheological behavior of the reactive system. Rheology has entered into science fields, such as biology and polymer science [13]. Historically, polymer science and rheology converge in what is known as rheokinetics. This field was created more than 30 years ago to have a better understanding of the phenomenological nature of polymerizations.

There are two main problems related to rheokinetics: the direct and inverse problems. The inverse problem, which is the principal focus of this work, deals with the determination of kinetic parameters given by the experimental data of viscosity-time curves. Equation (4) reproduces the viscosity-time curve behavior (rheokinetic model) and it was obtained from Eqs. (1–3). This equation assumes a linear free radical polymerization and it does not consider mass and energy transport effects. Equations (1) through (4) are deeply analyzed by Malkin, see [14].

$$\eta = Kx^b\bar{N}^a \quad (1)$$

$$x = 1 - \exp\left(-\frac{k_p k_d^{1/2} f^{1/2}}{k_t^{1/2}} [I]_o^{1/2} t\right) \quad (2)$$

$$\bar{N} = \frac{[M]_o}{[I]_o} x(1 - \exp(-k_d t)) \quad (3)$$

$$\eta = K[M]_o^a [I]_o^{-a} \left[1 - \exp\left(-\frac{2f^{1/2} k_p}{k_d^{1/2} k_t^{1/2}} [I]_o^{1/2} [1 - \exp(-k_d t)]\right)\right]^{a+b} \quad (4)$$

where η is the viscosity, t is the reaction time, \bar{N} is the polymerization degree, x is the conversion, $[M]_o$ is the initial monomer concentration, $[I]_o$ is the initial initiator concentration, K , a , b , and f are system parameters and k_p , k_t , k_d are the rate constants of propagation, termination, and initiation, respectively.

The ratio $k_p/k_t^{1/2}$ is estimated as proposed by **Figure 1**. To guarantee the quality of the adjustment, k_d must be a number between 0.01 and 1 [4]. To know which process dominates the polymerization, the magnitude of $k_p/k_t^{1/2}$ is used as an indicator. If the ratio is $k_p/k_t^{1/2} \gg 1$, the propagation of live chains dominates; on the contrary, when $k_p/k_t^{1/2} \ll 1$, the termination of macro radicals dominates.

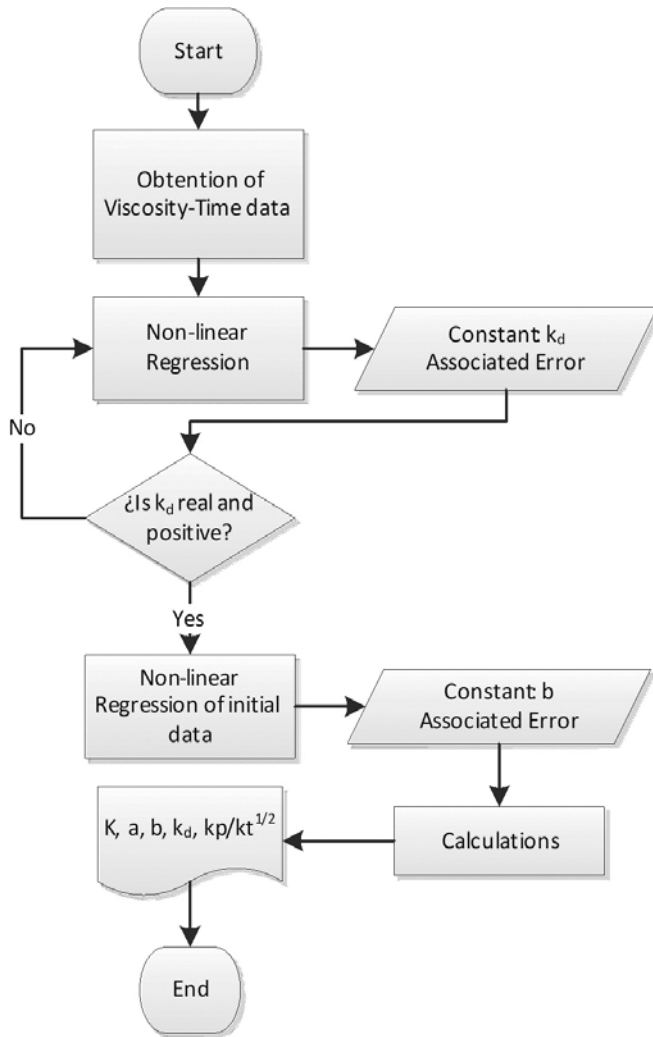


Figure 1. Estimation of $k_p/k_t^{1/2}$ from viscosity-time experimental data.

4. Computational fluid dynamics (CFD)

CFD is concerned with the numerical solution of the following partial differential equations that express the conservation principles of mass, energy, and momentum transport (5–7) [2].

$$\frac{\partial x_A}{\partial t} + (\nabla \cdot \mathbf{v}x_A) - (\nabla \cdot \nabla D_{AB}x_A) - R_A + S_A = 0 \tag{5}$$

$$\frac{\partial \rho C_p T}{\partial t} + (\nabla \cdot \mathbf{v} \rho C_p T) - (\nabla \cdot \nabla k \rho C_p T) - q_R + q_I = 0 \quad (6)$$

$$\rho \frac{\partial \mathbf{v}}{\partial t} + [\nabla \cdot \rho \mathbf{v} \mathbf{v}] - \mathbf{g} \rho + \nabla P + [\nabla \cdot \boldsymbol{\tau}] = \mathbf{0} \quad (7)$$

where x_A is the concentration of "A" species, T is the temperature, \mathbf{v} is the velocity, ρ is the density, C_p is the heat capacity, D_{AB} is the diffusion coefficient, k is the thermal conductivity, \mathbf{g} is the gravity, P is the pressure, $\boldsymbol{\tau}$ is the stress tensor, R_A y q_R are terms associated with the chemical reaction, S_A y q_I are source terms and $\nabla = \frac{\partial}{\partial x_i}$.

Equations (5–7) are supported in two assumptions. The first one is the conservation principle which states that mass, energy, and momentum are transformed without creating or destroying themselves and the second one is the continuum hypothesis which considers continuity of its physical properties [15].

When simplifying Eq. (7) by considering a fluid of constant density and viscosity and a linear relation between the shear rate and the shear stress, the Navier-Stokes equations can be obtained Eq. (8):

$$\rho \frac{D\mathbf{v}}{Dt} - \mathbf{g} \rho + \nabla P - \mu [\nabla \cdot \nabla \mathbf{v}] = \mathbf{0} \quad (8)$$

Navier-Stokes equations are the basis of CFD and its numerical solution is fundamental to understand and describe the phenomena of fluid flow.

A CFD simulation is limited by the data processing rates and storing capacity. Nevertheless, improvements of computers capacity have stimulated the growth and diversification of CFD applications [16]. Nowadays, there are several CFD software tools as COMSOL® and Fluent®.

5. Fluent® simulation

A typical simulation comprises the formulation of the problem, physical assumptions to simplify the mathematical model, the numerical solution of the conservation equations, data processing, and the discussion of results. The mathematical models, initial conditions, and other adjustments can be implemented through Fluent® software.

In **Figure 2**, there are at least two critical stages: convergence of the numerical solution and validation of the mathematical model.

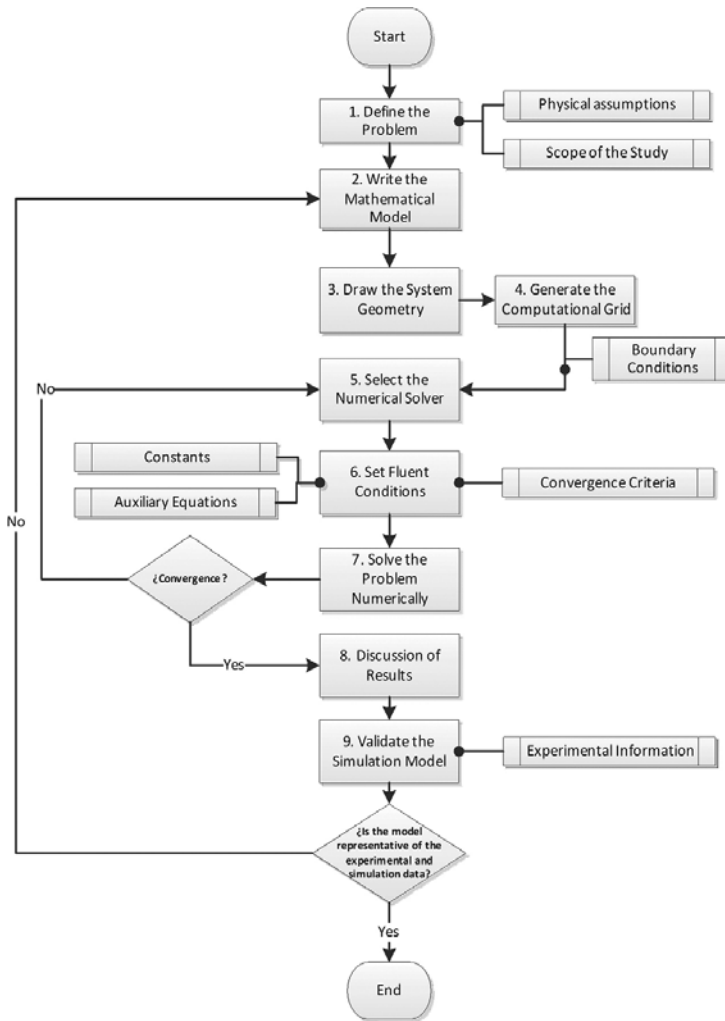


Figure 2. Development of a Fluent® simulation.

6. Turbulence and RANS equations

Turbulence is described as a random and chaotic movement of a fluid. Mathematically, a turbulence model is a nonlinear system in which a minimum modification on its boundary conditions produces severe alterations in the global behavior of the system [17]. Ranade proposes three approaches to model turbulence in fluids: statistical, deterministic, and structural [2]. Reynolds-average Navier-Stokes (RANS) equations are part of the statistical approximation in which turbulence is described as a combination of average variables (θ_1) and fluctuations θ_f [18]:

$$\theta_i = \bar{\theta}_i + \theta_f \tag{9}$$

Semi-empirical k - ϵ is a turbulence model commonly used in stirred tanks. The model assumes complete turbulence and neglects molecular viscosity effects. k - ϵ is part of the RANS equations and it is composed by a two-equation system with two parameters to solve: k (turbulence kinetic energy) and ϵ (turbulence dissipation rate). Standard k - ϵ was the first model; RNG (renormalization group theory) and realizable models were developed from subsequent modifications [19]. In contrast to standard k - ϵ , RNG improves flow with eddies and it adds a term to the ϵ equation ($R\epsilon$).

$$\frac{\partial(\rho k)}{\partial t} + \nabla \cdot \mathbf{v}(\rho k) = \nabla \cdot [\varpi_k \mu_{eff} \nabla k] + G_k + G_b - \rho \epsilon - Y_M + S_k \tag{10}$$

$$\frac{\partial(\rho \epsilon)}{\partial t} + \nabla \cdot \mathbf{v}(\rho \epsilon) = \nabla \cdot [\varpi_\epsilon \mu_{eff} \nabla \epsilon] + C_{1\epsilon} \frac{\epsilon}{k} (G_k + C_{3\epsilon} G_b) - C_{2\epsilon} \rho \frac{\epsilon^2}{k} - R_\epsilon + S_\epsilon \tag{11}$$

Realizable k - ϵ has a superior performance for rotational flows and for boundary layers under adverse conditions like high-pressure gradients, separation, and recirculation [18].

$$\frac{\partial(\rho k)}{\partial t} + \nabla \cdot \mathbf{v}(\rho k) = \nabla \cdot \left[\left(\mu + \frac{\mu_t}{\sigma_k} \right) \nabla k \right] + G_k + G_b - \rho \epsilon - Y_M + S_k \tag{12}$$

$$\frac{\partial(\rho \epsilon)}{\partial t} + \nabla \cdot \mathbf{v}(\rho \epsilon) = \nabla \cdot \left[\left(\mu + \frac{\mu_t}{\sigma_\epsilon} \right) \nabla \epsilon \right] + \rho C_{1\epsilon} S_\epsilon - \rho C_{2\epsilon} \frac{\epsilon^2}{k + \sqrt{V\epsilon}} + C_{1\epsilon} \frac{\epsilon}{k} C_{3\epsilon} G_b + S_\epsilon \tag{13}$$

$$C_1 = \max \left(0.43, \frac{\eta}{\eta + 5} \right) \tag{14}$$

$$S = \sqrt{2\mathbf{S}_{ij}\mathbf{S}_{ij}} \tag{15}$$

$$\eta = S \frac{k}{\epsilon} \tag{16}$$

where G_k is the generation of “ k ” by velocity gradients and G_b by buoyancy, S_k and S are source terms, C_2 and C_1 are constants, and σ_k and σ_ϵ are σ are the turbulent Prandtl numbers for k and ϵ , respectively. Turbulent viscosity (μ_t) is calculated as indicated by Eq. (17):

$$\mu_t = \rho C_\mu \frac{k^2}{\epsilon} \quad (17)$$

In contrast to RNG, realizable model uses a variable C_μ that satisfies the “realizability” through Schwarz shear rate inequality and by making the normal stress tensor positive.

$$C_\mu = \frac{1}{4.04 + \frac{\sqrt{6\cos\phi k U^*}}{\epsilon}} \quad (18)$$

U^* is calculated by Eq. (19), where $\overline{\Omega_{ij}}$ is the rotation average speed tensor on a rotating reference frame with angular velocity ω_k :

$$U^* = \sqrt{\mathbf{S}_{ij}\mathbf{S}_{ij} + \tilde{\Omega}_{ij}\tilde{\Omega}_{ij}} \quad (19)$$

$$\tilde{\Omega}_{ij} = \Omega_{ij} - 2\epsilon_{ijk}\omega_k \quad (20)$$

$$\Omega_{ij} = \overline{\Omega'_{ij}} - \epsilon_{ijk}\omega_k \quad (21)$$

7. Stirring model

CFD simulation of moving parts, e.g. impellers and turbines, requires approximations that consider the displacement and rotation of mechanical parts on a computational grid. The most used models for stirred tanks are the moving reference frame (MRF) and the sliding mesh (SM). In contrast to MRF, SM requires more computational resources and its convergence time is higher.

MRF is defined by a rotational and a stationary region. The equations are solved on a reference frame that rotates with the impeller and the problem is solved on a stationary grid [20]. When the momentum equation is solved, an additional acceleration term is incorporated in the velocity vector formulation as relative Eq. (22) or absolute Eq. (23).

$$\frac{\partial \rho \mathbf{v}_r}{\partial t} + [\nabla \cdot \rho \mathbf{v}_r \mathbf{v}_r] + \rho [2\mathbf{w} \times \mathbf{v}_r + \mathbf{w} \times \mathbf{w} \times \mathbf{r}] - \mathbf{g}\rho + \nabla P + [\nabla \cdot \boldsymbol{\tau}] = 0 \quad (22)$$

$$\frac{\partial \rho \mathbf{v}}{\partial t} + [\nabla \cdot \rho \mathbf{v}_r \mathbf{v}] + \rho [\mathbf{w} \times \mathbf{v}] - \mathbf{g}\rho + \nabla P + [\nabla \cdot \boldsymbol{\tau}_r] = \mathbf{0} \quad (23)$$

The term $\rho[2\mathbf{w} \times \mathbf{v}_r + \mathbf{w} \times \mathbf{w} \times \mathbf{r}]$ is composed by the Coriolis acceleration ($2\mathbf{w} \times \mathbf{v}_r$) and the centripetal acceleration ($\mathbf{w} \times \mathbf{w} \times \mathbf{r}$). The stress tensor $\boldsymbol{\tau}$, keeps its mathematical structure, but it uses relative velocities.

SM models the rotation of the grid by adding a source term as a function of time in Eq. (8) allowing a relative movement of the adjacent grids among themselves. The SM equation is formulated for a scalar (ϕ) as follows:

$$\frac{d}{dt} \int_V \rho \phi dV + \int_{\partial V} \rho \phi (\mathbf{u} - \mathbf{u}_g) \cdot d\mathbf{A} = \int_{\partial V} D \nabla \phi \cdot d\mathbf{A} + \int_V S_\phi dV \quad (24)$$

where V is the control volume, D is the diffusion coefficient, S_ϕ is a source term, \mathbf{u} is the flow velocity vector, \mathbf{u}_g is the velocity of the moving grid, and ∂V is the control volume interface.

A third manner to model the movement of mechanical parts is through the boundaries of the walls; this approximation was named tangential rotation (ROT) and holds true only for viscous flows (non-slip condition).

8. Numerical method

Two numerical solvers can be selected in Fluent[®]. The first is a pressure-based solver that was initially developed for high-speed incompressible flow. The second is a density-based that was developed for high-speed compressible flow. Regardless of the solver being used, the velocity field is calculated from the momentum equations [19]. The general solution algorithm can be divided in three stages:

1. Generation of the discrete volumes (computational grid).
2. Discretization of the conservation equations.
3. Linearization of the discretized equations and solution of the resulting system.

The pressure-based solver is established from the pressure-correction equation obtained from the momentum and continuity equations. Convergence is reached when the estimated velocity field satisfies the continuity condition:

$$\sum_f^{N_{faces}} J_f A_f = 0 \quad (25)$$

where J_f is the mass flux and A_f is the surface area of face " f ". In the pressure-based methods, there are segregated algorithms based on corrector-predictor approximations (e.g. SIMPLE, SIMPLEC and PISO). SIMPLE algorithm or semi-implicit method for pressure-linked equations satisfies Eq. (25) by correcting the flux J_f through J'_f and by the corrected pressure p' . The algorithm postulates that J'_f follows Eq. (26) [19]. J^*_f is calculated by using the pressure field p^* .

$$J_f' = d_f (p_{c0}' - p_{c1}') \quad (26)$$

$$J_f = J_f^* + J_f' \quad (27)$$

$$J_f = J_f^* + d_f (p_{c0}' - p_{c1}') \quad (28)$$

9. Methodology

The following materials were obtained from Sigma Aldrich (Munich, Germany) and were used without any further purification: AAm (99.8%) and AMPS (99%). Ammonium persulfate or APS (98%) was obtained from Tecsiquim (State of Mexico, Mexico). AMPSNa preparation is reported elsewhere [21]. The molar ratio of the monomers (1:1) was constant with a total initial concentration of 10.6% wt. The initial concentration of APS was kept constant at 0.5% wt. Polymerization progress was followed in an Anton Paar® MCR 301 Rheometer with a concentric cylinder geometry (CC27/CX) coated with polytetrafluoroethylene. A batch of reagents was prepared and then divided into seven samples that were polymerized at different shear rates as shown in **Table 1**.

| Experiment | C1 | C2 | C3 | C4 | C5 | C6 | C7 |
|-------------------------------|----|----|----|----|-----|-----|-----|
| Shear rate [s ⁻¹] | 10 | 30 | 60 | 90 | 120 | 150 | 200 |

Table 1. Set of AAm and AMPSNa copolymerization experiments at 60°C.

In relation to the CFD simulation, the geometry and the grid were constructed in Gambit®. The dimension of the geometry described the Parr® batch reactor used in the experimental work. Geometrically, the computational model is composed by a cylinder in whose interior a stirrer with rectangular impeller blades is located.

After designing the grid, sensitivity analysis was carried out to compare the velocity field magnitude in two grids with different cell sizes. The first grid (M_{200k}) contains 201,927 cells, while the second (M_{400k}) holds 482,312 cells. Pure water was used for both simulations.

Afterwards, Fluent® simulations were run to select a turbulence and stirring model. Experimental validation of the computational model was done by injecting 1 mL of 1 M sodium hydroxide solution (tracer). The response of the tracer was quantified with the multiparametric device OAKTON® PC 2700.

To correlate the shear rate and the stirrer speed in a batch stirred reactor, Eqs. (29) and (30) are used. This allows the comparison of stirring between the two systems used in this work, the reactor and the rheometer.

$$\dot{\gamma} = 0.107255N^{1.4} \quad (29)$$

$$N = \left(\frac{\dot{\gamma}}{0.107255} \right)^{\frac{1}{1.4}} \quad (30)$$

where $\dot{\gamma}$ is the shear rate [s^{-1}] and N [rpm] is the stirrer speed. This relation was studied theoretically and experimentally by Sanchez, see [22]. The Re number was used to verify the turbulence.

$$Re = 117.39 \cdot N \quad (31)$$

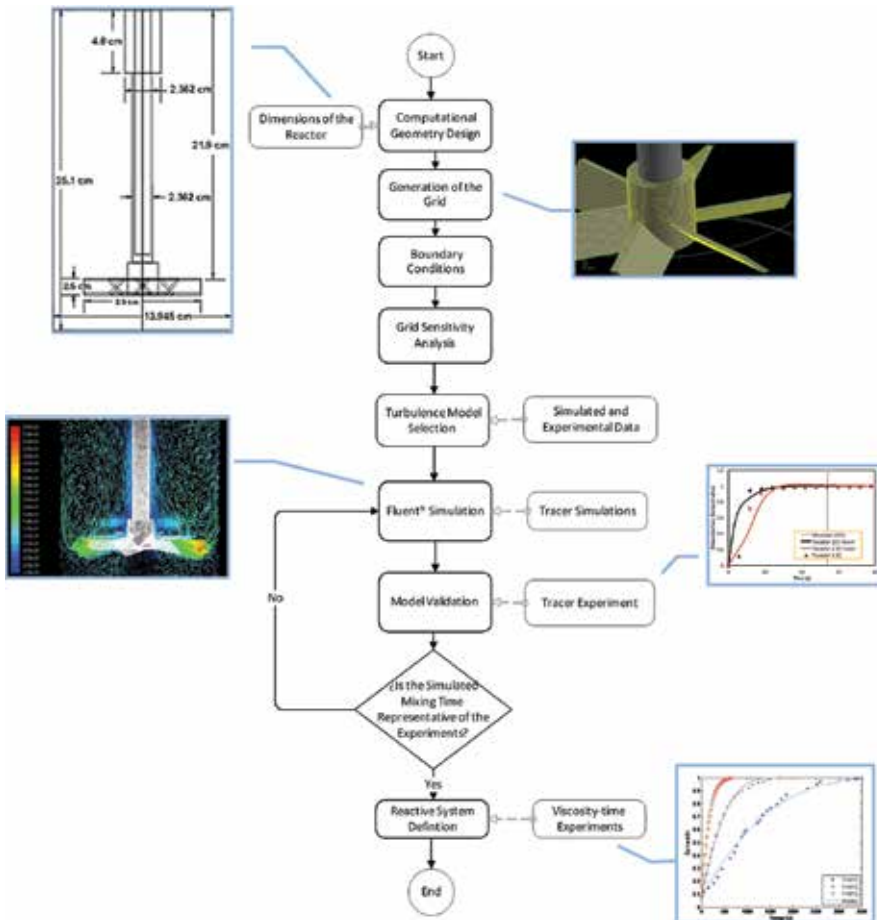


Figure 3. Work route for simulations of stirred tanks in Fluent®.

The number 117.39 was calculated for the reactor filled with liquid water (viscosity of 0.001 Pa·s and density of 998.2 kg/m³) and by using the geometrical dimension of the system.

The methodology used for the simulations is presented in **Figure 3**. The diagram contains the experimental test used to validate the simulation model.

10. Kinetics of polymerization

For the synthesized copolymers of **Table 1** the experimental viscosity-time curves are presented in **Figure 4**, an adjustment of experimental data was done by using Eq. (4).

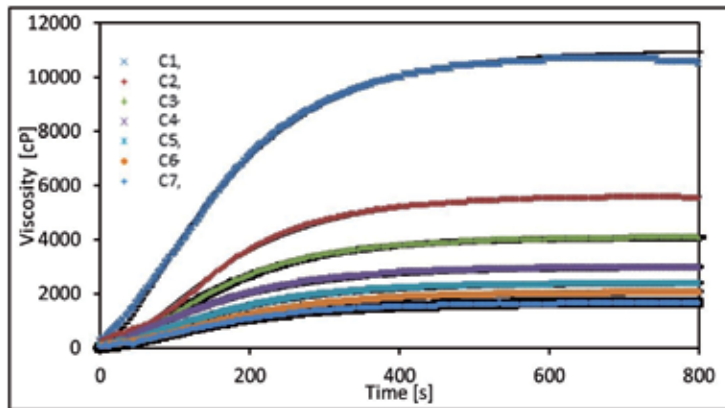


Figure 4. Viscosity-time data at 60°C and predicted data (–) from Eq. (4).

The numerical results of this regression are presented in **Table 2**.

| Experiment | Shear rate [s ⁻¹] | Stirrer speed [rpm] | k_v [s ⁻¹] | $k_p/k_t^{1/2}$ [L ^{1/2} mol ^{-1/2} s ^{-1/2}] |
|------------|-------------------------------|---------------------|--------------------------|---------------------------------------------------------------------------|
| C1 | 10 | 26 | 7.36×10^{-03} | 0.00034 |
| C2 | 30 | 56 | 7.87×10^{-03} | 0.00075 |
| C3 | 60 | 92 | 8.32×10^{-03} | 0.00074 |
| C4 | 90 | 123 | 7.21×10^{-03} | 0.00374 |
| C5 | 120 | 151 | 7.66×10^{-03} | 0.00715 |
| C6 | 150 | 177 | 7.03×10^{-03} | 0.00535 |
| C7 | 200 | 217 | 7.67×10^{-03} | 0.01099 |

Table 2. Kinetic parameters obtained from experimental data.

It was found that $k_p/k_t^{1/2}$ is proportional to the shear rate used in the synthesis. k_d values are kept constant through all experiments, concluding that the initiation kinetics is independent of the shear rate. The copolymers were characterized to obtain a better understanding of the chemistry involved in the synthesis.

All copolymers were characterized by the following techniques: Fourier transform infrared spectroscopy (FTIR) in a Cary 600 Series spectrometer from Agilent®; differential scanning calorimetry (DSC) in an HP DSC 1 STAR® from Mettler Toledo® and rheology with a Physica MCR-301 Rheometer from Anton Paar®. The results of all these characterizations are presented in **Table 3**.

| Experiment | Shear rate (s ⁻¹) | M _v (g/mol) | FTIR - F ₂ | DSC -T _g (°C) | DSC -T _f (°C) | T _g /T _f | k _p /k _t ^{1/2} |
|------------|-------------------------------|------------------------|-----------------------|--------------------------|--------------------------|--------------------------------|-----------------------------------------------|
| C1 | 10 | 2.18E+05 | 50% | 236.29 | 309.45 | 0.87 | 0.00034 |
| C2 | 30 | 1.37E+05 | 43% | 245.76 | 306.55 | 0.90 | 0.00075 |
| C3 | 60 | 1.17E+05 | 49% | 246.40 | 307.28 | 0.90 | 0.00074 |
| C4 | 90 | 1.44E+05 | 45% | 244.86 | 299.32 | 0.90 | 0.00374 |
| C5 | 120 | 1.40E+05 | 48% | 244.39 | 300.01 | 0.90 | 0.00715 |
| C6 | 150 | 3.78E+05 | 47% | 275.07 | 301.87 | 0.95 | 0.00535 |
| C7 | 200 | 4.26E+05 | 42% | 315.57 | 336.23 | 0.97 | 0.01099 |

Table 3. FTIR, DSC and rheological characterization of AAm-AMPSNa copolymers.

Based on the experimental results, the values of the M_v (molecular weight), T_g (glass transition temperature), and T_f (fusion temperature) increase according to the shear rate. M_v of polymers obtained under C6 and C7 conditions increased 281 and 317%, respectively, compared with C2. In all experiments, the AMPSNa molar composition of the copolymer chains was relatively constant (between 42 and 50%) according to the calculated F₂ parameter. This result was supported by the FTIR results.

Copolymers synthesized at 150 and 200 s⁻¹ increased their T_g by 12% and 29%, respectively, considering a reference value of T_g=245°C. Increased values of T_g and T_f are consequences of both M_v [23] and stiffness of the chains. The latter is a consequence of the incorporation of sulfonate groups (e.g. AMPSNa) into the polymer [24].

11. Geometry, grid, and boundary conditions

The configuration of the grids for each stirring model (ROT, MRF, and SM) is shown in **Table 4**. A non-structured grid was adapted to generate tetrahedral and hybrid volumes (Tet/Hybrid).

| Model | ROT | MRF | SM |
|---------------------------|-------------------------------|-----|----------|
| Cells | 381,352 | | 201,927 |
| Faces | 783,158 | | 439,109 |
| Nodes | 75,560 | | 40,052 |
| Volume elements | Mixed | | |
| Elements in face | Triangular and quadrilaterals | | |
| Volume (cm ³) | 3757.353 | | 3758.577 |
| Fluid regions | 1 | | 2 |

Table 4. Grid parameters for ROT, MRF, and SM models.

The geometry generated in Gambit® is presented in **Figure 5**. Zone A was defined as the stirred region, while zone B as the stationary region.

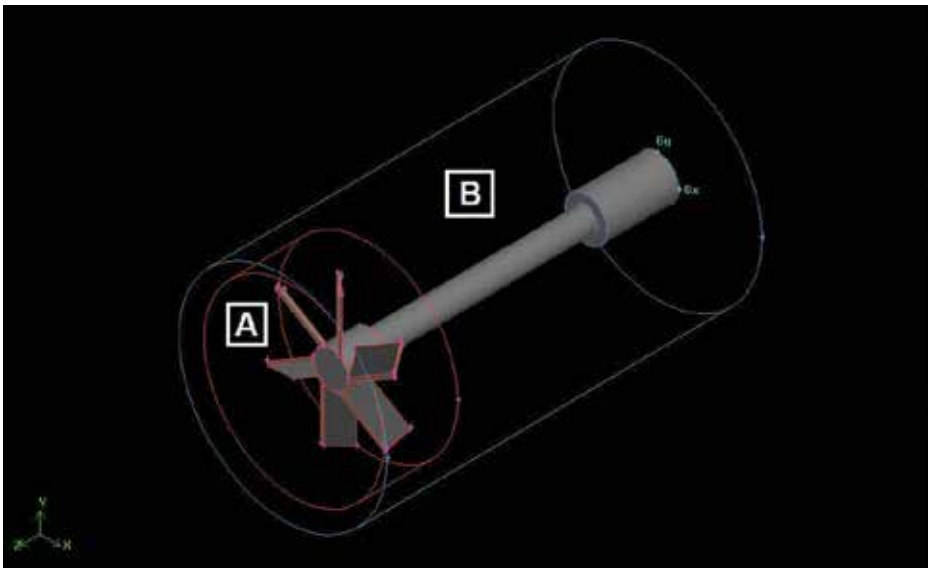


Figure 5. Isometric: stationary volume (A) and stirred volume (B).

The boundary conditions were defined as “walls” for the impeller and the reactor surfaces, which implies a no-slip condition. On the top face of the reactor, a zero-shear stress boundary condition was established, implying a free fluid movement. Region A was defined as “interior” during SM and MRF simulations. Only for SM an “interface” was defined in the boundary between the stirred and stationary volumes.

Using the original geometry, the effect of resized grid cells (M_{400k} and M_{200k}) on the mathematical simulation was analyzed through the velocity variation over a defined position within the reactor; such results are presented in **Figure 6**.

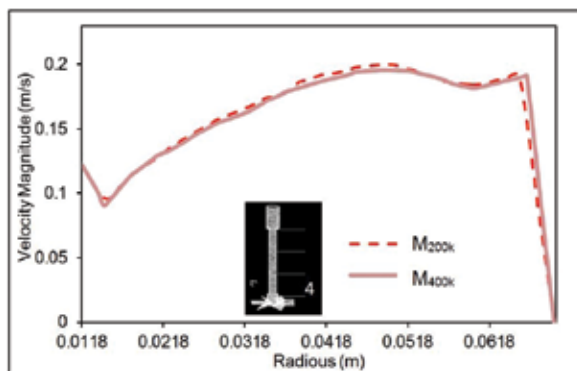


Figure 6. Radial velocity comparison between grids M_{400k} and M_{200k} .

12. Turbulence and stirring model selection

Standard, RNG and realizable $k-\epsilon$ were compared in terms of the convergence time. Global residual tolerances for all variables (velocity, continuity, $k-\epsilon$) were kept constant at 1×10^{-3} . Realizable $k-\epsilon$ was selected due to its reduced convergence time (1305 iterations), this being compatible with the literature recommendation for high-velocity rotational flows [25, 26].

Various simulations with liquid water were performed at 100 rpm ($Re=11,739$) to select a stirring model (ROT, MRF, or SM). All simulations were run using a 3D no-stationary solver. Cross-sections, as shown in **Figure 11**, were used to visualize velocity profiles in the stirred tank. **Figures 7–9** show a typical velocity behavior of stirred tanks: a mixing zone in the upper section, high velocity gradients close to the moving blades, and a dead recirculation zone below the impeller. The mathematical model was validated by comparing the mixing time obtained against experimental data.

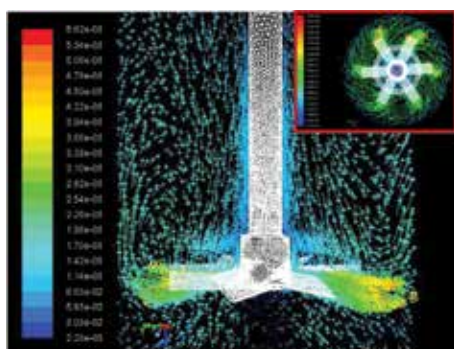


Figure 7. MRF, colored vectors by velocity magnitude in m/s (Scale/Omission relation of 50/1).

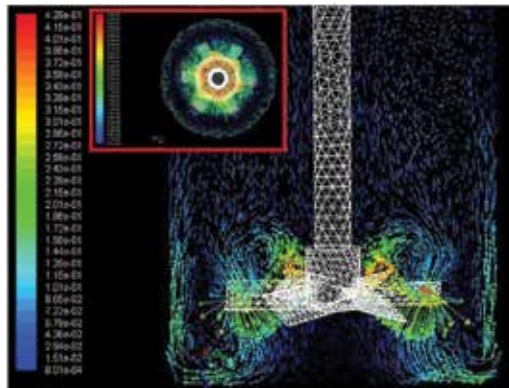


Figure 8. SM, colored vectors by velocity magnitude in m/s (Scale/Omission relation of 50/1).

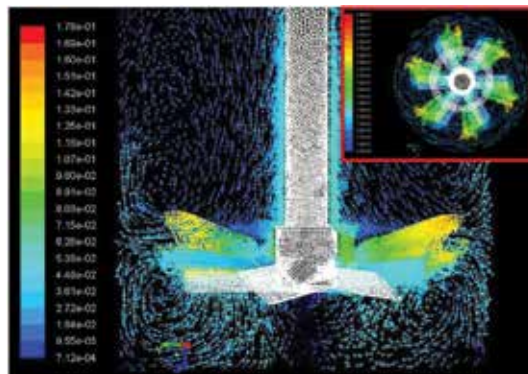


Figure 9. ROT, colored vectors by velocity magnitude in m/s (Scale/Omission relation of 50/1).

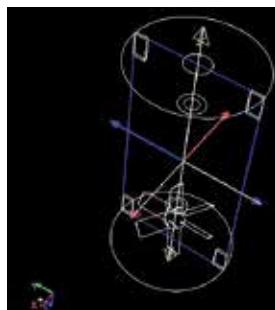


Figure 10. Cross-section for analysis of simulated data.

The graphics presented in **Figures 7–9** were taken from the cross-section defined in **Figures 10 and 11**. **Figures 7–9** show the velocity profiles of MRF, SM, and ROT models. The color

scale indicates the magnitude of each vector view from two planes: Y-Z and X-Y. All images enclosed in red squares are radial cross-sections near the blades.

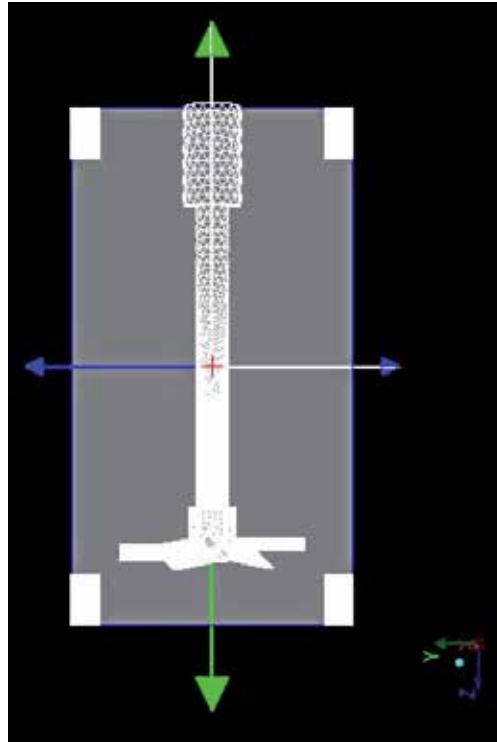


Figure 11. Cross-section defined in the Y-Z plane.

13. Tracer analysis in Fluent®

Tracer simulations were developed considering an unsteady state, using as initial condition, the data obtained at the stationary state solution ($t=0$). The stirrer speed was set at 100 rpm using liquid water and tracer as materials. Initial injection positions are shown in **Figure 12**. This configuration was used in all tracer simulations. Monitors were defined as spheres with a radius of 0.8 cm and were used to track the tracer concentration in a specific region (**Figure 13**).

Each monitor registers a mass fraction of tracer every 0.55 s. Results for all simulations are presented in dimensionless concentration.

Asymptotic behavior of the tracer concentration is a criterion to define the mixing time. Tracer curves for each model are shown in **Figures 14–16**.

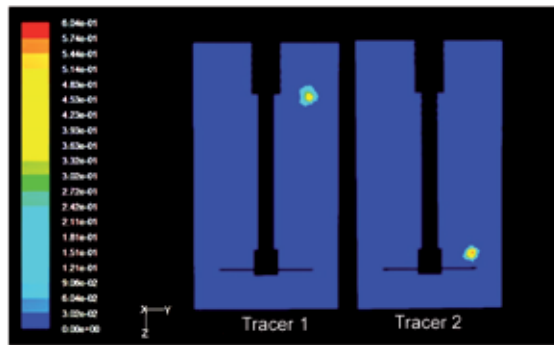


Figure 12. Tracer injection zones. Tracer 1 in (0, 4, 5) cm and Tracer 2 in (0, 4, 20) cm.

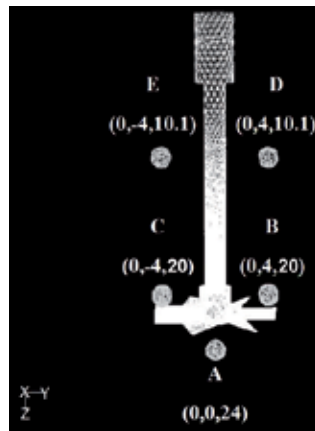


Figure 13. Spherical monitors and their spatial location.

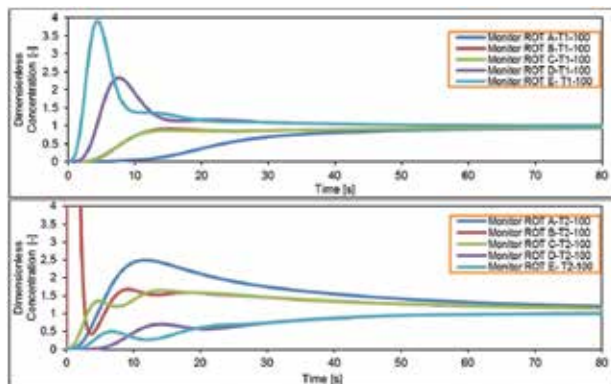


Figure 14. ROT tracer evolution curves after injection in regions 1 and 2.

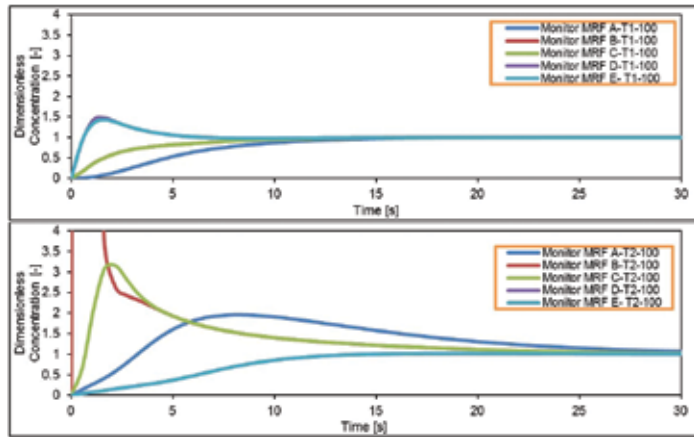


Figure 15. MRF tracer evolution curves after injection in regions 1 and 2.

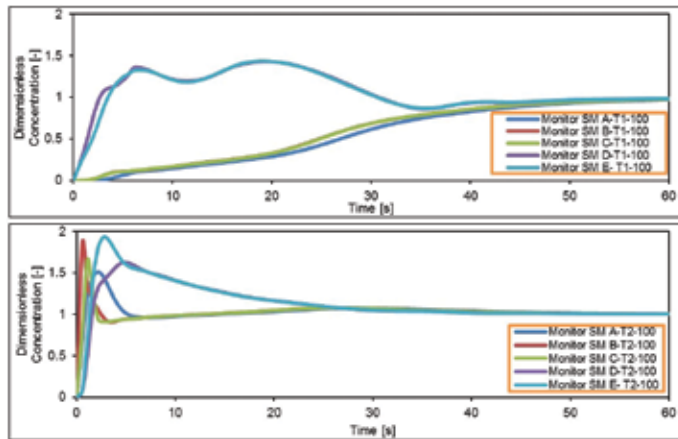


Figure 16. SM tracer evolution curves after injection in regions 1 and 2.

Mixing time of ROT simulations diverges drastically between injections. Tracer 1 curves start to become asymptotic at 80 s, while there is no clear tendency when the injection is made in region 2.

Results from **Figure 16** show a significant tracer concentration variation above 30 s. SM predicts that mixing time of all monitors is beyond 80 s.

SM tracer curves of **Figure 16** differ qualitatively and quantitatively from curves obtained in **Figures 14** and **15** (ROT and MRF). In general, the monitored tracer behavior is in agreement with the velocity field of a stirred tank.

Concentration contours are presented in **Table 5** for tracer 1 and 2. Mixing profiles are shown on a radial cross-section over the X-Y plane.

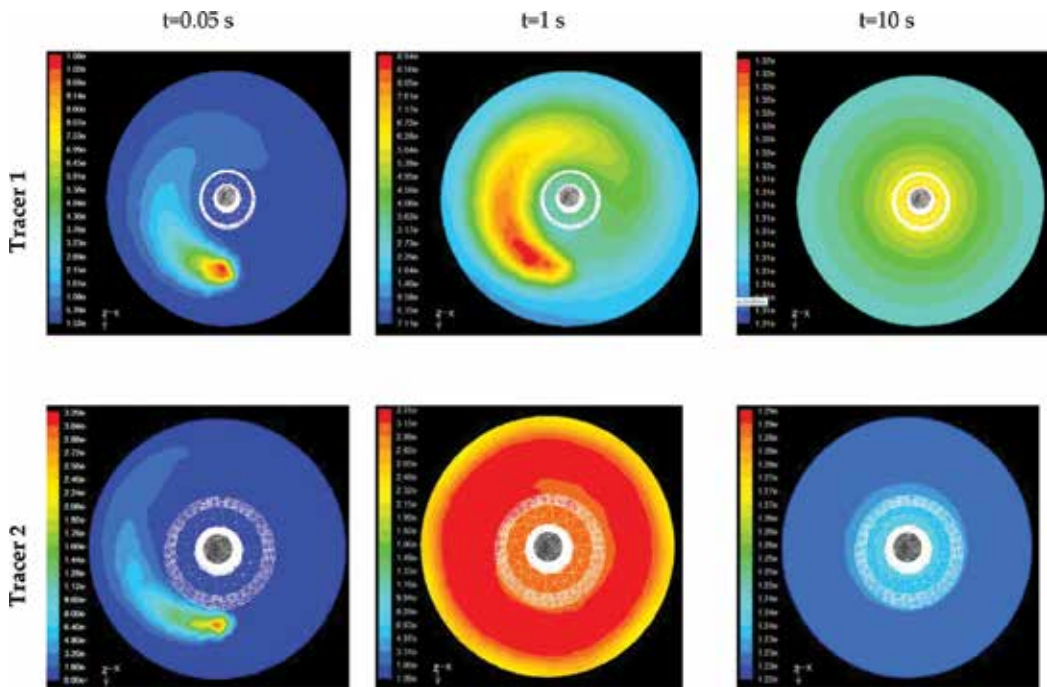


Table 5. Mass fraction of tracer dispersion at different times.

14. Validation of the computational model

The experimental mixing curves for Monitor C (Tracer 1) and E (Tracer 2) were obtained from pH data plots against time. Experimental and simulation data are compared in **Figure 17**.

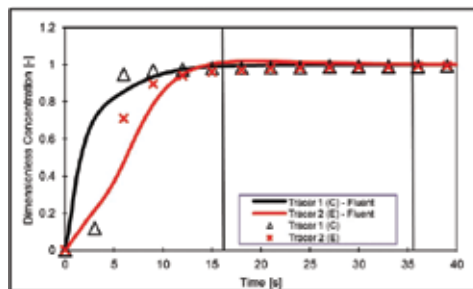


Figure 17. Comparison of experimental data (Δ, \times) and numerically ($-$) obtained solutions.

Simulated curves in **Figure 17** were obtained at a stirrer speed of 100 rpm with liquid water, using MRF and realizable $k-\epsilon$ as working models. The injections were made in the regions established in **Figure 12**.

The mixing time for tracer 1 has a value of 15.4 s and for tracer 2, a total of 35.8 s (**Figures 18 and 19**). The criterion used to define the mixing time was the standard deviation of the concentration data registered in all monitors [26].

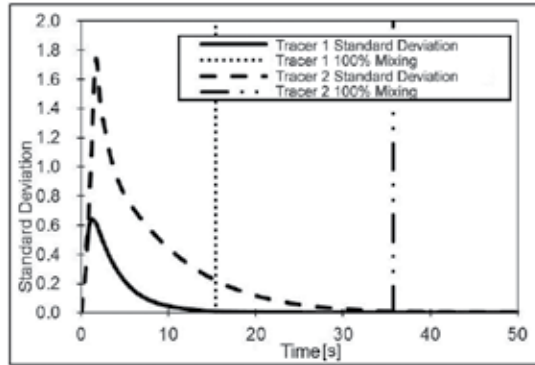


Figure 18. Standard deviation of data from MRF model at 100 rpm.

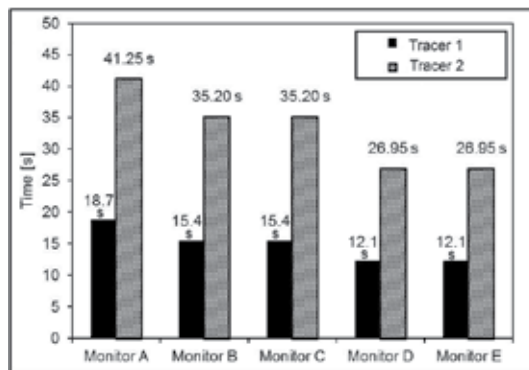


Figure 19. Mixing times of tracer 1 and tracer 2 (all monitors).

The experimental and numerical mixing times are shown in **Table 6**. The mixing time in Monitor C differs from the experimental value by 5 seconds, while Monitor E differs from it by 0.1 seconds. The resemblance between Monitors B-C and D-E is due to their spatial position.

| Monitor | Tracer 1 (C) | Tracer 2 (E) |
|------------------|--------------|--------------|
| Experimental | 21 s | 27 s |
| Simulated | 15.4 s | 26.9 s |
| Global simulated | 15.4 s | 35.8 s |

Table 6. Simulated and experimental mixing times for tracer 1 and 2.

The injection zone 1 (Tracer 1) allows a lower mixing time compared with the injection zone 2. However, mixing times of Monitors C and E are less sensitive to changes in stirrer speed.

The SM and ROT stirring models were discarded because the calculated mixing time does not correspond to the experimental data, as seen in **Figures 20** and **21**. Experimental mixing time is well fitted by MRF calculations.

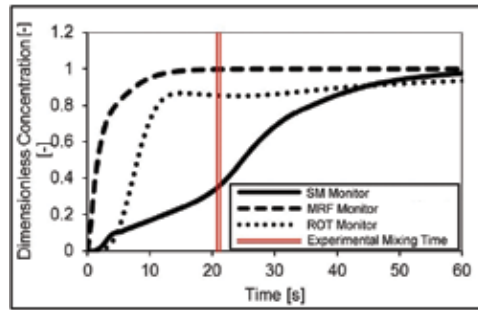


Figure 20. Tracer 1 curves, Monitor C (100 rpm) with 3 different models: MRF, SM, and ROT.

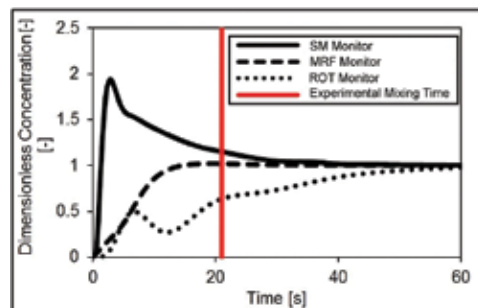


Figure 21. Tracer 2 curves, Monitor E (100 rpm) with 3 different models: MRF, SM, and ROT.

15. Effect of the stirring speed

Once MRF model was selected, a stirring speed swept from 100 to 300 rpm was done. Monitor C mixing time presents minor variations between 100 to 200 rpm; however, at 300 rpm the mixing time is drastically reduced (**Figure 22**). In contrast, in Monitor E the mixing time is reduced by increasing the stirring speed. An increase in the stirring speed leads to a reduced mixing time, allowing better contact among chemical species. Nevertheless, in the case of polymerization, a high stirring speed (above 300 rpm) can produce mechanical degradation of the formed chains.

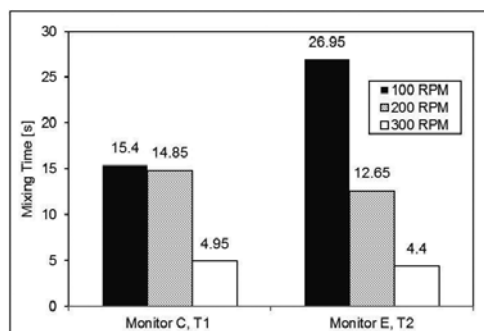


Figure 22. MRF simulated mixing times at 100, 200 and 300 rpm.

16. Conclusions

Chemical product design requires the development of standardized procedures to ensure reproducibility and quality of the synthesized product. If this is possible, then the impact of any experimental variation on the product properties can be properly analyzed and eventually, the optimization of the designed product can be reached.

To set up a procedure for the synthesis of an AAm-AMPSNa copolymer in a batch reactor, we have used CFD-simulations and rheokinetics. These tools were used to research the relationship between the polymerization reaction kinetics and the mixing process.

The AAm-AMPSNa copolymer properties (M_v , T_g and $k_p/k_t^{1/2}$) increase according to the shear rate (better mixing) in the synthesis. Specifically, the molecular weight of the polymer synthesized at the highest stirring speed (C7) increases up to 317% with respect to the lowest stirring speed in the stirred tank (C2), showing a direct relation between the mixing stirring times and the chemical kinetics.

MRF and realizable $k-\epsilon$ satisfactorily model the mixing process in the stirred tank. The tracer curves obtained numerically from CFD were experimentally validated using a 1 M NaOH tracer. The simulated mixing time differs by 0.4% with regard to the experimental value of Monitor E (Tracer 2).

According to the tracer analysis and the rheokinetics of the polymerization, it is recommended that reagents be injected (e.g. initiators or REDOX pairs) in the region defined as “Tracer 1,” operating the reactor at 217 rpm (200 s^{-1}) and controlling the temperature at 60°C .

To give continuity to this work, we suggest to include the rheokinetics model in the transport phenomena equations, to consider rheology progression and its effect on the flow pattern, as a consequence of the growing polymer chains.

Acknowledgements

We gratefully acknowledge financial support of this investigation from “Fondo Sectorial CONACyT-SENER Hidrocarburos” under grant #0185183, “Proceso de Recuperación Mejorada con la Tecnología de Inyección de Químicos (ASP) con Aplicación Mediante Prueba Piloto en el Campo Poza Rica”, and we sincerely thank the USIP from Facultad de Química, UNAM for the support. Finally, we appreciate the helpful suggestions of Ada Galena Barragán Aroche, for the grammar review on this manuscript.

Author details

Gerardo M. Pineda-Torres, Cecilia Durán-Valencia, Fernando Barragán-Aroche and Simon López-Ramírez*

*Address all correspondence to: simon.lopez.ramirez@gmail.com.

USIP, Chemistry Faculty, National Autonomous University of Mexico, Mexico City, Mexico

References

- [1] Froment, G., Bischoff, K. Chemical Reactor Analysis and Design. New Jersey: John Wiley & Sons, Inc; 1979. 765 p.
- [2] Ranade, V. Computational Flow Modelling for Chemical Reactor Engineering. Pune: Academic Press; 2002. 452 p.
- [3] Meyer, T., Keurentjes, J. Handbook of Polymer Reaction Engineering. Lausanne: Wiley-VCH; 2005. 1102 p.
- [4] Odian, G. Principles of Polymerization. 4th ed. New Jersey: John Wiley & Sons; 2004. 812 p.
- [5] Harris, C., Roekaets, F., Rosendal, F. Computational fluid dynamics for chemical reactor engineering. Chemical Engineering Science. 1996; 51: 1569–1594.
- [6] Patel, H., Ein-Mozaffari, F., Ramdhane, D. CFD analysis of mixing in thermal polymerization of styrene. Computers and Chemical Engineering. 2010; 34: 421–429.
- [7] Bird, R., Stewart, W., Lightfoot, E. Transport Phenomena. New Jersey: John Wiley & Sons, Inc; 2002. 897 p.
- [8] Levenspiel, O. Tracer Technology Modelling the Flow of Fluids. Berlin: Springer; 2012. 137 p.

- [9] Post, T. Understand the Real World of Mixing [Internet]. 2010. Available from: <http://www.postmixing.com/publications/100315ceparticle.pdf> [Accessed: 2016-03-01]
- [10] López-Ramírez, S., Barreto, J. de J., Vite-Martínez, P., Romero-Serrano, J. A., Durán-Valencia, C. Physical and mathematical determination of the influence of input temperature changes on the molten steel flow characteristics in slab tundishes. *Metallurgical and Materials Transactions B*. 2004; 35B: 957–966
- [11] Wever, D., Picchioni, F., Broekhuis, A. Polymers for enhanced oil recovery: a paradigm for structure-property relationship in aqueous solution. *Progress in Polymer Science*. 2011; 36: 1558–1628.
- [12] Durán-Valencia, C., Bai, B., Reyes, H., Fajardo-López, R., Barragán-Aroche, F., López-Ramírez, S. Development of enhanced nanocomposite preformed particle gels for conformance control in high-temperature and high-salinity oil reservoirs. *Polymer Journal*. 2014; 46: 277–284.
- [13] Barnes, H., Hutton, J., Walters, K. *An Introduction to Rheology*. Netherlands: Elsevier Science Publishers B.V.; 1989. 199 p.
- [14] Malkin, A., Kulichikhin, S. *Rheokinetics Rheological Transformations in Synthesis and Reactions of Oligomers and Polymers*. Moscow: Wiley-VCH; 1996. 326 p.
- [15] Brodke, R., Hershey, H. *Transport Phenomena a Unified Approach*. Ohio: McGraw-Hill; 1988. 847 p.
- [16] Wendt, J. *Computational Fluid Dynamics*. Berlin: Springer-Verlag Berlin Heidelberg; 2009. 332 p.
- [17] CFD-Online. History of CFD [Internet]. 2013. Available from: http://www.cfd-online.com/Wiki/History_of_CFD [Accessed: 2016-03-01]
- [18] Soto, D. *Análisis del mezclado en un reactor de polimerización de etileno*. Bogotá. Universidad Nacional de Colombia; 2013.
- [19] ANSYS Inc. *Ansys Fluent Theory Guide* [Internet]. [Updated: <http://orange.engr.ucdavis.edu/Documentation12.0/120/FLUENT/flth.pdf>]. Available from: 2010-03-01
- [20] Santos, V., Brunet, L., Rolland, M. Numerical CFD simulation of a batch stirred tank reactor with stationary catalytic basket. *Chemical Engineering Journal*. 2012; 207–208: 596–606.
- [21] Durmaz, S., Okay, O. Acrylamide/2-acrylamido-2-methylpropane sulfonic acid sodium salt-based hydrogels: synthesis and characterization. *Polymer*. 2000; 41: 3693–3704.
- [22] Sánchez, J., Casas, J., Fernández, J. Shear rate in stirred tank and bubble column bioreactors. *Chemical Engineering Journal*. 2006; 124: 1–5.

- [23] Chanda, M. Introduction to Polymer Science and Chemistry. Florida: Taylor & Francis; 2006. 640 p.
- [24] Carraher, C. Polymer Chemistry. 6th ed. New York: Marcel Dekker, Inc.; 2003. 902 p.
- [25] Marshall, E., & Bakker, A. Computational Fluid Mixing. Pennsylvania. ANSYS. Handbook of Mixing; 2001. TN144.
- [26] Vite-Martínez, P., Durán-Valencia, C., Cruz-Maya J.A., Ramírez-López A., López-Ramírez S. Optimization of reagents injection in a stirred batch reactor by numerical simulation. Computers and Chemical Engineering. 2014; 60: 307–314.

*Edited by Noreen Sher Akbar
and O. Anwar Beg*

This book features state-of-the-art contributions in mathematical, experimental and numerical simulations in engineering sciences. The contributions in this book, which comprise twelve chapters, are organized in six sections spanning mechanical, aerospace, electrical, electronic, computer, materials, geotechnical and chemical engineering. Topics include metal micro-forming, compressible reactive flows, radio frequency circuits, barrier infrared detectors, fiber Bragg and long-period fiber gratings, semiconductor modelling, many-core architecture computers, laser processing of materials, alloy phase decomposition, nanofluids, geo-materials and rheo-kinetics. Contributors are from Europe, China, Mexico, Malaysia and Iran. The chapters feature many sophisticated approaches including Monte Carlo simulation, FLUENT and ABAQUS computational modelling, discrete element modelling and partitioned frequency-time methods. The book will be of interest to researchers and also consultants engaged in many areas of engineering simulation.

Photo by polesnoy / iStock

IntechOpen

